学位論文

Spin waves and solitons in uniaxial chiral magnets

(一軸性カイラル磁性体のスピン波とソリトン)

平成28年12月博士（理学）申請

東京大学大学院理学系研究科

物理学専攻

正木 祐輔

Abstract

In this thesis, we develop theories to investigates chiral magnets, which have been a field of intensive study with various experimental techniques such as neutron scattering measurement, circular polarized X-ray diffraction, and the Lorentz transmission electron microscopy(TEM) as well as the material synthesis. Chiral magnets have antisymmetric spin interactions, called Dzyaloshinskii–Moriya interaction (DMI), which emerges because of broken inversion symmetry and strong spin-orbit coupling. The spin system has chirality due to the DMI, which induces non-trivial spin structures, e.g., helical and conical states, soliton lattice, skyrmions.

This thesis mainly focuses on a uniaxial chiral magnet represented by $Cr_{1/3}NbS_2$. The lattice structure of this material has the space group symmetry $P6_322$, but we simplify it as a tetragonal lattice system with a single type of DMI at zero magnetic field. This DMI induces a helical order with modulation along the helical axis. This system shows a rich phase structure with changing field strength and direction even at zero temperature. The field is rotated from perpendicular to parallel directions to the helical axis. When the field is applied along the perpendicular direction $\vec{H}_{\rm ex} = (H^x_{\rm ex}, 0, 0)$, the system shows a lattice structure of solitons, which have a highly nonlinear spatial pattern. The corresponding phase transition is unconventional because of its logarithmic singularity rather than conventional power law. When the field is applied along the parallel direction $\vec{H}_{\rm ex} = (0, 0, H^z_{\rm ex})$, the transition shows conventional power-law singularities, but non-reciprocity in the spin wave excitations develops for $H^z_{\rm ex} < H_{\rm c}$, where $H_{\rm c}$ is the critical field of the transition. The non-reciprocity is the asymmetry between the right- and left-propagations.

Main results of the present thesis consist of two parts. The first part is about the spin wave structure of the uniaxial chiral magnet under parallel field $(0, 0, H^z_{\rm ex})$, and it is discussed in Chap. 3. It is well known that the dispersions of spin wave excitation energy $E_{\boldsymbol{q}}$ are non-reciprocal $E_{\boldsymbol{q}} \neq E_{-\boldsymbol{q}}$ in the uniform state of the chiral magnets for $H^z_{\rm ex} > H_{\rm c}$. We have clarified how the non-reciprocity appears in the spin wave structure at $H^z_{\rm ex} < H_{\rm c}$. We study the excitation spectrum by calculating the dynamical spin structure factor $C^{\mu\nu}(q, \omega)$ for momentum q parallel to the helical axis. We find that the transverse component such as $C^{xx}(q, \omega)$ has two branches of its peak, and $C^{xx}(q, \omega) = C^{xx}(-q, \omega)$. Note that peak positions (q, ω) and $(-q, \omega)$ belong to different branches. Intensity of one branch increases with increasing field, while the other's decreases and disappears completely at the critical field $H_{\rm c}$. Hence the non-reciprocity develops through the asymmetry of spectral intensity $C^{xx}(q, \omega) \neq C^{xx}(-q, \omega)$, and finally there is only one non-reciprocal branch for $H^z_{\rm ex} \geq H_{\rm c}$. The uniaxial system is convenient to

observe this behavior since the system changes from the helical state to the uniformly saturated state through the conical state by increasing magnetic field along the chiral axis, and each step is feasible for thorough analysis.

The second part of the main results is discussed in Chap. 4 and it is about the phase diagram and surface effects in tilted magnetic field from the view point of chiral solitons. Laliena *et al.* obtained the phase diagram numerically, and found that it is separated into one ordered phase with periodic spatial modulation and one disordered phase in which spins are polarized by the field[Phys. Rev. B **93**, 134424 (2016)]. Their phase boundary consists of two lines of continuous phase transition and one line of discontinuous phase transition in between. The line of discontinuous transition connects with the two continuous transition lines at multicritical points. The continuous phase transition around $H_{\rm ex}^x \sim 0$ is called the instability-type one, while the other continuous phase transition around $H_{\rm ex}^z \sim 0$ is called the nucleation-type following de Gennes's classification. The standard picture of the latter transition is a condensation of solitons. Following the Schaub and Mukamel[Phys. Rev. B **32**, 6385 (1985)], we call the point connected to the instability-type the *tricritical point* and the point connected to the nucleation-type the *multicritical point*.

We perform a linear analysis which examines an asymptotic form of an isolated soliton or a sinusoidal mode for a small deviation from the uniform state. This analysis separates the phase diagram into three regions, and we find that the region described by a distorted conical order has the boundary consistent with the instability-type phase transition. In order to study this instability, we derive the Landau energy of this order starting from the microscopic Hamiltonian and determine the corresponding phase boundary and the location of the tricritical point. They are consistent with the numerical results, and this justifies our Landau expansion. We separate the other region where a soliton tail structure exists into two subregions depending on whether the tail oscillates or not and find that the soliton interaction changes its sign on the phase boundary at the multicritical point. Hence we confirm that the mechanism of the discontinuous phase transition is attractive interaction between solitons, as the same as that studied by Schaub and Mukamel. Then we determine more precisely the instability field of solitons since the linear analysis underestimates the soliton instability. We call the instability field the H_0 line and find that the instability is caused by the spin motion toward the helical axis.

We also study the surface effects preventing solitons from entering the system, and calculate a surface barrier, which is similar to the Bean–Livingston barrier of superconducting vortices. This may lead a hysteresis observed in experiments for micrometer-sized samples, which is not related to the discontinuous phase transition mentioned above. In experiment, a large jump is observed in decreasing field. Our theoretical result shows that the field at which the surface barrier disappears agrees with the field at jump in magneto-resistance experiments. We also apply this theory to the surface barrier of skyrmions, and find that its elongation instability to the soliton occurs before the surface barrier vanishes.

Finally Chap. 5 summarizes our main results, their implications, and future perspectives associated with this thesis.

Acknowledgment

I appreciate the large amount of support from many people, especially the people I list in the following, for completing this thesis.

First of all, I would like to express my sincere gratitude to Yusuke Kato. I have acquired a lot about not only physics but also, research morals, and research spirit from his advise as a collaborator, as a critic, and as a supervisor with his honest attitude. We spent a lot of time together discussing topics of many fields in physics. Thereby I achieved several interesting works on superconducting vortices too. I could never thank enough.

Second, I would like to thank Robert Stamps, who was a host at the university of Glasgow when I visited there twice. Back then, I was starting to study magnetism, and he devoted his time for checking my progress almost every day. His kind considerations made my stay in Glasgow extremely comfortable. In particular, I learned the importance of demagnetization for comparison with experiments. I hope for our continuous collaboration from now on.

Special thanks to Alex Bogdanov. He visited the Univ. of Tokyo's Komaba campus and gave us intensive lectures and very intensive private discussions in February, 2017. In these discussions, he explained me and my colleagues the importance of soft modulus effects in topological magnets, and introduced us Schaub and Mukamel's paper, which promotes our comprehension extraordinarily. In addition to this scientific part, I think we had a really good time chatting with strong coffee then.

I am indebted to Katsuya Inoue, Jun-ichiro Kishine, and Yoshihiko Togawa. Their kind supports, and sincere concerns and considerations for me are like my father's. Moreover Yoshi Togawa and his student Ryuya Aoki performed the experiments for this thesis in chapter 4.8. I really appreciate their efforts and kind help.

Victor Laliena and Javier Campo, and also their Ph.D student, German Albalate were perfect hosts when I visited Zaragoza with Prof. Kato. We enjoyed our daily worthwhile discussions and the delicious food and wine there. I hope everything goes well with our on-going and future collaborations.

I appreciate beneficial discussions with Misako Shinozaki and Yoshihiko Nishikawa about chiral magnets. They are insightful and in many cases the discussions stimulated my projects.

While working on chiral magnets, I sometimes need to blow away the cobwebs. In such a case, discussion about superconductivity and superfluidity with Yasumasa Tsutsumi was, no doubt, necessary for me. Obviously it was truly useful for my project on superconducting vortices, and will be helpful for my future work in superfluidity and superconductivity. I hope

we can accomplish our collaboration soon.

Special thanks also to all the people in physics group in Komaba campus and MCMP group and football mates in Glasgow. I had definitely a good time with them.

Lastly I am deeply grateful to my parents for supporting me throughout my life.

I would like to acknowledge the financial support of a Grant-in-Aid for JSPS Fellows (Grant No. 16J03224) and the Program for Leading Graduate Schools, the Ministry of Education, Culture, Sports, Science and Technology, Japan.

Contents

Chapter 1

Introduction

1.1 Background

Topology has been a concept of great importance in condensed matter physics for about half a century. It had been introduced into condensed matter physics as a mathematical tool in 1970s[1], to classify the topological defects, such as quantum vortices in magnetic systems, superconductors and superfluids, and dislocation and disclinations in crystals and liquid crystals. Many of topological defects are described and classified by homotopy groups, and are characterized by the corresponding integer called topological indices or winding numbers. For an example, a point defect in the two-dimensional space or a line defect in the three-dimensional space is described by the fundamental group $\pi_1(S^1) = \mathbb{Z}$, which is equivalent to how many times a particular quantity of the order parameter rotates while one rotates in the real space around the defect. An example of the higher homotopy group is $\pi_2(S^2)$ corresponding to the skyrmion number. Vortices and dislocations are very important to describe the phase transition in two-dimensional systems, so-called Kosterlitz–Thouless transition[2–4].

In 1980s, after the observation of the quantum Hall effect (QHE)[5] and accompanying theoretical works[6], a new type of topology was introduced, which is associated with Berry's geometrical phase. Thouless, Kohmoto, Nightingale, and den Nijs developed the TKNN number appearing in the quantized Hall conductivity[7]. The TKNN number picks up the topology of Bloch wave functions. Later Kohmoto clarified that the TKNN number is identified with the first Chern number[8]. Haldane constructed the model showing the QHE without a magnetic field[9], which is called quantum anomalous Hall effect (QAHE). The concept of the Berry phase is also important for the anomalous Hall effect[10–12]. Kane and Mele proposed the time-reversal-invariant version of QAHE, which is the quantum spin Hall effect (QSHE), in 2005[13, 14], motivated by the spin Hall effect[15, 16]. QSHE has attracted intensive attentions, opening the field of the topological insulator[17, 18]. The topological invariant charactering quantized spin Hall conductivity is given by $\mathbb{Z}_2$ invariant[14], which is the extension of the TKNN number describing the Haldane's model. The whole classification of topological insulators and topological superconductors based on the Altrand–Zirnbauer

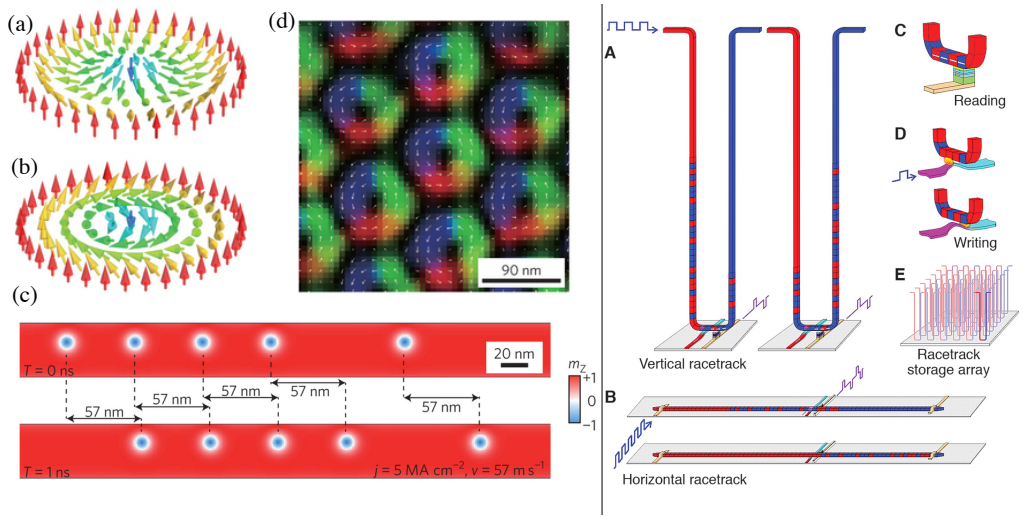

Figure 1.1: (Left) (a) Néel skyrmion. (b) Bloch skyrmion. (c) Skyrmion on racetrack memory. (d) Lorentz transmission electron microscopy. Figures (a)–(c) are from [24] and (d) is from [25]. (Right) Domain wall on racetrack memory. Figure is from Ref. [26]

symmetry groups[19] with the calculation of its Homotopy group was done by Ryu *et al.*[20–22]. It is a common property that the non-trivial topology in the bulk is reflected to the presence of edge mode, and it is so-called bulk-edge correspondence[23]. Topology in these cases is inherent in their Bloch wave functions in the momentum space and appears through the Berry curvature. In many topological systems in this family, the spin-orbit interaction (SOI) plays an important role instead of the magnetic field in QHE. The SOI opened up the field of the topological insulator in 2000s.

One of the most intensive study in these days may be the field of topological magnets: Much attention has been paid to studies of topological textures such as domain walls, magnetic bubbles or skyrmions and magnetic vortices appearing in magnets[27–34] since they are expected to work as information carriers in the memory device (the race track memory[24, 26, 35–38]) as well as fundamental interests in dynamics and statics associated with the topological textures. In particular, skyrmion has attracted more attention since skyrmion can be driven by lower spin-polarized current[39–41]. Figure 1.1 shows the images of skyrmions and the racetrack memory using domain wall[25, 26]. By the way, SOI is relevant also in magnets. Ferromagnets, where such topological textures are often observed, with strong coercive field are highly desired for stability. A strong coercive field is attributed to the anisotropy, which actually exists in a real magnetic system and originates from the SOI and crystal fields. SOI plays a role of reflecting the crystal symmetry in the anisotropy of the spin structure. Anisotropy has relevant effects on the topological textures: The domain wall width is determined by $\sqrt{A/K}$, where K is the anisotropy and A is a spin stiffness constant. This width is crucial to achieve a tiny information carrier and correspondingly a tiny magnetic memory device. A magnetic bubble is also (meta)stabilized by the anisotropy as well as the dipole-dipole interaction[28–30, 42].

Another important role of the SOI is the introduction of an antisymmetric interaction between spins with the combination of the lack of inversion symmetry or mirror symmetry.

The reason of the recent intensive studies is somewhat attributed to the experimental observations of topological textures in *chiral magnets*[34, 43] as well as the numerical progress in *frustrated magnets*[44–46]. The difference between these two is as follows: The chirality of the topological structures is fixed in chiral magnets, while left- and right-handed structures are degenerated in frustrated magnets[47]. [We make a remark on the term "chiral magnet": In a magnetic crystal with crystalline chirality or a magnetic chiral molecule, the chirality is transcribed to the magnetic interaction via spin-orbit coupling. The magnetic interaction is antisymmtric in the spin Hamiltonian and called Dzyaloshinskii–Moriya interaction (DMI)[48, 49]. The DMI gives chirality to a spin system and we use the chiral magnet for a magnetic system with DMI.] Thus we can say that the order or topological textures in chiral magnets are protected by its chirality, while not in frustrated magnets and separated into multiple domain structures, i.e., mixture of left- and right-handed orders. The stability of each state in chiral magnet is expected to be controllable because of this chiral protection. Another difference is the length scale of topological textures. The atomic scale of the modulation realizes in frustrated magnets, while the scale ranges from 1nm to 100nm in chiral magnets. This rather large length scale comes from the ratio of the exchange interaction and DMI. Because this long-scale modulation can be approximated as a smooth variation, the modulation is literally topologically protected. Therefore chiral magnets are appropriate subjects to study physics of the topological textures.

How does the DMI modulate spin structures? DMI takes the form of the vector product for two spins. Within a classical picture of a lattice model, it favors the orthogonal configuration of two spins, while the exchange interaction does the parallel or antiparallel alignment since it takes the form of the inner product. The competition leads to the helical structure with finite rotational angle. More complicated structures are caused by a magnetic field and/or more than one DMI. The DMI was first introduced by Dzyaloshinskii in order to explain the weak ferromagnetism of α-Fe_2O_3 and Cr_2O_3 on the basis of symmetry considerations[48]. Later Moriya derived it in a microscopic approach[49]. Their works clarified that the DMI originates from inversion-symmetry breaking and the SOI.

The recent remarkable developments of experimental techniques have actually revealed the modulated spin structures: non-trivial structures are observed using the small angle neutron scattering (SANS)[50–53] and high resolution magnetic microscopies[25, 54–57], and it is also highly developed to synthesize of bulk chiral magnets, and chiral magnetic thin film structures with interface induced DMIs[24, 58–60].

In this thesis, we mainly focus on the uniaxial chiral magnet. The material motivating us is $Cr_{1/3}NbS_2$, which belongs to the space group of $P6_322$[43, 61, 62]. The dominant DMI is along the c-axis of the crystal and we call this axis the helical axis. For the uniaxial chiral magnet, though the skyrmion states do not appear, there are still rich phenomena and states which are rather simple and pedagogical than those for the cubic materials such as MnSi[50, 63] and FeGe[54, 64]. The ordered state at zero field is a helical state propagating along the

helical axis. There are two characteristic directions for applications of magnetic field.

(i) One is parallel to the helical axis. This does not change the character of the ordered state. The ordered state is given by the helical order in the plane perpendicular to the helical axis in the spin space with the uniform component along the helical axis, which is called a conical state. However, excitations develop into the fully non-reciprocal magnon in the uniform state, which is given by $E_{\boldsymbol{k}} \neq E_{-\boldsymbol{k}}$ for a particular direction of $\boldsymbol{k}$. Here $E_{\boldsymbol{k}}$ is the excitation energy of a single magnon with momentum $\boldsymbol{k}$[65–73]. In the presence of the DMI, the magnon acquires the Berry phase during the hopping process. The phase from the uniform DMI is constant and thus does not contribute to the Hall conductivity[1], but it horizontally (i.e. parallel to a momentum axis) shifts the energy dispersion. This can be interpreted as an analogous situation for electrons as follows: the phase is equivalent to the constant vector potential, and the kinetic momentum can be given by the canonical momentum shifted by the vector potential. Shifted dispersion relation has similarity to the Rashba splitting of the electronic dispersion relation(, in more general, splitting because of an antisymmetric spin-orbit coupling)[78]. Magnetic field leaves one of these splitting bands, as the ferromagnetic spin waves have only one direction of the precession. The non-reciprocity is well known and experimentally confirmed, in the uniform state[69, 71–73]. The purpose of Chap. 3 is to investigate the non-reciprocity in the modulated state using the dynamical spin structure factor.

(ii) The other direction of a magnetic field is perpendicular to the helical axis. In this case, the spins are restricted in the plane perpendicular to the helical axis. This field introduces higher harmonics into the helical order of the single-q. The helical structure develops into the periodic structure of a discommensuration[79], so-called chiral soliton lattice[80]. The discommensuration here is a 2π-domain wall which we call a chiral soliton. We can characterize the chiral soliton by the topological charge or winding number defined by $w = (2\pi)^{-1} \int \mathrm{d}z \partial_z \varphi(z)$ with the in-plane angle $\varphi(z)$ of the spin at z, the coordinate along the helical axis. The inter-chiral-soliton distance, which is the period of the chiral soliton lattice, goes to infinity as the field approaches to the critical field and then transforms into the uniform state of the disordered phase. These chiral soliton lattice state and disordered-incommensurate (D-IC) transition are obtained by Dzyaloshinskii first through the analytical solution for the sine-Gordon model: [61, 62, 81–83]. Interestingly this phase transition is not accompanied by the instability, nevertheless the phase transition is continuous. The phase transition can be described by the melting of discommensurations and cannot be described by the Landau theory using a small and local parameter[79]. This is an example of unconventional continuous phase transition caused by topological textures, and this kind of transition is classified into the nucleation-type continuous phase transition by de Gennes[84]. Another example of this kind of transition is that at the lower critical field of type-II superconductors[85].

The whole phase diagram is not well understood yet even for uniaxial chiral magnet. Recently Laliena *et al.* theoretically addressed phase transitions under the tilted field connecting these two directions[86]. This work showed the presence of a discontinuous phase transition

[1]There are cases of magnon Hall effects because of Berry phases on a non-trivial lattice e.g. pyrochlore[74] or for non-trivial spin structure e.g. skyrmion[75–77].

line between two continuous-phase-transition lines and corresponding two critical points. The purpose of Chap. 4 is to comprehend the whole magnetic phase diagram and the origin of discontinuous phase transitions using the chiral solitons. It should be remarked that the phase diagram and phase boundary in cubic system are still controversial[53, 87]. In three dimensional systems, the skyrmion phase can stabilize only assisted by the thermal fluctuation[50]. Moreover, the presence of a fluctuation disordered phase and fluctuation-induced first-order phase transition are proposed near the skyrmion phase pocket called "A-phase"[53, 63, 88]. The reason of the complexity of the skyrmion phase diagram is the presence of a conical phase propagating along the magnetic field, which competes with the skyrmion phase. In contrary to the three dimensional case, a skyrmion phase can stabilize in a thin film which suppresses the stability of the conical phase[89]. In this limit it is predicted that the phase transition depends on whether the interaction between skyrmions is repulsive or attractive[90, 91]. This scenario was developed in the contexts of charge density waves by Jacob and Walker[92] and superconducting vortices in Refs. [93–96]. The magnetic phase diagram is constructed on the basis of the skyrmion states nevertheless they are not the most stable state. Even in the two dimensional system, the competition between skyrmion and helical order under the magnetic field complicates the phase diagram to see phase transition related to the attractive interaction between skyrmions in experiment. In addition, finite temperature makes the phase transition further complicated as there is a melting problem[97–99]. Even in the uniaxial chiral magnet, the controversy between the Monte Carlo simulation[100] and mean field calculation[101, 102] remains. In these senses, the exhaustive study of a simple uniaxial system at zero temperature under the tilted field is necessary for more fundamental understanding.

In addition, we describe a characteristic hysteresis observed in the recent magneto-resistance measurement for micrometer-sized samples[103, 104]. This hysteresis cannot be attributed to the thermodynamic first order phase transition because it is observed for much wider region in the phase diagram than that suggested as the first order phase transition. Also note that this characteristic hysteresis is observed for small samples. As de Gennes mentioned, the hysteresis is a rather frequent phenomenon for nucleation-type phase transition[84]. For superconducting vortices, the Bean–Livingston surface barrier causes the hysteresis[85, 105, 106]. We will discuss the surface barrier of chiral solitons and skyrmions as another example[107].

The purpose of this thesis is, for the uniaxial chiral magnet, to clarify the properties using the chiral solitons as a particle picture of topological textures and the helical order as a wave picture.

1.2 Structure of this thesis

We illustrate the structure of this thesis on the basis of the above background.

In Chap. 2, we review the derivation of SOI, DMI, and the Landau–Lifshitz–Gilbert equation. DMI is the origin of non-uniform structure in chiral magnets and always exist in this thesis. We also review the chiral sine–Gordon model describing chiral soliton lattice states

at zero temperature, Schaub and Mukamel's study on temperature effects, and de Gennes's classification of two continuous phase transitions.

Chapters 3 and 4 are the main results of this thesis.

In Chap. 3, we discuss the non-reciprocal spin wave excitations caused by DMI. In particular, we study the dynamical spin structure factor in order to deal with the non-reciprocity in non-uniform state.

In Chap. 4, we mainly study a uniaxial chiral magnet which is likely to be a simplified model of $Cr_{1/3}NbS_2$ in the presence of a tilted magnetic field in terms of two aspects: the zero temperature phase diagram in the thermodynamics limit, and the surface barrier of chiral soliton and hysteresis phenomena observed in experiment.

In Chap. 5, we summarize the main results achieved in Chaps. 3 and 4 and discuss the importance and future problems related to the present study.

Chapter 2

Several basics

In this chapter, we review several theoretical arguments important to this thesis. In the first two sections we summarize the derivation of SOI and DMI. Then in Sect. 2.3, we derive the Landau–Lifshitz–Gilbert equation, which is an equation of motion for the local magnetic moment. We use this equation to compare our theoretical arguments with the numerical calculation in Chap. 3. In Sect. 2.4, we review the chiral sine-Gordon model, which is expected to describe the uniaxial chiral magnet at zero temperature in the presence of a magnetic field perpendicular to the helical axis[81–83]. There we review a construction of the solutions to the sine-Gordon equation and discuss the stable state in the presence of DMI. In Sect. 2.5, we review the Schaub and Mukamel's study based on the Ginzburg–Landau (GL) model[101], which is equivalent to the GL expansion of the mean field approximation for a uniaxial chiral magnet in the presence of a magnetic field perpendicular to the helical axis for finite temperature. The GL expansion is given in Appendix A. Finally we summarize the two continuous phase transition classified by de Gennes[84]

2.1 Spin orbit interaction

The SOI can be derived from the Dirac equation by taking the non-relativistic limit[108]. The SOI is necessary to derive the DMI. In this section, we review the derivation of the SOI from the Dirac equation:

$$\left[\sum_{\mu=1}^{4}\gamma_\mu(\partial_\mu + \mathrm{i}(e/c)A_\mu) + mc\right]\vec{\phi} = \vec{0}, \tag{2.1}$$

where the electron charge is $-e$ and

$$\gamma_0 = \hat{\tau}_0 \otimes \hat{\sigma}_0,\ \gamma_j = \hat{\tau}_2 \otimes \hat{\sigma}_j,\ \gamma_4 = \hat{\tau}_3 \otimes \hat{\sigma}_0, \tag{2.2}$$

Note that $\hat{\sigma}_j(\hat{\tau}_j)$ denote the Pauli matrices in the spin (particle-hole) space, and 0-th component denotes the identity matrix. We define the time as fourth component of the position vector:

$x_4 = \mathrm{i}ct$. The greek subscripts take 1, 2, 3, or 4, and the roman ones take 1, 2, or 3. The four-component vector potential is defined as

$$A_\mu = (A_1, A_2, A_3, \mathrm{i}V)^{\mathrm{T}}, \tag{2.3}$$

where $\boldsymbol{A} = (A_1, A_2, A_3)$ and V are a vector and scalar potentials, respectively.

We consider an eigenstate of the form $\vec{\phi} = \vec{\psi} e^{-\mathrm{i}(mc^2+\epsilon)t}$ and assume a non-relativistic case $mc^2 \gg |\epsilon|$. Note that we neglect the time dependence of the scalar and vector potentials.

$$\hat{\sigma}_j P_j \psi_2 - [(\epsilon + eV)/c]\psi_1 = 0, \tag{2.4}$$
$$-\hat{\sigma}_j P_j \psi_1 + [(2mc^2 + \epsilon + eV)/c]\psi_2 = 0, \tag{2.5}$$

with $P_j \equiv p_j + (e/c)A_j$ and $p_j \equiv -\mathrm{i}\partial_j$. We remark that ψ_1 and ψ_2 are still two-component vectors in the spin space. The second equation tells us that the leading order of ψ_2 is the order of $\psi_1/\sqrt{mc^2}$. We are going to derive the wave equation of order $\bar{\epsilon}/(mc^2)$, where we write $\bar{\epsilon}$ as a characteristic energy of the system in the non-relativistic limit, and $\bar{\epsilon}$ is the order of ϵ, $P_j^2/2m$ and so on. We use the Einstein convention for repeated roman symbols. The second equation gives us that

$$\psi_2 = \frac{c}{2mc^2 + \epsilon + eV}\hat{\sigma}_j P_j \psi_1. \tag{2.6}$$

The integral of $\psi_2^\dagger \psi_2$ can be evaluated up to first order in $\bar{\epsilon}/(mc^2)$ as

$$\int dr \psi_2^\dagger \psi_2 = \int dr \psi_1^\dagger \frac{1}{2mc^2}\frac{1}{2m}\hat{\sigma}_i\hat{\sigma}_j P_i P_j \psi_1. \tag{2.7}$$

This means $\psi_2^\dagger\psi_2$ affects the normalization condition. To eliminate this, we take the unitary transformation such that

$$\begin{pmatrix} \tilde{\psi}_1 \\ \tilde{\psi}_2 \end{pmatrix} = \begin{pmatrix} 1 - \frac{1}{2}\left(\frac{\hat{\sigma}_i P_i}{2mc}\right)^2 & \frac{\hat{\sigma}_i P_i}{2mc} \\ -\frac{\hat{\sigma}_i P_i}{2mc} & 1 - \frac{1}{2}\left(\frac{\hat{\sigma}_i P_i}{2mc}\right)^2 \end{pmatrix} \begin{pmatrix} \psi_1 \\ \psi_2 \end{pmatrix} \equiv \begin{pmatrix} \psi \\ 0 \end{pmatrix} + O([\bar{\epsilon}/(mc^2)]^2), \tag{2.8}$$

where ψ is a normalized spinor and

$$\psi = \left[1 + \frac{1}{4mc^2}\frac{1}{2m}\hat{\sigma}_i\hat{\sigma}_j P_i P_j\right]\psi_1. \tag{2.9}$$

Here we take summation over i and j.

Next we multiply Eq. (2.4) by $(2mc^2 + \epsilon + eV)/c$ and using Eq. (2.5) we obtain

$$\hat{\sigma}_i\hat{\sigma}_j P_i P_j \psi_1 - \frac{e}{c}\hat{\sigma}_j(p_j V)\psi_2 - \left[2m(\epsilon + eV) + \left(\frac{\epsilon + eV}{c}\right)^2\right]\psi_1 = 0. \tag{2.10}$$

The first and third terms are on the order of $(\epsilon/mc^2)^0$ and thus by dealing with the second and fourth terms in an appropriate way as

$$\psi_2 \simeq \frac{c}{2mc^2}\hat{\sigma}_j P_j \psi_1,\ 2m(\epsilon + eV)\psi_1 \simeq \hat{\sigma}_i \hat{\sigma}_j P_i P_j \psi_1, \tag{2.11}$$

we obtain with the notation $\hat{\sigma}_j P_j = \hat{\boldsymbol{\sigma}} \cdot \boldsymbol{P}$ that

$$(\hat{\boldsymbol{\sigma}} \cdot \boldsymbol{P})^2 \psi_1 - \frac{e}{c}\hat{\boldsymbol{\sigma}} \cdot (\boldsymbol{p}V)\frac{c}{2mc^2}\hat{\boldsymbol{\sigma}} \cdot \boldsymbol{P}\psi_1 - 2m(\epsilon + eV)\left[1 + \frac{1}{2mc^2}\frac{(\hat{\boldsymbol{\sigma}} \cdot \boldsymbol{P})^2}{2m}\right]\psi_1 = 0. \tag{2.12}$$

Multiplying this by $[1 - \frac{1}{4mc^2}\frac{(\hat{\boldsymbol{\sigma}}\cdot\boldsymbol{P})^2}{2m}]$ and retain the terms up to first order in $\bar{\epsilon}/mc^2$

$$\begin{aligned}(\hat{\boldsymbol{\sigma}} \cdot \boldsymbol{P})^2 \left[1 - \frac{1}{4mc^2}\frac{(\hat{\boldsymbol{\sigma}} \cdot \boldsymbol{P})^2}{2m}\right]\psi_1 - \frac{e}{c}\hat{\boldsymbol{\sigma}} \cdot (\boldsymbol{p}V)\frac{c}{2mc^2}(\hat{\boldsymbol{\sigma}} \cdot \boldsymbol{P})\psi_1 \\ - \left[1 - \frac{1}{4mc^2}\frac{(\hat{\boldsymbol{\sigma}} \cdot \boldsymbol{P})^2}{2m}\right] 2m(\epsilon + eV)\left[1 + \frac{1}{2mc^2}\frac{(\hat{\boldsymbol{\sigma}} \cdot \boldsymbol{P})^2}{2m}\right]\psi_1 = 0.\end{aligned} \tag{2.13}$$

The second line can be transformed into

$$-2m(\epsilon + eV)\psi + \frac{1}{4mc^2}\left[(p^2 eV) + 2(\boldsymbol{p}eV) \cdot \boldsymbol{P}\right]\psi. \tag{2.14}$$

The leading order of the second term of Eq. (2.13) is

$$-e\hat{\boldsymbol{\sigma}} \cdot (\boldsymbol{p}V)\frac{1}{2mc^2}(\boldsymbol{\sigma} \cdot \boldsymbol{P})\psi = -\frac{e}{2mc^2}\left\{\hat{\boldsymbol{\sigma}} \cdot [(\boldsymbol{\nabla}V) \times \boldsymbol{P}] + (\boldsymbol{p}V) \cdot \boldsymbol{P}\right\}\psi, \tag{2.15}$$

which is relativistic correction. Note that the wave function is ψ rather than ψ_1 and that the second term of Eq. (2.15) and the last term of Eq. (2.14) cancel out. Then we summarize the above calculation.

$$\begin{aligned}\left\{\frac{(\hat{\boldsymbol{\sigma}} \cdot \boldsymbol{P})^2}{2m}\left(1 - \frac{1}{2mc^2}\frac{(\hat{\boldsymbol{\sigma}} \cdot \boldsymbol{P})^2}{2m}\right) - \frac{e}{4m^2c^2}\hat{\boldsymbol{\sigma}} \cdot [(\boldsymbol{\nabla}V) \times \boldsymbol{P}]\right. \\ \left. -(\epsilon + eV) + \frac{(p^2 eV)}{8m^2c^2}\right\}\psi = 0.\end{aligned} \tag{2.16}$$

Finally we rewrite the first and second terms. Note that $(\hat{\boldsymbol{\sigma}} \cdot \boldsymbol{P})^2 = P^2 + \frac{e}{c}\hat{\boldsymbol{\sigma}} \cdot \boldsymbol{B}$. We introduce the Bohr magneton $\mu_{\mathrm{B}} = e/2mc$. Therefore, the deduced non-relativistic Schrödinger equation is

$$\begin{aligned}\left\{\frac{P^2}{2m} - 2\mu_{\mathrm{B}}\left(-\frac{1}{2}\hat{\boldsymbol{\sigma}} \cdot \boldsymbol{B}\right) - eV - \frac{1}{2mc^2}\left[\frac{P^2}{2m} - 2\mu_{\mathrm{B}}\left(-\frac{1}{2}\hat{\boldsymbol{\sigma}} \cdot \boldsymbol{B}\right)\right]^2\right. \\ \left. -\frac{e}{4m^2c^2}\hat{\boldsymbol{\sigma}} \cdot [(\boldsymbol{\nabla}V) \times \boldsymbol{P}] + \frac{(p^2 eV)}{8m^2c^2}\right\}\psi = \epsilon\psi.\end{aligned} \tag{2.17}$$

2.2 Interaction in magnet

We will introduce several interactions appearing in magnets.

2.2.1 Exchange interaction

First we obtain the exchange interaction originally introduced by Heisenberg. Here we consider Wannier orbitals coming from d orbitals. Wannier orbitals on different sites are orthogonal and they include contributions from negative ions. Therefore we can explain the super-exchange interaction. The original Hamiltonian is given by

$$\mathcal{H} = \sum_{\sigma} \int \mathrm{d}\boldsymbol{r} \psi_{\sigma}^{\dagger}(\boldsymbol{r}) \mathcal{H}_0(\boldsymbol{r}) \psi_{\sigma}(\boldsymbol{r}) + \frac{1}{2} \sum_{\sigma\sigma'} \int \mathrm{d}\boldsymbol{r} \mathrm{d}\boldsymbol{r}' \mathcal{H}_1(\boldsymbol{r}-\boldsymbol{r}') \psi_{\sigma}^{\dagger}(\boldsymbol{r}) \psi_{\sigma'}^{\dagger}(\boldsymbol{r}') \psi_{\sigma'}(\boldsymbol{r}') \psi_{\sigma}(\boldsymbol{r}),$$
$$\mathcal{H}_0(\boldsymbol{r}) = -\frac{\nabla^2}{2m} + V(\boldsymbol{r}),\ \mathcal{H}_1(\boldsymbol{r},\boldsymbol{r}') = \frac{e^2}{|\boldsymbol{r}-\boldsymbol{r}'|}. \tag{2.18}$$

For the meanwhile, we omit the SOIs. The second term in the one body Hamiltonian $V(\boldsymbol{r})$ describes a periodic potential. The basis diagonalizing the one body Hamiltonian is given by Bloch wave functions with indices n and $\boldsymbol{k}$, which label a band and a crystal momentum in the first Brillouin zone, respectively. Then we assume that some of bands have large inner products with the linear combination of d-orbitals. From those bands, we construct the Wannier orbitals by

$$\phi_{n,i}(\boldsymbol{r}) \equiv \phi_n(\boldsymbol{r}-\boldsymbol{R}_i) = \frac{1}{\sqrt{N}} \sum_{\boldsymbol{k}} e^{-\mathrm{i}\boldsymbol{k}\cdot\boldsymbol{R}_i} \psi_{n\boldsymbol{k}}(\boldsymbol{r}). \tag{2.19}$$

Each orbital is no longer characterized by the original atomic orbitals. The field operator $\psi(\boldsymbol{r})$ can be expanded with this Wannier orbital as

$$\psi_{\sigma}(\boldsymbol{r}) = \sum_{n,i} \phi_{n,i}(\boldsymbol{r}) c_{n,i,\sigma}. \tag{2.20}$$

For simplicity, we omit the band index and assume that there is a single band. Then the Hamiltonian reduces to

$$\mathcal{H} = \sum_{i,j} t_{i,j} c_{i,\sigma}^{\dagger} c_{j,\sigma} + \frac{1}{2} \sum_{\sigma,\sigma'} \sum_{i,j,k,l} U_{i,j,k,l} c_{i,\sigma}^{\dagger} c_{j,\sigma'}^{\dagger} c_{l,\sigma'} c_{k,\sigma}, \tag{2.21}$$

$$t_{i,j} = \frac{1}{N} \sum_{\boldsymbol{k}} \epsilon_{\boldsymbol{k}} e^{\mathrm{i}\boldsymbol{k}(\boldsymbol{R}_i - \boldsymbol{R}_j)},\ U_{i,j,k,l} = \int \mathrm{d}\boldsymbol{r} \mathrm{d}\boldsymbol{r}' \phi_i^*(\boldsymbol{r}) \phi_j^*(\boldsymbol{r}') \frac{e^2}{|\boldsymbol{r}-\boldsymbol{r}'|} \phi_l(\boldsymbol{r}') \phi_k(\boldsymbol{r}). \tag{2.22}$$

The first term is called hopping term. The Wannier orbitals are well localized, and thus we do not have to consider all of the contributions from the above summation. We retain the

on-site contributions and the nearest-neighbour contribution from the hopping term. Ignoring the dependence of the hopping on its direction, we then obtain the Hubbard model as

$$\begin{aligned}\mathcal{H} &= \sum_{i,\sigma} \epsilon_d c^\dagger_{i,\sigma} c_{i,\sigma} - \sum_{\langle i,j\rangle,\sigma} t c^\dagger_{i,\sigma} c_{j,\sigma} + \frac{U}{2} \sum_{i,\sigma} c^\dagger_{i,\sigma} c^\dagger_{i,-\sigma} c_{i,-\sigma} c_{i,\sigma} \\ &= \sum_{i,\sigma} \epsilon_d c^\dagger_{i,\sigma} c_{i,\sigma} - \sum_{\langle i,j\rangle,\sigma} t c^\dagger_{i,\sigma} c_{j,\sigma} + U \sum_i n_{i,\uparrow} n_{i,\downarrow} = \mathcal{H}_0 + \mathcal{H}_t + \mathcal{H}_U. \end{aligned} \tag{2.23}$$

Note that $-\sigma$ describes the opposite direction of σ. Here we have introduced the following parameters:

$$\epsilon_d = \frac{1}{N} \sum_{\boldsymbol{k}} \epsilon_{\boldsymbol{k}}, \tag{2.24}$$

$$-t \sim -t_{\boldsymbol{\delta}} = \frac{1}{N} \sum_{\boldsymbol{k}} \epsilon_{\boldsymbol{k}} e^{\mathrm{i}\boldsymbol{k}\cdot\boldsymbol{\delta}} \text{ with a primitive translation vector } \boldsymbol{\delta}, \tag{2.25}$$

$$U = U_{i,j,k,l} \text{ for } i = j = k = l. \tag{2.26}$$

The first term of the Hubbard model is the "energy level" of the band n, and this just shifts the origin of the energy.

Kinetic exchange

We see that the above Hamiltonian leads to the interaction between the spins. Let us consider the case of $0 < t \ll U$ and the half-filled case. Then we can treat the hopping term as a perturbation and we easily see that the ground state of the unperturbed Hamiltonian is described by the presence of a single electron on a single Wannier orbital. Here we use the second order perturbation theory, and it suffices to consider two sites, which we label by j and l. There are two electrons in the half-filled case. The ground states with zero eigen energy have four-fold degeneracy and are given by $c^\dagger_{j,\sigma} c^\dagger_{l,\sigma'} |0\rangle \equiv |\sigma, \sigma'\rangle$ for $\sigma, \sigma' = \uparrow, \downarrow$. If we consider the whole system, the ground states have 2^N-fold degeneracy. We treat the hopping term by the perturbative method, and then the second order perturbation Hamiltonian is given by

$$\begin{aligned}\mathcal{H}^{(2)} &= \mathcal{H}_t \frac{1}{E_{\mathrm{G.S.}} - \mathcal{H}_U} \mathcal{H}_t \\ &= -\frac{t^2}{U} \sum_{\sigma,\sigma\prime} \left(c^\dagger_{j,\sigma} c_{l,\sigma} + c^\dagger_{l,\sigma} c_{j,\sigma} \right) \left(c^\dagger_{j,\sigma'} c_{l,\sigma'} + c^\dagger_{l,\sigma'} c_{j,\sigma'} \right). \end{aligned} \tag{2.27}$$

Here we have used the facts that energy of intermediate states is U and that the ground-state energy is zero. Note that the relations between the fermion operators and the spin operators on site j are given by

$$c^\dagger_{j,\sigma} c_{j,\sigma} = \frac{n_j + 2\sigma S^z_j}{2}, \; c^\dagger_{j,\sigma} c_{j,-\sigma} = S^\sigma_j. \tag{2.28}$$

The symbol σ on the right-hand side of the first relation takes $+$ or $-$, corresponding to $\uparrow$ or $\downarrow$. Then we can rewrite the above perturbation Hamiltonian in terms of spin operators. When $\sigma = \sigma'$,

$$\begin{aligned}\mathcal{H}^{(2)}_{\sigma=\sigma'} &= -\frac{t^2}{U}\sum_{\sigma=\uparrow,\downarrow}\left(c^\dagger_{j,\sigma}c_{l,\sigma} + c^\dagger_{l,\sigma}c_{j,\sigma}\right)\left(c^\dagger_{j,\sigma}c_{l,\sigma} + c^\dagger_{l,\sigma}c_{j,\sigma}\right) \\ &= -\frac{t^2}{4U}\sum_{\sigma=\pm}\left[(n_j + 2\sigma S^z_j)(2 - n_l - 2\sigma S^z_l) + (2 - n_j - 2\sigma S^z_j)(n_l + 2\sigma S^z_l)\right] \\ &= -\frac{4t^2}{U}\left[-16S^z_j S^z_l + (2-n_j)n_l + n_j(2-n_l)\right] = \frac{4t^2}{U}\left(S^z_j S^z_l - \frac{1}{2}\right). \end{aligned} \tag{2.29}$$

From the third line to the fourth line, the terms with σ become zero by the summation over $\sigma = \pm$, and in the last equality, we have used the fact that the states operated by this Hamiltonian has a single electron on each site. Next we calculate it for the case where $\sigma' = -\sigma$. Define the pair annihilation operator $b_j = c_{j,\uparrow}c_{j,\downarrow}$.

$$\begin{aligned}\mathcal{H}^{(2)}_{\sigma=-\sigma'} &= -\frac{t^2}{U}\sum_{\sigma=\uparrow,\downarrow}\left(c^\dagger_{j,\sigma}c_{l,\sigma} + c^\dagger_{l,\sigma}c_{j,\sigma}\right)\left(c^\dagger_{j,-\sigma}c_{l,-\sigma} + c^\dagger_{l,-\sigma}c_{j,-\sigma}\right) \\ &= -\frac{t^2}{U}\sum_{\sigma=\uparrow,\downarrow}\left(-S^\sigma_j S^{-\sigma}_l - S^{-\sigma}_j S^\sigma_l - b^\dagger_j b_l - b^\dagger_l b_j\right) = \frac{2t^2}{U}\left(S^+_j S^-_l + S^-_j S^+_l\right). \end{aligned} \tag{2.30}$$

Again we use the fact that the pair annihilation operator annihilates the states we are considering. Finally we can summarize the second order perturbation Hamiltonian as

$$\mathcal{H}^{(2)} = \frac{4t^2}{U}\left(\vec{S}_j \cdot \vec{S}_l - \frac{1}{2}\right) \equiv J_{\rm kin}\left(\vec{S}_j \cdot \vec{S}_l - \frac{1}{2}\right). \tag{2.31}$$

Note that $J_{\rm kin} > 0$, which means antiferromagnetic.

Potential exchange

Next we discuss an interaction between spins, which stems purely from the Coulomb interaction, called a potential exchange interaction. In the above derivation of the Hubbard model, we retain only the on-site contributions to the Coulomb interaction. Now we consider the Coulomb interaction between the different sites, in particular, the nearest neighbor sites. This can be written as

$$\begin{aligned}&\frac{1}{2}\sum_{\sigma,\sigma'}U_{j,l,j,l}c^\dagger_{j,\sigma}c^\dagger_{l,\sigma'}c_{l,\sigma'}c_{j,\sigma} + \frac{1}{2}\sum_{\sigma,\sigma'}U_{j,l,l,j}c^\dagger_{j,\sigma}c^\dagger_{l,\sigma'}c_{j,\sigma'}c_{l,\sigma} \\ &= \frac{1}{2}U_{j,l,j,l}n_j n_l - U_{j,l,l,j}\left(\vec{S}_j \cdot \vec{S}_l + \frac{1}{4}n_j n_l\right). \end{aligned} \tag{2.32}$$

The sign of $U_{j,l,l,j}$ is discussed as

$$U_{j,l,l,j} = \int \mathrm{d}\boldsymbol{r}\mathrm{d}\boldsymbol{r}' \phi_j^*(\boldsymbol{r})\phi_l^*(\boldsymbol{r}')\frac{e^2}{|\boldsymbol{r}-\boldsymbol{r}'|}\phi_j(\boldsymbol{r}')\phi_l(\boldsymbol{r}) = \int \frac{\mathrm{d}\boldsymbol{q}}{(2\pi)^3}\frac{4\pi e^2}{q^2}|\Phi_{jl}(\boldsymbol{q})|^2 > 0, \quad (2.33)$$

where $\Phi_{jl}(\boldsymbol{q})$ is the Fourier transform of $\phi_j^*(\boldsymbol{r})\phi_l(\boldsymbol{r})$. The positive $U_{j,l,l,j}$ gives a ferromagnetic spin coupling. Then it is important to consider the competition between kinetic and potential exchange interactions as well as other mechanism, such as higher order contributions.

2.2.2 Antisymmetric exchange interaction

Next we are going to discuss an antisymmetric exchange interaction, which is given by the form of the vector product as $\vec{D}\cdot(\vec{S}_j \times \vec{S}_l)$. This antisymmetric interaction should be zero when the system has inversion center and it is necessary to consider the inversion symmetry broken system.

First we discuss a derivation similar to that of the kinetic exchange interaction above. To take broken-inversion symmetry into account, we introduce the following antisymmetric hopping terms, which depend on the spin component.

$$\begin{aligned}\mathcal{H}^{\delta}_{\mathrm{s.o.}} &= \sum_i \left[(t_y + \mathrm{i}t_x)c^\dagger_{i,\uparrow}c_{i+\delta,\downarrow} + (-t_y + \mathrm{i}t_x)c^\dagger_{i,\downarrow}c_{i+\delta,\uparrow} + \mathrm{i}t_z(c^\dagger_{i,\uparrow}c_{i+\delta,\uparrow} - c^\dagger_{i,\downarrow}c_{i+\delta,\downarrow}) + \mathrm{h.c.}\right] \\ &= \sum_{i,\mu=x,y,z}\left(\mathrm{i}t_\mu c^\dagger_{i,\sigma}\sigma^\mu_{\sigma,\sigma'}c_{i+\delta,\sigma'} + \mathrm{h.c.}\right). \end{aligned} \quad (2.34)$$

The superscript of the Hamiltonian, δ, denotes the bond-direction of the hopping and takes x or y for the square lattice, for example, and $\sigma^\mu_{\sigma,\sigma'}$ is the Pauli matrix. We treat the hopping term and these antisymmetric hopping terms as a perturbation Hamiltonian. Then the second order perturbation theory gives us

$$\mathcal{H}^{(2)} = (\mathcal{H}_t + \mathcal{H}^{\delta}_{\mathrm{s.o.}})\frac{1}{E_{\mathrm{G.S.}} - \mathcal{H}_U}(\mathcal{H}_t + \mathcal{H}^{\delta}_{\mathrm{s.o.}}). \quad (2.35)$$

We consider the contributions associated with the sites j and $j+\delta \equiv l$. In the following calculations, we use the fact that the occupation number of each site for ground states is one. Note that energy for intermediate states is U. We use also the relation between fermion operators and spin operators given by Eq. (2.28). First we see in detail the contribution to the perturbation Hamiltonian, including tt_x as an example, which is given by

$$\begin{aligned} &-\mathrm{i}\frac{tt_x}{U}\sum_{\sigma,\sigma'}\left\{c^\dagger_{j,\sigma}c_{l,-\sigma} - c^\dagger_{l,\sigma}c_{j,-\sigma}, c^\dagger_{j,\sigma'}c_{l,\sigma'} + c^\dagger_{l,\sigma'}c_{j,\sigma'}\right\} \\ =&-\mathrm{i}\frac{tt_x}{U}\sum_{\sigma,\sigma'}\left(\left\{c^\dagger_{j,\sigma}c_{l,-\sigma}, c^\dagger_{l,\sigma'}c_{j,\sigma'}\right\} - \left\{c^\dagger_{l,\sigma}c_{j,-\sigma}, c^\dagger_{j,\sigma'}c_{l,\sigma'}\right\}\right). \end{aligned} \quad (2.36)$$

When $\sigma' = \sigma$, this reduces to

$$-\mathrm{i}\frac{tt_x}{U}\sum_{\sigma} 2\sigma \left(S_j^{\sigma} S_l^z - S_j^z S_l^{\sigma}\right) = \frac{4tt_x}{U}\left(S_j^y S_l^z - S_j^z S_l^y\right) = \frac{4tt_x}{U}\left(\vec{S}_j \times \vec{S}_l\right)^x. \tag{2.37}$$

In a similar way, we obtain the same contribution for $\sigma' = -\sigma$. Thus we have

$$\frac{8tt_x}{U}\left(\vec{S}_j \times \vec{S}_l\right)^x \equiv D_x \left(\vec{S}_j \times \vec{S}_l\right)^x. \tag{2.38}$$

The terms including tt_y and tt_z are obtained as

$$\frac{8tt_y}{U}(S_j^z S_l^x - S_j^x S_l^z) \equiv D_y \left(\vec{S}_j \times \vec{S}_l\right)^y, \tag{2.39}$$

$$\frac{8tt_z}{U}(S_j^x S_l^y - S_j^y S_l^x) \equiv D_z \left(\vec{S}_j \times \vec{S}_l\right)^z. \tag{2.40}$$

Up to the second order perturbation we can obtain terms which are anisotropic but symmetric. By defining

$$\Gamma_{\mu\nu} \equiv \frac{8t_\mu t_\nu}{U}(1 - \delta_{\mu\nu}), \tag{2.41}$$

we can write

$$\sum_{\mu\nu} \Gamma_{\mu\nu} S_j^{\mu} S_l^{\nu}. \tag{2.42}$$

Now we summarize the perturbation Hamiltonian for δ-bond which we derive from the second order perturbation theory as

$$\mathcal{H}^{(2)} = \sum_j \left[J_{\mathrm{kin}} \vec{S}_j \cdot \vec{S}_{j+\delta} + \vec{D} \cdot \left(\vec{S}_j \times \vec{S}_{j+\delta}\right) + \sum_{\mu\nu} \Gamma_{\mu\nu} S_j^{\mu} S_l^{\nu} \right]. \tag{2.43}$$

The second term is the Dzyaloshinskii–Moriya interaction. This derivation is essentially the same as that done by Moriya and written in his main text[49]. He considered the first principle Hamiltonian and also the orbital degrees of freedom. Our Hamiltonian used here is an effective Hamiltonian analyzed intensively to study the roles of antisymmetric spin-orbit terms in very wide field such as topological insulators and superconductors[17, 18].

Then we review the conventional derivation, which is referred in quite a lot of books and originally written in the appendix of Ref. [49]. In this part we consider the SOI as well as the terms considered in Eq. (2.18). The SOI Hamiltonian is expressed by

$$\mathcal{H}_{\mathrm{s.o.}} = \int \mathrm{d}\boldsymbol{r} \psi_{\sigma}^{\dagger}(\boldsymbol{r}) V_{\sigma,\sigma'}^{\mathrm{s.o.}} \psi_{\sigma'}(\boldsymbol{r}), \tag{2.44}$$

$$V_{\sigma,\sigma'}^{\mathrm{s.o.}}(\boldsymbol{r}) \simeq \sum_i \lambda(\boldsymbol{r} - \boldsymbol{R}_i) \vec{L}(\boldsymbol{r} - \boldsymbol{R}_i) \cdot \vec{S}_{\sigma,\sigma'} \equiv \sum_i \lambda_i(\boldsymbol{r}) \vec{L}_i(\boldsymbol{r}) \cdot \vec{S}_{\sigma,\sigma'} \text{ with } \vec{S} = \frac{1}{2}\vec{\sigma}. \tag{2.45}$$

Here $\vec{\sigma}$ is the 2 by 2 Pauli matrices. The field operator $\psi_\sigma(\boldsymbol{r})$ can be expanded using the Wannier function $\phi_{j,n}(\boldsymbol{r})$ and its annihilation operator $c_{j,n,\sigma}$, which is the Fourier transform of the Bloch wave function $\psi_{n,\boldsymbol{k}}(\boldsymbol{r})$ as an eigenfucntion of the Hamiltonian $\mathcal{H}_0$. We reduce the SOI Hamiltonian with $\phi_{j,n}(\boldsymbol{r})$ to

$$\begin{aligned}\mathcal{H}_{\text{s.o.}} &= \sum_{i,j,l,m,n,\sigma,\sigma'} \lambda\vec{L}_i(j,m;l,n)\cdot\vec{S}_{\sigma,\sigma'}c^\dagger_{j,m,\sigma}c_{l,n,\sigma'} \\ &\simeq \sum_{j,m,n,\sigma,\sigma'} \lambda\vec{L}_j(j,m;j,n)\cdot\vec{S}_{\sigma,\sigma'}c^\dagger_{j,m,\sigma}c_{j,n,\sigma'}, \qquad (2.46)\\ \lambda\vec{L}_i(j,m;l,n) &\equiv \int \mathrm{d}\boldsymbol{r}\phi^*_{j,m}(\boldsymbol{r})\lambda_i(\boldsymbol{r})\vec{L}_i(\boldsymbol{r})\phi_{l,n}(\boldsymbol{r}) = \lambda\vec{L}_0(j-i,m;l-i,n). \qquad (2.47)\end{aligned}$$

To obtain the second line, we use the approximation that the dominant contribution comes from the on-site integral. In the following we abbreviate $L_j(j,m;j,n)$ as $L_j(m,n)$. The reduced tight binding Hamiltonian can be written as

$$\mathcal{H} = \sum_{j,n,\sigma}\epsilon_n c^\dagger_{j,n,\sigma}c_{j,n,\sigma} + \sum_{i,j,m} t^m_{i,j}c^\dagger_{i,m,\sigma}c_{j,m,\sigma} + \sum_{j,m,n,\sigma,\sigma'}\lambda\vec{L}_j(m,n)\cdot\vec{S}_{\sigma,\sigma'}c^\dagger_{j,m,\sigma}c_{l,n,\sigma'} + \mathcal{H}_{\text{C}}, \qquad (2.48)$$

where $\epsilon_n = N^{-1}\sum_{\boldsymbol{k}}\epsilon_{n,\boldsymbol{k}}$ and $t^m_{i,j} = N^{-1}\sum_{\boldsymbol{k}}\epsilon_{m,\boldsymbol{k}}e^{\mathrm{i}\boldsymbol{k}\cdot(\boldsymbol{R}_i-\boldsymbol{R}_j)}$. We also use the simplified notation that $\sum_{m,n,\sigma,\sigma'}\vec{L}_j(m,n)\cdot\vec{S}_{\sigma,\sigma'}c^\dagger_{j,m,\sigma}c_{l,n,\sigma'} = \vec{L}_j\cdot\vec{S}_j$. The hopping term is irrelevant for the order of perturbation we will consider, as it does not change the spin state and thus in the following we do not consider this term. Then we discuss the important Coulomb terms included in $\mathcal{H}_{\text{C}}$. We consider the case where the on-site intra and inter band Coulomb interaction terms are unlimitedly large, and the double-occupancy of each site is forbidden. Generally speaking, the Coulomb terms include a term such that more than two sites involve. In the following, however, we focus on two electrons and two sites, which we call j and l, and consider only exchange integral terms rather than Coulomb (direct) integral terms. They can be written as

$$\begin{aligned}\mathcal{H}_{\text{C}} &= \frac{1}{2}\sum_{j,l,m',m,n',n,\sigma,\sigma'} U_{j,l}(m',m;n',n)c^\dagger_{l,m',\sigma}c^\dagger_{j,n',\sigma'}c_{l,n,\sigma'}c_{j,m,\sigma}, \\ U_{j,l}(m',m;n',n) &= \int \mathrm{d}\boldsymbol{r}\mathrm{d}\boldsymbol{r}'\phi^*_{l,m'}(\boldsymbol{r})\phi^*_{j,n'}(\boldsymbol{r}')\frac{e^2}{|\boldsymbol{r}-\boldsymbol{r}'|}\phi_{l,n}(\boldsymbol{r}')\phi_{j,m}(\boldsymbol{r}). \qquad (2.49)\end{aligned}$$

This model never gives antisymmetric spin-orbit coupling since this model itself does not include the terms breaking inversion symmetry. As we mention later, according to Moriya's rule DMI should be zero in this case. Nevertheless the following calculation is instructive and after the calculation we will discuss what should be changed in the model. The unperturbed Hamiltonian is the first term of Eq. (2.48) and consider the second order perturbation theory. We assume that $\epsilon_m \neq \epsilon_n$ for $m \neq n$ for simplicity, and thus the ground state $n = 0$ has only

spin-degeneracy in each site. The ground state is described as each site is occupied by a single electron. Let the perturbation Hamiltonian be

$$\mathcal{H}' = \sum_j \lambda \vec{L}_j \cdot \vec{S}_j + \mathcal{H}_{\rm C}. \tag{2.50}$$

We consider the perturbation process involving spin-orbit coupling on either site j or l and the Coulomb interaction, and obtain the following perturbation Hamiltonian:

$$\mathcal{H}^{(2)} = \sum_j \left(\lambda \vec{L}_j \cdot \vec{S}_j \frac{1}{E_{\rm G.S.} - \mathcal{H}^{(0)}} \mathcal{H}_{\rm C} + \mathcal{H}_{\rm C} \frac{1}{E_{\rm G.S.} - \mathcal{H}^{(0)}} \lambda \vec{L}_j \cdot \vec{S}_j \right). \tag{2.51}$$

Let us consider the projection operator $\mathcal{P} = \prod_{j,n\neq 0,\sigma}(1 - c^\dagger_{j,n,\sigma} c_{j,n,\sigma})$. Then a part of the perturbation Hamiltonian associated with the sites j and l is given by the following. The other part can be obtained by replacing $j \leftrightarrow l$.

$$\begin{aligned}
\mathcal{P}\mathcal{H}^{(2)}\mathcal{P} = \mathcal{P}\lambda \sum_{\mu,m,n} \sum_{\sigma,\sigma',\sigma_1,\sigma_2} & L^\mu_j(0,m) S^\mu_{\sigma,\sigma'} c^\dagger_{j,0,\sigma} c_{j,m,\sigma'} \\
& \times \frac{1}{\epsilon_0 - \epsilon_n} U_{j,l}(0,0;n,0) c^\dagger_{l,0,\sigma_1} c^\dagger_{j,n,\sigma_2} c_{l,0,\sigma_2} c_{j,0,\sigma_1} \mathcal{P} \\
+ \mathcal{P}\lambda \sum_{\mu,m,n} \sum_{\sigma,\sigma',\sigma_1,\sigma_2} & U_{j,l}(0,m;0,0) c^\dagger_{l,0,\sigma_1} c^\dagger_{j,0,\sigma_2} c_{l,0,\sigma_2} c_{j,m,\sigma_1} \\
& \times \frac{1}{\epsilon_0 - \epsilon_n} L^\mu_j(n,0) S^\mu_{\sigma,\sigma'} c^\dagger_{j,n,\sigma} c_{j,0,\sigma'} \mathcal{P} \\
= -\lambda \sum_{\mu,n,\sigma,\sigma',\sigma_1} & \frac{L^\mu_j(0,n) U_{j,l}(0,n;0,0)}{\epsilon_0 - \epsilon_n} S^\mu_{\sigma,\sigma'} \\
& \times \mathcal{P}(c^\dagger_{j,0,\sigma} c_{j,0,\sigma_1} c^\dagger_{l,0,\sigma_1} c_{l,0,\sigma'} - c^\dagger_{j,0,\sigma_1} c_{j,0,\sigma'} c^\dagger_{l,0,\sigma} c_{l,0,\sigma_1}) \mathcal{P}.
\end{aligned} \tag{2.52}$$

We have used the facts that $U_{i,j}(0,0;n,0)(= U_{j,i}(n,0;0,0)) = U_{i,j}(0,n;0,0)$ and that $L_j(0,n) = -L_j(n,0)$, which follows from the fact that non-degenerated eigenfunctions for a real Hamiltonian are real. (Proof: When $\phi_n(\boldsymbol{r})$ is an eigenfunction, $\phi^*_n(\boldsymbol{r})$ is also an eigenfunction. There is no degeneracy. Thus $\phi_n(\boldsymbol{r}) = \phi^*_n(\boldsymbol{r})$.) Our unperturbed Hamiltonian is real, but we note that the system does not have degeneracy on each site as the orthogonal eigenfunction is characterized by site and band indices. Also we remark that the angular momentum operator is pure imaginary and that $\lambda(\boldsymbol{r})$ is isotropic. We give a short proof for the matrix element of angular momentum below. Here we can shift the dummy variable in the integral from $\boldsymbol{r} \to \boldsymbol{r} + \boldsymbol{R}_j$ and

thus we just investigate it for $j = 0$.

$$\begin{aligned} L_0^\mu(0,n) &= \int \mathrm{d}\boldsymbol{r} \frac{1}{r}\frac{\mathrm{d}V(r)}{\mathrm{d}r}\phi_{0,0}(\boldsymbol{r})\epsilon_{\mu\nu\rho}r^\nu \left(-\mathrm{i}\frac{\partial\phi_{0,n}(\boldsymbol{r})}{\partial r^\rho}\right) \\ &= \int \mathrm{d}\boldsymbol{r} \left[\mathrm{i}\frac{\partial}{\partial r^\rho}\left(\frac{1}{r}\frac{\mathrm{d}V(r)}{\mathrm{d}r}\phi_{0,0}(\boldsymbol{r})\epsilon_{\mu\nu\rho}r^\nu\right)\right]\phi_{0,n}(\boldsymbol{r}) \\ &= \int \mathrm{d}\boldsymbol{r} \left[\mathrm{i}r^\rho\frac{\mathrm{d}}{\mathrm{d}r}\left(\frac{1}{r}\frac{\mathrm{d}V(r)}{\mathrm{d}r}\right)\phi_{0,0}(\boldsymbol{r}) + \frac{1}{r}\frac{\mathrm{d}V(r)}{\mathrm{d}r}\left(\mathrm{i}\frac{\partial\phi_{0,0}(\boldsymbol{r})}{\partial r^\rho}\right)\right]\epsilon_{\mu\nu\rho}r^\nu\phi_{0,n}(\boldsymbol{r}) \\ &= \int \mathrm{d}\boldsymbol{r}\frac{1}{r}\frac{\mathrm{d}V(r)}{\mathrm{d}r}\left(\mathrm{i}\frac{\partial\phi_{0,0}(\boldsymbol{r})}{\partial r^\rho}\right)\epsilon_{\mu\nu\rho}r^\nu\phi_{0,n}(\boldsymbol{r}) = -L_0^\mu(n,0), \end{aligned} \tag{2.53}$$

where we omit the surface integral. Also note that $L_0^\mu(0,n)$ is pure imaginary.

Then we reduce the operators in Eq. (2.52), particularly,

$$\sum_{\sigma,\sigma',\sigma_1} S^\mu_{\sigma,\sigma'}\left(c^\dagger_{j,0,\sigma}c_{j,0,\sigma_1}c^\dagger_{l,0,\sigma_1}c_{l,0,\sigma'} - c^\dagger_{j,0,\sigma_1}c_{j,0,\sigma'}c^\dagger_{l,0,\sigma}c_{l,0,\sigma_1}\right). \tag{2.54}$$

In the following we omit the band index "0". For $\mu = x$,

$$\begin{aligned} &\frac{1}{2}\sum_{\sigma,\sigma_1}\left(c^\dagger_{j,\sigma}c_{j,\sigma_1}c^\dagger_{l,\sigma_1}c_{l,-\sigma} - c^\dagger_{j,\sigma_1}c_{j,-\sigma}c^\dagger_{l,\sigma}c_{l,\sigma_1}\right) \\ &= \frac{1}{2}\sum_{\sigma}\left(c^\dagger_{j,\sigma}c_{j,\sigma}c^\dagger_{l,\sigma}c_{l,-\sigma} + c^\dagger_{j,\sigma}c_{j,-\sigma}c^\dagger_{l,-\sigma}c_{l,-\sigma} - c^\dagger_{j,\sigma}c_{j,-\sigma}c^\dagger_{l,\sigma}c_{l,\sigma} - c^\dagger_{j,-\sigma}c_{j,-\sigma}c^\dagger_{l,\sigma}c_{l,-\sigma}\right) \\ &= \frac{1}{4}\sum_{\sigma}\left[(n_j + 2\sigma S^z_j)S^\sigma_l + S^\sigma_j(n_l - 2\sigma S^z_l) - S^\sigma_j(n_l + 2\sigma S^z_l) - (n_j - 2\sigma S^z_j)S^\sigma_l\right] \\ &= -2\mathrm{i}\left(S^y_jS^z_l - S^z_jS^y_l\right) = -2\mathrm{i}\left(\vec{S}_j\times\vec{S}_l\right)^x. \end{aligned} \tag{2.55}$$

In similar ways, for $\mu = y$ and z, we obtain

$$-2\mathrm{i}\left(\vec{S}_j\times\vec{S}_l\right)^y \text{ for } \mu = y, \tag{2.56}$$

$$-2\mathrm{i}\left(\vec{S}_j\times\vec{S}_l\right)^z \text{ for } \mu = z. \tag{2.57}$$

Therefore by taking into account the counter part of $j \leftrightarrow l$, we obtain the antisymmetric spin-spin interactions in the following form:

$$\mathcal{H}^{(2)} = (\vec{D}_{jl} - \vec{D}_{lj})\cdot\left(\vec{S}_j\times\vec{S}_l\right), \tag{2.58}$$

$$\vec{D}_{jl} - \vec{D}_{lj} = 2\mathrm{i}\lambda\sum_n\left(\frac{L^\mu_j(0,n)U_{jl}(0,n;0,0)}{\epsilon_0 - \epsilon_n} - \frac{L^\mu_l(0,n)U_{jl}(0,0;0,n)}{\epsilon_0 - \epsilon_n}\right). \tag{2.59}$$

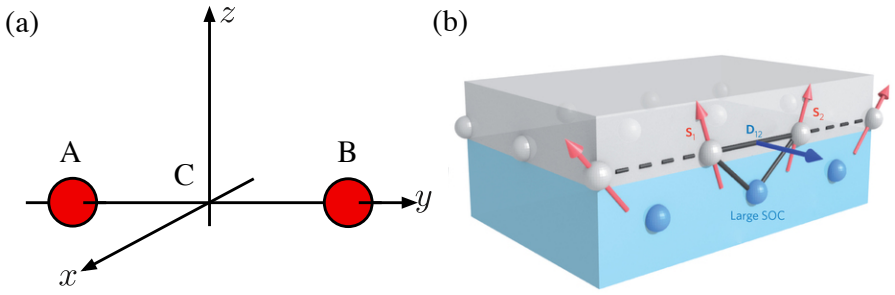

Figure 2.1: (a) Two magnetic ions are at the points A and B. The point C is the bisection. (b) Layered structure from [24].

This is always zero as we mentioned. Then we briefly argue about how to improve our model Hamiltonian (2.48). The Wannier orbital $\phi_{j,n}(\boldsymbol{r})$ is well localized at site j or in unit cell j. Now we consider the case where there are more than one atoms in a unit cell, which is labeled by $\alpha, \beta, \cdots$. Our new Wannier orbitals are defined by $\phi_{j,m}(\boldsymbol{r}) = \sqrt{N}^{-1} \sum_{\boldsymbol{k},n} U_{m,n}(\boldsymbol{k}) \psi_{n,\boldsymbol{k}} e^{i\boldsymbol{k}\cdot\boldsymbol{R}_j}$. Now m can be labeled as (α, m_α), which denote the αth atom and its m_αth level, respectively. Finally we deduce the model Hamiltonian by omitting the hopping terms between atoms and levels on an atom. We could apply the above argument for electrons on α site and α' site of the deduced model, and in that case generally speaking the term $\vec{D}_{\alpha\alpha'} - \vec{D}_{\alpha'\alpha}$ is non-zero.

We summarize the Moriya rule here[49]. Let two magnetic ions be at positions "A" and "B", and we call the bisection point of the line "AB " "C".

1. When a center of inversion is located at C, $\vec{D} = 0$.
2. When a mirror plane perpendicular to AB passes through C, $\vec{D} \parallel$ mirror place.
3. When there is a mirror plane including A and B, $\vec{D} \perp$ mirror plane.
4. When a two-fold rotation axis perpendicular to AB passes through C, $\vec{D} \perp$ two-fold axis.
5. When there is an n-fold axis $(n \geq 2)$ along AB, $\vec{D} \parallel$ AB.

Concerning 3 and 4, the directions are unique except their signs.

Here we only prove the rule 3. We assume that the mirror plane is yz-plane. The mirror operation transforms the spins as

$$S^x_{\mathrm{A(B)}} = S^x_{\mathrm{A(B)}},\ S^y_{\mathrm{A(B)}} = -S^y_{\mathrm{A(B)}},\ \text{and}\ S^z_{\mathrm{A(B)}} = -S^z_{\mathrm{A(B)}}. \tag{2.60}$$

Thus the DM vector can take the x-direction only as only $D^x(S^y_{\mathrm{A}} S^z_{\mathrm{B}} - S^z_{\mathrm{A}} S^y_{\mathrm{B}})$ is even under the operation.

Now we consider the direction of interfacial DMI proposed by Fert and Levy[58], where we consider the magnetic layer on a heavy metal layer with strong spin-orbit coupling. The

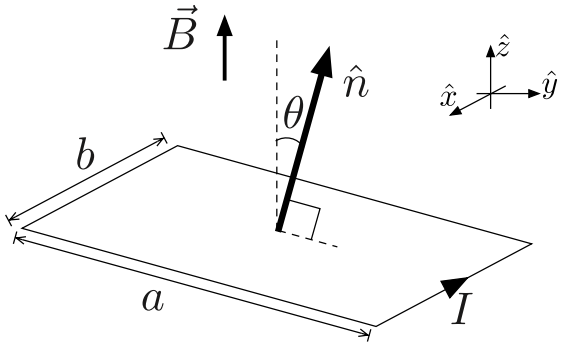

Figure 2.2: Schematic picture of the magnetic moment equivalent to the loop current. The magnetic moment tilts from the magnetic field by angle θ.

configurations of atoms are shown in Fig. 2.1(b). We can take the mirror plane including two spins and the heavy metal atom. According to the rule 3, the direction of the DM vector is allowed as shown in the figure.

2.3 Magnetization dynamics

We review the derivation of the equation of motion for local magnetic moments called Landau–Lifshitz–Gilbert (LLG) equation. The equation without the Gilbert damping, $\alpha = 0$, is used in Chap. 3

2.3.1 Torque on magnetic moment

We start by studying a torque on a magnetic moment exerted by magnetic field. One can consider the magnetic moment, $\vec{\mu}$, being created by a loop current, I, as shown in Fig. 2.2.

$$\vec{\mu} = IS\hat{n}. \tag{2.61}$$

When the magnetic moment tilts from the field-direction by the angle θ, the Lorentz forces acting on the edges AB and CD are $\vec{F}_{\rm AB} = BIa\hat{x} = -\vec{F}_{\rm CD}$, which have no contribution to the torque, and on the other edges are $\vec{F}_{\rm BC} = BIb\hat{y} = -\vec{F}_{\rm DA}$, which give the following torque on the system:

$$\vec{N} = \tfrac{1}{2}BIab\sin\theta \times 2\hat{x} = \vec{\mu} \times \vec{B}. \tag{2.62}$$

The torque causes the change of the angular momentum given by

$$\frac{\mathrm{d}\vec{J}}{\mathrm{d}t} = \vec{N}. \tag{2.63}$$

The magnetic moment is related to the angular momentum through the gyromagnetic ratio $\gamma = g\frac{e}{2m}$ by

$$\vec{\mu} = -\gamma \vec{J}. \tag{2.64}$$

Here g is a g factor and its value depends on the kinds of angular momentum and the carrier. In the present case, as we consider the orbital moment, $g = 1$. Therefore we obtain the equation of motion for magnetic moment as

$$\frac{\mathrm{d}\vec{\mu}}{\mathrm{d}t} = -\gamma \vec{\mu} \times \vec{B}. \tag{2.65}$$

2.3.2 Landau–Lifshitz equation

In real system, there are contributions to the magnetic moment from not only orbital moments but also spin moments. For a spin moment of a free electron, the g factor included in the gyromagnetic ratio takes the value of $2.0023\cdots$ very close to 2. The deviation stems from the interaction between electron and photon. Hence we can describe the motion of the magnetic moment in the presence of spin moments by choosing the gyromagnetic ratio, while it is important to derive the equation of motion in spin systems, where the system is described by a spin Hamiltonian. We start with the action appearing in the path integral expression for a spin system given with use of the coherent state by

$$S[\theta, \phi] = \int \mathrm{d}t \left\{ \int \frac{\mathrm{d}\boldsymbol{r}}{a^3} \left[\hbar S \frac{\mathrm{d}\phi_{\boldsymbol{r}}}{\mathrm{d}t} (\cos\theta_{\boldsymbol{r}} - 1) \right] - \mathcal{H} \right\} \equiv \int \mathrm{d}t L, \tag{2.66}$$

where the localized spin is described by

$$\vec{S}_{\boldsymbol{r}} = S\hat{n}_{\boldsymbol{r}} = S(\sin\theta_{\boldsymbol{r}} \cos\phi_{\boldsymbol{r}}, \sin\theta_{\boldsymbol{r}} \sin\phi_{\boldsymbol{r}}, \cos\theta_{\boldsymbol{r}}). \tag{2.67}$$

The notation $\theta_{\boldsymbol{r}}$ means that θ is a function of $\boldsymbol{r}$ and so do others. The action $S[\theta, \phi]$ is the functional of $\theta_{\boldsymbol{r}}$ and $\phi_{\boldsymbol{r}}$, and we can obtain the equation of motion by taking the variation with respect to θ and ϕ as follows:

$$\frac{\mathrm{d}}{\mathrm{d}t}\frac{\delta L}{\delta \dot{\theta}_{\boldsymbol{r}}} - \frac{\delta L}{\delta \theta_{\boldsymbol{r}}} = 0, \ \frac{\mathrm{d}}{\mathrm{d}t}\frac{\delta L}{\delta \dot{\phi}_{\boldsymbol{r}}} - \frac{\delta L}{\delta \phi_{\boldsymbol{r}}} = 0. \tag{2.68}$$

They reduce, respectively, to

$$\frac{\hbar}{a^3} S\dot{\phi}_{\boldsymbol{r}} \sin\theta_{\boldsymbol{r}} + \frac{\delta \mathcal{H}}{\delta \theta_{\boldsymbol{r}}} = \frac{\hbar}{a^3} S\dot{\phi}_{\boldsymbol{r}} \sin\theta_{\boldsymbol{r}} + \frac{\partial \hat{n}_{\boldsymbol{r}}}{\partial \theta_{\boldsymbol{r}}} \frac{\delta \mathcal{H}}{\delta \hat{n}_{\boldsymbol{r}}} = 0, \tag{2.69}$$

$$\frac{\hbar}{a^3} S\frac{\mathrm{d}}{\mathrm{d}t}(\cos\theta_{\boldsymbol{r}} - 1) + \frac{\delta \mathcal{H}}{\delta \phi_{\boldsymbol{r}}} = -\frac{\hbar}{a^3} S\dot{\theta}_{\boldsymbol{r}} \sin\theta_{\boldsymbol{r}} + \frac{\partial \hat{n}_{\boldsymbol{r}}}{\partial \phi_{\boldsymbol{r}}} \frac{\delta \mathcal{H}}{\delta \hat{n}_{\boldsymbol{r}}} = 0. \tag{2.70}$$

Note that the time derivative of $\hat{n}_{\boldsymbol{r}}$ is given by

$$\frac{\mathrm{d}\hat{n}_{\boldsymbol{r}}}{\mathrm{d}t} = \dot{\theta}_{\boldsymbol{r}}\frac{\partial\hat{n}_{\boldsymbol{r}}}{\partial\theta_{\boldsymbol{r}}} + \dot{\phi}_{\boldsymbol{r}}\frac{\partial\hat{n}_{\boldsymbol{r}}}{\partial\phi_{\boldsymbol{r}}} \equiv \dot{\theta}_{\boldsymbol{r}}\hat{e}_{\theta,\boldsymbol{r}} + \dot{\phi}_{\boldsymbol{r}}\sin\theta_{\boldsymbol{r}}\hat{e}_{\phi_{\boldsymbol{r}}}, \tag{2.71}$$

we can combine this with the above coupled equation of motion as

$$\begin{aligned}
\sin\theta_{\boldsymbol{r}}\frac{\hbar}{a^3}\frac{\mathrm{d}\vec{S}}{\mathrm{d}t} = \sin\theta_{\boldsymbol{r}}\frac{\hbar}{a^3}S\frac{\mathrm{d}\hat{n}_{\boldsymbol{r}}}{\mathrm{d}t} &= \left(\sin\theta_{\boldsymbol{r}}\hat{e}_{\phi,\boldsymbol{r}}\frac{\delta\mathcal{H}}{\delta\hat{n}_{\boldsymbol{r}}}\right)\hat{e}_{\theta,\boldsymbol{r}} - \left(\hat{e}_{\theta,\boldsymbol{r}}\frac{\delta\mathcal{H}}{\delta\hat{n}_{\boldsymbol{r}}}\right)\sin\theta_{\boldsymbol{r}}\hat{e}_{\phi,\boldsymbol{r}}, \\
\leftrightarrow \frac{\hbar}{a^3}\frac{\mathrm{d}\vec{S}^j}{\mathrm{d}t} &= -\sum_k\left(\hat{e}^j_{\phi,\boldsymbol{r}}\hat{e}^k_{\theta,\boldsymbol{r}} - \hat{e}^j_{\theta,\boldsymbol{r}}\hat{e}^k_{\phi,\boldsymbol{r}}\right)\frac{\delta\mathcal{H}}{\delta\hat{n}^k_{\boldsymbol{r}}} = -\sum_k\epsilon_{jkl}\left(\hat{e}_{\phi,\boldsymbol{r}}\times\hat{e}_{\theta,\boldsymbol{r}}\right)_l\frac{\delta\mathcal{H}}{\delta\hat{n}^k_{\boldsymbol{r}}} \\
&= -\left(\hat{n}_{\boldsymbol{r}}\times\frac{\delta\mathcal{H}}{\delta\hat{n}_{\boldsymbol{r}}}\right)^j.
\end{aligned} \tag{2.72}$$

Note that the terms for $k = j$ are always zero on the second line. We have used that $\hat{n}_{\boldsymbol{r}} = \hat{e}_{\theta,\boldsymbol{r}}\times\hat{e}_{\phi,\boldsymbol{r}}$. Finally the relation $\vec{M}_{\boldsymbol{r}} = -\gamma\hbar\vec{S}_{\boldsymbol{r}}/a^3$ reduces this to

$$\frac{\mathrm{d}\vec{M}_{\boldsymbol{r}}}{\mathrm{d}t} = -\gamma\vec{M}_{\boldsymbol{r}}\times\left(-\frac{\delta\mathcal{H}}{\delta\vec{M}_{\boldsymbol{r}}}\right) \equiv -\gamma\vec{M}_{\boldsymbol{r}}\times\vec{B}^{\mathrm{eff}}_{\boldsymbol{r}}. \tag{2.73}$$

This equation is called Landau–Lifshitz equation, and describes the time evolution of local magnetic moments. Any terms of the spin Hamiltonian $\mathcal{H}$ possibly contribute to the effective field as well as external magnetic field. This is the generalization of Eq. (2.65), in which we can obtain the Landau–Lifshitz equation by replacing $\vec{B}$ by $\vec{B}^{\mathrm{eff}}_{\boldsymbol{r}}$.

2.3.3 Gilbert damping

The above equation of motion successfully explains the precession motion of the magnetic moment. However in realistic cases, the magnetic moment relaxes to the direction of the external or effective magnetic field with precession motion (see Fig. 2.3). Thus we need to modify the above equation since it conserves the magnetic moment. Although there are a lot of studies concerning the microscopic derivation of the relaxation, we treat this, for simplicity, by introducing the Rayleigh's dissipation function, which is common in classical mechanics. Analogous to the friction force, the dissipation function is given by

$$F = \int\mathrm{d}\boldsymbol{r}\frac{\alpha}{2}\frac{\hbar}{a^3S}\left(\dot{\vec{S}}\right)^2 = \int\mathrm{d}\boldsymbol{r}\frac{\alpha}{2}\frac{\hbar S}{a^3}\left(\dot{\theta}^2_{\boldsymbol{r}} + \sin^2\theta_{\boldsymbol{r}}\dot{\phi}^2_{\boldsymbol{r}}\right) = \int\mathrm{d}\boldsymbol{r}\frac{\alpha}{2}\frac{a^3}{\gamma\hbar M_0}\left(\dot{\vec{M}}\right)^2. \tag{2.74}$$

We add the dissipation term to the Euler–Lagrange equation:

$$\frac{\mathrm{d}}{\mathrm{d}t}\frac{\delta L}{\delta\dot{x}_\mu} - \frac{\delta L}{\delta x_\mu} = -\frac{\delta F}{\delta\dot{x}} \text{ with } x_\mu = \theta, \phi_{\boldsymbol{r}}. \tag{2.75}$$

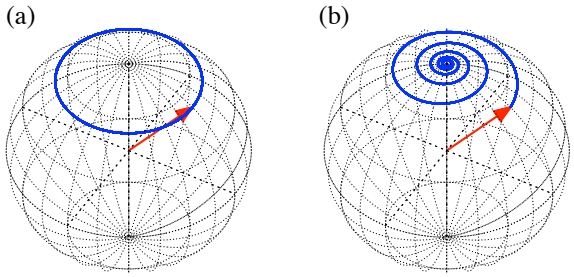

Figure 2.3: Precession motion (a) without the Gilbert damping and (b) with the Gilbert damping.

The dissipation function is not negative since it can be interpreted as the energy loss rate as

$$\begin{aligned}\frac{\mathrm{d}E}{\mathrm{d}t} &= \frac{\mathrm{d}}{\mathrm{d}t}\left(\int \mathrm{d}\boldsymbol{r}\dot{x}_\mu \frac{\delta L}{\delta \dot{x}_\mu} - L\right) = \int \mathrm{d}\boldsymbol{r}\dot{x}_\mu \left(\frac{\mathrm{d}}{\mathrm{d}t}\frac{\delta L}{\delta \dot{x}_\mu} - \frac{\delta L}{\delta \dot{x}_\mu}\right) \\ &= -\int \mathrm{d}\boldsymbol{r}\left(\dot{x}_\mu \frac{\delta F}{\delta \dot{x}_\mu}\right) = -2F < 0. \end{aligned} \tag{2.76}$$

For the last equality, we have used the Euler's homogenous function theorem as F is homogenous of degree 2 with respect to the time derivatives $\dot{x}_\mu$.

Then the dissipation function contributes to the Landau–Lifshitz equation as a torque term as

$$\frac{\hbar}{a^3}\frac{\mathrm{d}\vec{S}}{\mathrm{d}t} = -\left(\vec{S}\times\frac{\delta\mathcal{H}}{\delta\vec{S}}\right) - \alpha\frac{\hbar}{a^3 S}\left(\vec{S}\times\frac{\mathrm{d}\vec{S}}{\mathrm{d}t}\right), \tag{2.77}$$

or by using $\vec{M} = -\gamma\hbar\vec{S}/a^3$ and $M_0 = \gamma\hbar S/a^3$

$$\frac{\mathrm{d}\vec{M}}{\mathrm{d}t} = -\gamma\vec{M}\times\vec{B}^{\mathrm{eff}} + \frac{\alpha}{M_0}\left(\vec{M}\times\frac{\mathrm{d}\vec{M}}{\mathrm{d}t}\right). \tag{2.78}$$

This is called the Landau–Lifshitz–Gilbert equation. We remark that there is another but equivalent expression. That is given by

$$(1+\alpha^2)\frac{\mathrm{d}\vec{M}}{\mathrm{d}t} = -\gamma\vec{M}\times\vec{B}^{\mathrm{eff}} - \gamma\frac{\alpha}{M_0}\vec{M}\times\left(\vec{M}\times\vec{B}^{\mathrm{eff}}\right). \tag{2.79}$$

The last term on the right-hand side is the torque tilting the magnetic moment along the effective magnetic field, which is called a damping torque.

2.4 Chiral soliton lattice at zero temperature

In this section, we review the analysis of uniaxial chiral helimagnet based on the chiral sine-Gordon model[81–83, 109], which describes the chiral soliton states and the transition between the disordered and incommensurate states. We represent a classical spin using the polar coordinates as $\vec{M}(z) = S(\cos\varphi(z)\sin\theta(z), \sin\varphi(z)\sin\theta(z), \cos\theta(z))$. Here we consider one dimensional modulation in the z-direction. In the following, for convenience we omit the argument of $\vec{M}$, θ, and φ.

The energy functional of the chiral sine-Gordon model is given by

$$E = J_{\parallel} S^2 a \int \mathrm{d}z \left[\frac{1}{2} \left(\frac{\mathrm{d}\theta}{\mathrm{d}z} \right)^2 + \frac{1}{2} \sin^2\theta \left(\frac{\mathrm{d}\varphi}{\mathrm{d}z} \right)^2 - Q_0 \sin^2\theta \frac{\mathrm{d}\varphi}{\mathrm{d}z} - m^2 \sin\theta\cos\varphi \right], \quad (2.80)$$

where Q_0 and m^2 are determined by the parameters defined in the lattice model which will be introduced in the following chapters: $Q_0 = D/(J_{\parallel}a)$, $m^2 = H_{\mathrm{ex}}/(J_{\parallel}Sa^2)$. $J_{\parallel}$, D, H_{ex}, and a are strength of the exchange interaction between nearest neighbor spins along the z-direction and the DMI, an external magnetic field perpendicular to the helical axis $\vec{H}_{\mathrm{ex}} = (H_{\mathrm{ex}}, 0, 0)$, and the lattice constant, respectively. Since the constant polar angle $\theta = \pi/2$ satisfies the Euler–Lagrange equation of the functional (2.80) with respect to θ, we focus on this case. The spatial structure appears through φ, which is determined by the following Euler–Lagrange equation for φ:

$$\frac{\mathrm{d}^2\varphi}{\mathrm{d}z^2} = m^2 \sin\varphi. \quad (2.81)$$

Note that the equation itself does not contain the DMI. For convenience to seek for solutions, we transform this into

$$\frac{\mathrm{d}^2\tilde{\varphi}}{\mathrm{d}z^2} = -m^2 \sin\tilde{\varphi}\cos\tilde{\varphi}, \text{ with } \tilde{\varphi} = \frac{\varphi - \pi}{2}. \quad (2.82)$$

We can construct the solution by considering the Jacobi's amplitude function, which is given by

$$\tilde{\varphi}_{\mathrm{am}} = \mathrm{am}(u,\kappa), \; u = \int_0^{\tilde{\varphi}_{\mathrm{am}}} \frac{\mathrm{d}\theta}{\sqrt{1-\kappa^2\sin^2\theta}}. \quad (2.83)$$

This is related to the Jacobi's elliptic functions as

$$\mathrm{sn}(u,\kappa) = \sin[\mathrm{am}(u,\kappa)], \; \mathrm{cn}(u,\kappa) = \cos[\mathrm{am}(u,\kappa)], \quad (2.84)$$

$$\mathrm{dn}(u,\kappa) = \sqrt{1-\kappa^2\sin^2[\mathrm{am}(u,\kappa)]}. \quad (2.85)$$

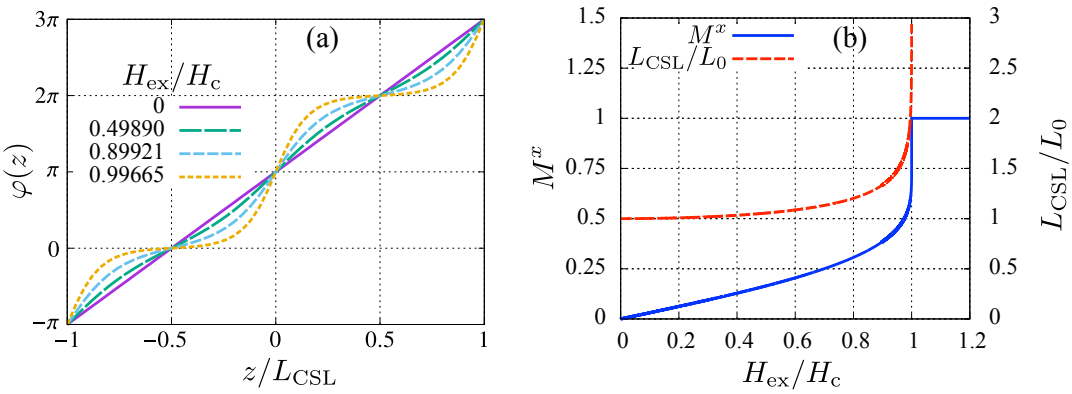

Figure 2.4: (a) Spatial dependence of φ for several values of field and corresponding κ through Eq. (2.97). The horizontal axis is normalized by the period for given parameters. (b) $H_{\rm ex}/H_{\rm c}$ dependence of the magnetization M^x and the period $L_{\rm CSL}/L_0$, whose values are indicated on the left- and right-vertical axes, respectively.

The second order derivative of $\tilde{\varphi}_{\rm am}$ with respect to u is given by

$$\frac{{\rm d}\tilde{\varphi}_{\rm am}}{{\rm d}u} = \sqrt{1-\kappa^2\sin^2\tilde{\varphi}_{\rm am}} = {\rm dn}(u,\kappa), \tag{2.86}$$

$$\frac{{\rm d}^2\tilde{\varphi}_{\rm am}}{{\rm d}u^2} = -\kappa^2{\rm sn}(u,\kappa){\rm cn}(u,\kappa) = -\kappa^2\sin\tilde{\varphi}_{\rm am}\cos\tilde{\varphi}_{\rm am}. \tag{2.87}$$

Therefore the solution to Eq. (2.81) is given by

$$\varphi = \pi + 2\tilde{\varphi} = \pi \pm 2{\rm am}(mz/\kappa,\kappa). \tag{2.88}$$

The modulus κ determines the period $L_{\rm CSL} = 2\kappa K(\kappa)/m$,[1] and the sign of the amplitude function control whether the spin structure is right-handed or left-handed. Spatial profiles of φ are shown in Fig. 2.4(a). Here we connect $m \propto H_{\rm ex}^{1/2}$ and κ through the energy minimization condition Eq. (2.97), and thus the label of each curve is given by $H_{\rm ex}/H_{\rm c}$. The field induces higher harmonics into the linear evolution of φ at $H_{\rm ex} = 0$. The sign of Q_0 favors the happy

[1]Note that $K(\kappa)$ is the complete elliptic integral of the first kind, defined by

$$K(\kappa) = \int_0^{\pi/2} \frac{{\rm d}\theta}{\sqrt{1-\kappa^2\sin^2\theta}}. \tag{2.89}$$

We also use the complete elliptic integral of the second kind $E(\kappa)$ defined by

$$E(\kappa) = \int_0^{\pi/2} {\rm d}\theta\sqrt{1-\kappa^2\sin^2\theta}. \tag{2.90}$$

direction. The in-plane spin structure is given by

$$\cos\varphi = 2\sin^2\tilde{\varphi} - 1 = 2\mathrm{sn}^2(mz/\kappa,\kappa) - 1 = \frac{2}{\kappa^2}\left[1 - \mathrm{dn}^2(mz/\kappa,\kappa)\right] - 1, \tag{2.91}$$

$$\sin\varphi = -2\sin\tilde{\varphi}\cos\tilde{\varphi} = \mp 2\mathrm{sn}(mz/\kappa,\kappa)\mathrm{cn}(mz/\kappa,\kappa). \tag{2.92}$$

The sign in the second line corresponds to the sign in Eq. (2.88). The energy per one period is given by[2]

$$E_{\mathrm{CSL}} \equiv \frac{E}{J_\parallel S^2 a L_{\mathrm{CSL}}} = \frac{4E(\kappa)}{K(\kappa)}\left(\frac{m}{\kappa}\right)^2 - m^2\left(\frac{2}{\kappa^2} - 1\right) \mp \frac{\pi Q_0 m}{\kappa K(\kappa)}. \tag{2.94}$$

To determine the modulus κ, which is an integral constant, we minimize the energy with respect to κ. The relations

$$\frac{\mathrm{d}K(\kappa)}{\mathrm{d}\kappa} = \frac{1}{\kappa}\left(\frac{E(\kappa)}{1-\kappa^2} - K(\kappa)\right), \ \frac{\mathrm{d}E(\kappa)}{\mathrm{d}\kappa} = \frac{1}{\kappa}\left(E(\kappa) - K(\kappa)\right) \tag{2.95}$$

lead to

$$\frac{\mathrm{d}E_{\mathrm{CSL}}}{\mathrm{d}\kappa} = \frac{2m^2E(\kappa)}{K^2(\kappa)\kappa^2(1-\kappa^2)}\left(-\frac{2E(\kappa)}{\kappa} \pm \frac{\pi Q_0}{2m}\right) = 0, \tag{2.96}$$

$$\rightarrow \pm\frac{m}{\kappa} = \frac{\pi Q_0}{4E(\kappa)}. \tag{2.97}$$

The sign is determined according to the sign of Q_0, and the other sign gives neither energy minimum nor maximum solution. Equation (2.97) in the limit $\kappa \to 1$ gives the critical field of D-IC transition

$$\frac{H_{\mathrm{c}}}{J_\parallel S^2 a} = \left(\frac{\pi Q_0}{4}\right)^2. \tag{2.98}$$

The field dependence of the period for the stable states and its behavior in the H_{c} limit are given by

$$L_{\mathrm{CSL}} = \frac{2\kappa K(\kappa)}{m} \rightarrow \frac{4}{\pi Q_0}\ln\frac{16H_{\mathrm{c}}}{H_{\mathrm{c}} - H_{\mathrm{ex}}} \tag{2.99}$$

[2]We use $[\varphi]_{z=0}^{z=L_{\mathrm{CSL}}} = \pm 2\pi$ and

$$\int_0^{2K}\mathrm{d}u\mathrm{dn}^2(u,\kappa) = 2\int_0^{\pi/2}\mathrm{d}\varphi\sqrt{1-\kappa^2\sin^2\varphi} = 2E(\kappa). \tag{2.93}$$

We have used $K(\kappa) \to \ln(4/\sqrt{1-\kappa^2})$, $E(\kappa) \to 1$, and $(H_{\rm c} - H_{\rm ex})/H_{\rm c}. \to 2(1-\kappa)$ in this limit. The average magnetic moment of the system is given by

$$\frac{M^x}{SL} = \frac{1}{L_{\rm CSL}} \int_0^{L_{\rm CSL}} {\rm d}z \cos\varphi = \frac{2}{\kappa^2} - 1 - \frac{2}{\kappa^2}\frac{E(\kappa)}{K(\kappa)} \tag{2.100}$$

$$\to 1 - 4\left[\ln\left(H_{\rm c}/(H_{\rm c} - H_{\rm ex})\right)\right]^{-1} (H_{\rm ex} \to H_{\rm c}), \tag{2.101}$$

which is shown in Fig. 2.4(b) and its value is indicated on the left-vertical axis. We also show the corresponding period $L_{\rm CSL}/L_0$ on the right-axis for $H_{\rm ex} < H_{\rm c}$. The period diverges when field approaches the critical value, and it is reflected in the slope of the magnetization at $H_{\rm c}$. The differential susceptibility is given by

$$\chi = \frac{1}{SL}\frac{{\rm d}M^x}{{\rm d}H_{\rm ex}} = \frac{1}{H_{\rm c}}\frac{E^3(\kappa)}{2\kappa K(\kappa)}\frac{2}{\kappa^3}\left(\frac{E^2(\kappa)}{K^2(\kappa)}\frac{2}{1-\kappa^2} + \frac{E(\kappa)}{K(\kappa)} - 1\right). \tag{2.102}$$

2.5 Review of Schaub–Mukamel's study

In this section, we summarize the study in Ref. [101] by Schaub and Mukamel, as it will be discussed in Chap. 4.

2.5.1 Model

First we explain the model introduced in Ref. [101]. Essentially their model is equivalent to the uniaxial chiral magnet at finite temperatures, and the free energy is a functional of the two component field $\vec{M}(z) = (M^x(z), M^y(z)) = M(z)(\cos\varphi(z), \sin\varphi(z))$. They consider a spatial modulation of the field $\vec{M}$ only in z-direction. For convenience we omit the argument of $\vec{M}$, $M^{x,y}$, M, and φ. The average of the free energy density functional is given by

$$F[\vec{M}] = \frac{1}{L}\int {\rm d}z f(z), \tag{2.103}$$

$$f(z) = \frac{1}{2}rM^2 + M^4 + \frac{1}{2}\left(M^x\frac{\partial M^y}{\partial z} - M^y\frac{\partial M^x}{\partial z}\right) + \frac{1}{2}\left[\left(\frac{\partial M^x}{\partial z}\right)^2 + \left(\frac{\partial M^y}{\partial z}\right)^2\right] - vM^x. \tag{2.104}$$

They explicitly mentioned that this model is appropriate for describing the ferromagnetic Dzyaloshinskii spirals under external magnetic field v perpendicular to the helical axis. The coefficient of the first term r denotes temperature. As we will see later, this model has a phase diagram with two multicritical points which separate the phase boundary into two continuous phase transition sectors, and one discontinuous phase transition sector in between. There is only one phase boundary, and the ordered phase touches the disordered phase on this line.

2.5.2 Instability-type transition

For understanding whether two continuous phase transition sectors are different or not, it is important to study instability of the disordered phase. As a result, we see that one sector can be obtained as a stability limit of the disordered phase, while the other is not. In addition, we see that one of the multicritical points is a tricritical point, where the fourth order term in the Landau free energy changes its sign.

From the disordered (uniform) state $\vec{M}_c = (M_c, 0)$, we consider the following expansion of $\vec{M}$:

$$M^x = \bar{M} + \xi\sigma_x \cos(qz) + \xi^2\bar{\sigma}_x \cos(2qz) + \xi^3\tilde{\sigma}_x \cos(3qz) + \cdots , \tag{2.105}$$

$$M^y = -\left[\xi\sigma_y \sin(qz) + \xi^2\bar{\sigma}_y \sin(2qz) + \xi^3\tilde{\sigma}_y \sin(3qz) + \cdots\right], \tag{2.106}$$

$$\bar{M} = M_c + \alpha\xi^2 + \beta\xi^4 + \cdots , \quad q = q_c + \bar{\alpha}\xi^2 + \bar{\beta}\xi^4. \tag{2.107}$$

Here $\vec{M}_c$ satisfies the saddle point condition of the free energy, which reads

$$rM_c + 4M_c^3 - v = 0. \tag{2.108}$$

Substituting these into the free energy, we obtain the coefficients in the expansion in ξ

$$F(\xi) \simeq a_0 + a_2\xi^2 + a_4\xi^4 + \cdots , \tag{2.109}$$

where

$$a_0 = \frac{r}{2}M_c^2 + M_c^4 - vM_c, \tag{2.110}$$

$$a_2 = \frac{r}{4} + M_c^2(2\sigma_x^2 + 1) + \frac{1}{4}q_c^2 - \frac{1}{2}q_c\sigma_x\sigma_y, \tag{2.111}$$

$$\begin{aligned} a_4 = {} & \frac{r}{4}(\bar{\sigma}_x^2 + \bar{\sigma}_y^2 + 2\alpha^2) + 6\alpha^2 M_c^2 + \frac{3 - 4\sigma_x^2\sigma_y^2}{8} \\ & + M_c^2(3\bar{\sigma}_x^2 + \bar{\sigma}_y^2) + 2(2\sigma_x^2 + 1)\alpha M_c + 2M_c\sigma_x\sigma_y\bar{\sigma}_y + M_c\bar{\sigma}_x(3\sigma_x^2 - \sigma_y^2) \\ & + (\bar{\sigma}_x^2 + \bar{\sigma}_y^2)q_c^2 - q_c\bar{\sigma}_x\bar{\sigma}_y + \frac{q_c - \sigma_x\sigma_y}{2}\bar{\alpha}. \end{aligned} \tag{2.112}$$

We have used Eq. (2.108) for simplifying a_4. The parameters should be determined by satisfying $\partial a_2/\partial q_c = 0$, and $\partial a_2/\partial\sigma_x = 0$. They lead to

$$\frac{\partial a_2}{\partial q_c} = \frac{q_c - \sigma_x\sigma_y}{2} = 0 \to q_c = \sigma_x\sigma_y, \tag{2.113}$$

$$\frac{\partial a_2}{\partial \sigma_x} = 4M_c^2\sigma_x - \frac{q_c}{2}\left(\sigma_y - \frac{\sigma_x^2}{\sigma_y}\right) \to 8M_c^2 + \sigma_x^2 - \sigma_y^2 = 0. \tag{2.114}$$

With use of $\sigma_x^2 + \sigma_y^2 = 1$, we get

$$\sigma_x^2 = \frac{1}{2}(1 - 8M_c^2), \sigma_y^2 = \frac{1}{2}(1 + 8M_c^2), q_c = \frac{1}{2}\sqrt{1 - 64M_c^4}, \tag{2.115}$$

$$a_2 = \frac{r}{4} + 2M_c^2(1 - 4M_c^2) - \frac{1}{16} + 4M_c^4. \tag{2.116}$$

The instability occurs at $a_2 = 0$ and this condition is satisfied when the magnetization takes the following value:

$$4M_c^2 = 1 - \sqrt{r + 3/4}. \tag{2.117}$$

Note that M_c should be a decreasing function of r, and we find $r < 1/4$. We also find that $r > -1/2$ from Eqs. (2.115) and (2.117), since σ_x and q_c are real. Finally we get the value of the critical field

$$v = \frac{1}{2}\left[1 - \left(r + \frac{3}{4}\right)^{1/2}\right]^{1/2}\left[r + 1 - \left(r + \frac{3}{4}\right)^{1/2}\right]. \tag{2.118}$$

This line is shown in Fig. 2.5(a). The transition is continuous if $a_4 \geq 0$ at $a_2 = 0$, and the tricritical point is the place where $a_2 = 0$ and $a_4 = 0$. Using the conditions obtained above, a_4 is reduced to

$$\begin{aligned} a_4 = r\frac{\bar{\sigma}_x^2 + \bar{\sigma}_y^2 + 2\alpha^2}{4} + 6\alpha^2 M_c^2 + 1 - \frac{4}{3}\sigma_x^2\sigma_y^2 + M_c^2(3\bar{\sigma}_x^2 + \bar{\sigma}_y^2) + 2(2\sigma_x^2 + 1)\alpha M_c \\ + 2M_c\sigma_x\sigma_y\bar{\sigma}_y + M_c\bar{\sigma}_x(3\sigma_x^2 - \sigma_y^2) + (\bar{\sigma}_x^2 + \bar{\sigma}_y^2)\sigma_x^2\sigma_y^2 - \sigma_x\sigma_y\bar{\sigma}_x\bar{\sigma}_y. \end{aligned} \tag{2.119}$$

Other parameters can be also determined by the conditions that $\partial a_4/\partial\alpha = 0$:

$$(r + 12M_c^2)\alpha + 2(2\sigma_x^2 + 1)M_c = 0 \to \alpha = -\frac{2(2\sigma_x^2 + 1)M_c}{r + 12M_c^2}, \tag{2.120}$$

and that $\partial a_4/\partial\bar{\sigma}_x = 0$, $\partial a_4/\partial\bar{\sigma}_y = 0$:

$$\begin{pmatrix} \frac{r}{2} + 2\sigma_x^2\sigma_y^2 + 6M_c^2 & -\sigma_x\sigma_y \\ -\sigma_x\sigma_y & \frac{r}{2} + 2\sigma_x^2\sigma_y^2 + 2M_c^2 \end{pmatrix}\begin{pmatrix} \bar{\sigma}_x \\ \bar{\sigma}_y \end{pmatrix} = \begin{pmatrix} M_c(1 - 4\sigma_x^2) \\ -2M_c\sigma_x\sigma_y \end{pmatrix}. \tag{2.121}$$

From these, the tricritical point can be evaluated as $r_{\rm TC} \simeq 0.192$ and $v_{\rm TC} \simeq 0.019$. Equation (2.118) for $r_{\rm TC} < r < 1/4$ is shown in Fig. 2.5(a) by the solid line and also shown in Fig. 2.5(b) as the line I.

For determining the whole phase diagram, one need to solve the stationary condition of the free energy:

$$\frac{{\rm d}^2 M}{{\rm d}z^2} - M\left(\frac{{\rm d}\varphi}{{\rm d}z}\right)^2 - M\frac{{\rm d}\varphi}{{\rm d}z} + v\cos\varphi - rM - 4M^3 = 0, \tag{2.122}$$

$$M^2\frac{{\rm d}^2\varphi}{{\rm d}z^2} - vM\sin\varphi + 2M\frac{{\rm d}M}{{\rm d}z}\frac{{\rm d}\varphi}{{\rm d}z} + M\frac{{\rm d}M}{{\rm d}z} = 0, \tag{2.123}$$

which have several solutions for a fixed parameters (r, v), and we need to compare the free energy to determine the realized state. Note that the above analysis works for $-1/2 < r < 1/4$,

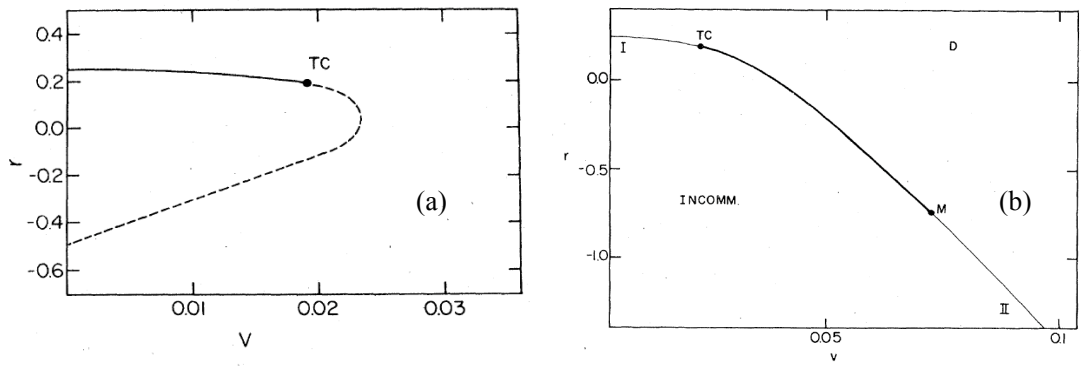

Figure 2.5: Phase diagram obtained by Schaub and Mukamel[101]. The horizontal and vertical axes represent r and v, respectively. (a) The solid line ($r_{\rm TC} < r < 1/4$) and the dashed line ($-1/2 < r < r_{\rm TC}$) are given by Eq. (2.118). TC denotes the tricritical point. (b) The whole phase boundary consists of instability-type phase transition line (I), discontinuous phase transition line (thick line), and nucleation-type phase transition line (II). The symbols M, D, and INCOMM represent the multicritical point, disordered phase, and incommensurate phase, respectively.

and the continuous phase transition accompanied by the instability of the uniform state occurs for $r_{\rm TC} < r < 1/4$. In the low temperature limit $r \to -\infty$, the model is reduced to the chiral sine-Gordon model[110, 111]. The stable ordered state is a periodic structure with higher harmonics and the phase transition is continuous, as reviewed in the previous section. In such a case, we cannot explain the continuous phase transition with an instability of the uniform state by a single q mode. The whole phase boundary is determined as follows: We can solve Eqs. (2.122) and (2.123), and obtain a single soliton with a periodic boundary condition for a fixed sized system Δz. The solution corresponds to the periodic structure of solitons with period Δz, and we can obtain the most stable state for a given (r, v) by minimizing the free energy with respect to Δz. The phase boundary is given by (r, v) such that the minimized free energy is the same as that of the uniform state. The whole phase boundary is shown in Fig. 2.5(b). Actually we can see that the line obtained through the above analysis is equivalent to a part of the phase boundary for $r_{\rm TC} < r < 1/4$. Moreover the detailed numerical calculations clarify that there is another multicritical point around $r_{\rm MC} \sim -0.74$, and the phase transition between $r_{\rm MC} < r < r_{\rm TC}$ is discontinuous. As we will see later, a soliton picture is effective and a linear analysis introduced in the following subsection is powerful in order to understand the phase diagram.

2.5.3 Linear analysis

As mentioned in the previous section, solitons characterize the ordered state in the low temperature side. Near the phase boundary of the continuous phase transition $r < r_{\rm MC}$, soliton density is dilute and its property is determined by the asymptotic region of a soliton. In order to study how the tail structure of a soliton approaches the uniform background $\vec{M}_c$ in the asymptotic region, we perform the linear analysis regarding the small deviation of $\vec{M}$ from $\vec{M}_c$.

A linear analysis using the asymptotic behavior tells us information about the multicritical points. Let the soliton center be at the origin $z = 0$, and set the angle $\varphi(z = 0) = \pi$ there. For $z \to +\infty$, $\vec{M}$ relaxes to $\vec{M}_c$ and φ approaches 2π. In the region far from the center, we can describe the asymptotic behavior of the soliton as

$$|\vec{M}| \approx M_c + A_1 \exp(-\kappa z),\ \varphi \approx 2\pi + A_2 \exp(-\kappa z). \tag{2.124}$$

Substituting these into the equation of motion (2.122) and (2.123), we obtain

$$\begin{pmatrix} 12M_c^2 + r - \kappa^2 & -M_c\kappa \\ M_c\kappa & vM_c - M_c^2\kappa^2 \end{pmatrix} \begin{pmatrix} A_1 \\ A_2 \end{pmatrix} = \begin{pmatrix} 0 \\ 0 \end{pmatrix}. \tag{2.125}$$

The condition for the presence of a non-trivial solution is the zero determinant of the coefficient matrix, which is the quadratic equation of κ^2 given by

$$M_c^2\kappa^4 - [(12M_c^2 + r)M_c^2 + vM_c - M_c^2]\kappa^2 + (12M_c^2 + r)M_c v = 0. \tag{2.126}$$

We can distinguish the type of solution depending on whether the solution κ^2 is real or complex. The discriminant of this quadratic equation is

$$\begin{aligned} \mathsf{D} &= [(12M_c^2 + r)M_c^2 + vM_c - M_c^2]^2 - 4M_c^3(12M_c^2 + r)v \\ &= 64M_c^4 - 32M_c^2 + 1 - 4r. \end{aligned} \tag{2.127}$$

For $\mathsf{D} < 0$, both κ^2 and κ are complex, while κ^2 is real if $D > 0$. When $\kappa^2 > 0$, κ is real, while when $\kappa^2 < 0$, κ is pure imaginary[3]. When κ has a finite imaginary part, we can equivalently consider the real part of $\vec{M}(z)$ within the linear approximation. Note that when $\kappa^2 = 0$, the left-hand side of Eq. (2.126) is

$$(12M_c^2 + r)v = (12M_c^2 + v/M_c)v > 0, \tag{2.128}$$

which means that two real solutions of κ^2 have the same sign. We notice that the condition $\mathsf{D} = 0$ coincides with the line of $a_2 = 0$. Let us reconsider the behavior of $\vec{M}(z)$ when κ is pure imaginary, $\kappa = \mathrm{i}q$ (q: real). In this case, we assume a small deviation in $\vec{M}(z)$ by taking $A_1 = \xi\sigma_x$ and $A_2 = \mathrm{i}\xi\sigma_y/M_c$ where ξ is sufficiently small and $\sigma_x^2 + \sigma_y^2 = 1$ holds. We can see

[3]When κ is pure imaginary, there is no relaxation to $\vec{M}_c$. In this case, we assume that (A_1, A_2) is infinitesimal to guarantee the linear approximation.

why there is a prefactor i on A_2 from the coupled equation of A_1 and A_2. Note that in this case there is no longer soliton at $z = 0$. Instead we write down the field $\vec{M}$ up to first order in ξ as

$$M^x = M\cos\varphi \approx M \approx M_c + \xi\sigma_x e^{\mathrm{i}qz} + \cdots , \tag{2.129}$$

$$M^y = M\sin\varphi \approx M\varphi \approx \mathrm{i}\xi\sigma_y e^{\mathrm{i}qz} + \cdots . \tag{2.130}$$

This is equivalent to the expansion we used to study the instability-type transition up to first order in ξ. When κ has a positive real part, there is an asymptotic solution of an isolated soliton[4]. The parameter region of pure imaginary κ faces the region of complex κ on the line $\mathsf{D} = 0$.

We have seen the meanings of pure imaginary. Next, we consider the soliton interaction and the difference between real κ and complex κ. Jacob and Walker discussed the interaction energy between two isolated discommensurations with a finite distance[92]. The conclusion is that whether κ is real or complex is reflected in whether the interaction is repulsive or attractive. Let us write the free energy for the uniform state as $F_{\mathrm{uni}} = \frac{r}{2}M_c^2 + M_c^4 - vM_c$ and measure the free energy of a single soliton from it: $\Delta F_{\mathrm{single}} = F_{\mathrm{single}} - F_{\mathrm{uni}}$. Now we define the binding energy of N solitons as

$$\Delta F_{\mathrm{bind}}^{(N)} = F_{\mathrm{chain}}^{(N)} - F_{\mathrm{uni}} - N\Delta F_{\mathrm{single}}. \tag{2.131}$$

Here $F_{\mathrm{chain}}^{(N)}$ denotes the free energy of the N-soliton state, and we call the binding energy F_{bind} the interaction energy ΔF_{int} when $N = 2$. The interaction energy depends on the inter-soliton distance Δz. Near the phase transition the soliton density is relatively dilute, and thus we consider only the two body interaction ΔF_{int}. Consider the repulsive interaction corresponding to a real κ. Typically ΔF_{int} exponentially decays with the inter-soliton distance Δz, and its range is characterized by the soliton size $(\mathrm{Re}\kappa)^{-1}$. The equilibrium distance is determined through the competition between $\Delta F_{\mathrm{single}}$ and ΔF_{int} when $\Delta F_{\mathrm{single}} < 0$, while there is no soliton when $\Delta F_{\mathrm{single}} > 0$. Therefore the nucleation-type continuous phase transition line is given by $\Delta F_{\mathrm{single}} = 0$.

When the tail of the single soliton oscillates in space, we could show that the interaction energy oscillates with the distance analytically for $\Delta z \gg (\mathrm{Re}\kappa)^{-1}$. According to Ref. [101], it is given for the parameter such that $\Delta F_{\mathrm{single}} = 0$ by

$$\Delta F_{\mathrm{int}} = (-\alpha A_1^2 + \alpha M_c^2 A_2^2 - M_c A_1 A_2)\exp(-\kappa\Delta z) + \mathrm{c.c.} \tag{2.132}$$

When κ is complex, the interaction can be negative in some regions of the inter-soliton distance. This means that there is a lower energy state than the single soliton solution when the free energy of the single soliton solution is the same as that of the disordered state ($\Delta F_{\mathrm{single}} = 0$).

[4]This is a necessary condition for the existence of an isolated soliton in terms of its asymptotic form.

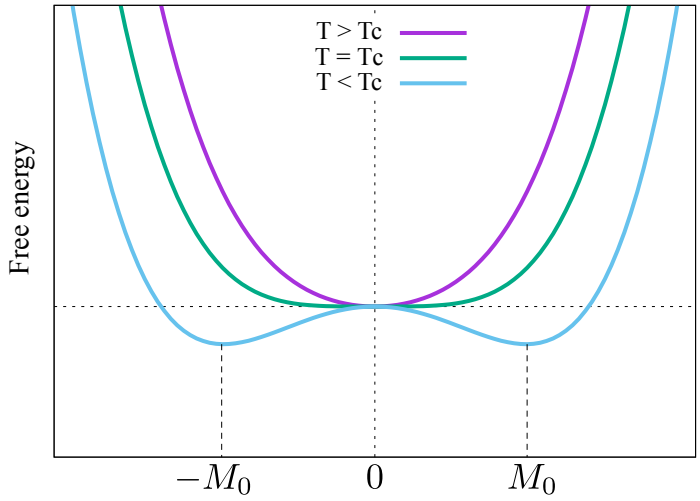

Figure 2.6: Examples of the Landau free energy.

2.6 Two kinds of continuous phase transitions

Phase transitions are distinguished depending on whether it is continuous or discontinuous with respect to the first order derivatives of a free energy, such as magnetization and entropy. Moreover, de Gennes classified continuous phase transitions into two subclasses: instability-type and nucleation-type[84]. Although de Gennes's classification might be for general continuous phase transitions in three dimensions, we restrict ourselves into ordered phases with periodic modulations for clarity. In the following subsections, we first introduce de Gennes's argument on the basis of familiar examples for each class. Second we clarify the classification for continuous phase transitions with periodic orders.

2.6.1 Instability-type phase transition

First we explain the instability-type phase transition, which is well-known as it is described by the Landau theory of the phase transition. The ordered phase can be characterized by a small and local order parameter, which is in general observable[5]. A familiar example is a ferromagnetic system, and the magnetization M denotes the order parameter. The Landau free

[5]Note that in superconductor, the macroscopic wave function of the condensation is an order parameter, but it is not observable.

energy $F(M)$ is given by

$$F(M) = a_2(T)M^2 + a_4M^4 \text{ with } a_2 = a_t(T - T_c), \tag{2.133}$$

where $a_2(T)$ is a function of temperature T with a positive constant a_t, and a_4 is a positive constant. The sign of $a_2(T)$ changes at $T = T_c$, and $F(M)$ takes a minimum at $M = 0$ for $T > T_c$, and at $|M| = M_0 \equiv [a_t(T_c - T)/a_4]^{1/2}$ for $T < T_c$, as sketched in Fig. 2.6. When T approaches to T_c from above, the positive curvature of the free energy around $M = 0$ becomes smaller. This represents the enhancement of the susceptibility $\chi \propto [\partial^2 F/\partial M^2|_{M=0}]^{-1} = [a(T - T_c)]^{-1}$ near T_c, namely, a small magnetic field induces a large magnetic moment.

In uniaxial chiral magnets, a transition between a uniformly polarized state and a conical state under magnetic field is an example with a periodic order. We do not explain the detail, but obtain the Landau free energy as a special case of the Landau expansion in Sect. 4.4:

$$E(\xi) = (2J_\parallel + H^z_{\rm ex}) - \frac{H_c - H^z_{\rm ex}}{4}\xi^2 + \frac{H^z_{\rm ex}}{32}\xi^4 \text{ with } H_c = 2\left(\sqrt{J_\parallel^2 + D^2} - J_\parallel\right). \tag{2.134}$$

Here we set $K = 0$ and $H^x_{\rm ex} = 0$ in Sect. 4.4. An order parameter ξ appears in the magnetic moment $\vec{M}_l$ within the Landau expansion as

$$\vec{M}_l \approx \begin{pmatrix} \xi\cos(q_c x_l)/\sqrt{2} \\ \xi\sin(q_c x_l)/\sqrt{2} \\ 1 - \xi^2/4 \end{pmatrix} \text{ with } q_c a = \tan^{-1} D/J_\parallel \text{ and } x_l = al. \tag{2.135}$$

In this case, we can say that the order parameter is $\vec{M}_{q_c}$, a Fourier component of M_l. The Landau free energy (2.134) takes the same form as Eq. (2.133), but in this case a small helical field, $\vec{H}(\boldsymbol{r}) = H_{q_c}(\cos q_c z, \sin q_c z, 0)$, induces a large helical moment near the critical field. It is important that the single mode with wave number q_c contributes the phase transition, which characterizes its period, and its higher harmonics do not.

2.6.2 Nucleation-type phase transition

Next we explain the nucleation-type continuous phase transition. On the basis of de Gennes's argument[84], we consider a ferromagnetic sphere with macroscopic size in a magnetic field. The uniformly magnetized state is not the most stable state below a threshold field, and a domain structure appears because the surface creates the demagnetizing field. For the field just below the threshold field, the uniform state is stable against all small local fluctuations of magnetization, and the corresponding Hessian[6] remains positive definite. Domains, the Bloch walls in this case, are related to distortions with the large amplitude and they nucleate near defects or the surface. Thereby the transition is called nucleation-type. We could not assign

[6] A Hessian is a matrix consisting of the second order derivatives of the Hamiltonian or free energy with respect to the degree of freedom in fluctuations.

a small and local order parameter in the sense of the Landau theory, although it is possible to characterize the state using topological properties corresponding to the number of domains. There are several examples of the nucleation-type continuous phase transitions, and one of them is the transition at the lower critical field in type-II superconductors. The transition occurs between the Meissner state and the mixed state, and quantized vortices enter the system above the lower critical field.

The nucleation-type phase transition is characterized by emergent particles such as quantized vortices and domain walls, and topological constraints interpreted as the number of the particles is kind of an order parameter. In the superconducting vortex case, it is the winding number, i.e., the number of flux quanta, associated with the magnetization. The emergent particle picture describes this transition well, in which we consider the competition between the single particle energy of the emergent particle and its interaction energy, as was reviewed in Sect. 2.5.3. In the vicinity of the transition in the ordered phase, the interaction is very weak since it has a finite range. Thus it is possible to form many nearly free particles, which results in the steep change of the physical quantities such as magnetization. These transitions are continuous, but do not have the small fluctuations leading to the instability and often show hysteresis. In the superconducting case, the Bean–Livingston barrier[105] causes the hysteresis, as we see later.

We characterize this phase transition for periodic orders in more explicit way. The Abrikosov vortex lattice is a periodic structure, and other examples are the D-IC transition in the Dzyaloshinskii helimagnet, as was reviewed in Sect. 2.4 and the Freédericksz transition in chiral liquid crystals. The first important feature is the divergence of the period. Let $\boldsymbol{Q}$ be the corresponding wave vector, and it approaches $\mathbf{0}$ when the phase boundary is approached in the ordered phase. The second one is the presence of higher harmonics. Let $O(\boldsymbol{r})$ be the field to describe the system. $O(\boldsymbol{r})$ can be the condensation wave function for superconductors, or spins for the Dzyaloshinskii helimagnet. In the same limit to the phase boundary as above, higher harmonics of the fundamental wave exist since there is a localized emergent particle. Thus for its Fourier components $O(\boldsymbol{q})$, the ratio $O(n\boldsymbol{Q})/O(\boldsymbol{Q})$ is finite in this limit. The third one is the stability against small and local fluctuations. As mentioned above, the Hessian of the uniform state remains positive definite even after the phase transition to the ordered phase, and the Hessian of a state with a finite topological number does in the disordered phase to some extent. In addition, a topological number changes in the ordered phase without accompanied by the instability. The fourth feature is the absence of a small and local order parameter related to the third one. The helical order parameter of the instability-type phase transition is small and local near the phase transition. The small and local order parameter is necessary to lead the instability of the disordered phase. Consider the emergent particle density given by the topological number per a volume. One might construct the Landau free energy for this density since this vanishes at the transition line and finite in the ordered phase. However the construction of the Landau free energy does not necessarily mean that the continuous phase transition is instability-type because the states with different densities are distant in the configuration space of the original field O, and a process with an infinitesimal distortion to change the density

	Q	$O(nQ)/O(Q)$	Hessian	OP
instability	finite	0	positive & negative	✓
nucleation	0	finite	positive definite	✗

Table 2.1: Summary of continuous phase transitions associated with periodic orders. The wave vector Q characterizes the inverse of the period of the periodic structure. We define $O(q)$ by the Fourier component of the field describing the system, and the third column describes whether the ratios of the higher harmonics to $O(Q)$ remain finite or not. The Hessian of the state which is the most stable before a transition has negative eigenvalues after the transition for instability-type, while does not for the nucleation-type. The last column about OP explains the presence/absence of a small and local order parameter.

does not exist. Also one might try to construct the Landau free energy of an order ξ such that $O(n\boldsymbol{Q}) = \xi f_n$ with a form factor f_n. Thereby we can take account of higher harmonics and nonzero ratio of $O(n\boldsymbol{Q})/O(\boldsymbol{Q})$ at the transition. However it is difficult to determine the form factors for all n, and obtain the Landau free energy. Even if one did it, again it would not mean that an instability accompanied the transition because the assembly of the form factor represents the localized structure of an emergent particle, and $O(\boldsymbol{r})$ is not infinitesimal. We remark that it might be possible to describe the nucleation-type phase transition using the above Landau expansions in a proper way. However the emergent particle picture is much more effective to describe the phase transition and multicritical point if exists since derivations of the Landau free energy require tough calculation to obtain a logarithmic divergence of a distance between emergent particles $\Delta l_{\rm e.p.}$ and a corresponding singular behavior of magnetization *et al.* Note that $\Delta l_{\rm e.p.} \propto \ln(H_{\rm c} - H_{\rm ex})$ [see Eq. (2.99) in the soliton case], and the density of emergent particles is given by $n_{\rm e.p.} = 1/\Delta l_{\rm e.p.}$ for a soliton lattice and $n_{\rm e.p.} = 1/\Delta l_{\rm e.p.}^2$ for a vortex lattice. Magnetization can be described by the the magnetization of a single emergent particle multiplied by the density $n_{\rm e.p.}$. For example the constitutive relation of type-II superconductors near the lower critical field is given by

$$B(H) = 4\pi M + H = \frac{2\phi_0}{\sqrt{3}\lambda^2}\left\{\ln\left[\frac{3\phi_0}{4\pi\lambda^2(H - H_{\rm c1})}\right]\right\}^{-2} \tag{2.136}$$

with the magnetic flux quantum ϕ_0 and the penetration depth λ. These logarithmic behaviors can be easily obtained through the competition between the energy of a single emergent particle and its interaction energy[112, 113].

2.6.3 Summary of classification

We summarize the two types of continuous phase transition between the periodic ordered phase and disordered phase in Table 2.1. Here we have listed four points.

In the case of the instability-type phase transition, there exists a small and local order parameter with a finite period, i.e. a finite wave vector $\boldsymbol{Q}$, and its higher harmonics do not contribute at the transition. The presence of the small and local order parameter at the transition means that the instability of the disordered phase exists there. Thus its Hessian of the uniform state has negative eigenvalues in the ordered state.

On the other hand, in the case of the nucleation-type phase transition, the period diverges, i.e., $\boldsymbol{Q} \to 0$ in the limit to the phase transition with higher harmonics but without a small and local order parameter. Correspondingly the Hessian remains positive definite for a state which is not the most stable state. Since such a state is stable against infinitesimally small fluctuations, the change of the state is driven by the nucleation of the emergent particles. For type-II superconductors and Dzyaloshinskii helimagnets, magnetization curves have logarithmically diverging slopes at the transition, which can be described well by the emergent particle picture.

Chapter 3

Non-reciprocal magnon in chiral magnet

In this chapter, we investigate the non-reciprocity in spin waves developed by a magnetic field parallel to the direction of DMI. The non-reciprocal spin waves are well known in the uniform state of non-centrosymmetric ferromagnets. First we review their theory. Then for uniaxial chiral ferromagnets we introduce a simplified model and calculate the dynamical spin structure factor to study the non-reciprocal spectral structure in a non-uniform state. Since it is easy to investigate the spectral structure of the uniaxial chiral antiferromagnet, we calculate it and discuss the difference from that in the ferromagnetic case. Finally we compare this result with numerical results calculated by Monte Carlo simulation and simulation based on the Landau–Lifshitz equation.

3.1 Introduction

Recent studies on chiral magnets are triggered by the observations of several non-trivial magnetic states and topological textures stabilized by the DMI[48, 49] such as chiral skyrmions and chiral solitons[34, 43]. Although a helical (or cycloidal) order due to the competition between the DMI and the Heisenberg exchange interaction is not a topological texture, the DMI affects spin wave excitations and leads to a non-reciprocal propagation in the presence of magnetic field. An example of effects of antisymmetric SOI is the Rashba splitting in the single-electron energy spectrum in non-centrosymmetric system[78]. A corresponding phenomenon in magnets is non-reciprocal spin wave propagation in non-centrosymmetric ferromagnets[65, 66]. The non-reciprocal spin wave propagation means that spin waves with the wave vector $\boldsymbol{k}$ and $-\boldsymbol{k}$ have different energies, $E_{-\boldsymbol{k}} \neq E_{\boldsymbol{k}}$. In particular, the group velocity of the spin wave with $\boldsymbol{k} = 0$ is finite, and its sign depends on the direction of the magnetic field. Whereas non-reciprocity can appear in the surface state called Damon–Eschbach mode in ferromagnets and antiferromagnets[114–117], our present concern is in asymmetric dispersion relations in the bulk spin wave excitations governed entirely by the DMI. The physical mechanism of non-reciprocity is as follows: In the presence of the DMI, a magnon acquires the Berry phase during the hopping process and this phase shifts the wave vector[72]. We can understand this

on the basis of an analogous situation for electrons as follows: the phase is equivalent to a constant vector potential, and the kinetic momentum can be given by the canonical momentum shifted by the vector potential. The shift is in one direction owing to the fixed direction of the precession, and leads to asymmetry in the spin wave dispersion. Observing this effect is connected to experimental measurement of antisymmetric interactions of spins, i.e. the DMI, [67–73] and this effect may be used as a logic gate in magnonics field[118].

An important issue is "non-reciprocity" in a non-uniform state, because dispersion is not defined in non-uniform states such as helical and conical states, instead the elementary excitation is labeled by a pseudo momentum. Thus it is an interesting issue what is a concept of non-reciprocity in a non-uniform state, which is naturally connected to that in the uniform state. A conical state is a field-induced intermediate state between the uniform and helical states, and it is also interesting to see how magnetic field develops the non-reciprocity in the conical state toward the uniform state. In Ref. [66], Kataoka argued that the spin wave dispersion in the uniform state does not coincide with "dispersion" in the conical state at $H = H_{\rm c}$, though the elementary excitation in the conical state is labeled by a pseudo momentum[1]. A recent experiment based on an asymmetric microwave response did not exhibit an evidence of the non-reciprocity below $H_{\rm c}$[73]. When the non-reciprocity is concerned, it is not adequate to use a pseudo momentum labeling the elementary excitations, and thus we study the dynamical spin structure factor[2]. We examine here spin waves on the uniaxial chiral magnet, which is one of the simplest systems and a model of $Cr_{1/3}NbS_2$[61, 62]. The ground state configuration at zero field is a single helix caused by the DMI propagating along the DM vector $\vec{D}$ which appears in the DMI as $\vec{D} \cdot (\vec{S}_j \times \vec{S}_l)$. Note that $\vec{D}$ is parallel to the bond direction in this case. We call this direction the helical axis. Magnetic field applied along the DM vector changes the helical state into a conical state, and above a critical field, polarizes it into a uniform alignment. The spin configuration is shown in Fig. 3.1 for the three phases. One can go *continuously* from a helical state to a uniform spin structure by varying the applied field strength.

We find that there are three branches in the helical state. We define the branch by the peak position of the dynamical spin structure factor $C^{\mu\nu}(q,\omega)$ where $\mu,\nu = x,y,z$.[3] One of them appears in $C^{zz}(q,\omega)$ and the other two do in $C^{\mu\nu}(q,\omega)$ with $\mu,\nu = x,y$. These two are inverse images of each other obtained by shifting the wave vector by the modulation vector $\pm\vec{Q}$. The branches and their intensities are symmetric in the helical state. Furthermore when the magnetic field is applied along the DM vector, we find that the intensity of one branch decreases while the other increases in the transverse spin correlations in the conical state. The decreasing intensity finally becomes zero, when the system is in the uniform state, and then the branch is non-reciprocal.

This chapter is organized as follows. On the basis of a chiral ferromagnetic model, we

[1]Note that he argued that inelastic neutron scattering experiment would not exhibit any discontinuous change there

[2]A paper appears on the preprint server during the revision of this thesis, which discusses the dynamical spin structure factor as well for a cubic helimagnets[119].

[3]Within the spin wave approximation, spectrum has δ function and we define a branch by its support.

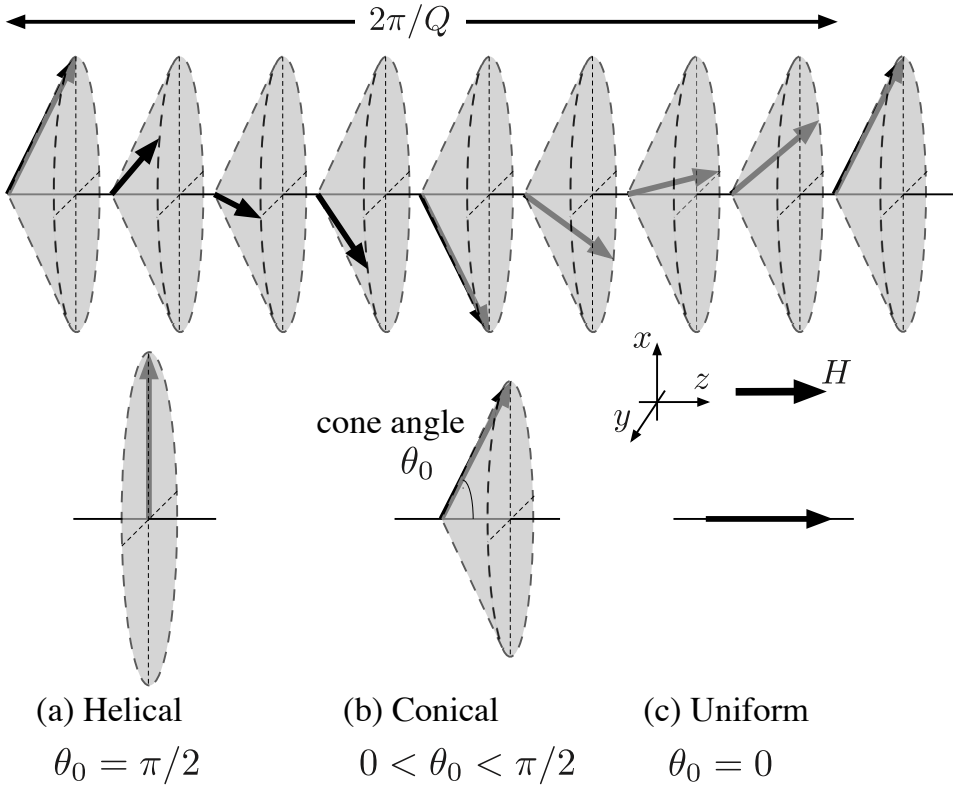

Figure 3.1: Sketches of the three states in the chiral magnet: helical, conical, and uniform. The top image describes the directions of spins $\{\vec{S}_j\}$ in the original frame, which have the cone angle θ_0 defined by the angle between $\vec{S}_j$ and the helical axis parallel to $\vec{D}$. (a) The helical state is described by $\theta_0 = \pi/2$, (b) the conical state when $0 < \theta_0 < \pi/2$, and (c) the uniform state by $\theta_0 = 0$ in the frame of $\{\vec{S}_j\}$.

first obtain the spin wave excitations and calculate the spin correlation functions, and discuss non-reciprocity in the correlation function. We next consider antiferromagnetic interactions and find that, as well as the ferromagnetic case, the spin wave modes separate into distinct branches and show the non-reciprocity in the presence of the magnetic field. In contrast to the ferromagnetic case, remarkable changes appear in the branches in addition to the intensity since the Néel-type properties disappear in increasing field. Finally we compare these analytical results with numerical calculations.

3.2 Non-reciprocal magnon

In this section, first we review the non-reciprocal magnon spectrum in the uniform state under the magnetic field along the helical axis, by introducing the following Hamiltonian:

$$\begin{aligned}\mathcal{H} &= \sum_{\boldsymbol{j}} \left[-J_{\parallel} \vec{S}_{\boldsymbol{j}} \cdot \vec{S}_{\boldsymbol{j}+\hat{z}} - D \left(S^x_{\boldsymbol{j}} S^y_{\boldsymbol{j}+\hat{z}} - S^y_{\boldsymbol{j}} S^x_{\boldsymbol{j}+\hat{z}} \right) - H S^z_{\boldsymbol{j}} + \mathcal{H}_{\perp,\boldsymbol{j}} \right] \\ &= \sum_{j} \left\{ -\frac{\tilde{J}}{2} \left[e^{\mathrm{i}Qa} S^+_{\boldsymbol{j}} S^-_{\boldsymbol{j}+\hat{z}} + e^{-\mathrm{i}Qa} S^-_{\boldsymbol{j}} S^+_{\boldsymbol{j}+\hat{z}} \right] - J_{\parallel} S^z_{\boldsymbol{j}} S^z_{\boldsymbol{j}+\hat{z}} - H S^z_{\boldsymbol{j}} + \mathcal{H}_{\perp,\boldsymbol{j}} \right\}, \qquad (3.1) \\ \mathcal{H}_{\perp,\boldsymbol{j}} &= -\sum_{\mu=x,y} J_{\perp} \vec{S}_{\boldsymbol{j}} \cdot \vec{S}_{\boldsymbol{j}+\hat{\mu}}. \qquad (3.2)\end{aligned}$$

Here $J_{\parallel}$ and D are the exchange and Dzyaloshinskii–Moriya interactions between the nearest neighbor spins respectively along the z-direction, which is parallel to the helical axis. $\tilde{J} = \sqrt{J_{\parallel}^2 + D^2}$ and $Qa = \tan^{-1}(D/J_{\parallel})$ with a lattice constant a. The subscript $\boldsymbol{j}$ denotes the site in the three dimensional cubic lattice and $\hat{\mu}$ for $\mu = x, y, z$ is the unit vector of the lattice translation in the μ-direction. We simply use the same lattice constant, a, in any direction. The magnetic field H is applied along the helical axis. Using the Holstein–Primakoff transformation

$$S^+_{\boldsymbol{j}} = \sqrt{2S} \left(1 - \frac{n_{\boldsymbol{j}}}{2S} \right)^{\frac{1}{2}} a_{\boldsymbol{j}}, \; S^-_{\boldsymbol{j}} = \sqrt{2S} a^\dagger_{\boldsymbol{j}} \left(1 - \frac{n_{\boldsymbol{j}}}{2S} \right)^{\frac{1}{2}}, \; S^z_{\boldsymbol{j}} = S - n_{\boldsymbol{j}}, \qquad (3.3)$$

with the number operator $n_{\boldsymbol{j}} = a^\dagger_{\boldsymbol{j}} a_{\boldsymbol{j}}$ and the Fourier transform:

$$a_{\boldsymbol{k}} = \frac{1}{\sqrt{N}} \sum_{\boldsymbol{j}} a_{\boldsymbol{j}} e^{\mathrm{i}\boldsymbol{k}\cdot\boldsymbol{j}a}, \; a^\dagger_{\boldsymbol{k}} = \frac{1}{\sqrt{N}} \sum_{\boldsymbol{j}} a^\dagger_{\boldsymbol{j}} e^{-\mathrm{i}\boldsymbol{k}\cdot\boldsymbol{j}a}, \qquad (3.4)$$

we obtain

$$\mathcal{H} = -N \left(J_{\parallel} S^2 - K S^2 + H S \right) + \sum_{\boldsymbol{q}} \left(E_{\perp,\boldsymbol{q}} + E_{\parallel,\boldsymbol{q}} \right) a^\dagger_{\boldsymbol{q}} a_{\boldsymbol{q}}, \qquad (3.5)$$

up to second order in $a_{\boldsymbol{k}}$ and $a^\dagger_{\boldsymbol{k}}$ operators with

$$\begin{aligned} E_{\perp,\boldsymbol{q}} &= 2 J_{\perp} S \left[2 - \cos(q^x a) - \cos(q^y a) \right], \qquad (3.6) \\ E_{\parallel,\boldsymbol{q}} &= 2 \tilde{J} S \left\{ 1 - \cos[(q^z - Q)a] \right\} + H - H_{\mathrm{c}}, \qquad (3.7) \end{aligned}$$

and the critical field $H_{\mathrm{c}} = 2S(\tilde{J} - J_{\parallel})$. The energy spectrum consists of two parts: $E_{\parallel,\boldsymbol{q}}$ and $E_{\perp,\boldsymbol{q}}$. $E_{\parallel,\boldsymbol{q}}$ can be regarded as the energy spectrum of the one dimensional spin chain, independent of the in-plane momenta q^x or q^y, while it is not symmetric between q^z and $-q^z$, which means that the propagation of the spin wave along the helical axis is non-reciprocal.

$E_{\perp,\boldsymbol{q}}$ comes from the in-plane exchange interaction and is independent of q^z. In addition, $E_{\perp,\boldsymbol{q}}$ is symmetric with respect to $(q^x, q^y) \to (-q^x, q^y)$, $(q^x, -q^y)$, and $(-q^x, -q^y)$. In general, $E_{\perp,\boldsymbol{q}} + E_{\parallel,\boldsymbol{q}}$ is symmetric under the sign reversals of q^x or q^y in the presence of one dimensional modulations along the z-direction, and we do not consider the in-plane propagation of spin waves in the following: we consider only the q^z-dependence and set $q^x = q^y = 0$. Since we neglect quantum fluctuation effects on the equilibrium states in the following, it is equivalent to considering the Hamiltonian for the one dimensional chain.

3.3 Chiral ferromagnetic chain

3.3.1 Hamiltonian

From now on we consider a one-dimensional periodic structure under the magnetic field along z-direction, which is parallel to the helical axis, in addition to the uniform state considered in the previous section. We assume that the spin structure is uniform in the xy-plane. Because we do not consider the in-plane propagation, we focus on the sites on the particular chain, $\boldsymbol{j} = l\hat{z}$. The Hamiltonian is

$$\begin{aligned}\mathcal{H} &= -\sum_l \left[J_\parallel \vec{\tilde{S}}_l \cdot \vec{\tilde{S}}_{l+1} + D\left(\tilde{S}_l^x \tilde{S}_{l+1}^y - \tilde{S}_l^y \tilde{S}_{l+1}^x\right) + H\tilde{S}_l^z - K\left(\tilde{S}_l^z\right)^2 \right], \\ &= -\sum_l \left\{ \frac{\tilde{J}}{2}\left[e^{\mathrm{i}Qa}\tilde{S}_l^+ \tilde{S}_{l+1}^- + e^{-\mathrm{i}Qa}\tilde{S}_l^- \tilde{S}_{l+1}^+ \right] + J_\parallel \tilde{S}_l^z \tilde{S}_{l+1}^z + H\tilde{S}_l^z - K\left(\tilde{S}_l^z\right)^2 \right\}. \end{aligned} \tag{3.8}$$

The parameters are the same as those of the Hamiltonian Eq. (3.1) except K, which denotes the hard-axis anisotropy about the helical axis. Let N_z be the number of sites in each chain.

In the following calculations, we rotate locally the spin space so that the z-direction is parallel to the equilibrium spin direction. Note that we have chosen the sign of H such that the spin favors the $+z$-direction[4]. According to Refs. [109, 120], the spin operators in these two frames are related as follows:

$$\tilde{S}_l^z = -\frac{1}{2}\sin\theta_0 (S_l^+ + S_l^-) + \cos\theta_0 S_l^z, \tag{3.9}$$

$$\tilde{S}_l^\pm = \frac{1}{2}\left[(\cos\theta_0 \pm 1) S_l^+ + (\cos\theta_0 \mp 1) S_l^- + 2\sin\theta_0 S_l^z \right] e^{\pm \mathrm{i}Qal}. \tag{3.10}$$

Here θ_0 is a cone angle as shown in Fig. 3.1. We substitute these relations into the original

[4]The actual direction of magnetic field is opposite, i.e., $-z$-direction because of the relation $\vec{M} = -g\mu_{\mathrm{B}}\vec{S}$ with the g factor and the Bohr-magneton, and $g\mu_{\mathrm{B}}$ positive.

Hamiltonian Eq. (3.8), and obtain

$$\begin{aligned}\mathcal{H} = -\sum_l \Bigg[& \frac{\tilde{J}(\tilde{\gamma}-1)}{4}\left(S_l^+ S_{l+1}^+ + S_l^- S_{l+1}^-\right) + \frac{\tilde{J}(\tilde{\gamma}+1)}{4}\left(S_l^+ S_{l+1}^- + S_l^- S_{l+1}^+\right) \\ & + \tilde{J}\tilde{\lambda} S_l^z S_{l+1}^z + (\tilde{J} - J_\parallel)\sin\theta_0\cos\theta_0 (S_l^x S_{l+1}^z + S_l^z S_{l+1}^x) \\ & + H(-\sin\theta_0 S_l^x + \cos\theta_0 S_l^z) - K(-\sin\theta_0 S_l^x + \cos\theta_0 S_l^z)^2 \Bigg]. \end{aligned} \tag{3.11}$$

For simplicity, we have introduced

$$\tilde{\gamma} = \cos^2\theta_0 + (J_\parallel/\tilde{J})\sin^2\theta_0, \tag{3.12}$$

$$\tilde{\lambda} = \sin^2\theta_0 + (J_\parallel/\tilde{J})\cos^2\theta_0. \tag{3.13}$$

3.3.2 Holstein–Primakoff transformation

We perform the Holstein–Primakoff transformation by introducing boson operators a_l and $a_l^\dagger$

$$S_l^+ = \sqrt{2S}\left(1 - \frac{n_l}{2S}\right)^{\frac{1}{2}} a_l,\ S_l^- = \sqrt{2S} a_l^\dagger \left(1 - \frac{n_l}{2S}\right)^{\frac{1}{2}},\ S_l^z = S - n_l, \tag{3.14}$$

and retain quadratic terms with respect to a_l and $a_l^\dagger$. The equilibrium condition implies that the coefficient of $(a_l + a_l^\dagger)$ vanishes and therefore,

$$\sin\theta_0 \left[2(\tilde{J} - J_\parallel + K)S\cos\theta_0 - H\right] = 0. \tag{3.15}$$

Ignoring the irrelevant constant energy, we obtain the following quadratic Hamiltonian:

$$\mathcal{H} \simeq \sum_k \left[\frac{A_k}{2}(a_k^\dagger a_k + a_{-k} a_{-k}^\dagger) + \frac{B_k}{2}(a_{-k} a_k + a_k^\dagger a_{-k}^\dagger)\right] \tag{3.16}$$

using the Fourier transform defined by $a_k = \sum_l a_l e^{-\mathrm{i}kal}/\sqrt{N_z}$ and $a_k^\dagger = \sum_l a_l^\dagger e^{+\mathrm{i}kal}/\sqrt{N_z}$. Here $-\pi \le ka = 2\pi m/N_z < \pi$ with integer m, and we have introduced

$$\begin{aligned} A_k = & -\tilde{J}S\left[(\tilde{\gamma}+1)\cos(ka) - 2\right] + KS\sin^2\theta_0 \\ & - \cos\theta_0\left[2(\tilde{J} - J_\parallel + K)S\cos\theta_0 - H\right], \end{aligned} \tag{3.17}$$

$$B_k = -\tilde{J}S(\tilde{\gamma}-1)\cos(ka) + KS\sin^2\theta_0. \tag{3.18}$$

Let us use the following Bogoliubov transformation to diagonalize the Hamiltonian with real coefficients u_k and v_k satisfying the condition $u_k^2 - v_k^2 = 1$:

$$a_k = u_k\alpha_k + v_k\alpha_{-k}^\dagger, \tag{3.19}$$

$$a_{-k}^\dagger = v_k\alpha_k + u_k\alpha_{-k}^\dagger. \tag{3.20}$$

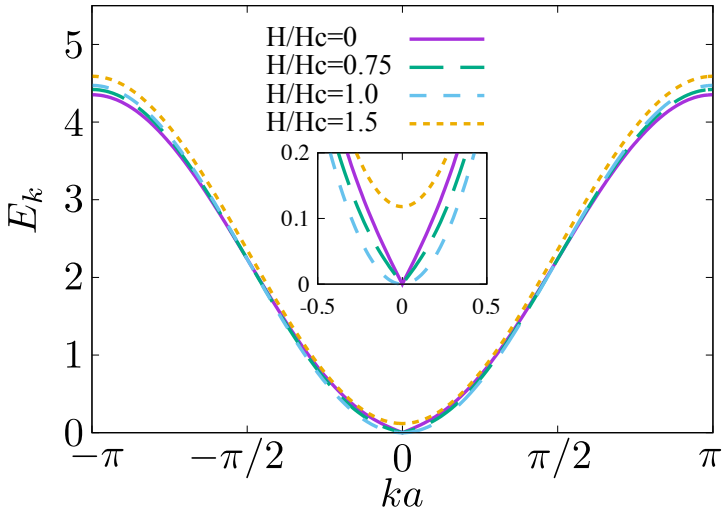

Figure 3.2: Behaviors of E_k for several values of the magnetic field. We set $D/J_{\parallel} = 0.5$ and $K = 0$. The inset is the magnified image around $k = 0$.

The Hamiltonian without irrelevant constants reduces to

$$\mathcal{H} = \sum_k \left\{ \left[\frac{A_k}{2}(u_k^2 + v_k^2) + B_k u_k v_k \right] (\alpha_k^\dagger \alpha_k + \alpha_{-k}^\dagger \alpha_{-k}) \right. \\ \left. + \left[A_k u_k v_k + \frac{B_k}{2}(u_k^2 + v_k^2) \right] (\alpha_k^\dagger \alpha_{-k}^\dagger + \alpha_{-k}\alpha_k) \right\}. \tag{3.21}$$

The condition of vanishing anomalous terms is given by

$$A_k u_k v_k + \frac{B_k}{2}(u_k^2 + v_k^2) = 0, \tag{3.22}$$

and the Hamiltonian is diagonalized as

$$\mathcal{H} = \sum_k E_k \alpha_k^\dagger \alpha_k, \; E_k = \sqrt{A_k^2 - B_k^2}, \; u_k^2 + v_k^2 = \frac{A_k}{E_k}, \; 2u_k v_k = -\frac{B_k}{E_k}. \tag{3.23}$$

Note that the energy always has the relation $E_k = E_{-k}$. One should also note that k is not the wave number in the laboratory frame. We show the behavior of E_k for several values of the field in Fig. 3.2. The linear dispersion around $ka = 0$ holds for $H < H_c$. It becomes quadratic at $H = H_c$ and then acquires a gap for $H > H_c$.

3.3.3 Spectral intensity

We consider the dynamical spin structure factor, which shows the structure of the excitation spectrum in the energy-momentum space. Using the above quantities, now we can calculate the correlation functions, $C^{\mu\nu}(q,t)$, of $\Delta\tilde{S}_q^\mu \equiv \tilde{S}_q^\mu - \langle \tilde{S}_q^\mu \rangle$ for $\mu = x, y, z$, where the Fourier transforms are defined as

$$\tilde{S}_q^\pm = \frac{1}{\sqrt{N}} \sum_l \tilde{S}_l^\pm e^{\mp \mathrm{i} q r_l}, \; S_q^\pm = \frac{1}{\sqrt{N}} \sum_l S_l^\pm e^{\mp \mathrm{i} q r_l}. \tag{3.24}$$

Here $\Delta\tilde{S}^{\mu}_{q}(t)$ is the time evolution of $\Delta\tilde{S}^{\mu}_{q}$ and defined by $\Delta\tilde{S}^{\mu}_{q}(t) = e^{\mathrm{i}\mathcal{H}t}\Delta\tilde{S}^{\mu}_{q}e^{-\mathrm{i}\mathcal{H}t}$. We define the x-component of the correlation function as

$$C^{xx}(q,t) \equiv \langle \Delta\tilde{S}^{x}_{q}(t)\Delta\tilde{S}^{x}_{-q}\rangle = \frac{\langle(\Delta\tilde{S}^{+}_{q}(t) + \Delta\tilde{S}^{-}_{-q}(t))(\Delta\tilde{S}^{+}_{-q} + \Delta\tilde{S}^{-}_{q})\rangle}{4}. \tag{3.25}$$

There are three independent components except for trivially zero components. Non-zero (and non-trivially zero) components are $C^{xx}(q,\omega) = C^{yy}(q,\omega)$, $C^{xy}(q,\omega) = -C^{yx}(q,\omega)$, and $C^{zz}(q,\omega)$. We find that $\langle\Delta\tilde{S}^{+}_{q}(t)\Delta\tilde{S}^{+}_{q}\rangle$ and $\langle\Delta\tilde{S}^{-}_{q}(t)\Delta\tilde{S}^{-}_{q}\rangle$ are zero, because they do not include the expectation value of the number operator in terms of the Holstein–Primakoff bosons such as $\langle\alpha^{\dagger}_{q}\alpha_{q}\rangle$ in their expansion. Non-zero contributions come from the other two expectation values. We write down $\langle\Delta\tilde{S}^{+}_{q}(t)\Delta\tilde{S}^{-}_{q}\rangle$ in terms of Holstein–Primakoff bosons as

$$\begin{aligned}\langle\Delta\tilde{S}^{+}_{q}(t)\Delta\tilde{S}^{-}_{q}\rangle = \frac{S}{2}\Big[&(\cos^2\theta_0 - 1)\langle a_{q-Q}(t)a_{-(q-Q)}\rangle + (\cos\theta_0+1)^2\langle a_{q-Q}(t)a^{\dagger}_{q-Q}\rangle \\ &+(\cos\theta_0-1)^2\langle a^{\dagger}_{-(q-Q)}(t)a_{-(q-Q)}\rangle + (\cos^2\theta_0-1)\langle a^{\dagger}_{-(q-Q)}(t)a^{\dagger}_{q-Q}\rangle\Big].\end{aligned} \tag{3.26}$$

The other term, $\langle\Delta\tilde{S}^{-}_{-q}(t)\Delta\tilde{S}^{+}_{-q}\rangle$, is also represented as

$$\begin{aligned}\langle\Delta\tilde{S}^{-}_{-q}(t)\Delta\tilde{S}^{+}_{-q}\rangle = \frac{S}{2}\Big[&(\cos^2\theta_0 - 1)\langle a_{q+Q}(t)a_{-(q+Q)}\rangle + (\cos\theta_0-1)^2\langle a_{q+Q}(t)a^{\dagger}_{q+Q}\rangle \\ &+(\cos\theta_0+1)^2\langle a^{\dagger}_{-(q+Q)}(t)a_{-(q+Q)}\rangle + (\cos^2\theta_0-1)\langle a^{\dagger}_{-(q+Q)}(t)a^{\dagger}_{q+Q}\rangle\Big].\end{aligned} \tag{3.27}$$

To calculate the expectation values, we substitute the Bogoliubov transformations into Eqs. (3.26) and (3.27). The time evolutions of Bogoliubov boson operators are given by $\alpha^{\dagger}_{q}(t) = \alpha^{\dagger}_{q}e^{\mathrm{i}E_q t}$ and $\alpha_{q}(t) = \alpha_{q}e^{-\mathrm{i}E_q t}$, respectively. The dynamical spin structure factor, can be obtained by the time-Fourier transform of the correlation function.

$$C^{\mu\nu}(q,\omega) = \int_{-\infty}^{\infty} dt C^{\mu\nu}(q,t)e^{\mathrm{i}\omega t}. \tag{3.28}$$

For convenience, we consider only positive-frequency region. Thus we need to retain only the terms like $\langle\alpha_{q}(t)\alpha^{\dagger}_{q}\rangle = e^{-\mathrm{i}E_q t}[1 + n_{\mathrm{B}}(E_q)]$ with the Bose distribution function $n_{\mathrm{B}}(\omega) = (\exp[\beta\omega]-1)^{-1}$.

$$\begin{aligned}\langle\Delta\tilde{S}^{+}_{q}(t)\Delta\tilde{S}^{-}_{q}\rangle = \frac{S}{2}&\left[\cos\theta_0(u_{q-Q}+v_{q-Q}) + (u_{q-Q}-v_{q-Q})\right]^2\langle\alpha_{q-Q}(t)\alpha^{\dagger}_{q-Q}\rangle \\ &+ (\text{other terms}).\end{aligned} \tag{3.29}$$

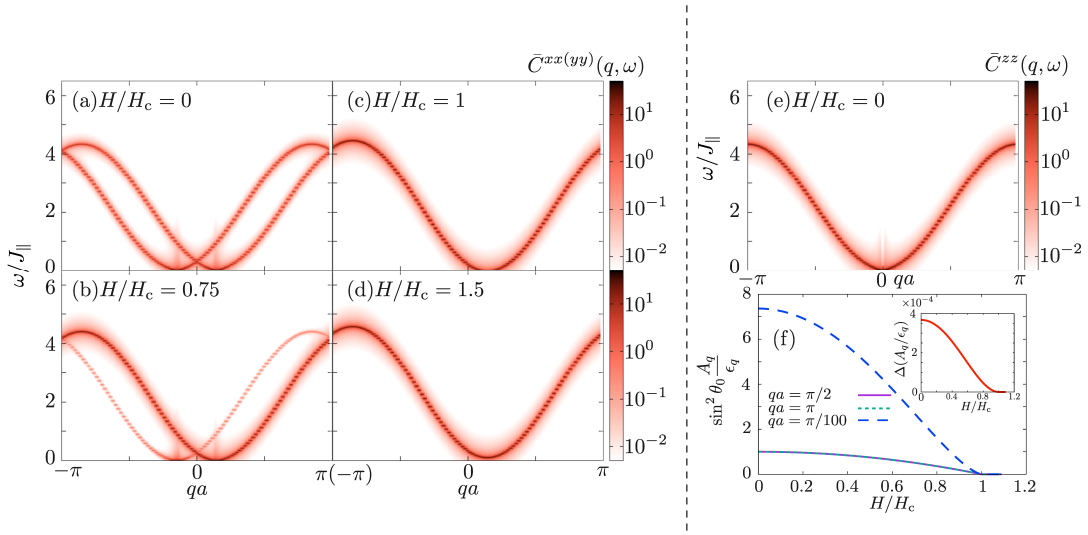

Figure 3.3: Dynamical spin structure factor of the chiral ferromagnetic chain with $D = 0.5J_\parallel$ and $K = 0$. The panels (a)–(d) show its $x(y)$-component, while the panel (e) shows the z-component. The panel (f) shows the H-dependence of the strength of z component at peak position. There is a slight difference between $qa = \pi$ and $\pi/2$, which is shown in the inset as $\Delta(x_q) = (x_{q=\pi} - x_{q=\pi/2})/x_{q=\pi/2}$ with $x = A/E$.

We can calculate also $\langle \Delta\tilde{S}^-_q(t)\Delta\tilde{S}^+_q\rangle$ similarly. The time-Fourier transform of $C^{xx}(q,t) = [\langle \Delta\tilde{S}^+_q(t)\Delta\tilde{S}^-_q\rangle + \langle \Delta\tilde{S}^-_q(t)\Delta\tilde{S}^+_q\rangle]/4$ gives

$$
\begin{aligned}
C^{xx}(q,\omega) = {} & \frac{\pi S}{4}\left[1 + n_{\rm B}(\omega)\right] \\
& \times \left[\delta(\omega - E_{q-Q})\left(\cos^2\theta_0 \frac{A_{q-Q} - B_{q-Q}}{E_{q-Q}} + \frac{A_{q-Q} + B_{q-Q}}{E_{q-Q}} + 2\cos\theta_0\right)\right. \\
& \left. + \delta(\omega - E_{q+Q})\left(\cos^2\theta_0 \frac{A_{q+Q} - B_{q+Q}}{E_{q+Q}} + \frac{A_{q+Q} + B_{q+Q}}{E_{q+Q}} - 2\cos\theta_0\right)\right] \qquad (3.30) \\
\equiv {} & \frac{\pi S}{4}\left[1 + n_{\rm B}(\omega)\right]\left[|U_+(q)|^2\delta(\omega - E_{q-Q}) + |U_-(q)|^2\delta(\omega - E_{q+Q})\right] \qquad (3.31) \\
\equiv {} & \frac{\pi S}{4}\left[1 + n_{\rm B}(\omega)\right]\bar{C}^{xx}(q,\omega). \qquad (3.32)
\end{aligned}
$$

In a similar way, we calculate C^{yy} and find that $C^{yy}(q,\omega) = C^{xx}(q,\omega)$. We will discuss C^{xy} and C^{yx} later. This result shows that the spectrum consists of two δ-functions at energies $\omega_+(q) \equiv E_{q-Q}$ and $\omega_-(q) \equiv E_{q+Q}$. Each branch has a dispersion of E_q with q shifted by $\pm Q$. Reciprocity among these branches are given by $\omega_\pm(q) = \omega_\mp(-q)$. Coefficients of delta functions depend on θ_0, i.e., the cone angle. This implies that the spectral intensity changes as

a function of the magnetic field. In the laboratory frame, the wave number is no longer a good quantum number, and an elementary excitation consists of intensities for three wave numbers. Two of them are $q-Q$ and $q+Q$ for given ω. The third one comes from the z-component given by the following.

$$\begin{aligned} C^{zz}(q,\omega) &= \int dt\, \langle \Delta\tilde{S}^z_q(t)\Delta\tilde{S}^z_{-q}\rangle\, e^{\mathrm{i}\omega t} \\ &= \int dt e^{\mathrm{i}\omega t}\frac{2S}{4}\sin^2\theta_0\left[\langle a_q(t)a_q^\dagger + a_{-q}^\dagger(t)a_{-q}\rangle\right] \\ &= \int dt e^{\mathrm{i}\omega t}\frac{S}{2}\sin^2\theta_0(u_q^2+v_q^2)\,\langle \alpha_q(t)\alpha_q^\dagger\rangle \\ &= \pi S\left[1+n_{\mathrm{B}}(\omega)\right]\sin^2\theta_0\frac{A_q}{E_q}\delta(\omega-E_q) \qquad (3.33) \\ &\equiv \pi S\left[1+n_{\mathrm{B}}(\omega)\right]|U_z(q)|^2\delta(\omega-E_q) \equiv \pi S\left[1+n_{\mathrm{B}}(\omega)\right]\bar{C}^{zz}(q,\omega). \qquad (3.34) \end{aligned}$$

Figures 3.3(a)–(d) show $\bar{C}^{xx}(q,\omega)$ for different H's , while the panel (e) shows $\bar{C}^{zz}(q,\omega)$. Figure 3.3(f) explicitly shows the intensity changes of $\bar{C}^{zz}$ as a function of magnetic field. In the figures we replace the δ-functions by Lorentzian $\pi\delta(\omega-E_q)=\delta/[(\omega-E_q)^2+\delta^2]$ with $\delta/J_\parallel = 10^{-2}$. We set N_z to 100 and the frequency mesh, $\Delta\omega$, to $0.0128J_\parallel$ there.

In the absence of the field, there are the three branches with the same shape, but they are shifted along the horizontal direction. This holds also for $H<H_{\mathrm{c}}$. We can see these two aspects from the analytic expressions Eqs. (3.30) and (3.33), where the peaks are located at E_{q-Q}, E_{q+Q}, and E_q. The transverse correlation functions $C^{xx}(q,\omega)$ and $C^{yy}(q,\omega)$ have two branches given by E_{q-Q} and E_{q+Q}. Since $\cos\theta_0$ in Eq. (3.30) is zero in the absence of the magnetic field, $|U_+(q)|^2$ and $|U_-(-q)|^2$ are the same, and the intensities are reciprocal as well as their branches. We show the q-dependence of the intensity $|U(q)|^2$'s defined in Eqs. (3.31) and (3.34) in Fig. 3.4(a). Reciprocal relations $|U_z(q)|^2=|U_z(-q)|^2$ and $|U_+(q)|^2=|U_-(-q)|^2$ hold.

Then let us examine the results for the finite magnetic field. Figure 3.3(b) corresponds to an intermediate field below H_{c}, where the conical state occurs. It is obvious that the spectral intensity of the branch $\omega_-(q)$ decreases, while that of $\omega_+(q)$ increases. We show q-dependence $|U(q)|^2$'s for $H/H_{\mathrm{c}}=0.75$ in Fig. 3.4(b). The q-dependence is not remarkable except near zero energy in each branch. In contrast to the panel (a), the asymmetry between $|U_+(q)|^2$ and $|U_-(-q)|^2$ appears obviously, while $|U_z(q)|^2=|U_z(-q)|^2$ holds. Note that the magnetic field reduces $|U_z(q)|^2$. We can conclude that the spectral function is non-reciprocal in its intensity, although the branches are still reciprocal. A stronger magnetic field drives the conical state to the uniform state. At the critical field H_{c}, the spectral intensity of the $\omega_-(q)$ branch vanishes, while the $\omega_+(q)$ branch keeps a finite intensity. At this point, the energy branch becomes non-reciprocal. It is obvious that this single, non-reciprocal branch has a gap for $H>H_{\mathrm{c}}$, as was shown in the earlier work by Kishine et al.[109]. Our new finding is that non-reciprocity in spectral intensity grows in the intermediate state. The intensity of the longitudinal component, $C^{zz}(q,\omega)$, is reciprocal and decreases with increasing field. Figure 3.3(f) shows the intensity

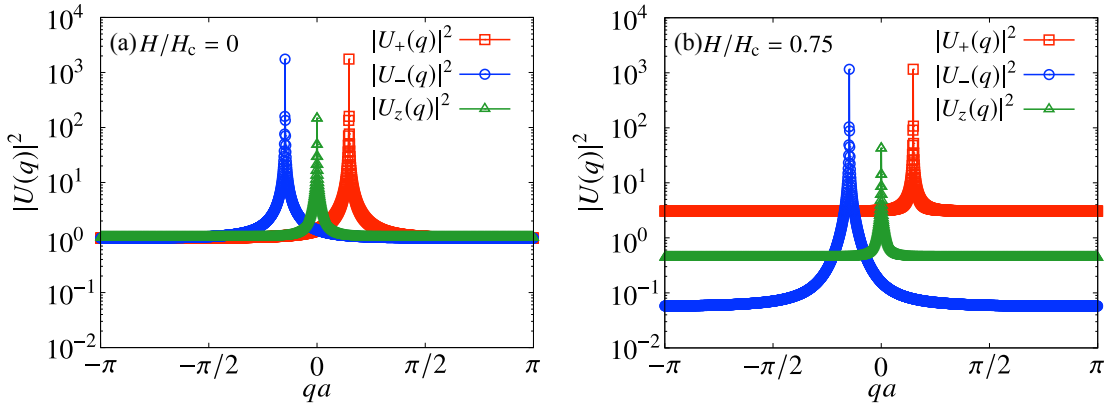

Figure 3.4: Intensities $|U(q)|^2$'s as a function of qa for $H/H_c = 0$ (a) and $H/H_c = 0.75$ (b) on a log scale. We set $D/J_{\parallel} = 0.5$ and $K = 0$.

changes as functions of the magnetic field. Inset shows the difference between $q = \pi a$ and $q = \pi a/2$ since they are hardly distinguished in the main plot. As seen in Figs. 3.4(a) and (b), the q-dependence is remarkable only near $q \approx 0$. This can be understood as follows: $|U_z(q)|^2$ is given by the ratio of the arithmetic mean to the geometric mean between $2\tilde{J}(1-\cos qa)$ and $2\tilde{J}(1-\tilde{\gamma}\cos qa)$. Here $1-\tilde{\gamma} \approx 0.11$ is small. Thus the q-dependence of $|U_z(q)|^2$ appears only when $(1-\tilde{\gamma})\cos qa \gtrsim (1-\cos qa)$, otherwise it vanishes through the cancelation between both means.

As another remark, we perform the principal axis transformation for the correlation function. Defining

$$\bar{C}^{yy}(q,\omega) = 4C^{yy}(q,\omega)/[\pi(1+n_{\rm B}(\omega))], \tag{3.35}$$
$$\bar{C}^{xy}(q,\omega) = -\bar{C}^{yx}(q,\omega) = 4C^{xy}(q,\omega)/[\pi(1+n_{\rm B}(\omega))], \tag{3.36}$$

we can write down them with symbolic notations as

$$\bar{C}^{xx}(q,\omega) = \bar{C}^{yy}(q,\omega) = |U_+(q)|^2\delta(\omega - E_{q-Q}) + |U_-(q)|^2\delta(\omega - E_{q+Q}), \tag{3.37}$$
$$\bar{C}^{xy}(q,\omega) = -\bar{C}^{yx}(q,\omega) = \mathrm{i}\left[|U_+(q)|^2\delta(\omega - E_{q-Q}) - |U_-(q)|^2\delta(\omega - E_{q+Q})\right], \tag{3.38}$$
$$\bar{C}^{zz}(q,\omega) = |U_z(q)|^2\delta(\omega - E_q). \tag{3.39}$$

Diagonalizing the 3×3 matrix $\bar{C}^{\alpha\beta}$ for a given (q,ω), we obtain

$$\mathrm{diag}\left[2\bar{C}^{+-}(q,\omega), 2\bar{C}^{-+}(q,\omega), \bar{C}^{zz}(q,\omega)\right], \tag{3.40}$$

where

$$\bar{C}^{+-}(q,\omega) = |U_+(q)|^2\delta(\omega - E_{q-Q}),\ \bar{C}^{-+}(q,\omega) = |U_-(q)|^2\delta(\omega - E_{q+Q}) \tag{3.41}$$

and these are related to the Fourier transform of $\langle \Delta\tilde{S}^+_q(t)\Delta\tilde{S}^-_{-q}\rangle$ and $\langle \Delta\tilde{S}^-_q(t)\Delta\tilde{S}^+_{-q}\rangle$.

3.4 Antiferromagnetic system with uniaxial chirality

We also study a chiral chain with antiferromagnetic exchange interaction. The material $Ba_2CuGe_2O_7$ shows an almost-antiferromagnetic cycloidal state, because of a uniform DMI with $\vec{D}$ vector perpendicular to the bond direction [121–128]. This material also has a staggered DMI, and its DM vector is perpendicular to both the bond direction and the DM vector of the uniform DMI. This staggered DMI induces the weak ferromagnetism and thus the coexistence of the weak ferromagnetism and chiral modulation is expected[129]. Moreover, the fluctuation-induced weak first order phase transition is suggested[128]. Another model material of this type is $BiFeO_3$ [130–133]. Non-reciprocal spin wave spectrum in a non-centrosymmetric antiferromagnet was recently observed in α-$Cu_2V_2O_7$ for collinear spin structure using inelastic neutron scattering measurements[134, 135].

Therefore it is important to study the spin wave spectra in the non-uniform state of the uniaxial chiral antiferromagnet. We repeat the analysis in the previous section for the antiferromagnetic chain with the single DMI. Our starting Hamiltonian is almost the same as that in the case of the chiral ferromagnet except the sign of exchange coupling:

$$\mathcal{H} = \sum_l \left[J_\parallel \vec{\tilde{S}}_l \cdot \vec{\tilde{S}}_{l+1} - D\left(\tilde{S}_l^x \tilde{S}_{l+1}^y - \tilde{S}_l^y \tilde{S}_{l+1}^x\right) - H\tilde{S}_l^z + K\left(\tilde{S}_l^z\right)^2 \right] \quad (J_\parallel > 0) \tag{3.42}$$

$$= \sum_l \left[-\frac{\tilde{J}}{2}\left(e^{-\mathrm{i}(Q+Q_{\mathrm{AF}})a}\tilde{S}_l^+ \tilde{S}_{l+1}^- + e^{\mathrm{i}(Q+Q_{\mathrm{AF}})a}\tilde{S}_l^- \tilde{S}_{l+1}^+\right) + J_\parallel \tilde{S}_l^z \tilde{S}_{l+1}^z \right.$$
$$\left. - H\tilde{S}_l^z + K\left(\tilde{S}_l^z\right)^2 \right]. \tag{3.43}$$

The difference from the ferromagnetic case consists of two points: $Q \to -(Q + Q_{\mathrm{AF}})$ with antiferromagnetic wave number $Q_{\mathrm{AF}}a = \pi$ and $J_\parallel \to -J_\parallel$. Correspondingly the following changes are required:

$$\tilde{S}_l^z = -\frac{1}{2}\sin\theta_0 (S_l^+ + S_l^-) + \cos\theta_0 S_l^z, \tag{3.44}$$

$$\tilde{S}_l^\pm = \frac{1}{2}\left[(\cos\theta_0 \pm 1)S_l^+ + (\cos\theta_0 \mp 1)S_l^- + 2\sin\theta_0 S_l^z\right] e^{\mp \mathrm{i}(Q+Q_{\mathrm{AF}})l}, \tag{3.45}$$

$$\tilde{\gamma} = \cos^2\theta_0 - (J_\parallel/\tilde{J})\sin^2\theta_0, \tag{3.46}$$

$$\tilde{\lambda} = \sin^2\theta_0 - (J_\parallel/\tilde{J})\cos^2\theta_0. \tag{3.47}$$

Using Eqs. (3.44)–(3.47), the Hamiltonian is reduced to

$$\begin{aligned}\mathcal{H} = -\sum_l \Bigg[& \frac{\tilde{J}(\tilde{\gamma}-1)}{4}\left(S_l^+ S_{l+1}^+ + S_l^- S_{l+1}^-\right) + \frac{\tilde{J}(\tilde{\gamma}+1)}{4}\left(S_l^+ S_{l+1}^- + S_l^- S_{l+1}^+\right) \\ & + \tilde{J}\tilde{\lambda} S_l^z S_{l+1}^z + (\tilde{J}+J_\parallel)\sin\theta_0\cos\theta_0 (S_l^x S_{l+1}^z + S_l^z S_{l+1}^x)\Bigg] \\ & - H\sum_l (-\sin\theta_0 S_l^x + \cos\theta_0 S_l^z) + K\sum_l (-\sin\theta_0 S_l^x + \cos\theta_0 S_l^z)^2. \end{aligned} \tag{3.48}$$

Using the Holstein-Primakoff transformation, Eq. (3.14), we obtain the following Hamiltonian up to quadratic order in a and $a^\dagger$:

$$\mathcal{H} = \sum_k \left[\frac{A_k}{2}(a_k^\dagger a_k + a_{-k} a_{-k}^\dagger) + \frac{B_k}{2}(a_{-k} a_k + a_k^\dagger a_{-k}^\dagger)\right], \tag{3.49}$$

with

$$\begin{aligned} A_k = & -\tilde{J}S\left[(\tilde{\gamma}+1)\cos(ka) - 2\right] \\ & + KS\sin^2\theta_0 - \cos\theta_0[2(\tilde{J}+J_\parallel+K)S\cos\theta_0 - H], \end{aligned} \tag{3.50}$$

$$B_k = -\tilde{J}S(\tilde{\gamma}-1)\cos(ka) + KS\sin^2\theta_0. \tag{3.51}$$

To obtain Eq. (3.49), we have used the equilibrium condition

$$\sin\theta_0\left[2(\tilde{J}+J_\parallel+K)S\cos\theta_0 - H\right] = 0. \tag{3.52}$$

Performing the Bogoliubov transformation as in the ferromagnetic case, we diagonalize the Hamiltonian:

$$\mathcal{H} = \sum_k E_k \alpha_k^\dagger \alpha_k, \tag{3.53}$$

$$E_k = \sqrt{A_k^2 - B_k^2},\ u_k^2 + v_k^2 = \frac{A_k}{E_k},\ 2u_k v_k = -\frac{B_k}{E_k}. \tag{3.54}$$

The dynamical spin structure factor is calculated in a similar way, and its transverse component

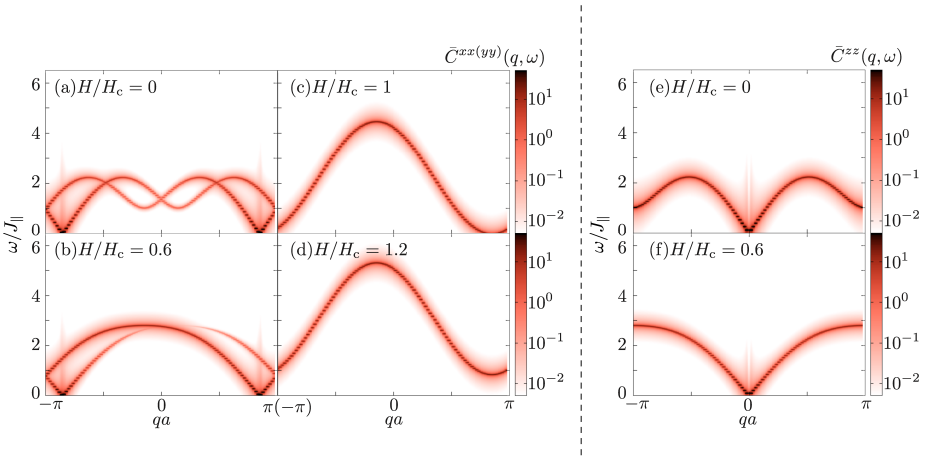

Figure 3.5: Dynamical spin structure factor for the chiral antiferromagnetic chain with $D = 0.5J_\parallel$ and $K = 0$. The panels (a)–(d) show the $x(y)$-component, while the panels (e) and (f) show the z-component.

is

$$
\begin{aligned}
C^{xx}(q,\omega) = \frac{\pi S}{4}\left[1+n_{\rm B}(\omega)\right] \\
\times\Bigg\{\delta(\omega - E_{q+Q+Q_{\rm AF}})\Bigg[(1-\cos^2\theta_0)\frac{B_{q+Q+Q_{\rm AF}}}{E_{q+Q+Q_{\rm AF}}} \\
+\frac{(1+\cos\theta_0)^2}{2}\left(\frac{A_{q+Q+Q_{\rm AF}}}{E_{q+Q+Q_{\rm AF}}}+1\right)+\frac{(1-\cos\theta_0)^2}{2}\left(\frac{A_{q+Q+Q_{\rm AF}}}{E_{q+Q+Q_{\rm AF}}}-1\right)\Bigg] \\
+\delta(\omega - E_{q-Q+Q_{\rm AF}})\Bigg[(1-\cos^2\theta_0)\frac{B_{q-Q+Q_{\rm AF}}}{E_{q-Q+Q_{\rm AF}}} \\
+\frac{(1-\cos\theta_0)^2}{2}\left(\frac{A_{q-Q+Q_{\rm AF}}}{E_{q-Q+Q_{\rm AF}}}+1\right)+\frac{(1+\cos\theta_0)^2}{2}\left(\frac{A_{q-Q+Q_{\rm AF}}}{E_{q-Q+Q_{\rm AF}}}-1\right)\Bigg]\Bigg\} \qquad (3.55) \\
= \frac{\pi S}{4}\left[1+n_{\rm B}(\omega)\right]\bar{C}^{xx}(q,\omega). \qquad (3.56)
\end{aligned}
$$

Note that A_q and B_q take different forms from those in the ferromagnetic case. The relation $C^{yy}(q,\omega) = C^{xx}(q,\omega)$ holds again. The result for the z-component is

$$
C^{zz}(q,\omega) = \pi S\left[1+n_{\rm B}(\omega)\right]\sin^2\theta_0\frac{A_q}{E_q}\delta(\omega-E_q) \equiv \pi S\left[1+n_{\rm B}(\omega)\right]\bar{C}^{zz}(q,\omega). \qquad (3.57)
$$

Figures 3.5(a)–(d) and (e)–(f) correspond to $\bar{C}^{xx}(q,\omega)$ and $\bar{C}^{zz}(q,\omega)$, respectively. We start to discuss the spin wave branches of the chiral antiferromagnetic chain. It is well known that there are two linear branches at around $qa = (0,\cdots,0)$ and $(\pi,\cdots,\pi)$ in the case of

the usual antiferromagnet. The usual antiferromagnetic case is obtained by taking the limit $D \to 0$ and correspondingly $Qa \to 0$. Thus the linear branch near zone boundary in Fig. 3.5 corresponds to that appearing at $qa = \pi$ in the usual antiferromagnet. On the other hand, we can see that the local minimum near $qa = 0$ has no longer zero energy and acquires a gap. This is because the DMI plays a role of a hard axis anisotropy along the helical axis. This kind of gap appears at around $qa = \pi$ for the z-component, since the anisotropy does not allow the out-of phase mode in the z-component to have zero energy. Compared to the ferromagnetic case, the field increasing process shows a complicated behavior since there are two kinds of transition: One is a transition from the helical to the uniform state, where characters of the helical state disappear. One of its characters is represented by the reciprocal spectral intensities in $C^{xx}(q, \omega)$, which becomes non-reciprocal with increasing field. The other is a transition from antiferromagnetic to the uniform states, where the characters of antiferromagnetic state disappear. As we mentioned, the linear dispersion relation appears at $qa = 0$ in the usual antiferromagnetic case. The depression at around $qa \sim 0$ comes from this linear branch by opening the gap because of DMI. This depression-structure disappears with increasing field, and the energy branch takes maximum at around $qa \sim 0$ as that in the ferromagnetic case does at around $qa \sim \pi$.

3.5 Comparison with numerical results

We confirm this non-reciprocity in the spectral intensity by direct numerical calculation. Here we combine a classical Monte Carlo simulation and the Landau–Lifshitz equation (2.73) as a standard method to calculate the dynamical spin structure factor of classical spin systems at finite temperatures [136]. Here we do not discuss the temperature dependence of $C^{\mu\nu}(q, \omega)$ and thus we choose one very low temperature. We remark that the field direction is opposite to that in the previous sections, since we take the field direction such that the classical magnetic moment precesses counterclockwise as in Fig. 2.3.

First we review the numerical scheme. The correlation function is defined as follows:

$$C^{\mu\nu}(\boldsymbol{r}, t) = \frac{1}{N'_{\boldsymbol{r}} N'_t} \sum_{\boldsymbol{r}', t'} \left[\langle S^\mu(\boldsymbol{r} + \boldsymbol{r}', t + t') S^\nu(\boldsymbol{r}', t') \rangle - \langle S^\mu(\boldsymbol{r} + \boldsymbol{r}', t + t') \rangle \langle S^\nu(\boldsymbol{r}', t') \rangle \right],$$

which is spatially averaged by the summation over $\boldsymbol{r}'$. Here the angle bracket $\langle O \rangle$ denotes the ensemble average of an observable O. The dynamical spin structure factor is calculated as the Fourier transform of $C^{\mu\nu}(\boldsymbol{r}, t)$. We transform it under the periodic boundary condition with $N'_{\boldsymbol{r}} = N_{\boldsymbol{r}} = N_x N_y N_z$ as

$$C^{\mu\nu}(\boldsymbol{q}, t) = \frac{1}{N_{\boldsymbol{r}} N'_t} \sum_{t'} \left[\langle S^\mu(\boldsymbol{q}, t + t') S^\nu(-\boldsymbol{q}, t') \rangle - \langle S^\mu(\boldsymbol{q}, t + t') \rangle \langle S^\nu(-\boldsymbol{q}, t') \rangle \right]. \quad (3.58)$$

In this scheme, we replace the ensemble average by the average over the samples which is

described with the number of samples A and the index s labeling a sample as

$$\langle O \rangle = \frac{1}{A} \sum_s O_s. \tag{3.59}$$

We prepare A initial states for solving the Landau–Lifshitz equation by performing a classical Monte Carlo simulation A times at temperature T, where each state is obtained after sufficiently long relaxation process. Then solving the Landau–Lifshitz equation for an initial state labeled by s, $\vec{S}_{s=1,\cdots,A}(\boldsymbol{q}, t=0)$, we obtain the Fourier transform of the spin configuration at time t, $\vec{S}_s(\boldsymbol{q}, t)$, and calculate the correlation function based on Eq. (3.58).

We discretize time $t = n\Delta t$ to solve the Landau–Lifshitz equation using the standard Runge–Kutta method or "RK4" with time step $\Delta t = 0.01 J_\parallel^{-1}$. We have confirmed that there is no visible Δt-dependence by comparing it with smaller time steps. The summation over t' is taken with $N_t' = 200$ and the different time step $\Delta \bar{t} = 10\Delta t$ for numerical efficiency.

Finally we perform the Fourier transform in time as

$$C^{\mu\nu}(\boldsymbol{q}, \omega) = \sum_t C^{\mu\nu}(\boldsymbol{q}, t) e^{\mathrm{i}\omega t - \frac{1}{2}(\delta_\omega t)^2} \tag{3.60}$$

with time step $\Delta \bar{t}$ since we do not need the higher frequency than the upper band edge of single magnon excitations[5]. Here the Gaussian factor, $e^{-(\delta_\omega t)^2/2}$ is introduced to smooth the ω-dependence as was used in Ref. [136], but here we have not adjusted the parameter δ_ω.

We summarize the parameters used here:

- DMI: $D/J_\parallel = 0.5$
- Temperature used in Monte Carlo: $T/J_\parallel = 0.05$
- The number of samples $A = 200$
- System size: $N_x = 1, N_y = 1, N_z = 128$
- Time step: $\Delta t = 0.01 J_\parallel^{-1}$, and time length: $t_{\max} = 4000 J_\parallel^{-1}$
- Smearing parameter: $\delta_\omega = 0.04 J_\parallel$

Then in Fig. 3.6 we show the numerical results of the correlation functions. We also plot by black solid lines the analytical branches, given by E_{q+Q} and $E_{q-Q+Q_{\mathrm{AF}}}$ for the ferromagnetic and antiferromagnetic cases, respectively. The spin wave approximation well describes the branches in $C^{xx}(q, \omega)$ obtained numerically even in the antiferromagnetic case, although upon changing the field the branch shape changes more drastically in the antiferromagnetic case than that in the ferromagnetic case. Slight differences in the dispersion relations may be due to finite

[5]The frequency range is determined by the resolution in time, i.e. $\Delta \bar{t}$. Note that the Landau–Lifshitz equation should be solved using time step Δt to guarantee the precision of solutions.

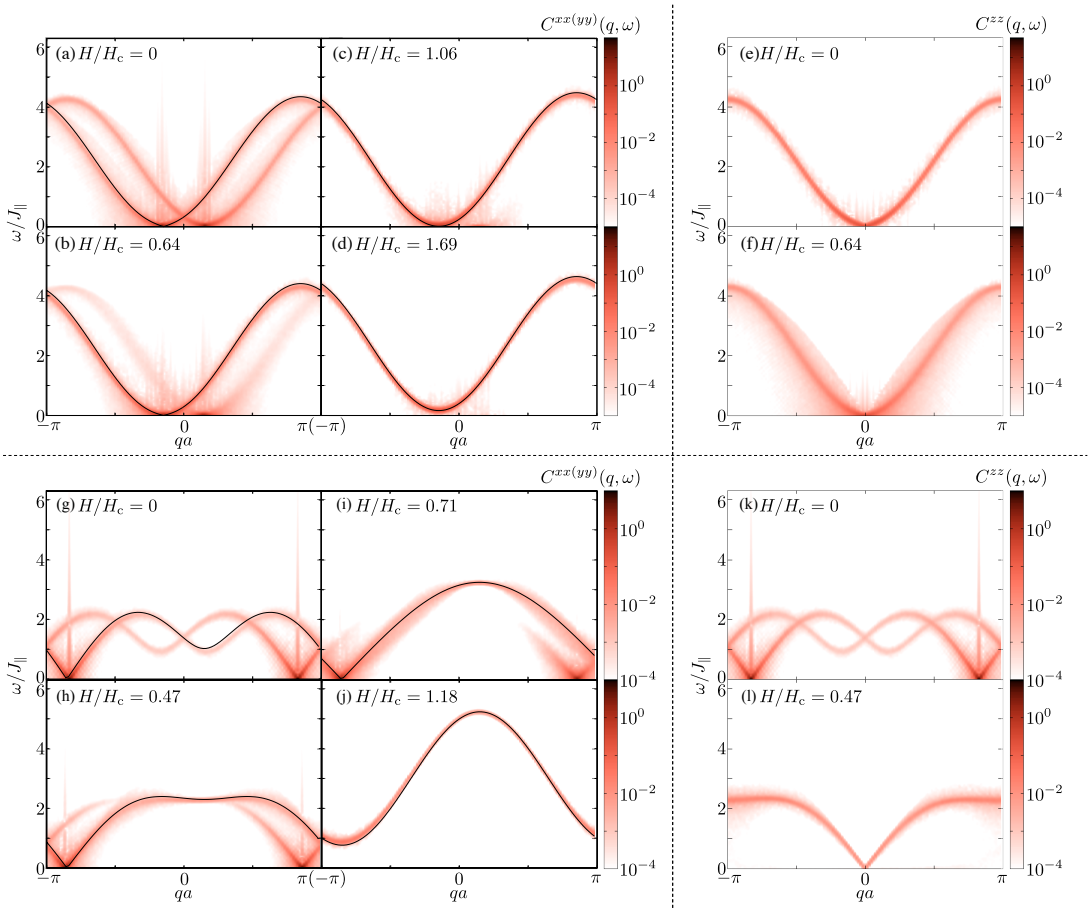

Figure 3.6: Numerical simulations of dynamical spin structure factors for chiral ferromagnets [(a)–(f)] and chiral antiferromagnets [(g)–(l)]. We set $D = 0.5J_\parallel$ and $K = 0$. The values of the critical field are based on the expression that $H_c = 2(\tilde{J} \mp J_\parallel)S$ with $S = 1$ for ferromagnetic and antiferromagnetic cases, respectively. Thus we do not take account of the effect that the expectation value of the spin magnitude reduces on the critical field. The black solid lines in left panels for the ferromagnetic and antiferromagnetic cases are the branches represented by E_{q-Q} and $E_{q-Q+Q_{\rm AF}}$, respectively.

size effects. The periodic structure with an incommensurate wave vector $Qa = \tan^{-1}(D/J_\parallel)$ usually never realizes on a lattice system under the periodic boundary condition, which leads to errors of $\Delta qa \sim 0.025$ in ferromagnetic cases or 0.049 in antiferromagnetic cases. However, the deviation observed in Fig. 3.6(g) is about 0.076 and this is not so small as expected from the finite-sized correction, and this requires further analysis. In addition, the difference is likely to come from the reduction of the effective moment amplitude and interactions between spin waves at the finite temperatures. This appears in the difference of H_c. The value of the critical field is calculated on the basis of the expression $2S(\tilde{J} - J_\parallel)$, but S should be renormalized

as $|\langle\vec{S}\rangle|$. Thus the values of the critical field would be overestimated and the field ratios in the figure are underestimated. This may be the reason that the gaps in the panels (c) and (j) are larger than the analytical values. As a whole, however, the predictions based on the spin wave approximation do not differ from the numerical results very much, and this relatively good agreement is owing to the low temperature, where these effects are not large. We expect at higher temperatures that the energy branch deviates from the analytical results as well as spectral broadening.

Then we focus on how the spectral intensity evolves with the magnetic field, which is the main issue of this chapter. As we have discussed in the former sections, the intensity increases in only one branch, while decreases in the other two branches as the magnetic field increases in both the ferromagnetic and antiferromagnetic cases. The consistent behavior is confirmed at low temperature regarding the evolution of the non-reciprocity predicted by the analytical calculation. The intensity of the $\omega_+(q)$ branch decreases in the numerical simulation while that of the $\omega_-(q)$ branch decreases in the analytical calculation. This is because the field direction is opposite in these two cases.

Here we make a few remarks about this simulation. First is about the temperature effects. We prepare a set of initial conditions by a classical Monte Carlo simulation at the very low temperature. Then we simulate the dynamics by the Landau–Lifshitz equation at zero temperature. In this case we would wonder if we could take account of the temperature effect successfully or not. It is considered that the zero temperature dynamics based on the Landau–Lifshitz equation corresponds to dynamics under the micro-canonical ensemble, while the canonical ensemble dynamics corresponds to dynamics based on the Landau–Lifshitz–Gilbert equation with a Langevin torque term. Thus the equivalence of two ensembles in the thermodynamic limit guarantees to some extent for finite-sized system that the simulation describes spin dynamics under temperature about $T/J_{\parallel} = 0.05$. Note that we do not discuss the temperature effects quantitatively. Then once we understand this, we would have a question about the validity of the finite temperature dynamics in the one dimensional system. In a one dimensional classical system, there is no long range order at finite temperature, thus we could not expect the conical state. On the other hand, as temperature goes to zero, the short range order grows up and the correlation length becomes longer. Our simulation has been performed for a finite-sized system and if the correlation length exceeds the system size, we may consider that the system has long range order practically. Thus it is likely that our simulation of the classical spin systems at finite temperature is valid.

3.6 Summary of this chapter

In this chapter, we have clarified the non-reciprocity appearing in the dynamical spin structure factor $C^{\mu\nu}(q,\omega)$ under the magnetic field. This has three branches, $\omega_\pm(q) = E_{q\mp Q}$ and $\omega_z(q) = E_q$ determined from the peak positions of $C^{\mu\mu}(q,\omega)$. There exist the reciprocal relations $\omega_\pm(q) = \omega_\mp(-q)$ and $\omega_z(q) = \omega_z(-q)$. To discuss the evolution of non-reciprocity,

one needs to focus on $C^{xx}(q,\omega)$ or equivalently $C^{yy}(q,\omega)$, and intensities at $\omega_{\pm}(q)$ show non-reciprocity in the presence of the magnetic field below the critical field. With approaching the critical field $H_{\rm c}$, the intensity of one branch, $\omega_{+(-)}(q)$, decreases. It finally vanishes at $H_{\rm c}$ and the dispersion relation, $\omega_{-(+)}(q)$, becomes non-reciprocal above $H_{\rm c}$. Kataoka discussed the discontinuous change of the dispersion relation[66] and obtained the dispersion described as q^2 at $H = H_{\rm c} - 0$. Above $H_{\rm c}$, the dispersion relation shows a finite group velocity at $q = 0$. We find that the non-reciprocity appears continuously through the difference of the spectral intensity rather than discontinuously at the critical field.

Chapter 4

Chiral solitons under tilted field

In this chapter, we consider the zero-temperature magnetic phase diagram of a uniaxial chiral spin system under the tilted magnetic field. A candidate material is $Cr_{1/3}NbS_2$, and its helical spin structure propagates along the c-axis. We call the c-axis the helical axis. This uniaxial system shows the chiral conical state when we apply magnetic field along the helical axis, while shows the chiral soliton lattice state for the field perpendicular to the helical axis. The phase transitions for both directions of the field are continuous, but the inherent characters are different. The non-linear property never appears for the parallel field and a single q mode plays a role of an order parameter. On the other hand, the chiral soliton plays an important role in the phase transition for the perpendicular field. Therefore a natural question is brought about: How are these two states connected? An earlier work by Laliena *et al.* approached this problem, and clarified there are two tricritical points which separates these two continuous phase transitions[86]. The phase boundary between the two tricritical points shows the discontinuous phase transition. In the first part of this chapter, we show that the properties of the discontinuous phase transition can be explained using the soliton picture. The linear analysis with respect to the asymptotic behavior of the soliton or a helical mode tells us the positions of two multicritical points on the phase boundary. In the second part, we study the surface barrier which soliton feels when it enters or escapes from the system through the surface. In experiments for micrometer-sized samples, magneto-resistance shows clear hysteresis in the wider region in the phase diagram than the region where the discontinuous phase transition is theoretically predicted. We compare our theoretical results with experimental data and conclude that the hysteresis observed in experiment is attributed to the surface barrier of the soliton.

4.1 Introduction

The uniaxial chiral magnet, $Cr_{1/3}NbS_2$, has a strong hard-axis anisotropy along the helical axis, and thus the magnetic properties under the magnetic field perpendicular to the helical axis are well-distinguished from those for the field parallel to the helical axis[43, 109]. In this chapter, we call the former field configuration the perpendicular field, and the latter the

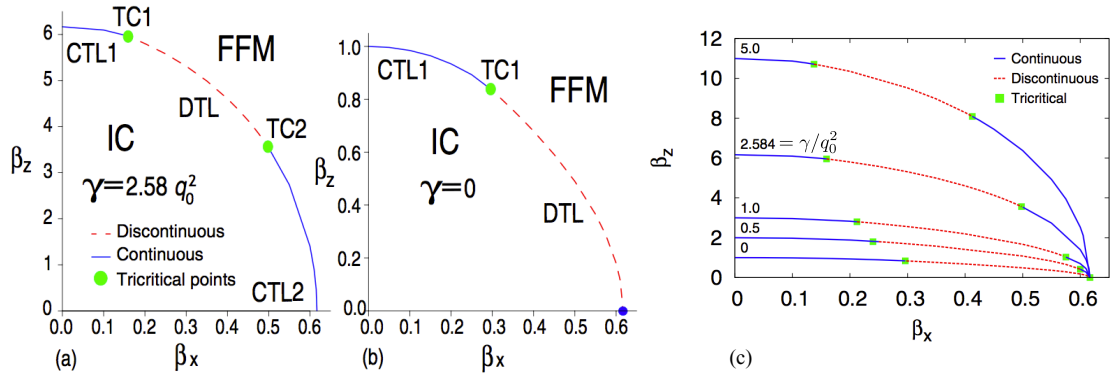

Figure 4.1: Phase diagram obtained for the continuum model by Laliena *et al.*[86]. γ/q_0^2 stands for the anisotropy, and is almost equivalent to $K/(2H_{\rm d})$ in our definition. $\beta_{\mu=x,z}$ are the perpendicular and parallel magnetic fields, corresponding to $H_{\rm ex}^{\mu}/H_{\rm d}$. The left panel (a) is the phase diagram for the realistic value of the anisotropy, while the middle panel (b) is that for the zero anisotropy case. The anisotropy dependence of the phase diagram is shown in the right panel (c). Here "TC" denotes the tricritical point, while "CTL" and "DTL" are the continuous and discontinuous transition lines, respectively. IC and FFM are the incommensurate phase and the "forced ferromagnetic" phase, respectively, and the latter is nothing but the uniformly polarized state.

parallel field. The perpendicular field induces the higher harmonics in the helical order and the spin configuration forms a so-called chiral soliton lattice, i.e. a periodic structure of chiral solitons. Here a chiral soliton is a 2π domain wall separating the uniformly aligned region and it is equivalent to the discommensuration proposed by McMillan[79]. This chiral soliton is topologically stable because of the strong anisotropy, and the control of this soliton is desirable for application. The parallel field induces the chiral conical phase, in which the spin wave propagation is non-reciprocal as we have seen in the previous chapter. In this case, the spin structure does not have the higher harmonics[1].

Recently Laliena *et al.* studied the magnetic states under a tilted magnetic field using a continuum model[86]. They minimized an energy functional numerically to obtain the ground state and found that there were two tricritical points on the phase boundary as shown in Fig. 4.1. The phase boundary separates the ordered and disordered phases. The segment between the two tricritical points on the phase boundary shows the discontinuous phase transition, while the other segments are continuous phase transitions. The two limiting cases, i.e., perpendicular and parallel fields, lead to the continuous phase transition, but these two continuous phase transitions are different, because of the presence/absence of chiral solitons and actually the different behaviors of the observables at the critical fields between two continuous transition

[1]The spin configuration of the conical state is given by $\vec{M}_l = {M_q}^t(\cos(qal), \sin(qal), 0) + M_0\hat{z}$, and the order parameter is given by the amplitude of M_q.

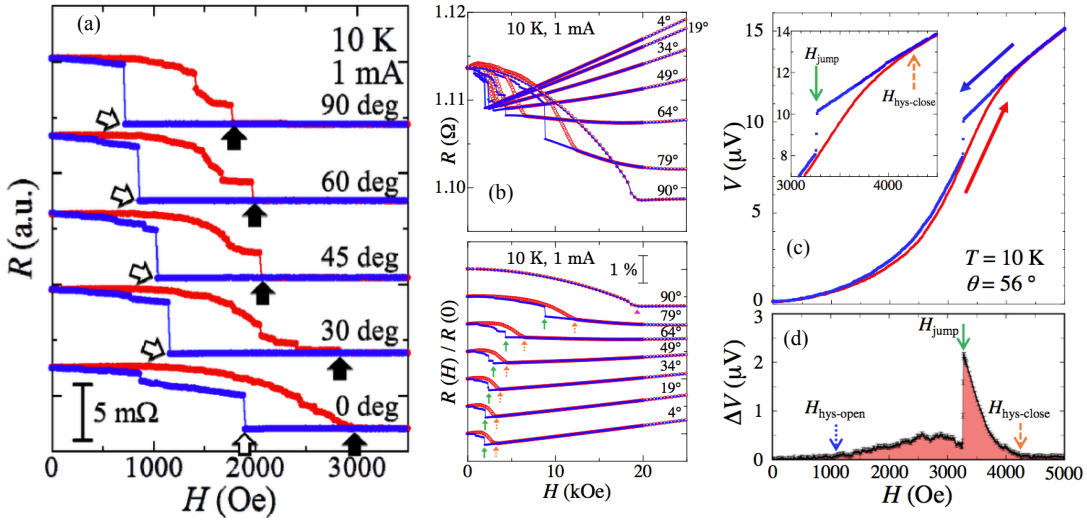

Figure 4.2: Experimentally observed hysteresis. The left panel (a) is the magneto-resistance for a thin film under the perpendicular field and the helical axis is in the plane. The angles of the field, which is shown in the figure, are measured from the normal direction to the film. Note that the field is always perpendicular to the helical axis. The middle panel (b) shows the field dependence of the magneto-resistance for several tilted angles of the field. Here the field is rotated in the plane including the helical axis. The upper panel shows the raw data and the lower shows the normalized resistance by $R(0)$ and data are arranged for visibility. The right panels are the hysteresis appearing in the magnetic torque measurement, and the upper (c) shows the typical increasing and decreasing field processes and the lower (d) shows the difference of these two processes, i.e., the magnitude of the hysteresis. Figures are from Refs. [103, 104].

lines were discussed. However it has not been clear why there are two tricritical points and what are the roles of helical order and chiral solitons in each part of the phase transition. Experiments were performed by Togawa's group with a purpose to test the theoretical prediction of two tricritical points. They investigated the field-increasing and decreasing processes and observed a large hysteresis, as shown in Fig. 4.2[103]. The large hysteresis was also observed for magneto-resistance measurement of the micrometer-sized sample with the field perpendicular to the helical axis [Fig. 4.2(a)]. Their sample was a thin film of $13\mu\mathrm{m} \times 0.5\mu\mathrm{m} \times 13\mu\mathrm{m}$ (helical axis), and the field is rotated in the plane normal to the helical axis. We see that 0 degs., which is normal to the film, has the largest effect of demagnetizing field.

Large hysteresis for the tilted field in the plane including the helical axis is observed in the magneto-resistance measurement for the sample of $10\mu\mathrm{m} \times 0.5\mu\mathrm{m} \times 10\mu\mathrm{m}$ (helical axis) [Fig.4.2(b)] and in the magnetic torque measurement for the sample of $13.4\mu\mathrm{m} \times 12.0\mu\mathrm{m} \times 17.6\mu\mathrm{m}$ (helical axis) [Figs. 4.2(c) and (d)] [104]. In the magneto-resistance measurement, the field is applied in the plane spanned by the helical axis and the direction normal to the

film. The hysteresis of the magneto-resistance similar to that for the perpendicular field is obtained for almost all the region except the vicinity of the parallel field (89 and 90 degs.) [Fig. 4.2(b)]. Also the magnetic torque measurement is useful for the tilted field configuration since the magnetization $\vec{M}$ is not parallel to the applied field $\vec{H}_{\rm ex}$, which induces the non-zero torque proportional to $\vec{M} \times \vec{H}_{\rm ex}$. Magnetic torque is sensitive to a relative and small change of the magnetization. In both experiments, they found the indication of TC1, which is the tricritical point near the parallel field configuration as shown in Fig. 4.1 judging from the presence/absence of the hysteresis, and there is no signature of TC2.

In this chapter, we will clarify the mechanisms of the phase transitions and roles of chiral solitons in the discontinuous phase transition and two continuous phase transitions under tilted magnetic field. Also we will show that the characteristic large jump in the decreasing field process is due to the surface barrier of a chiral soliton. In contrary to the earlier work[86], we use a lattice model in the present study.

4.2 Model and mean field equation

We start with the following spin Hamiltonian for classical spins on a cubic lattice:

$$\mathcal{H} = -\sum_{\boldsymbol{j}} \left[J_{\parallel} \vec{S}_{\boldsymbol{j}} \cdot \vec{S}_{\boldsymbol{j}+\hat{z}} + D \left(\vec{S}_{\boldsymbol{j}} \times \vec{S}_{\boldsymbol{j}+\hat{z}} \right)_z - \frac{K}{2} \left(S^z_{\boldsymbol{j}} \right)^2 + \vec{H}_{\rm ex} \cdot \vec{S}_{\boldsymbol{j}} + J_{\perp} \sum_{\mu=x,y} \vec{S}_{\boldsymbol{j}} \cdot \vec{S}_{\boldsymbol{j}+\hat{\mu}} \right]. \tag{4.1}$$

We consider $|\vec{S}_{\boldsymbol{j}}| = 1$ just for simplicity. $\hat{\mu}$ is the unit vector of μ-direction in the real space. The summation index $\boldsymbol{j}$ takes all of the lattice sites under the appropriate boundary conditions discussed later. The first and second terms are the Heisenberg exchange interaction, and the DMI, respectively, on the nearest neighbor pairs along the helical axis. The third term is a single ion anisotropy energy, and when K is positive, the helical axis is a hard axis. The fourth term describes the tilted magnetic field, which suggests that $\vec{H}_{\rm ex}$ has x- and z-components, and the last term is the inter-chain exchange interaction. We consider the zero temperature case, and consider here only spin configurations that have no modulation in the xy-plane, i.e. the spin structure has one dimensional modulation. In this case, the spin structure is specified only by the layer index l. We introduce $\vec{M}_l = \vec{S}_{\boldsymbol{j}}$ for $\boldsymbol{j} \cdot \hat{z} = l$ for integer $l = -\infty, \cdots, -1, 0, 1, 2, \cdots, \infty$. For this configuration, the last term of the Hamiltonian just shifts the origin of the energy. For the configuration $\vec{M}_l$, we normalize the energy by the number of in-plane spins $N_{\rm 2d}$ and subtract the energy of in-plane exchange couplings as

$$\begin{aligned} E &= \frac{\mathcal{H}}{N_{\rm 2d}} + \frac{zN_z}{2} J_{\perp} \\ &= -\sum_{l} \left[J_{\parallel} \vec{M}_l \cdot \vec{M}_{l+1} + D \left(\vec{M}_l \times \vec{M}_{l+1} \right)^z - \frac{K}{2} \left(M^z_l \right)^2 + \vec{H}_{\rm ex} \cdot \vec{M}_l \right]. \end{aligned} \tag{4.2}$$

Here $z = 4$ denoting the number of the nearest sites in xy-plane, and N_z denotes the number of layers. The equilibrium condition, i.e. the equation for $\vec{M}_l$ is given by the zero-torque condition. The effective field on the site l, $\vec{H}_l^{\rm eff}$ is given by the variation of the energy with respect to $\vec{M}_l$, and the torque is zero when the magnetic moment is parallel to the effective field. At zero temperature, the modulus of the moment is always 1. Therefore the equation can be summarized as follows:

$$\vec{M}_l = \hat{H}_l^{\rm eff} = \vec{H}_l^{\rm eff}/|\vec{H}_l^{\rm eff}|, \tag{4.3}$$

$$\vec{H}_l^{\rm eff} = J_{\parallel}(\vec{M}_{l-1} + \vec{M}_{l+1}) + D\vec{e}^z \times (\vec{M}_{l-1} - \vec{M}_{l+1}) - KM_l^z\vec{e}^z + \vec{H}_{\rm ex}, \tag{4.4}$$

where $\vec{e}^z$ denotes the unit vector of z-direction in the spin space The solution is the same as that to the LLG equation in the stationary case. We can obtain this by letting the time derivative be zero in Eq. (2.78). Equations (4.3) and (4.4) are the non-linear coupled equations, and determine all static spin profiles: isolated soliton state, soliton lattice state, conical state, and their mixtures.

4.3 Linear analysis for soliton

In this section, we study the condition of the presence of soliton solution. Since numerical search of soliton solution takes time and is not easy to cover the whole parameter space, we try an alternative approach and analyze a small deviation from the uniform state on the basis of Eqs. (4.3) and (4.4) up to its linear order. This provides a necessary condition for a soliton solution, and the sufficient condition is discussed in Sect. 4.6.3.

The phase diagram includes the two types of continuous phase transitions: instability-type in the parallel field configuration and nucleation-type in the perpendicular field configuration. Near the latter-type transition, solitons are nucleated and their interactions determine the critical properties at the transition. Since the soliton density is small near the transition, the interaction is mainly determined by the tail structure of an isolated soliton, and we will study it in the following.

To this end, we study the asymptotic properties for coupled linear equations (4.3) and (4.4). As reviewed in Sect 2.5.3, let us assume the presence of an isolated soliton in the uniform background, and its tail structure described by

$$\vec{M}_l = \vec{M}_{\rm u} + \vec{A}\exp(-\kappa x_l) \text{ with } x_l = la \ (l \gg 1). \tag{4.5}$$

The deviation $\vec{A}e^{-\kappa x_l}$ is a small quantity far from the soliton center. We expand the equations (4.3) and (4.4) up to its linear order and examine the condition that the asymptotic form of a soliton exists. Note that this is a necessary condition for the existence of an isolated soliton. Its sufficient condition will be discussed in Sect. 4.6.3.

The uniform background should be determined for each value of external field, and we can write it as $\vec{M}_{\rm u} = (M_{{\rm u},\perp}, 0, M_{{\rm u},\parallel})$ with the normalization condition $|\vec{M}_{\rm u}|^2 = 1$. Note that $M_{\rm u}^y = 0$ since $H_{\rm ex}^y = 0$.

The vector $\vec{A} = (A^x, A^y, A^z)$ and κ are quantities to be determined. The real part of κ is the inverse decay-length of the soliton. Note that the deviation in Eq. (4.5) describes not only a soliton tail but also other types of stable spin structure. When κ is pure imaginary $\kappa = \mathrm{i}q$, it corresponds to a distorted conical structure with the wave number q, and this solution can be also examined by the same linear analysis when the amplitude is small, $|\vec{A}| \ll 1$. We call the order whose leading term is described by Eq. (4.5) with $\kappa = \mathrm{i}q$ the *distorted conical order*.

We expand Eqs. (4.3) and (4.4) up to first order with respect to the second term of Eq. (4.5), in which either $\vec{A}$ or $\exp(-\kappa x_l)$ is considered to be sufficiently small. Let us expand the amplitude of the moment and reduce the number of components of $\vec{A}$.

$$1 = |\vec{M}_l|^2 \simeq |\vec{M}_{\mathrm{u}}|^2 + 2\vec{M}_{\mathrm{u}} \cdot \vec{A} \exp(-\kappa x_l) \to \vec{M}_{\mathrm{u}} \cdot \vec{A} = M_{\mathrm{u},\perp} A^x + M_{\mathrm{u},\parallel} A^z = 0. \tag{4.6}$$

Thus, there exists a relation between A^x and A^z. Then we expand the effective field. For convenience we define the following quantities:

$$H^x_{\mathrm{u}} = 2J_\parallel M_{\mathrm{u},\perp} + H^x_{\mathrm{ex}}, \tag{4.7}$$
$$H^z_{\mathrm{u}} = 2J_\parallel M_{\mathrm{u},\parallel} - K M_{\mathrm{u},\parallel} + H^z_{\mathrm{ex}}, \tag{4.8}$$
$$H_{\mathrm{u}} = \sqrt{(H^x_{\mathrm{u}})^2 + (H^z_{\mathrm{u}})^2}, \tag{4.9}$$

and the effective field can be described up to first order in the deviation as follows:

$$H^x_l = H^x_{\mathrm{u}} + [2J_\parallel \cosh(\kappa a) A^x + 2D \sinh(\kappa a) A^y] \exp(-\kappa x_l), \tag{4.10}$$
$$H^y_l = [2J_\parallel \cosh(\kappa a) A^y - 2D \sinh(\kappa a) A^x] \exp(-\kappa x_l), \tag{4.11}$$
$$H^z_l = H^z_{\mathrm{u}} + [2J_\parallel \cosh(\kappa a) - K] A^z \exp(-\kappa x_l), \tag{4.12}$$
$$\begin{aligned} |\vec{H}_l|^2 = H^2_{\mathrm{u}} + \big\{ & 2H^x_{\mathrm{u}} [2J_\parallel \cosh(\kappa a) A^x + 2D \sinh(\kappa a) A^y] \\ & + H^z_{\mathrm{u}} [2J_\parallel \cosh(\kappa a) - K] A^z \big\} \exp(-\kappa x_l). \end{aligned} \tag{4.13}$$

Note that $x_{l+1} - x_l = a$. The mean field equation $\vec{M}_l = \hat{H}^{\mathrm{eff}}_l$ leads to the coupled equations using complementary relation (4.6). Its x-component reads

$$\begin{aligned} & M_{\mathrm{u},\perp} + A^x \exp(-\kappa x_l) \\ & \quad \simeq \frac{H^x_{\mathrm{u}}}{H_{\mathrm{u}}} + \frac{(H^z_{\mathrm{u}})^2}{H^2_{\mathrm{u}}} \frac{[2J_\parallel \cosh(\kappa a) A^x + 2D \sinh(\kappa a) A^y] \exp(-\kappa x_l)}{H_{\mathrm{u}}} \\ & \qquad\qquad - \frac{H^x_{\mathrm{u}} H^z_{\mathrm{u}} [2J_\parallel \cosh(\kappa a) - K] A^z \exp(-\kappa x_l)}{H^3_{\mathrm{u}}}, \end{aligned} \tag{4.14}$$

and the y-component is

$$A^y \exp(-\kappa x_l) \simeq \frac{[2J_\parallel \cosh(\kappa a) A^y - 2D \sinh(\kappa a) A^x] \exp(-\kappa x_l)}{H_{\mathrm{u}}}. \tag{4.15}$$

The equation for z-component is equivalent to the first one through the relation (4.6). From the first equation, we obtain the equation for the uniform component

$$\vec{M}_{\rm u} = \vec{H}_{\rm u}/H_{\rm u} \to \left(1 - \frac{K}{H^z_{\rm ex}} M_{\rm u,\parallel}\right) M_{\rm u,\perp} - \frac{H^x_{\rm ex}}{H^z_{\rm ex}} M_{\rm u,\parallel} = 0, M_{\rm u,\perp} = \sqrt{1 - M^2_{\rm u,\parallel}}. \tag{4.16}$$

When $H^z_{\rm ex} = 0$, $M_{\rm u,\perp} = 1$ and $M_{\rm u,\parallel} = 0$. When $K = 0$, $M_{\rm u,\perp(\parallel)} = H^{x(z)}_{\rm ex}/H_{\rm ex}$. From this, we see that the relation (4.6) reads $\vec{H}_{\rm u} \cdot \vec{A} = 0$. We obtain the coupled equation for (A^x, A^y)

$$\begin{pmatrix} (2J_\parallel \cosh(\kappa a) - K M^2_{\rm u,\perp}) - H_{\rm u} & M^2_{\rm u,\parallel} 2D \sinh(\kappa a) \\ -2D \sinh(\kappa a) & 2J_\parallel \cosh(\kappa a) - H_{\rm u} \end{pmatrix} \begin{pmatrix} A^x \\ A^y \end{pmatrix} = 0 \tag{4.17}$$

The condition that the nontrivial mode exists is given by the null determinant of the coefficient matrix. The determinant takes the form that

$$A \cosh^2(\kappa a) + B \cosh(\kappa a) + C = 0, \tag{4.18}$$

where

$$A = 4(J^2_\parallel + D^2 M^2_{\rm u,\parallel}),\ B = -2J_\parallel(2H_{\rm u} + K M^2_{\rm u,\perp}), \tag{4.19}$$

$$C = -4D^2 M^2_{\rm u,\parallel} + H_{\rm u}(H_{\rm u} + K M^2_{\rm u,\perp}). \tag{4.20}$$

This can be regarded as the quadratic equation with respect to $\cosh(\kappa a)$. We can distinguish a solution κa on the basis of the discriminant of the quadratic equation.

$$\mathsf{D} = \frac{B^2}{4} - AC,\ \cosh(\kappa a) = \frac{-B \pm \sqrt{B^2 - 4AC}}{2A}. \tag{4.21}$$

When D is positive, $\cosh \kappa a$ is real. The condition for real κa is given by $\cosh \kappa a \geq 1$, while pure imaginary κa is obtained for $\cosh \kappa a \leq 1$. When D is negative κa is complex. The complex κa means that the tail of the soliton is damped oscillation. We will show the typical profiles and that they are related to the interaction potential of solitons in Sect. 4.6. The pure imaginary κa means that the trial form we assumed has no decaying solution, but oscillation of a single q mode. As we see in the next section, this regime is described by a wave structure with a helical pitch q and roughly speaking the Fourier amplitude with q is the order parameter in the Landau theory. Note that when κa has a finite imaginary part, we consider the real part of Eq. (4.5).

4.4 Instability-type phase transition

In the previous section, we determined the region of solutions with pure imaginary $\kappa = {\rm i}q$ and its boundary $\mathsf{D} = 0$. In this region, an isolated soliton cannot exist, and the ordered phase is

described by the distorted conical spin structure. The line of $D = 0$ is the instability-field line of the uniform state. In this subsection, we study the phase boundary between the distorted conical and disordered phases, and determine it by more rigorous criterion on the basis of energy analysis. Instead of the microscopic energy functional (4.2), we analyze the Landau energy of the distorted conical order parameter. Following the Schaub–Mukamel's study[101], we expand the spin structure using the order parameter ξ as

$$\begin{pmatrix} M_l^x \\ M_l^y \end{pmatrix} \simeq \begin{pmatrix} M_c^x \\ 0 \end{pmatrix} + \xi \begin{pmatrix} \sigma_x \cos(qx_l) \\ \sigma_y \sin(qx_l) \end{pmatrix} + \xi^2 \begin{pmatrix} \bar{\sigma}_x \cos(2qx_l) \\ \bar{\sigma}_y \sin(2qx_l) \end{pmatrix} + \xi^3 \begin{pmatrix} \tilde{\sigma}_x \cos(3qx_l) \\ \tilde{\sigma}_y \sin(3qx_l) \end{pmatrix}, \quad (4.22)$$

$$M_c^x \simeq M_{\mathrm{u},\perp} + \alpha\xi^2 + \beta\xi^4,\ q = q_c + \bar{\alpha}\xi^2 + \bar{\beta}\xi^4. \quad (4.23)$$

Here $\sigma_{x,y}$ with the normalization $\sigma_x^2 + \sigma_y^2 = 1$, $\bar{\sigma}_{x,y}$, $\tilde{\sigma}_{x,y}$, α, $\bar{\alpha}$, β, $\bar{\beta}$, and q_c are parameters to be determined for minimizing the energy for a given ξ. This expansion includes the single q mode and its self-interactions[2]. These terms should be enough to describe the instability-type phase transition, but we make a few remarks. First, the fourth-order harmonic term $\cos 4qx_l$ or $\sin 4qx_l$ is not necessary, because we do not consider the case $q = 0$, $\pi/2a$, or π, and its contribution vanishes after site summation. In a similar way, an initial phase ϕ which appears by shifting $qx_l \to qx_l + \phi = y_l$, is not necessary either since $\sum_l \cos(nqy_l) = 0$ when qa is neither 0 nor π/n for $n = 1, \cdots, 4$. Second, the odd-order terms in ξ do not appear in M_c and q. We can prove this as follows: First we do not expand M_c and q with respect to ξ, and calculate the energy density. As we see later, it depends only on even-order terms in ξ. We obtain ξ dependence of M_c and q from the minimization condition of the energy with respect to M_c and q, and the equations include the even-order terms in ξ. Thus we can expand M_c and q as Eq. (4.23). Physically, this means that transformation $\xi \to -\xi$ corresponds to shifting of the spin structure as $x_l \to x_l + \pi/q$, and it does not change the uniform magnetization. These considerations on commensurate wave number q are needed for lattice models in contrast to continuum models such as a model in Ref. [101].

Another difference from the study [101] is the presence of the third component M_l^z, but this is only technical at zero temperature, and the normalization condition determines it as $M_l^z = \sqrt{1 - (M_l^x)^2 - (M_l^y)^2}$. Calculations of the Landau energy becomes easier using M_l^z expanded up to ξ^4:

$$M_l^z \simeq M_c^z + (\xi\sigma_z + \xi^3\sigma_z')\cos qx_l + (\xi^2\bar{\sigma}_z + \xi^4\bar{\sigma}_z')\cos 2qx_l + (\xi^3\tilde{\sigma}_z)\cos 3qx_l \quad (4.24)$$

[2]The nth-order harmonic term is accompanied by ξ^n.

with $M_c^z = M_{\mathrm{u},\parallel} + \alpha_z \xi^2 + \beta_z \xi^4$ and

$$\sigma_z = -\frac{M_{\mathrm{u},\perp}}{M_{\mathrm{u},\parallel}} \sigma_x, \tag{4.25}$$

$$\alpha_z = -\frac{1}{4M_{\mathrm{u},\parallel}} \left(1 + 4\alpha M_{\mathrm{u},\perp} + \frac{M_{\mathrm{u},\perp}^2}{M_{\mathrm{u},\parallel}^2} \sigma_x^2 \right), \tag{4.26}$$

$$\bar{\sigma}_z = -\frac{1}{4M_{\mathrm{u},\parallel}} \left(\frac{\sigma_x^2}{M_{\mathrm{u},\parallel}^2} - \sigma_y^2 + 4M_{\mathrm{u},\perp} \bar{\sigma}_x \right), \tag{4.27}$$

$$\sigma_z' = -\frac{1}{2M_{\mathrm{u},\parallel}} \left[2\alpha\sigma_x + 2\alpha_z \sigma_z + \sigma_x \bar{\sigma}_x + \sigma_y \bar{\sigma}_y + \sigma_z \bar{\sigma}_z \right], \tag{4.28}$$

$$\tilde{\sigma}_z = -\frac{1}{2M_{\mathrm{u},\parallel}} \left[\sigma_x \bar{\sigma}_x - \sigma_y \bar{\sigma}_y + \sigma_z \bar{\sigma}_z + 2M_{\mathrm{u},\perp} \tilde{\sigma}_x \right], \tag{4.29}$$

$$\beta_z = -\frac{1}{2M_{\mathrm{u},\parallel}} \left(\alpha^2 + \alpha_z^2 + 2M_{\mathrm{u},\perp}\beta + \frac{\bar{\sigma}_x^2 + \bar{\sigma}_y^2 + \bar{\sigma}_z^2}{2} + \sigma_z \sigma_z' \right). \tag{4.30}$$

Here we keep q without the expansion. Note that the term with $4q$ modulation is not necessary for the same reason as the above.

4.4.1 Energy density

We substitute the above forms of $\vec{M}_l$ into Eq. (4.2), and write the Landau energy density up to fourth order in ξ as $E(\xi) = a_0 + a_2 \xi^2 + a_4 \xi^4$. In this subsection, we first expand each term of the Hamiltonian up to fourth order in ξ and calculate a_2 and a_4. Expansions are given in the following.

Exchange

$$-\frac{J_\parallel}{N_z} \sum_l \vec{M}_l \cdot \vec{M}_{l+1} \approx -J_\parallel \left\{ |\vec{M}_{\mathrm{u}}|^2 + \left[2(M_{\mathrm{u},\perp}\alpha + M_{\mathrm{u},\parallel}\alpha_z) + \frac{1}{2}\left(1 + \sigma_z^2\right) \cos qa \right] \xi^2 \right.$$
$$\left. + \left[\alpha^2 + \alpha_z^2 + 2(M_{\mathrm{u},\perp}\beta + M_{\mathrm{u},\parallel}\beta_z) + \frac{1}{2}(\bar{\sigma}_x^2 + \bar{\sigma}_y^2 + \bar{\sigma}_z^2) \cos 2qa + \sigma_z \sigma_z' \cos qa \right] \xi^4 \right\} \tag{4.31}$$

$$\approx -J_\parallel \left[M_{\mathrm{u}}^2 - \frac{\xi^2}{2} \left(1 + \frac{M_{\mathrm{u},\perp}}{M_{\mathrm{u},\parallel}} \sigma_x^2 \right) (1 - \cos q_c a) \right] + O(\xi^4). \tag{4.32}$$

DMI

$$-\frac{D}{N_z}\sum_l \left(\vec{M}_l \times \vec{M}_{l+1}\right)^z \approx -D\left(\xi^2\sigma_x\sigma_y \sin qa + \xi^4\bar{\sigma}_x\bar{\sigma}_y \sin 2qa\right) \tag{4.33}$$

$$\approx -D\xi^2\sigma_x\sigma_y \sin q_c a + O(\xi^4). \tag{4.34}$$

Anisotropy

$$\frac{K}{2N_z}\sum_l (M_l^z)^2 \approx \frac{K}{2}\left[M_{\mathrm{u},\parallel}^2 + \left(2M_{\mathrm{u},\parallel}\alpha_z + \frac{1}{2}\sigma_z^2\right)\xi^2 + \left(\alpha_z^2 + 2M_{\mathrm{u},\parallel}\beta_z + \frac{1}{2}\bar{\sigma}_z^2 + \sigma_z\sigma_z'\right)\xi^4\right] \tag{4.35}$$

$$\approx \frac{K}{2}\left[M_{\mathrm{u},\parallel}^2 - \frac{\xi^2}{2}\left(1 + 4\alpha M_{\mathrm{u},\perp}\right)\right] + O(\xi^4). \tag{4.36}$$

Zeeman coupling

$$-\frac{1}{N_z}\sum_l \vec{H}_{\mathrm{ex}}\cdot\vec{M}_l \approx -\vec{H}_{\mathrm{ex}}\cdot\vec{M}_c \tag{4.37}$$

$$\approx -\vec{H}_{\mathrm{ex}}\cdot\vec{M}_{\mathrm{u}} + \xi^2\left[\frac{H_{\mathrm{ex}}^z}{4M_{\mathrm{u},\parallel}}\left(1 + \frac{M_{\mathrm{u},\perp}^2}{M_{\mathrm{u},\parallel}^2}\sigma_x^2\right) + \alpha\left(\frac{M_{\mathrm{u},\perp}}{M_{\mathrm{u},\parallel}}H_{\mathrm{ex}}^z - H_{\mathrm{ex}}^z\right)\right] + O(\xi^4). \tag{4.38}$$

The total energy up to the order ξ^2 is obtained as follows by taking l-sum, which vanishes the spatially dependent terms.

$$\begin{aligned}\frac{E}{N_z} =& \frac{(\vec{H}_{\mathrm{u}} + \vec{H}_{\mathrm{ex}})\cdot\vec{M}_{\mathrm{u}}}{2} \\ &+ \frac{\xi^2}{2}\left\{\left[-J_\parallel \cos q_c a + \left(\frac{H_{\mathrm{u}}^z}{2M_{\mathrm{u},\parallel}} + \frac{K}{2}\right)\right]\left(1 + \frac{M_{\mathrm{u},\perp}^2\sigma_x^2}{M_{\mathrm{u},\parallel}^2}\right) - 2D\sigma_x\sigma_y \sin q_c a - \frac{K}{2}\right\}.\end{aligned} \tag{4.39}$$

Therefore we conclude that

$$a_2 = \frac{1}{2}\left[-J_\parallel \cos q_c a + \left(\frac{H_{\mathrm{u}}^z}{2M_{\mathrm{u},\parallel}} + \frac{K}{2}\right)\right]\left(1 + \frac{M_{\mathrm{u},\perp}^2\sigma_x^2}{M_{\mathrm{u},\parallel}^2}\right) - D\sigma_x\sigma_y \sin q_c a - \frac{K}{4}. \tag{4.40}$$

The derivative of a_2 with respect to $q_c a$ is given by

$$2M_{\mathrm{u},\parallel}^2\frac{\partial a_2}{\partial(q_c a)} = J_\parallel\left(M_{\mathrm{u},\parallel}^2 + M_{\mathrm{u},\perp}^2\sigma_x^2\right)\sin q_c a - 2DM_{\mathrm{u},\parallel}^2\sigma_x\sigma_y \cos q_c a = 0. \tag{4.41}$$

The derivative of a_2 with respect to σ_x is given by[3]

$$2M_{\mathrm{u},\parallel}^2\sigma_y\frac{\partial a_2}{\partial\sigma_x}=\left(-2J_\parallel\cos q_ca+\frac{H_\mathrm{u}^z}{M_{\mathrm{u},\parallel}}+K\right)M_{\mathrm{u},\perp}^2\sigma_x\sigma_y-2DM_{\mathrm{u},\parallel}^2\left(\sigma_y^2-\sigma_x^2\right)\sin q_ca=0. \tag{4.42}$$

Usually $|q_ca|<\pi/2$ for ferromagnetic systems, and $q_ca>0$ is due to a positive D. By considering that $\sin q_ca,\cos q_ca>0$, we see that $\sigma_x\sigma_y>0$ and $\sigma_x^2-\sigma_y^2<0$ from Eqs. (4.41) and (4.42), respectively. The relation that $H_\mathrm{u}=H_\mathrm{u}^x/M_{\mathrm{u},\perp}=H_\mathrm{u}^z/M_{\mathrm{u},\parallel}$ is useful. Let us combine $a_2=0$ and Eq. (4.42), and then we obtain the following equation from $2a_2\sigma_xM_{\mathrm{u},\parallel}^2+M_{\mathrm{u},\parallel}^2\sigma_y^2\partial a_2/\partial\sigma_x=0$ and $2a_2\sigma_y-\sigma_x\sigma_y\partial a_2/\partial\sigma_x=0$:

$$\begin{pmatrix}2J_\parallel\cos q_ca-H_\mathrm{u}-K & 2DM_{\mathrm{u},\parallel}^2\sin q_ca\\ 2D\sin q_ca & 2J_\parallel\cos q_ca-H_\mathrm{u}\end{pmatrix}\begin{pmatrix}\sigma_x\\ \sigma_y\end{pmatrix}=\begin{pmatrix}0\\ 0\end{pmatrix}. \tag{4.43}$$

The condition for the existence of the non-trivial set of σ_x and σ_y is given by for the null determinant of the coefficient matrix:

$$A\cos^2 q_ca+B\cos q_ca+C=0, \tag{4.44}$$

where A, B, and C are defined by Eqs. (4.19) and (4.20), and we find that

$$(\sigma_x,\sigma_y)=(2J_\parallel\cos q_ca-H_\mathrm{u},-2D\sin q_ca)/W \tag{4.45}$$

with

$$W=\sqrt{(2J_\parallel\cos q_ca-H_\mathrm{u})^2+4D^2\sin^2 q_ca}. \tag{4.46}$$

Using Eqs. (4.44) and (4.45), Eq. (4.41) is reduced to

$$\mp(J_\parallel B+AH_\mathrm{u})\frac{\sqrt{B^2-4AC}}{2A}+\frac{J_\parallel B^2}{2A}+\frac{H_\mathrm{u}B}{2}+J_\parallel(-C+J_\parallel H_\mathrm{u}^2+4D^2M_{\mathrm{u},\parallel}^2)=0.$$

Note that $\cos q_ca$ is a solution to Eq. (4.44). We focus on the terms other than the first one.

$$\frac{J_\parallel B^2}{2A}-J_\parallel\left[H_\mathrm{u}(2H_\mathrm{u}+KM_{\mathrm{u},\perp}^2)+C-H_\mathrm{u}^2-4D^2M_{\mathrm{u},\parallel}^2\right]=J_\parallel\left(\frac{B^2}{2A}-2C\right). \tag{4.47}$$

Therefore using $\mathsf{D}=B^2/4-AC$, we have

$$\pm\sqrt{\mathsf{D}}\left[2J_\parallel\frac{-B\pm2\sqrt{\mathsf{D}}}{2A}-H_\mathrm{u}\right]=\pm\sqrt{\mathsf{D}}\left[2J_\parallel\cos q_ca-H_\mathrm{u}\right]=0. \tag{4.48}$$

Noting that $J_\parallel\cos q_ca-H_\mathrm{u}=J_\parallel\cos q_ca-H_\mathrm{u}^x/M_{\mathrm{u},\perp}=-J_\parallel(1-\cos q_ca)-H_\mathrm{ex}^x/M_{\mathrm{u},\perp}<0$, we can conclude that $\mathsf{D}=0$, i.e., $a_2=0$ is equivalent to $\mathsf{D}=0$. This is reasonable because the expansion Eqs. (4.22) and (4.24) up to order ξ is the same as the expansion Eq. (4.5).

[3]Note that σ_y is related to σ_x through $\sigma_x^2+\sigma_y^2=1$.

4.4.2 Fourth order terms in ξ^4

In this subsection, we derive the coefficient a_4 in the Landau energy. Here ξ is a scalar order parameter associated with this phase transition ($a_2 = 0$), and $a_4\xi^4$ is the only form of the fourth-order invariants in the Landau expansion. Note that q has a ξ^2 term. The fourth order term in each part of the energy is given as follows:

Exchange

$$J_\parallel \left[\frac{\bar{\alpha}a}{2}(1+\sigma_z^2)\sin q_c a + \frac{\bar{\sigma}_x^2+\bar{\sigma}_y^2+\bar{\sigma}_z^2}{2}(1-\cos 2q_c a) + \sigma_z\sigma_z'(1-\cos q_c a) \right] \xi^4 \tag{4.49}$$

DMI

$$-D\left[\bar{\alpha}a\sigma_x\sigma_y\cos q_c a + \bar{\sigma}_x\bar{\sigma}_y\sin 2q_c a\right]\xi^4 \tag{4.50}$$

Anisotropy

$$\frac{K}{2}\left(\alpha_z^2 + 2M_{\mathrm{u},\parallel}\beta_z + \frac{1}{2}\bar{\sigma}_z^2 + \sigma_z\sigma_z'\right)\xi^4 \tag{4.51}$$

Zeeman coupling

$$-\left(H_{\mathrm{ex}}^x\beta + H_{\mathrm{ex}}^z\beta_z\right)\xi^4 \tag{4.52}$$

We sum up them and obtain a_4 using $1-\cos 2q_c a = 2\sin^2 q_c a$ as

$$\begin{aligned} a_4 = {} & J_\parallel\left[\left(\bar{\sigma}_x^2+\bar{\sigma}_y^2+\bar{\sigma}_z^2\right)\sin^2 q_c a + \sigma_z\sigma_z'(1-\cos q_c a)\right] - D\bar{\sigma}_x\bar{\sigma}_y\sin 2q_c a \\ & - \frac{K}{2}\left(\alpha^2 + \frac{\bar{\sigma}_x^2+\bar{\sigma}_y^2}{2}\right) + \frac{H_{\mathrm{ex}}^z}{2M_{\mathrm{u},\parallel}}\left(\alpha^2+\alpha_z^2+\frac{\bar{\sigma}_x^2+\bar{\sigma}_y^2+\bar{\sigma}_z^2}{2}+\sigma_z\sigma_z'\right). \end{aligned} \tag{4.53}$$

Parameters $\bar{\sigma}_x$, $\bar{\sigma}_y$, and α should be determined through the stationary condition of a_4 with respect to them. The derivative with respect to α leads to

$$\begin{aligned} \frac{\partial a_4}{\partial\alpha} &= J_\parallel\sigma_z\frac{\partial\sigma_z'}{\partial\alpha}(1-\cos q_c a) - K + \frac{H_{\mathrm{ex}}^z}{M_{\mathrm{u},\parallel}}\left(\alpha - \frac{M_{\mathrm{u},\perp}}{M_{\mathrm{u},\parallel}}\alpha_z + \frac{\sigma_z}{2}\frac{\partial\sigma_z'}{\partial\alpha}\right) \\ &= -\left(K - \frac{H_{\mathrm{ex}}^z}{M_{\mathrm{u},\parallel}^3}\right)\alpha + \frac{H_{\mathrm{ex}}^z}{M_{\mathrm{u},\parallel}}\frac{M_{\mathrm{u},\perp}}{4M_{\mathrm{u},\parallel}^2}\left(1+\frac{M_{\mathrm{u},\perp}^2}{M_{\mathrm{u},\parallel}^2}\sigma_x^2\right) \\ &\qquad - \left[J_\parallel(1-\cos q_c a) + \frac{1}{2}\frac{H_{\mathrm{ex}}^z}{M_{\mathrm{u},\parallel}}\right]\frac{\sigma_x\sigma_z}{M_{\mathrm{u},\parallel}^3} = 0. \end{aligned} \tag{4.54}$$

The derivatives with respect to $\bar{\sigma}_x$ and $\bar{\sigma}_y$ are given by

$$\begin{pmatrix} \frac{2J_\parallel}{M_{\mathrm{u},\parallel}^2}\sin^2 q_c a - \frac{K}{2} + \frac{H_{\mathrm{ex}}^z}{2M_{\mathrm{u},\parallel}^3} & -D\sin 2q_c a \\ -D\sin 2q_c a & 2J_\parallel \sin^2 q_c a - \frac{K}{2} + \frac{H_{\mathrm{ex}}^z}{2M_{\mathrm{u},\parallel}} \end{pmatrix} \begin{pmatrix} \bar{\sigma}_x \\ \bar{\sigma}_y \end{pmatrix} = \begin{pmatrix} y_x \\ y_y \end{pmatrix}, \quad (4.55)$$

$$y_x = \left[-\frac{M_{\mathrm{u},\perp}}{4M_{\mathrm{u},\parallel}^2} \left(\frac{\sigma_x^2}{M_{\mathrm{u},\parallel}^2} - \sigma_y^2 \right) \left(2J_\parallel \sin^2 q_c a + \frac{H_{\mathrm{ex}}^z}{2M_{\mathrm{u},\parallel}} \right) + \frac{\sigma_x \sigma_z}{2M_{\mathrm{u},\parallel}^3} \left(J_\parallel (1 - \cos q_c a) + \frac{H_{\mathrm{ex}}^z}{2M_{\mathrm{u},\parallel}} \right) \right], \quad (4.56)$$

$$y_y = \frac{\sigma_y \sigma_z}{2M_{\mathrm{u},\parallel}} \left(J_\parallel 2\sin^2 q_c a + \frac{H_{\mathrm{ex}}^z}{2M_{\mathrm{u},\parallel}} \right). \quad (4.57)$$

We can easily obtain α, $\bar{\sigma}_x$, and $\bar{\sigma}_y$, and we find a_4 on the basis of Eq. (4.53) for a given $\vec{H}_{\mathrm{ex}}$. The condition $a_4 = 0$ on the line $a_2 = 0$ leads to the tricritical point, and its value will be shown in Sect. 4.6.1

4.5 Numerical techniques

Before going further, we briefly explain a few numerical techniques, which will be used in the numerical results shown in the following sections. For each problem we use a corresponding appropriate method from what we list here. The equation to solve is a kind of the self-consistent one and we solve it by an iterative manner with a given boundary condition. First we choose an initial condition and calculate the effective field from Eq. (4.4). Then we update all of the spin configuration by Eq. (4.3). We repeat to this procedure until achieving precision we want[4].

The boundary condition we use is the periodic boundary condition or the free boundary condition, which is given, respectively, as follows:

$$\begin{cases} \vec{M}_{l=N_z} = \vec{M}_{l=0} & \text{periodic boundary condition,} \\ \vec{M}_{l=N_z} = \vec{M}_{l=-1} = 0 & \text{free boundary condition.} \end{cases} \quad (4.58)$$

In both cases, there are N_z spins in the system. The boundary conditions are used to calculate the effective field. In the updating process, we sometimes impose a condition to fix the soliton position at the site l_{s}. For this condition, we choose two methods. One update fixes the direction of the in-plane component of $\vec{M}_{l=l_{\mathrm{s}}}$:

$$\vec{M}_{l_{\mathrm{s}}} = (-|H_{l_{\mathrm{s}}}^{\mathrm{eff},xy}|, 0, H_{l_{\mathrm{s}}}^{\mathrm{eff},z})/|H_{l_{\mathrm{s}}}^{\mathrm{eff}}| \text{ with } |H_{l_{\mathrm{s}}}^{\mathrm{eff},xy}| = \sqrt{\left(H_{l_{\mathrm{s}}}^{\mathrm{eff},x}\right)^2 + \left(H_{l_{\mathrm{s}}}^{\mathrm{eff},y}\right)^2} \quad (4.59)$$

[4]Our convergence condition is $\max_l |\Delta\vec{M}_l| < 5.0 \times 10^{-15}$ with the change of the moment at site l after one iteration, $\Delta\vec{M}_l$, except for the case of calculating the phase diagram. In this case, the condition is $\max_l |\Delta\vec{M}_l| < 1.0 \times 10^{-18}$, and $\Delta\vec{M}_l$ is the change after 1000 iterations.

for $H^x_{\rm ex} > 0$, and the other update completely fixes the direction of $\vec{M}_{l=l_{\rm s}}$:

$$\vec{M}_{l_{\rm s}} = (M^{x,*}_{l_{\rm s}}, 0, M^{z,*}_{l_{\rm s}}) \equiv \vec{M}^*_{l_{\rm s}} \text{ with } (M^{x,*}_{l_{\rm s}})^2 + (M^{z,*}_{l_{\rm s}})^2 = 1, \tag{4.60}$$

where $\vec{M}^*_l$ is a given vector to fix the direction of the moment at the soliton center. In contrast to Eq. (4.60), Eq. (4.59) imposes the condition that the x-component is non-positive and does not fix the direction of the moment. Note that the solutions obtained under these constraints are not guaranteed to be stable when we do not impose the constraints. In other words, we can discuss also a solution which is stable in the restricted configuration space but unstable in the whole configuration space.

We also mention how to choose initial configurations. There are a lot of solutions which are stable against all the local and small perturbations when it is related to the nucleation-type phase transition[5]. The different solutions are characterized by different topological indices, although such a stability is lost in some region, for example near the instability-type phase transition. This requires us to compare the energy (or free energy) between solutions with different topological indices. We define the following quantity with the parametrization $\vec{M}_l = (\cos\varphi_l \sin\theta_l, \sin\varphi \sin\theta_l, \cos\theta_l)$:

$$w = \frac{1}{2\pi}\sum_l (\varphi_{l+1} - \varphi_l) \text{ where } -\pi < \varphi_{l+1} - \varphi_l \le \pi, \tag{4.61}$$

which is a topological index of this system under the periodic boundary condition. We can easily imagine that the winding number stands for how many times in-plane spins rotate about the helical axis in the spin space along the chain direction. For the solution with a specified winding number, we choose the simple state in which spins rotate with a constant angle as initial states:

$$\vec{M}_l = (\cos\varphi_l, \sin\varphi_l, 0) \text{ with } \varphi_l = 2\pi w l/N_z. \tag{4.62}$$

When the field is applied to the perpendicular direction, this single-harmonic state evolves into a state with its higher harmonics but the winding number does not change. Note that this does not necessarily hold. For a field particularly in the region of the phase diagram where κa is pure imaginary, a state with a winding number far from $w_0 = (2\pi)^{-1} N_z \tan^{-1}(D/J_\parallel)$ may change its winding number to an integer value closer to w_0. As another case, consider a state with $w = 1$ when the perpendicular component of the magnetic field is not very weak. This state is well localized in sufficiently large systems, and it is very different from the initial sinusoidal state depending on the system size. When the difference is extremely large, the sinusoidal state

[5]These many stable states in this sense do not necessarily lead to the thermodynamic discontinuous phase transition. In the thermodynamic limit, all physical quantities show continuous changes except at the thermodynamic discontinuous phase transition. The metastable states with respect to the Hessian with positive eigenvalues can be distinguished from the thermodynamic metastable states, which is related to the thermodynamic discontinuous phase transition. Here we call them solutions to distinguish them from the thermodynamic metastable states.

with winding number $w = 1$ does not evolve into a soliton state. In this case, we need to choose a trial single soliton solution in a different way. One possibility is

$$\varphi_l = \pi[1 + \tanh(l/\Delta l)], \tag{4.63}$$

or under the periodic boundary condition

$$\varphi_l = \pi\{2 + \tanh(l/\Delta l) + \tanh[(l - N_z + 1)/\Delta l]\}. \tag{4.64}$$

Here Δl denotes the width of soliton and is taken as, for example of order 50. This trial state can be generalized to an initial state with $N_{\rm s}$ solitons with or without the surface configuration which contributes to non-integer part of w when it exists. On the other hand, the number of solitons $N_{\rm s}$ is the same as the integer part of w.

Once we construct a localized solution at some value of field, then for close values of field we may adopt this solution as an initial condition, which facilitates calculation. We also use the initial condition

$$\vec{M}_l = (M^x_{\rm u} \cos\varphi_l, M^x_{\rm u} \sin\varphi_l, M^z_{\rm u}) \text{ with } \varphi_l = 2\pi w l/N_z, \tag{4.65}$$

in a large parallel field under the periodic boundary condition. We have adopted $\vec{M}_{\rm u}$ for the coefficients as an example.

4.6 Phase diagram

The numerical results in this section are obtained for $N_z = 4000$ unless explicitly remarked. Figure 4.3 shows the phase diagram for the set of the realistic parameters of $Cr_{1/3}NbS_2$. The horizontal axis is the perpendicular field, $H^x_{\rm ex}/H_{\rm d}$, while the left vertical axis is the parallel field, $H^z_{\rm ex}/H_{\rm d}$. Here $H_{\rm d} = 2[(J_\parallel^2 + D^2)^{1/2} - J_\parallel]$. The phase boundaries are represented with several symbols corresponding to the types of phase transition. In addition, we show $1 - |\vec{M}|$ with the uniform magnetization $\vec{M} = \sum_l \vec{M}_l/N_z$ as the limit from the low-field side to the phase boundary by the symbol of inverted triangles, which helps us to understand where discontinuous phase transitions occur. The values are indicated on the right vertical axis. The two solid rhombuses on the phase boundary are the multicritical points. One is the tricritical point labeled T and the other is the multicritical point labeled M, which are respectively referred to as TC1 and TC2 in Ref. [86]. Here point TC1 is a tricritical point in the sense that the point is determined by $a_2 = 0$ and $a_4 = 0$ with the coefficients of ξ^2 and ξ^4 in the Landau energy. On the other hand, we call TC2 the multicritical point following the Schaub and Mukamel's study[101]. They suggested that the multicritical point at which the nucleation-type phase transition line and discontinuous phase transition line meet is not a tricritical point, but is of different nature(, though the difference is not clear in Ref. [101]). Since we could not exclude this possibility, we do not identify the multicritical point as the tricritical point. We discuss one possible difference in Sect. 4.6.2.

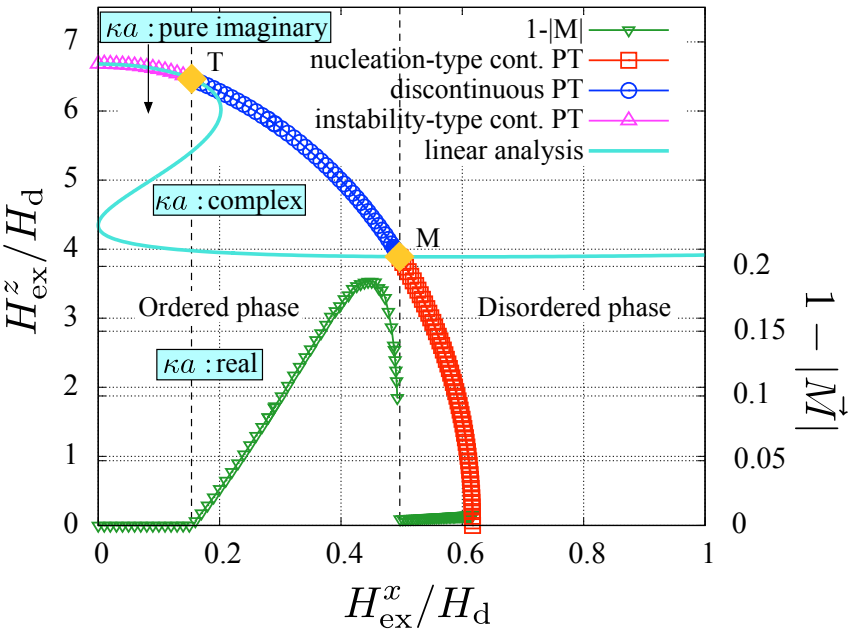

Figure 4.3: Phase diagram for realistic parameters: $D/J_{\parallel} = 0.16$ and $K/H_{\rm d} = 5.68$. Two points denoted by "T" and "M" are the tricritical point and the multicritical point, respectively, and separate the phase boundary into three segments: nucleation-type continuous phase transition line, the discontinuous phase transition line, and the instability-type continuous phase transition line denoted by red squares, blue circles, and pink triangles, respectively. The light-blue solid line labeled "linear analysis" is the crossover line obtained by the linear analysis, discussed in Sect. 4.3. In addition, we plot a quantity $1 - |\vec{M}|$ defined in the text, which is denoted by green inverted-triangles and the values are indicated on the right vertical axis.

Figures 4.4(a) and (b) are the magnified images of Fig. 4.3 around these points. The solid line colored with light blue separates three regions with different character of κa, and this is determined by the linear analysis in Sect. 4.3.

4.6.1 Tricritical point

First we consider the tricritical point, T ($\vec{H}_{\rm tri}$), and the phase boundary of continuous phase transition ($H_{\rm ex}^x < H_{\rm tri}^x$). Numerically obtained this phase boundary is consistent with the analytical line based on the instability-type phase transition. Thus we conclude that the phase transition in this region is the instability-type continuous one which can be described by the Landau theory of the helical order. The tricritical point appears when the coefficients of the second

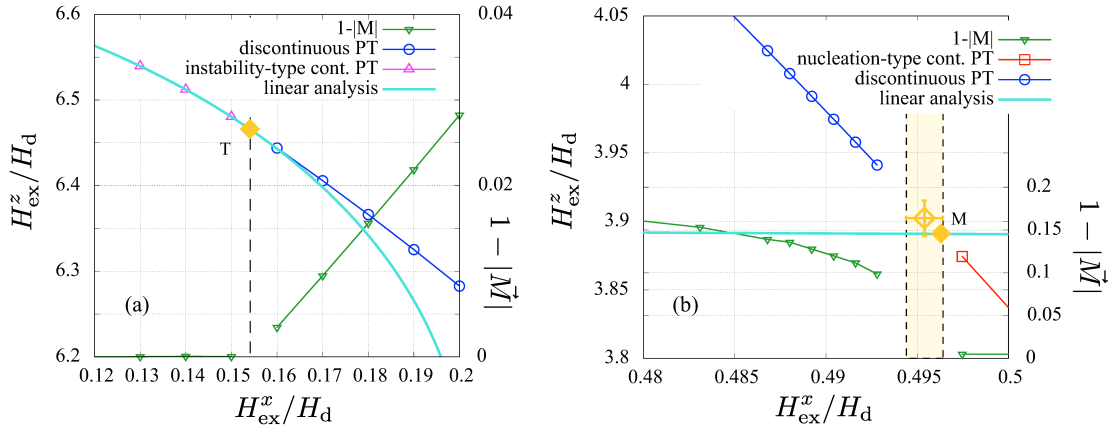

Figure 4.4: Magnified phase diagrams around (a) the tricritical point and (b) the multicritical point. The open rhombus in the panel (b) is a multicritical point with error bars estimated by the curve fitting.

and fourth order terms of the order parameter in the Landau energy both become zero, and the analysis in the last section gives its position $(H^x_{\rm tri}, H^z_{\rm tri}) = (0.003920828, 0.164476007)J_\parallel = (0.1541313188, 6.465703164)H_{\rm d}$. This result is in good agreement with the numerical calculation as shown in Fig 4.4(a); The quantity $1-|\vec{M}|$ stays zero on the instability-type transition line and becomes finite on the line being the other side of the tricritical point. The discontinuous transition line near the tricritical point can be described by taking account of the sixth order term of the Landau expansion but we do not go further. Instead we make a remark on the discontinuity; Figure 4.4(a) shows that it depends linearly on $H^x_{\rm c} - H^x_{\rm tri}$ with the x-component of discontinuous transition field $H^x_{\rm c}$. We assume that the coefficient of ξ^6 in the Landau expansion $a_6 > 0$, and a_4 changes its sign at the tricritical point along the phase boundary as $\bar{a}_4(H^x_{\rm tri} - H^x_{\rm c})/H^x_{\rm tri}$ with $\bar{a}_4 > 0$. The discontinuity of ξ^2 is given by $-a_4/(2a_6) = [\bar{a}_4/(2a_6)](H^x_{\rm c} - H^x_{\rm tri})/H^x_{\rm tri}$. The leading order of the total magnetization in ξ is calculated from the expansion forms (4.22)–(4.24) and M^z_c as follows:

$$\vec{M} = \frac{1}{N_z}\sum_l \vec{M}_l \simeq (M^x_c, 0, M^z_c) \to |\vec{M}| \approx 1 + (M_{\rm u,\perp}\alpha + M_{\rm u,\parallel}\alpha_z)\xi^2,$$
$$\to 1 - |\vec{M}| \approx \frac{M^2_{\rm u,\parallel} + M^2_{\rm u,\perp}\sigma^2_x}{4M^2_{\rm u,\parallel}}\xi^2 \approx \frac{M^2_{\rm u,\parallel} + M^2_{\rm u,\perp}\sigma^2_x}{4M^2_{\rm u,\parallel}}\frac{\bar{a}_4}{2a_6}\frac{H^x_{\rm c} - H^x_{\rm tri}}{H^x_{\rm tri}}. \tag{4.66}$$

We thus obtain the linear dependence of $1-|\vec{M}|$.

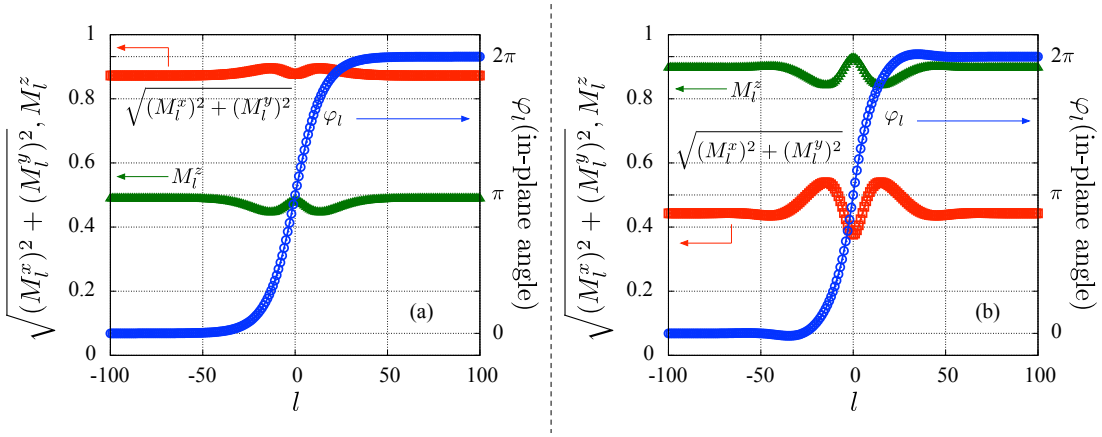

Figure 4.5: Typical spin structures of isolated solitons. In both panels, red squares, green triangles, and blue circles with lines stand for the in-plane spin amplitude ($= \sqrt{(M_l^x)^2 + M_l^y)^2}$), M_l^z, and in-plane angle ($= \tan^{-1}(M_l^y, M_l^x)$). The left panel (a) shows them for the field in the repulsive region of the phase diagram, $\vec{H}_{\rm ex} = (0.4, 0.0, 3.0)H_{\rm d}$, while the right panel (b) for the field in the attractive region $\vec{H}_{\rm ex} = (0.3, 0.0, 5.7)H_{\rm d}$.

4.6.2 Multicritical point

Next we see how we can understand the multicritical point, M. The phase boundary crosses the crossover line obtained using the linear analysis at M in Fig. 4.3. The crossover line is defined by the null discriminant, and separates the phase diagram into three regions on the basis of the types of κa. For a complex κa, the tail of an isolated soliton decays with oscillation. For a real κa, the tail exponentially decays without oscillation.

We confirm these for each representative in Fig. 4.5. The left (a) and right (b) panels show the spin structures of the isolated solitons for real and complex κa, respectively. The field values are shown in the caption. The isolated soliton solutions are obtained with the periodic boundary condition for sufficiently large systems, and here we set N_z = 2000. We impose an additional condition for the in-plane angle $\varphi_{l=0} = \pi$ to fix the soliton position. In-plane amplitude in the left panel shows a small dip at the soliton center and increases with distance, then finally approaches the asymptotic value from above. On the other hand, the right panel apparently shows that the asymptotic value is approached from below. Precisely speaking, the amplitude has damped oscillation and hence has local maxima and minima after the obvious local minimum near $l_{\rm s} = 50$. Whether an isolated soliton has an oscillating structure or not can be seen more easily in the in-plane angle. In the left panel, the angle increases monotonically, while not in the right panel. We show the oscillation structure appearing in the in-plane amplitude and angle in Fig. 4.6(b). They are shown as the absolute values of the deviation from the asymptotic values. For comparison, we show those for a real κa in Fig. 4.6(a). For these spin configurations, then we see the interaction energy of two isolated solitons. To eliminate the

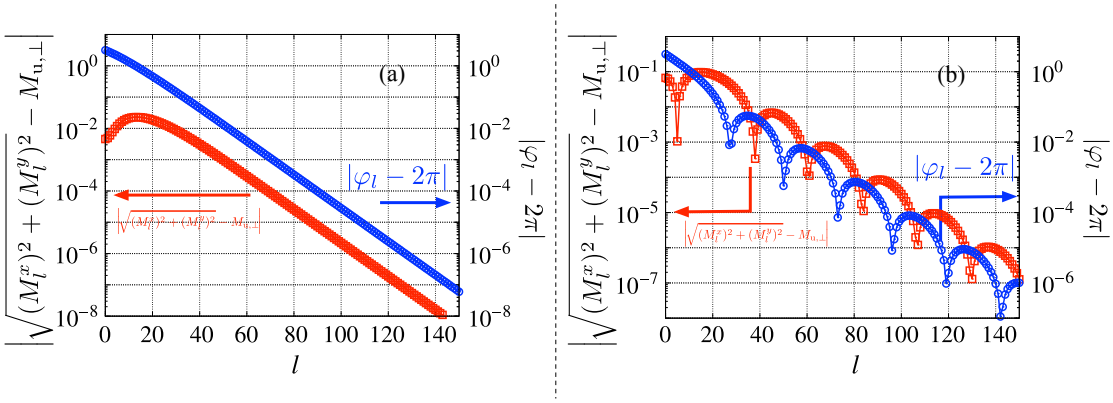

Figure 4.6: Deviations of in-plane amplitude (red squares, left axis) and phase (blue circles, right axis) from the asymptotic values in log scale for (a) real κa and (b) complex κa. Parameters are the same as in Fig. 4.5.

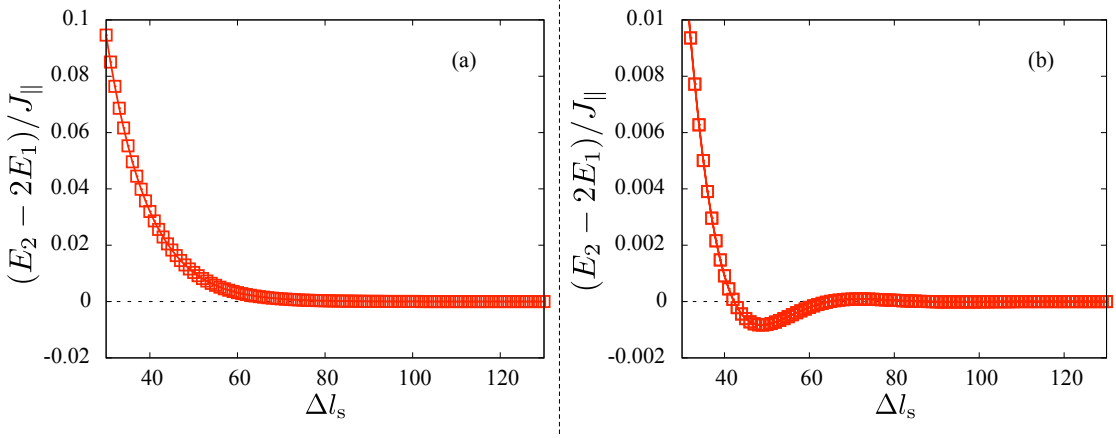

Figure 4.7: Interaction energy of two solitons as a function of inter-soliton distance Δl_s, which is the variable of horizontal axes. Each vertical axis is the two soliton energy measured from $2E_1$ with the single soliton energy E_1, and the unit of the energy is the intra-chain exchange coupling. The values of the field are the same as those in Fig. 4.5. The detail including the definition of energy is described in the text.

system size dependence, we measure the energy of w soliton (winding) state from the energy of the uniform state with the moment $\vec{M}_l = \vec{M}_{\rm u}$:

$$E_w = E - E_{\rm uni} \text{ with } E_{\rm uni} = -N_z(J_\parallel|\vec{M}_{\rm u}|^2 + \vec{H}_{\rm ex}\cdot\vec{M}_{\rm u} - K(M^z_{\rm u})^2/2). \tag{4.67}$$

Then we obtain the interaction energy of two isolated solitons as

$$E_{\rm int}(\Delta l_{\rm s}) = E_2(\Delta l_{\rm s}) - 2E_1, \tag{4.68}$$

which is a function of the distance between the two solitons, $\Delta l_{\rm s}$, and we explicitly show the argument. We again use the periodic boundary condition and impose the two soliton conditions. In this case, we set N_z to 500, which is sufficiently large for the interaction potential to decay well, as seen in Figs. 4.7(a) and (b). The values of the magnetic field for (a) and (b) are the same as in Figs. 4.5(a) and (b), respectively. Figure 4.7(a) shows that the interaction is repulsive, namely the energy becomes lower as the inter-soliton distance increases. From this, we can understand the nucleation-type continuous phase transition through the following emergent-particle picture: When the field is lower than the value at $E_1 = 0$, adding solitons into the system lowers the energy owing to negative single soliton energy, which contrasts with the positive interaction energy. Their competition determines the number of solitons in the system. The condition can be approximated as $E_1 + E_{\rm int}(\Delta l_{\rm s} = N_z/w) = 0$ under the periodic boundary condition, where we can neglect more than two body interactions near the phase boundary. The negative E_1 approaches zero with the increasing field, and finally $w = 1$ is achieved and the critical field is given by the condition $E_1 = 0$. In the thermodynamic limit, the winding number density defined by $\bar{w} = \lim_{N_z\to\infty} w/N_z$ changes from $(2\pi)^{-1}\tan^{-1} D/J_\parallel$ to 0 continuously. For a fixed $H^z_{\rm ex}$, we explain the diverging behavior of the period at $H^x_{\rm ex} \lesssim H^x_{\rm c}$. First we approximate the single soliton energy and the interaction energy as

$$E_1 = \epsilon_1(H^x_{\rm ex} - H^x_{\rm c})/H_{\rm c},\ E_{\rm int} = \epsilon_{\rm int}e^{-\kappa\Delta l_{\rm s}}. \tag{4.69}$$

Consider the balance condition of these two energies and obtain a finite inter-soliton distance, i.e. a period of the soliton lattice for $H^x_{\rm ex} < H^x_{\rm c}$:

$$\Delta l_{\rm s} = \frac{1}{\kappa}\ln\left(\frac{\epsilon_{\rm int}}{\epsilon_1}\frac{H^x_{\rm c}}{H^x_{\rm c} - H^x_{\rm ex}}\right). \tag{4.70}$$

This logarithmic divergence is consistent with the result of chiral sine-Gordon model Eq. (2.99) in Sect. 2.4.

On the other hand, the right panel is more complex; the interaction potential steeply decays as well, but with oscillation which comes from the oscillation of each soliton profile. As a consequence, the interaction energy has local minima, and the global minimum point is around $\Delta l_{\rm s} = 50$. How does this change the above mechanism? Again we consider a field smaller than the field giving $E_1 = 0$. The inter-soliton distance is determined from the competition between the negative single soliton energy and the repulsive interaction for close distances. As

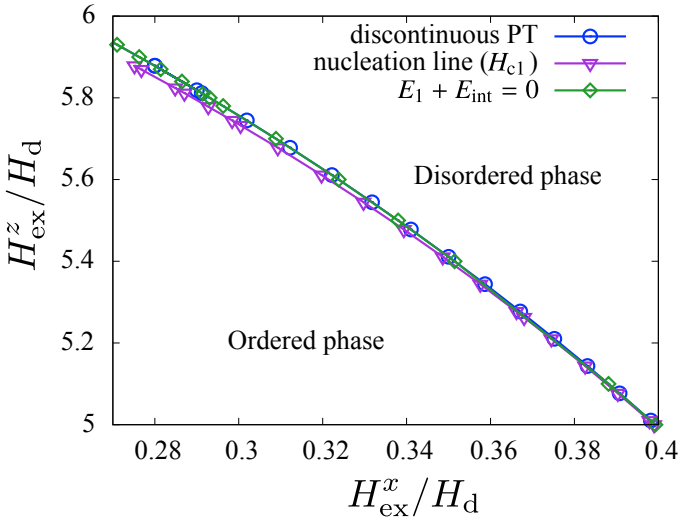

Figure 4.8: Phase boundary of discontinuous phase transitions. Blue circles, purple inverted-triangles, and green rhombuses represent the discontinuous phase transition line, nucleation line $\vec{H}_{c1}$, and the line determined by the condition that $E_1 + E_{int}(\Delta l_{s,min}) = 0$. See the text for their definitions.

the field increases, the single soliton energy goes to zero from below. When $E_1 = 0$, the total energy is the same as the condensation energy of multiple solitons, and takes the minimum at the finite inter-soliton distance. This distance is approximated by the point which gives the minimum of interaction energy of two solitons, $\Delta l_{s,min}$, depending on $\vec{H}_{ex}$: if $\vec{H}_{ex}$ is close to $\vec{H}_{multi}$, the distance goes to infinity. The total energy takes the minimum for the finite distance, which means that the periodic structure of multiple solitons is favored rather than the single soliton state. This is the soliton lattice state. The single soliton energy becomes positive as the field increases further. This energy competes with the negative interaction energy and gives an optimal inter-soliton distance. One finds that the field at which the energy of the soliton lattice becomes the same as for the uniform state. This is the thermodynamic discontinuous phase transition point. We consider only the two body interaction, i.e., the global minimum of the interaction potential, to simplify this picture[6], and calculate the magnetic field such that $E_1 + E_{int}(\Delta l_{s,min}) = 0$. The line of this magnetic field is shown in Fig. 4.8 with green rhombuses. In Fig. 4.8, we also show the discontinuous phase transition line (blue circles) and the nucleation line $\vec{H}_{c1}$ (purple inverted-triangles), defined by $E_1 = 0$. The nucleation line underestimates the phase boundary of the discontinuous phase transition and is in the ordered state, while it is the phase boundary when the phase transition is the continuous one of the nucleation-type. In contrast to H_{c1}, the curves designated with green rhombuses agrees quite well, and thus the emergent particle picture is effective.

Now we know theoretically that the sign of the interaction between solitons determines whether the phase transition is continuous one of nucleation-type or discontinuous one. According to the numerical results shown in Fig. 4.4(b), the crossover line obtained by the linear analysis crosses the phase boundary between the two end points, the blue circle and the red square, and thus the calculated data are consistent with the linear analysis. The linear analysis

[6]Interaction potential decays fast and the other local minimum hardly contributes.

parameters	values	errors	parameters	values	errors
$H^x_{\rm multi}/H_{\rm d}$	0.495396	0.001010	$H^z_{\rm multi}/H_{\rm d}$	3.90238	0.01287
f_x	468.162	164.4	f_z	215.505	49.76
e_x	0.321416	0.04625	e_z	0.334825	0.04636

Table 4.1: Fitting parameters.

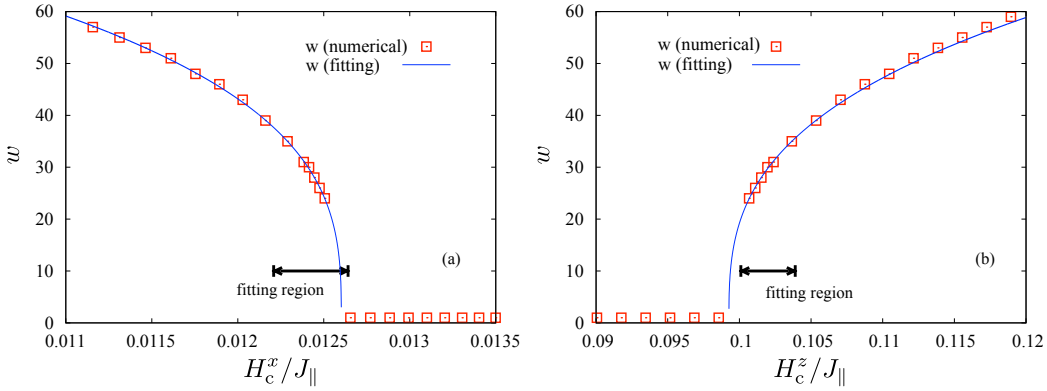

Figure 4.9: Curves obtained through the fitting method. The black arrows represent the region where we use the curve fitting.

is helpful in determining the multicritical point with high accuracy. The multicritical point is a critical point at which the sign of the soliton interaction changes. Since the phase boundary of the nucleation-type continuous phase transition is the same as the nucleation line, we can identify the multicritical point as the crossing point of the nucleation line and the line obtained by the linear analysis. The nucleation line can be calculated much more easily than the discontinuous phase transition line. Its value is $(H^x_{\rm multi}, H^z_{\rm multi}) \simeq (0.49632895, 3.8909051)H_{\rm d}$.

The multicritical point can be evaluated also using the numerical data about the discontinuous jump in the winding number, w, at the discontinuous transition. We perform curve fitting with a function $w = f_\mu[(H^\mu_{\rm c} - H^\mu_{\rm multi})/J_\parallel]^{e_\mu} (\mu = x, z)$ along the phase boundary $(H^x_{\rm c}, H^z_{\rm c})$, where f_μ, $H^\mu_{\rm multi}$, and e_μ are fitting parameters. Here e_μ is a critical exponent of the discontinuity w of the discontinuous phase transition around the multicritical point. We obtain the fitting parameters, as shown in Table 4.1, and the obtained fitting curve agrees with the raw data as shown in Fig. 4.9. As seen from both Table 4.1 and Fig. 4.4(b), the point obtained by the fitting method is consistent with the calculated multicritical point within the error-bars.

The critical behavior of $1 - |\vec{M}|$ near the multicritical point M is not linear. Because an inter-soliton distance $\Delta l_{\rm s}$ is large, we can expect that $1 - |\vec{M}| \approx w|\Delta\vec{M}|$, where $\Delta\vec{M} = N_z^{-1}\sum_l(\vec{M}_{\rm u} - \vec{M}_l)$ with a single soliton profile $\vec{M}_l$.[7] The magnetization reduction owing to a

[7]The expectation can be valid since the inter-soliton distance diverges as M is approached. Even in our

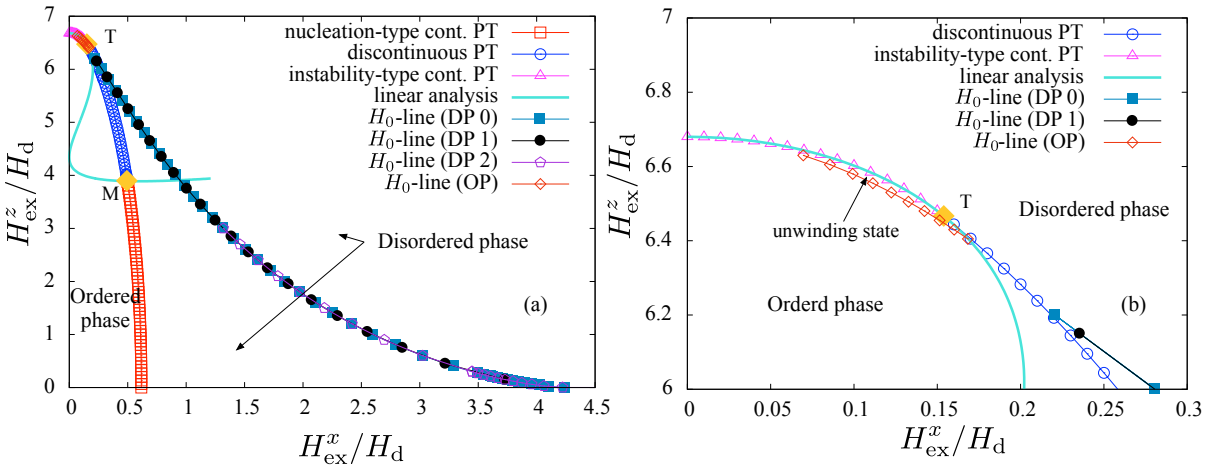

Figure 4.10: (a) H_0 line shown in the whole phase diagram and (b) its magnified image around the instability-type phase transition. The same symbols are used as in Fig. 4.3 for the phase boundaries, critical points, and the line obtained by the linear analysis. The H_0 lines are plotted from the several aspects. Here DP (OP) stands for the disordered (ordered) phase. See the text for the difference between DP 0, DP 1, and DP 2.

single soliton, $\Delta\vec{M}$ does not change from that at M, and thus the behavior may be almost the same as that of w, i.e.,

$$1 - |\vec{M}| \propto \left| \frac{H^\mu_{\rm c} - H^\mu_{\rm multi}}{H^\mu_{\rm multi}} \right|^{e_\mu} \quad \text{for } \mu = x, z. \tag{4.71}$$

We remark that the errors in $f_\mu(\mu = x, z)$ are large, and there are two possibilities to improve this: perform further calculations near M and/or prepare another function to describe the critical behavior rather than power law. However the critical behavior is different from the linear one, and in that sense, M is different from T.

4.6.3 H_0 line

Finally we discuss H_0 lines in the ordered and disordered phases. They are defined as follows: In the ordered phase, the line is the boundary where the x-components of the most stable state become non-negative[8], i.e., the winding number is zero for $H > H_0$[101]. In the disordered phase, we define the H_0 line by the limit of the metastability of an isolated soliton, i.e., an isolated soliton no longer exists in the high field side of this line. We remark that the necessary

calculated data, solitons are separated from each other: $120 \lesssim \Delta l_{\rm s} \lesssim 200$ are used for the curve fitting, while the size of a single soliton is about 50.

[8]for all l, $M^x_l \geq 0$

condition for existence of an isolated soliton is that $\mathrm{Re}(\kappa a) > 0$, and the H_0 line marks the territory of the soliton in the high field side. The low field boundary is qualitatively given by the crossover line separating the regions of complex κa and pure imaginary κa. However, the assumption of small amplitude $\vec{A}$ is not valid in the ordered phase, and the line determined by the linear analysis shifts to slightly lower $H^x_{\rm ex}$ side than the actual one. We call the instability at this line the inflation instability and will discuss this in Sect. 4.8.3.

The H_0 line in the disordered phase was originally considered for skyrmions in a two-dimensional chiral ferromagnetic system by Leonov *et al.*[137]. This line gives the upper bound of the field for possible observation of the remnant solitons. Numerically the H_0 line is obtained by seeking for the field between the highest field at which an isolated soliton can be constructed and the lowest field at which an isolated soliton can not be constructed; In the latter case, the initial profile of an isolated soliton goes to the uniform state. We seek for the field corresponding to H_0 using the bisection method. We use the previous isolated soliton solution as an initial condition in this seeking process.

The instability of an isolated soliton has three origins: (i) The first one is the spin motion towards the helical axis. The soliton can be unwound via the zero in-plane amplitude state. The method to seek for the H_0 line in this origin is discussed in detail later. (ii) The second one is that, when the temperature is finite, thermal fluctuations reduce the moment locally, which unwinds the soliton through vanishing moment at the soliton center. This was originally discussed for skyrmion unwinding, and the H_0 line was introduced for that system[137]. (iii) The third origin is specific to the lattice model; At sufficiently large field, the width of the soliton becomes narrow. No matter how narrow the soliton is, it can exist in the continuum model. In the lattice model, however, an extremely narrow soliton with the width shorter than the lattice constant is neither stable nor well defined. In the present case of zero temperature and small D, we will see that the origin (i) is dominant. Thus we study the H_0 line from this viewpoint.

First of all, the whole structure of the H_0 line in the phase diagram is shown in Fig. 4.10(a). The H_0 line can be calculated in several ways, though they are consistent with each other. Figure 4.10(b) shows a magnified figure of the H_0 line in the ordered phase. The H_0 line in the ordered phase actually terminates at $\vec{H}_{\rm c} = (0, 0, H^z_c)$: the critical field for the z-direction, although that part is not shown in the figure. There are non-uniform but unwinding states in the region between the H_0 line and the phase boundary. All of the M^x_l's are positive in this region and the winding number is always zero; The in-plane angle is bounded between $-\pi/2$ and $\pi/2$. This means that the order near the instability-type-phase boundary is the helical state rather than the soliton lattice state.

Now let us go to the H_0 line in the disordered phase, which is labeled "H_0-line (DP)" in Fig. 4.10. In the disordered phase and the outside of the limit of metastability of the ordered phase, there is no unwinding-helical state, and we consider the instability field of an isolated soliton, which is the H_0 line in the disordered phase. Note that an isolated soliton can exist as a metastable state in the disordered phase below the H_0 line. As we mentioned, there are several ways to calculate the H_0 line in the disordered state. A simple way is to seek the field where an

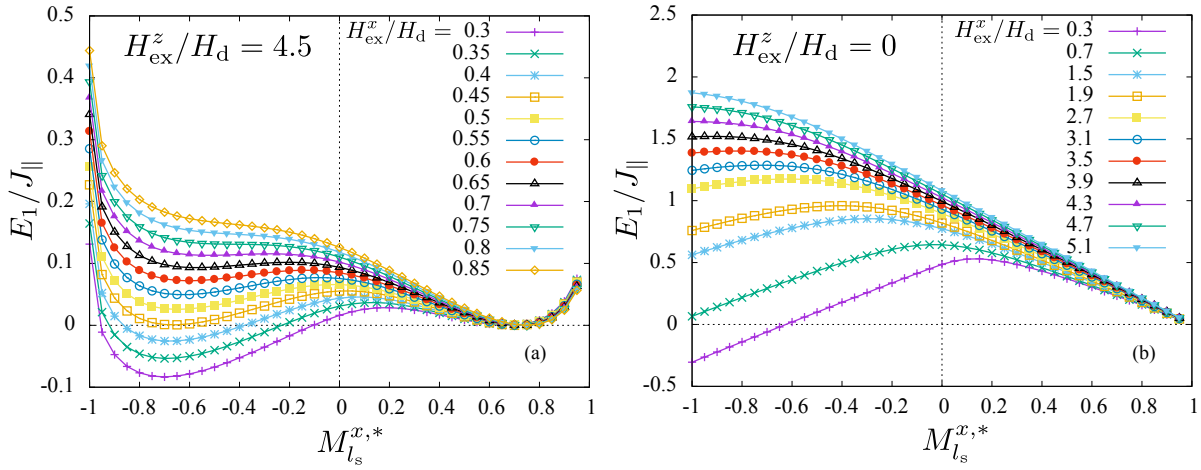

Figure 4.11: Energy landscapes for $M^{x,*}_{l_{\rm s}}$. The parallel field, $H^z_{\rm ex}$ is set to (a) $4.5H_{\rm d}$ and (b) 0.

isolated soliton disappears by increase of the magnetic field. In this case, for the lattice model, there are two choices regarding whether the soliton center is on a site or between sites. We call the former "direct search 1" and the latter "direct search 2". If the soliton is very narrow, the latter case is more stable just because one more spin has a negative x-component compared with the former case. In Fig. 4.10(a), we have labeled the former one "H_0-line (DP 1)" and the latter one "H_0-line (DP 2)", where DP stands for the disordered phase. From the figure, these two choices are basically the same. The agreement of DP1 and DP2 suggests that the origin of the instability is related to the out-of-plane motion mentioned above rather than the narrowing width. The configuration of an isolated soliton has a negative value M^x_l at $l = l_{\rm s}$, i.e. the soliton center. The condition for a stable soliton is that its total energy should be minimized for some value $M^x_l < 0$ at least locally. Since we have checked that the soliton center position or not is not important, we let $M^y_{l=l_{\rm s}} = 0$. Now the problem is the variation of the energy with respect to one parameter, $M^x_{l=l_{\rm s}}$, as $M^z_{l=l_{\rm s}}$ is related to $M^x_{l=l_{\rm s}}$ by the normalization condition. In numerical calculations, we repeat iteration with fixing $M^x_{l_{\rm s}}$ to a specified value $M^{x,*}_{l_{\rm s}}$ in the update of the variables. We call this scheme "variational search". Let us see examples. Figure 4.11(a) shows the energy landscape as a function of $M^{x,*}_{l=l_{\rm s}}$ for $H^z_{\rm ex}/H_{\rm d} = 4.5$, and the different curves correspond to the different values of $H^x_{\rm ex}/H_{\rm d}$. We find two local minima for low $H^x_{\rm ex}$: one is for positive $M^{x,*}_{l_{\rm s}}$ and the other for negative $M^{x,*}_{l_{\rm s}}$. The local minimum in the positive side corresponds to the uniform state. This value of $M^{x,*}_{l_{\rm s}}$ is equivalent to $M^x_{\rm u}$ and the energy is actually zero. Note that we measure the energy from that of the uniform state. The local minimum in the negative side corresponds to an isolated soliton solution. We also find that at higher $H^x_{\rm ex}$ the local minimum disappears in the negative side, which means there is no stable isolated soliton. This disappearance of the local minimum determines the instability field H_0: $\partial E_1/\partial M^{x,*}_{l_{\rm s}} = 0$ and $\partial^2 E_1/\partial (M^{x,*}_{l_{\rm s}})^2 = 0$. The H_0 line thus obtained is referred to as "H_0-line (DP 0)" and it is marked by solid squares in Fig. 4.10(a). This line overlaps with the

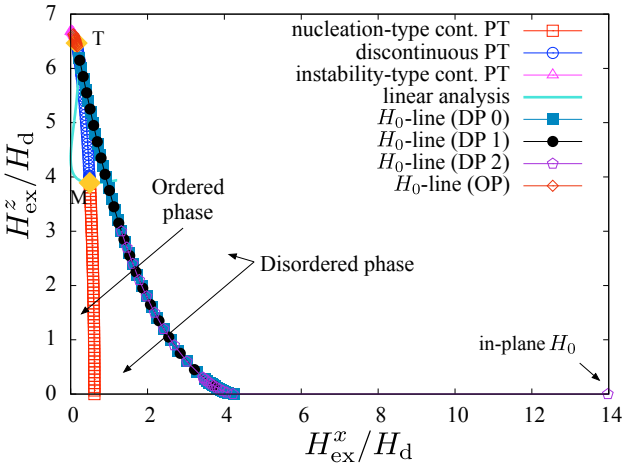

Figure 4.12: Instability field concerning the soliton size marked by the open pentagon. The value of "in-plane H_0" is around $14H_{\rm d}$. This H_0^x obtained using the direct search 2 is high because the out-of-plane component of spin is not taken into account.

lines obtained by direct searches, and the origin of the soliton instability of an isolated soliton is confirmed. Namely the increasing field destabilizes a soliton with negative $M^x_{l_{\rm s}}$ and changes it to the uniform state.

Interestingly, when $H^z_{\rm ex} = 0$ as shown in Fig. 4.12, the direct search 2 gives pretty high value of H_0^x,[9] which is different from its limiting value at $H^z_{\rm ex} = 0$. The direct search for $H^z_{\rm ex} = 0$ restricts the spherical spin space to the xy-plane, and the soliton cannot unwind through pointing the moment to the z-direction at the soliton center. In this case, the increasing field squeezes the soliton width, which leads to the instability only in the lattice model. The rather high H_0 field is attributed to this mechanism, i.e. in-plane constraint. The lower value of H_0^x obtained by the variational search, is also indicated in the energy landscape for $H^z_{\rm ex} = 0$ shown in Fig. 4.11(b). The local minimum structure collapses at around $H^x_{\rm ex}/H_{\rm d} \simeq 4.3$, which is consistent with the limiting value from the finite $H^z_{\rm ex}$. For this realistic parameters of $Cr_{1/3}NbS_2$, this mechanism is dominant for the instability of an isolated soliton.

Let us consider which mechanism is more dominant for which case, since the instability of the narrow soliton is not forbidden in principle. If the spins are restricted in the plane, the motion to the out-of-plane is forbidden. This corresponds to the infinitely large anisotropy. On the other hand, the narrow soliton is only unstable in the lattice model. This means that the continuum limit ($D \to 0$ or $a \to 0$) never leads to the instability of the narrow soliton. From this brief consideration, the motion towards the helical axis is dominant instability for small D or K, while the narrowing width is dominant in the opposite case. Usually the information about the hard axis anisotropy K does not appear in the uniaxial chiral magnet with the perpendicular field and can be obtained by measuring the parallel critical field $(0, 0, H^z_{\rm c})$. However, if the H_0 field depends on K, this effect is important for determining anisotropy

[9] Direct search 1 basically gives the same value of H_0, since the soliton center shifts to the middle point of two neighboring sites, and thus it is equivalent to the direct search 2.

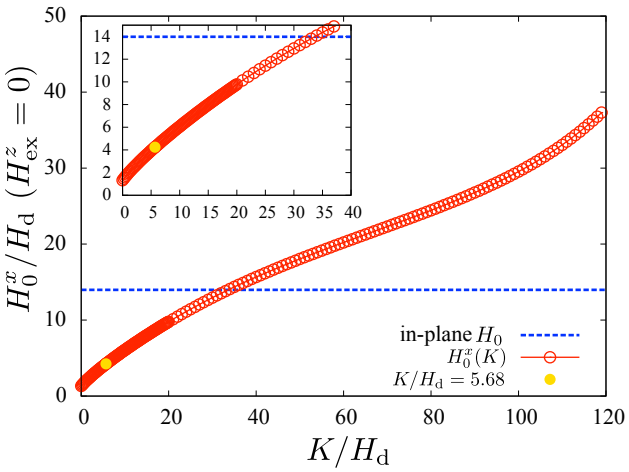

Figure 4.13: K dependence of H_0 for $H_{\rm ex}^z = 0$. Open circles are obtained using the variational search for the energy landscape as a function of $M_{l_{\rm s}}^{x,*}$. The blue dashed line is obtained by the direct search. This method is independent of the anisotropy. The solid circle is for the realistic value of the anisotropy of $Cr_{1/3}NbS_2$. We set $D = 0.16 J_{\parallel}$.

in experiment. To check this, we calculate the K dependence of H_0 using the variational search. Note that for $H_{\rm ex}^z = 0$, the variational search cannot access to the soliton narrowing instability, while the direct search cannot examine the instability of the spin z-component. The obtained result is shown in Fig. 4.13. For $D = 0.16 J_{\parallel}$, the instability mechanism changes at around $K/H_{\rm d} \sim 34$, since H_0 related to the hard axis motion becomes larger than the value of narrowing instability. It should be mentioned that the large anisotropy of $Cr_{1/3}NbS_2$ is $K/H_{\rm d} = 5.68$, which leads to ten times larger critical field in the direction parallel to the helical axis than that in the perpendicular direction. For larger D, the narrowing width instability is more feasible. $YbNi_3Al_9$ is a material with short range helical structure, which is probably caused by the next nearest exchange interaction in addition to the DMI. It should be interesting to examine which kind of instability is dominant for the helical structure with such a short period. The opposite limit is a continuum model such as the chiral sine-Gordon model, in which the instability of the narrow width of the soliton never occurs. Therefore we expect that the H_0 field obtained by the variational search describes the H_0 field of the chiral sine-Gordon model as well. We study this further in the next subsection.

4.6.4 H_0 field : chiral sine-Gordon model

We study the instability field of a soliton in the chiral sine-Gordon model given by

$$E = J_{\parallel} S^2 a \int {\rm d}z \left[\frac{1}{2} \left(\frac{{\rm d}\theta}{{\rm d}z} \right)^2 + \frac{1}{2} \sin^2\theta \left(\frac{{\rm d}\varphi}{{\rm d}z} \right)^2 - Q_0 \sin^2\theta \frac{{\rm d}\varphi}{{\rm d}z} \right.$$
$$\left. - m^2 \sin\theta\cos\varphi + \frac{\gamma^2}{2}\cos^2\theta \right]. \qquad (4.72)$$

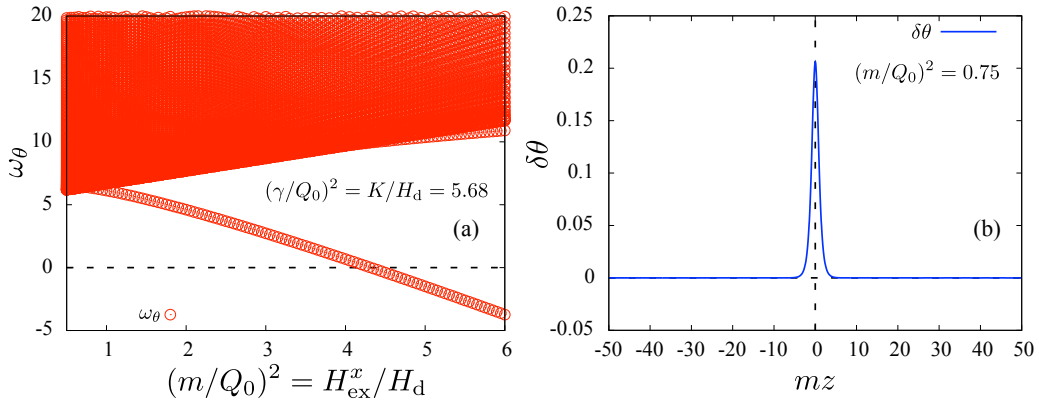

Figure 4.14: (a) $(m/Q_0)^2$ dependence of the excitation energies for the anisotropy $(\gamma/Q_0)^2 = 5.68$. (b) Bound state eigenfunction for $(m/Q_0)^2 = 0.75$.

Here θ and φ are the variables of the moment in polar coordinates. The model is basically the same as that introduced in Sect. 2.4: Q_0 and m^2 are the magnitude of the DMI and the magnetic field and related to the parameters of the lattice model as $Q_0 = D/(J_\parallel a)$ and $m^2 = H_\mathrm{ex}/(J_\parallel S a^2)$, respectively. The last term describes the hard axis anisotropy along the helical axis: $\gamma^2 = K/(J_\parallel S^2 a^2)$. Since the solutions are constructed with modulus κ as shown in Eq. (2.88) in Sect. 2.4, we can write down a single soliton solution by taking the limit $\kappa \to 1$. Note that $\mathrm{am}(u, \kappa \to 1) = 2\tan^{-1}(e^u) - \pi/2$, and $Q_0 > 0$. Using a constant of integral z_s denoting the soliton center position, we have

$$\varphi_0(z) = 4\tan^{-1}[e^{m(z-z_\mathrm{s})}] \tag{4.73}$$

for $\vec{M} = S(\cos\varphi, \sin\varphi, 0)$. We consider a small fluctuation around this solution: $\theta = \pi/2 + \delta\theta$ and $\varphi = \varphi_0 + \delta\varphi$. Here $\varphi_0 = 4\tan^{-1}(e^{mz})$ with $z_\mathrm{s} = 0$ without loss of generality. The energy functional is expanded up to second order in $\delta\theta$ and $\delta\varphi$ as follows:

$$E \approx E_0 + JS^2 a \int \mathrm{d}z \left\{ \frac{1}{2}\left(\frac{\mathrm{d}\delta\theta}{\mathrm{d}z}\right)^2 + \frac{1}{2}\left(\frac{\mathrm{d}\delta\varphi}{\mathrm{d}z}\right)^2 - \left[\frac{1}{2}\left(\frac{\mathrm{d}\varphi_0}{\mathrm{d}z}\right)^2 - Q_0\frac{\mathrm{d}\varphi_0}{\mathrm{d}z}\right]\delta\theta^2 + \frac{m^2}{2}\cos\varphi_0\left(\delta\varphi^2 + \delta\theta^2\right) + \frac{\gamma^2}{2}\delta\theta^2 \right\}, \tag{4.74}$$

$$E_0 = JS^2 a \int \mathrm{d}z \left[\frac{1}{2}\left(\frac{\mathrm{d}\varphi_0}{\mathrm{d}z}\right)^2 - Q_0\frac{\mathrm{d}\varphi_0}{\mathrm{d}z} - m^2\cos\varphi_0\right]. \tag{4.75}$$

By taking variations, we obtain the eigenequations for $\delta\theta$ and $\delta\varphi$:

$$\hat{\mathcal{L}}_\theta \delta\theta = \omega_\theta \delta\theta,\ \hat{\mathcal{L}}_\theta = -\frac{\mathrm{d}^2}{\mathrm{d}z^2} - \left[\left(\frac{\mathrm{d}\varphi_0}{\mathrm{d}z}\right)^2 - 2Q_0\frac{\mathrm{d}\varphi_0}{\mathrm{d}z} - m^2\cos\varphi_0 - \gamma^2\right], \tag{4.76}$$

$$\hat{\mathcal{L}}_\varphi \delta\varphi = \omega_\varphi \delta\varphi,\ \hat{\mathcal{L}}_\varphi = -\frac{\mathrm{d}^2}{\mathrm{d}z^2} + m^2\cos\varphi_0. \tag{4.77}$$

We can rewrite $\hat{\mathcal{L}}_\theta = -\mathrm{d}^2/\mathrm{d}z^2 - \Delta(z)$ with the spatially dependent potential

$$\Delta(z) = m^2\left(\frac{6}{\cosh^2 mz} - 1 - \frac{4Q_0}{m\cosh mz} - \frac{\gamma^2}{m^2}\right). \tag{4.78}$$

In the following, we calculate the lowest eigenvalue of $\delta\theta$-mode. Figure 4.14(a) shows that for low field, $\delta\theta$-mode has an energy gap, and increasing field closes the gap, which determine the instability field. One mode is separated from the continuum and the panel (b) shows that fluctuations of this mode are well localized around the soliton center. As shown in Eq. (4.78), the anisotropy γ^2 plays a role of the energy shift. In this case, it is easy to determine the instability anisotropy for the fixed magnetic field m. For convenience, let us consider the potential $\tilde{\Delta}(z) = \Delta(z) + \gamma^2$ and the eigenenergy $\tilde{\omega}(m)$ for the operator $-\mathrm{d}^2/\mathrm{d}z^2 - \tilde{\Delta}(z)$. Since the true eigenenergy is $\omega = \tilde{\omega}(m) + \gamma^2$, the instability anisotropy which satisfies the condition $\omega = 0$ is given as a function of $m_0 = [H_0/(J_\parallel S a^2)]^{1/2}$ by

$$\gamma_0^2 = -\tilde{\omega}(m_0) \leftrightarrow m_0 = \tilde{\omega}^{-1}(\gamma_0^2). \tag{4.79}$$

The anisotropy dependence of the instability field is shown in Fig. 4.15 by green inverted-triangles. We have added the instability fields of the lattice model for $D/J_\parallel = 0.32$, 0.16, and 0.08 for references. The instability fields determined by the in-plane constraint are shown by dashed lines. This instability is unique in lattice models. The panel (a) shows the instability fields for the smaller region, and the results for different D's are close to each other. Actually, while the continuum limit corresponds to the limit of $D \to 0$, its result is quite similar to that for $D = 0.08 J_\parallel$. The difference between the continuum limit and the lattice model becomes visible when the result obtained by the variational search becomes as high as that obtained with the in-plane constraint, as seen in Fig. 4.15(b). For both $D/J_\parallel = 0.32$ and 0.16, a peculiar increasing behavior, i.e. downward convex curve is observed and this may be caused by unphysical narrow soliton. Here we use the word unphysical because the field is higher than the H_0 determined by the in-plane constraint. For $K/H_\mathrm{d} < 120$, on the other hand, this increase cannot be seen for $D/J_\parallel = 0.08$ because H_0 determined by the in-plane constraint is rather high. In fact, this increase can be seen at around $K/H_\mathrm{d} \sim 450$.

We conclude that the K-dependence of H_0 has monotonic increase with upward convex if the instability field of the hard axis motion is lower than the narrowing width instability field, and otherwise, H_0 is independent of K since it is dominated by the narrowing width instability.

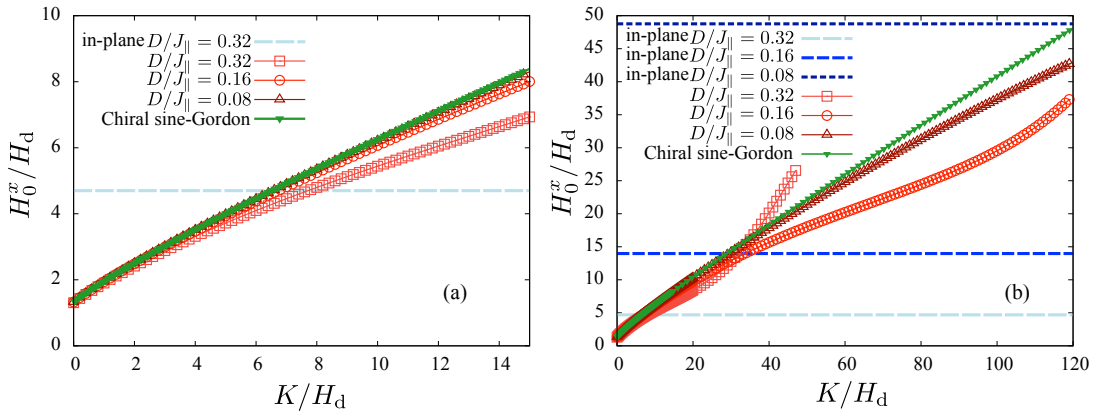

Figure 4.15: Instability field of an isolated soliton using chiral sine-Gordon model (green inverted-triangles). Red circles are the same as those in Fig. 4.13 with the in-plane instability field represented by the blue dashed line. For different values of DMI, the instability fields are shown by the different colors and symbols (see the legends). The left panel (a) is for the small anisotropy region, while the right panel (b) is for the larger region of the anisotropy, in which difference between the lattice model and continuum model is visible. Note that the normalization in the chiral sine-Gordon model is done using $H_\mathrm{d} = D^2/J_\parallel$. In the chiral sine-Gordon model, $H_\mathrm{ex}^x/H_\mathrm{d}$ and K/H_d are the parameters and there is no explicit D dependence.

4.7 Discussion on temperature effects

We briefly discuss the similarity and the difference in the phase structure between H_ex^x–H_ex^z and H_ex^x–T phase diagrams[101, 102, 138, 139]. Two phase diagrams share the case of $\vec{H}_\mathrm{ex} = (H_\mathrm{ex}^x, 0, 0)$ at $T = 0$ and let us discuss their similarity by considering the effects of either T or H_ex^z. The common feature is the softening of the in-plane amplitude $\sqrt{(M_l^x)^2 + (M_l^y)^2}$: The presence of the out-of-plane component in the tilted magnetic field is equivalent to the reduction of in-plane amplitude, and the reduction is also caused by the temperature effect.

We make a few remarks. Using the realistic material parameters of $Cr_{1/3}NbS_2$, the attractively interacting solitons appear in the very small region of the H_ex^x–T phase diagram, so that it may be impossible to observe an evidence of the thermodynamic discontinuous phase transition or even oscillation in spin profiles. Moreover temperature in that region is relatively high, and thus a question whether the thermal fluctuation changes the scenario or not may be brought about, which remains unclear as it stands[100]. In the tilted field case, the range where the softening effect can be visible is relatively large. Because it is zero temperature, there might be a question about the effect of the quantum fluctuation, but $Cr_{1/3}NbS_2$ has the spin length of 3/2. We may expect that the fluctuation effect is not essential. The tilted field configuration is experimentally promising in that the richness of the phase diagram can be observed in the wide region without affected by thermal or quantum fluctuations.

4.8 Surface barrier

In this section, we consider a surface barrier of chiral solitons and compare the results with hysteresis accompanied by a sharp jump in magneto-resistance observed in experiment for micrometer-sized samples[103, 104].

4.8.1 Hysteresis in nucleation-type phase transition

In many cases, hysteresis accompanies a thermodynamic discontinuous phase transition, and originates from the potential barrier of a metastable state towards the equilibrium state. As was explained in Sect. 4.1, micrometer-sized samples of $Cr_{1/3}NbS_2$ show a clear hysteresis and a sharp jump at a field called the jump field in magneto-resistance measurements[103, 104]. This jump field in decreasing field is highly reproducible in small samples at low temperatures and observed in a fairly wide region of the phase diagram. We will show that this region is consistent with the region where solitons exist rather than the region of the discontinuous phase transition. This hysteresis is not directly related to the bulk free energy, but to the metastable dynamics of solitons. Our purpose is to clarify the mechanisms of this hysteresis on the basis of solitons.

Emergent particles associated with the nucleation-type phase transition sometimes cause hysteresis[84]. An example is a hysteresis due to the Bean–Livingston barrier of superconducting vortices[105]. We study the surface barrier of chiral solitons, and obtain a quantitative agreement with experimental data on the jump field. Our results suggest that a hysteresis is described by a classical motion of solitons subject to the surface barrier. At the barrier field, the surface barrier vanishes and solitons start to enter the system. We note that this simple picture should be modified in large samples by taking account of thermal fluctuations in the bulk and inhomogeneity at the surface. These effects smear out this type of hysteresis and sharp jumps, but this is beyond the scope of this thesis.

Before starting with the surface barrier of solitons, we briefly review the Bean–Livingston barrier in type-II superconductors[105]. In a proper theory of superconductors in magnetic field, the solution of vortex line near the surface is constructed by imposing the boundary condition that no current flows perpendicular to the surface, which is equivalent to the presence of an image vortex with opposite vorticity. Since the vortex-antivortex interaction is attractive, the vortex is attracted to the surface while the screening current near the surface push it away from the system. The competition of these two forces creates a local maximum of the free energy near the surface. This is the surface barrier. The surface barrier prevents vortices from entering or escaping from the system, which leads to a hysteresis behavior in magnetization curves [140], even though the bulk thermodynamic phase transition is continuous. This surface barrier exists for the field ranging from zero to some value of the field, which we call the barrier field $H_{\rm b}$. We might conclude that the vortices enter the system at $H = H_{\rm b}$ in increasing field, while they do not escape from the system in decreasing field because the surface barrier exists down to the zero field. However we have to note that, as discussed by Bean and Livingston,

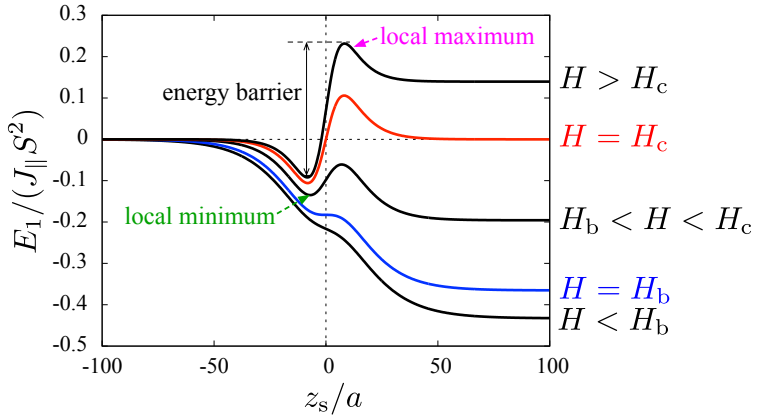

Figure 4.16: Energy profiles (E_1) for the position of isolated soliton (z_s/a). Several lines are shown corresponding to the values of the magnetic field. The blue one ($H = H_b$) and the red one ($H = H_c$) describe the profiles at the barrier and critical fields respectively.

local defects on the surface assist vortices to enter through the following mechanism. The field is not completely uniform on the whole surface, and vortices choose the place with higher field to enter.

We remark that the barrier mechanism is different from that of solitons in chiral magnets as we will see in the following subsections. In addition, the corresponding field effect is opposite. Vortices enter the system in the Meissner state above H_{c1}, while solitons enter chiral magnets below the transition field H_c. Otherwise, they are similar and the soliton surface barrier vanishes at a field different from the thermodynamic critical field. In the following, we first study the spatial profile of the surface barrier of repulsive and attractive chiral solitons in detail, and second perform a quantitative comparison with experimental data. Finally we study the surface barrier of skyrmions and discuss the possibility of related jump behaviors.

4.8.2 Surface barrier of chiral soliton

In chiral magnets, we neglect the dipole-dipole interaction and thus we do not have the magnetostatic potential. We impose the free boundary condition on spins. Under this boundary condition, the surface barrier was obtained by Iwasaki *et al.* for the lattice model[107]. It is pedagogical to review the barrier field in the chiral sine-Gordon model[141], since we can construct the same single soliton solution for the semi-infinite system as that in Sect. 4.6.4. The energy functional is given by

$$E = J_\parallel S^2 a \int_0^\infty \mathrm{d}z \left[\frac{1}{2} \left(\frac{\mathrm{d}\varphi}{\mathrm{d}z} \right)^2 - Q_0 \frac{\mathrm{d}\varphi}{\mathrm{d}z} - m^2 \cos\varphi \right] \tag{4.80}$$

for $\vec{M} = S(\cos\varphi, \sin\varphi, 0)$. Note that the integration interval is from 0 to ∞. Its stationary solution is determined by the sine-Gordon equation, and the single soliton $\varphi_0(z)$ is identical to Eq. (4.73). The energy can be calculated by evaluating the integration directly, but here we

measure the energy from the uniform state.

$$E_1 \equiv E + J_\parallel S^2 a \int_0^\infty \mathrm{d}z m^2 \\ = J_\parallel S^2 a \left[4m(1+\tanh mz_\mathrm{s}) - Q_0 \left(2\pi - 4\tan^{-1} e^{-mz_\mathrm{s}} \right) \right]. \tag{4.81}$$

The thermodynamic critical field of D-IC transition is given by the field at which the energy E_1 vanishes for $z_s \to \infty$, and we get $m_\mathrm{c} = \pi Q_0/4$. This is equivalent to Eq. (2.98). The derivative of the energy with respect to z_s reads

$$\frac{\mathrm{d}E_1}{\mathrm{d}z_\mathrm{s}} = \frac{4J_\parallel S^2 am}{\cosh^2 mz_\mathrm{s}} \left(m - \frac{Q_0}{2} \cosh mz_\mathrm{s} \right). \tag{4.82}$$

A positive slope of the energy as a function of z_s at $z_\mathrm{s} = 0$ corresponds to the energy barrier when a soliton enters the system. We can easily see that

$$\left. \frac{\mathrm{d}E_1}{\mathrm{d}z_\mathrm{s}} \right|_{z_\mathrm{s}=0} = 4J_\parallel S^2 am \left(m - \frac{Q_0}{2} \right) \tag{4.83}$$

changes the sign at $m_\mathrm{b} = Q_0/2$, and the corresponding field $H_\mathrm{b} = m_\mathrm{b}^2 J_\parallel S a^2$ is the barrier field. For $m < m_\mathrm{b}$, there is no surface barrier when a soliton enters. The ratio of H_b to H_c is given by $(m_\mathrm{b}/m_\mathrm{c})^2 = 4/\pi^2$, which is independent of Q_0. The relation $H_\mathrm{b}/H_\mathrm{c} \sim 0.4$ was first found by a numerical calculation for the lattice spin model[142]. Though this shows the presence of the surface barrier when the soliton enters the system, a question is whether there is also an energy barrier when the soliton escapes from the system. We find a finite barrier also for this case. For $m > m_\mathrm{b}$ the energy has a maximum where $\mathrm{d}E_1/\mathrm{d}z_\mathrm{s} = 0$, and the maximum position is given by

$$z_\mathrm{s,max} = \frac{1}{m} \cosh^{-1} \frac{m}{m_\mathrm{b}}, \tag{4.84}$$

which is 0 at $m = m_\mathrm{b}$ and approaches zero again for $m \to \infty$ as $m^{-1} \log m$, and therefore $z_\mathrm{s,max}$ has a finite maximum value. We show in Fig. 4.16 the energy profiles of the isolated soliton solutions for several values of the magnetic field. We see that when $H_\mathrm{ex}^x > H_\mathrm{b}$, there is a local maximum inside the system and a local minimum outside the system. The local maximum structure describes the surface barrier, while the local minimum structure is related to the surface twisted state[107, 143, 144]. We call the modulated profile around the surface the surface twisted state following Refs. [143, 144]. We show this later through a direct comparison between the tail of a virtual soliton and the actual surface twisted state. The surface twisted state and the surface barrier are the two sides of the same physics.

On the other hand, it is difficult to construct the analytic solution with modulated in-plane-amplitude of spins under the tilted field[10]. We, hence, adopt a numerical method to construct

[10]There is the difficulty also in the case of finite temperature which modulates the amplitude of spin in-plane components.

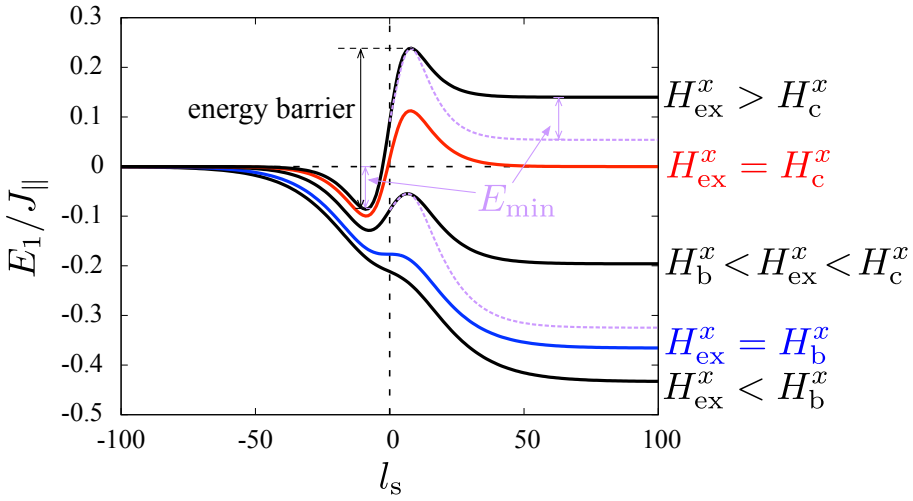

Figure 4.17: Energy profiles of an isolated soliton. Several curves correspond to different values of $H^x_{\rm ex}$. We set $H^z_{\rm ex} = 0$. The purple dashed lines describe the energy profiles calculated by Method II. They agree quite well with the results of Method I near the surface barrier. Far from the surface, a spin profile constructed using Method II includes a single soliton and the surface twisted structure, and thus the energy is lower than the energy obtained using Method I by the energy of the surface twisted energy, which is the value of the local minimum in Method I. The energy profiles shown with red and blue colors correspond to the cases of $H^x_{\rm ex} = H^x_{\rm c}$ and $H^x_{\rm b}$, respectively. The precise values of the field are $0.2H_{\rm d}, H^x_{\rm b}, 0.4H_{\rm d}, H^x_{\rm c}, 0.8H_{\rm d}$ from the lowest field, where $H_{\rm d} = 2(\sqrt{J_\parallel^2 + D^2} - J_\parallel)$.

the solution. In this case, we should be careful about the surface modulation. When the soliton is deeply inside the system, there is a surface twisted modulation, and this is a realistic situation. Actually there is an interaction between the soliton and the surface modulation depending on its position. Thus we consider the position dependence of the single soliton energy while noting contributions from the surface modulation. We describe how to construct a single soliton solution with its center at the position $l_{\rm s}$. We use two methods.

Method I For a given field value, we first construct a single soliton solution with its center at $l_{\rm s} = 0$ on the lattice of $N_z = 2000$ using the periodic boundary condition. Let the obtained spin profiles be $\vec{M}_{l,1}$. Then for the soliton with the center at the position $l_{\rm s}$, the solution is $\vec{M}_l = \vec{M}_{l-l_{\rm s},1}$ for $l \geq l_{\rm s}$ and $\vec{M}_l = \vec{M}_{l-l_{\rm s}+N_z,1}$ for $0 \leq l < l_{\rm s}$. Here we take $-100 \leq l_{\rm s} \leq 100$, and evaluate the energy by summing up in Eq. (4.2) for the sites $0 \leq l \leq N_z/2 = 1000$, subtracting the energy of the uniform state. Even for $l_{\rm s} = 100$, the decays are fast enough in this summation. Note that N_z is sufficiently large and we reduce the finite size effect by using the periodic boundary condition. The advantage of

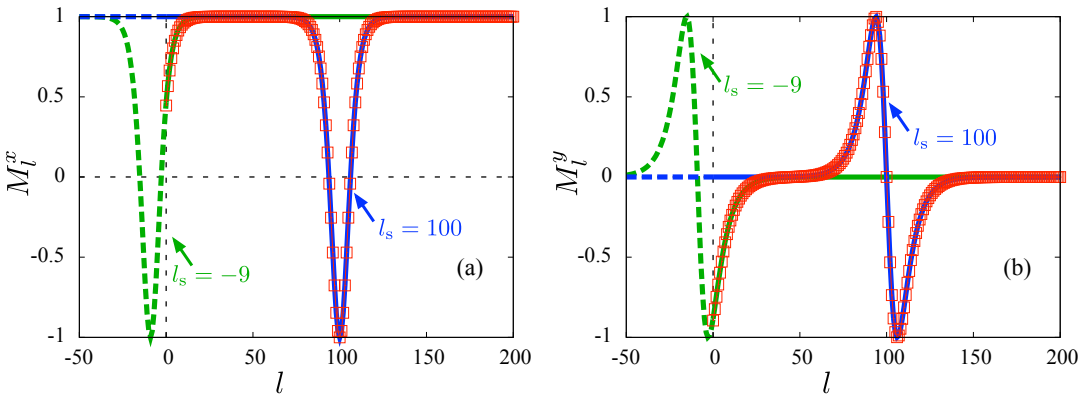

Figure 4.18: Comparison of spin profiles between Method I and Method II for $H_{\rm ex}^x = 0.8H_{\rm d}$. The left panel (a) shows the x-component, while the right panel (b) does the y-component. Note that $M_l^z = 0$ since we set $H_{\rm ex}^z = 0$. $l_{\rm s} = -9$ is a point which gives the local minimum of the soliton energy as shown in Fig. 4.17. The red squares with a line stand for results obtained using Method II when a the soliton center is fixed at $l_{\rm s} = 100$. The blue and green lines are the spin profiles with $l_{\rm s} = 100$ and -9, respectively, through Method I. The dashed lines describe the virtual spin structures outside the system.

this method is that we can consider the case of the soliton outside the system, and also the case of a single soliton for magnetic field lower than the barrier field $H_{\rm b}$. In the latter case, multiple solitons actually enter the system from the surface because the surface barrier is absent.

Method II We directly construct an isolated soliton solution using the free boundary condition. The system in this case has a surface twisted structure for the field $H > H_{\rm b}$. We fix the position of the soliton center at $l = l_{\rm s}$ by imposing the condition that $\varphi_{l_{\rm s}} = \pi$ in updating. This is basically consistent with $M_{l_{\rm s}}^x < 0$ and $M_{l_{\rm s}}^y = 0$. This method is more realistic to consider surface effects, since the surface twisted structure is present and interacts with the soliton in the system. The disadvantage of this method is basically equivalent to the advantage of Method I. We cannot consider negative values of $l_{\rm s}$, and the energy profile of a single soliton for the field lower than the barrier field.

First we show in Fig. 4.17, the energy profiles. Here we fix $H_{\rm ex}^z = 0$, and change $H_{\rm ex}^x$. The solid lines are the results using Method I, while the dashed lines are obtained using Method II. At $H_{\rm ex}^z = 0$, $H_{\rm b}^x \simeq 0.250H_{\rm d}$ and $H_{\rm c}^x \simeq 0.616H_{\rm d}$. The solid lines are calculated for $H_{\rm ex}^x = 0.2H_{\rm d}$, $H_{\rm b}^x$, $0.4H_{\rm d}$, $H_{\rm c}^x$, and $0.8H_{\rm d}$ for both positive and negative $l_{\rm s}$. The negative $l_{\rm s}$ describes the situation where the soliton center is outside of the system.

The figure shows that there is a local minimum structure for negative $l_{\rm s}$, which traps a soliton easily. In this case, its tail appears in the system ($l \geq 0$) and shows a modulated spin

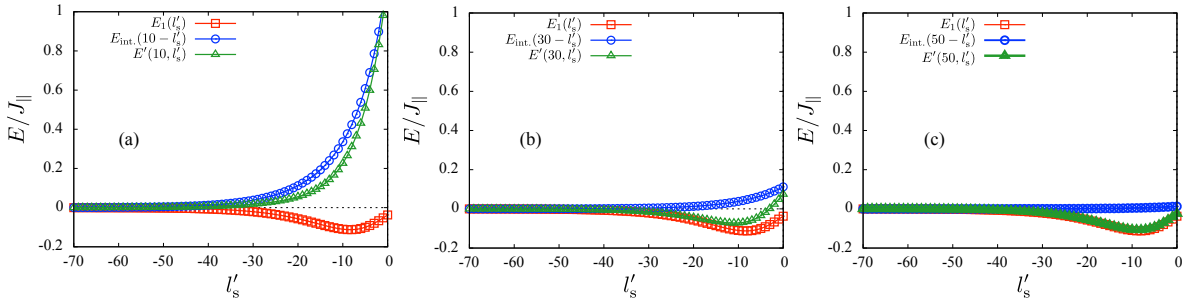

Figure 4.19: Energy profiles of the single soliton energy (red squares), the interaction energy (blue circles) of the virtual soliton at $l'_{\rm s}$ with the soliton in the system at (a) $l_{\rm s} = 10$, (b) 30, and (c) 50 , and the total energy (green triangles) of these two. We set $H^z_{\rm ex} = 0$ and $H^x_{\rm ex} = 0.5H_{\rm d}$.

structure near the surface. This is related to the surface twisted state, proposed before[107, 143–147]. To see this directly, we show the spin profiles determined in both ways in Fig. 4.18 for $H^x_{\rm ex} = 0.8H_{\rm d}$. The left and right panels show the x- and y-components of spin profiles, respectively. The red squares with lines are the results using Method II when the center is at $l_{\rm s} = 100$, while the blue and green lines without symbols are the results for $l_{\rm s} = 100$ and -9, respectively, using Method I. Note that solid and dashed lines are used for $l \geq 0$ and $l < 0$, respectively. The results using Method II show not only the soliton profile around $l = 100$ but also the modulated profile around $l = 0$. They are well separated and described by the results using Method I as we see in the following. The isolated soliton structures at $l = 100$ obtained using Method I and Method II are the same. As shown in Fig. 4.17, the energy has a local minimum at $-9 < l_{\rm s} < -8$. The surface modulated structure shown by squares symbols is well described by considering another soliton with its center at $l = -9$. Therefore we can consider the surface modulation as a soliton that virtually exists at l which gives a local minimum of the energy profile outside the system.

We remark that the energy profile of a single soliton using Method II is possible only for $H^x_{\rm ex} > H^x_{\rm b}$. This is because Method II allows multiple solitons to enter the system if $H^x_{\rm ex} < H^x_{\rm b}$, and hence it is impossible to construct a single soliton solution. For simplicity, we fix $H^z_{\rm ex}$ and change $H^x_{\rm ex}$; $\vec{H}_{\rm b} = (H^x_{\rm b}, 0, H^z_{\rm ex})$. Thus Method I is more useful for $\vec{H}_{\rm ex}$ around $\vec{H}_{\rm b}$. Now let us compare the energy profile using Method I with that using Method II. The energy profiles with Method II are drawn by purple dashed lines in Fig. 4.17 and the energy profiles with Method I and Method II are almost the same near the energy barrier. This means that when the soliton is very near the surface, the surface twisted state is not important. We can infer that the repulsive interaction energy is larger than the binding energy of the virtual soliton outside the system, and that is why the surface twisted state is not important in this case. On the other hand when the soliton is deeply inside the sample, it is well separated from the virtual soliton, and their repulsive energy is smaller than that by the energy of the virtual soliton. We assume that the

total energy of these two solitons is given as follows:

$$E(l_{\rm s}) = \min_{l'_{\rm s}\le 0} \left[E_1(l_{\rm s}) + E_1(l'_{\rm s}) + E_{\rm int}(l_{\rm s} - l'_{\rm s})\right] \equiv \min_{l'_{\rm s}\le 0} \left[E_1(l_{\rm s}) + E'(l_{\rm s}, l'_{\rm s})\right], \tag{4.85}$$

where $E_1(l_{\rm s})$ denotes the energy profile obtained by Method I and the interaction energy, $E_{\rm int}(\Delta l_{\rm s})$, has been introduced in Eq. (4.68) in Sect.4.6. Note that $\lim_{l_{\rm s}\to\infty} E_1(l_{\rm s}) = E_1$, which is the single soliton energy in the bulk introduced in Sect.4.6 and that $\lim_{l_{\rm s}\to-\infty} E_1(l_{\rm s}) = 0$ measured from $E_{\rm uni}$. The barrier field may be given by the condition that both of the interaction energy and the energy barrier of $E_1(l_{\rm s})$ vanish, which can be satisfied simultaneously in this case. As examples, we show $E'(l_{\rm s}, l'_{\rm s})$ for $l_{\rm s} = 10$, 30, and 50 in Fig. 4.19 for $H^z_{\rm ex} = 0$ and $H^x_{\rm ex} = 0.5H_{\rm d}$. The square symbols stand for $E_1(l'_{\rm s})$ which takes minimum at around $l'_{\rm s} \simeq -8$. This is the energy of the surface modulation and corresponds to $\lim_{l_{\rm s}\to\infty} \min_{l'_{\rm s}\le 0} E'(l_{\rm s}, l'_{\rm s})$. The interaction energy $E_{\rm int}(l_{\rm s}, l'_{\rm s})$ is shown by circles for three typical values of $l_{\rm s}$. The sum of these two energies, $E'(l_{\rm s}, l'_{\rm s})$, is shown by triangles. The value of $l'_{\rm s}$ which gives the minimum of $E'(l_{\rm s}, l'_{\rm s})$ describes the position of the virtual soliton attributed to the surface modulation. In Fig. 4.19(a), the soliton inside the system is close to the surface, $l_{\rm s} = 10$. At the minimum position of $E_1(l'_s)$, $l'_{\rm s} \sim -8$, the interaction energy is larger than the absolute value of the binding energy and thus the virtual soliton is pushed to $-\infty$, which means that the surface modulation is absent. Figures 4.19(b) and (c) show the appearance of a surface modulation. For $l_{\rm s} = 50$, the soliton in the system is well separated from the virtual soliton and the interaction energy is negligible: $E(l_{\rm s} = 50) \approx E_1(l_{\rm s} = 50) + E_1(l'_{\rm s} = -8)$. The intermediate stage can be seen for $l_{\rm s} = 30$; the virtual soliton is located at $l'_{\rm s} \sim -11$ and the interaction is visible. The surface barrier which the soliton inside the system feels is given by twice the energy of the surface modulation.

We next study the surface barrier when the soliton interaction is attractive. For the parallel field, $H^z_{\rm ex} = 4.5H_{\rm d}$, we study the energy profiles for $H^x_{\rm ex} = 0.15H_{\rm d}$, $H^x_{\rm b}$, $0.3H_{\rm d}$, $H^x_{\rm c1}$, and $0.5H_{\rm d}$. The whole structure of $E_1(l_{\rm s})$[Fig. 4.20(a)] is quite similar to the repulsive case, while there is small oscillation [(b) and (c)]. In attractive case, the phase transition is discontinuous. For convenience, we use $H^x_{\rm c1}$ at which the energy of the single soliton in the bulk is zero, instead of the thermodynamic transition field $H^x_{\rm c}$, at which the phase transition occurs. There is an oscillation structure in the energy profiles associated with the oscillation of the asymptotic behavior and this leads to tiny local minimum structures, though they are not visible in this scale. To visualize the local minimum structure, we magnify the profiles near the first local minimum in Fig. 4.20(b) or (c). We expect that the local minimum structure attracts a metastable isolated soliton to the surface, which can be an evidence of the attractive interaction. The binding energy of the local minimum in (c) is approximated as $5 \times 10^{-6} J_{\parallel}$ per chain. We consider the ab-plane of $1\mu{\rm m} \times 1\mu{\rm m}$, which reads $N_{\rm 2d} = 4 \times 10^6$. Noting that $J_{\parallel}/k_{\rm B} \sim 10{\rm K}$, the binding energy of the soliton in the three dimensional system is on the order of $200{\rm K}$.

Finally we discuss the surface twisted state for the field larger than the H_0 line. The H_0 line is defined, here, by the instability point of an isolated soliton in the disordered phase. Nevertheless there is a surface twisted state, which is interpreted as a virtual soliton outside the sample as discussed above. An isolated soliton is absent inside the system, but Fig. 4.21 shows

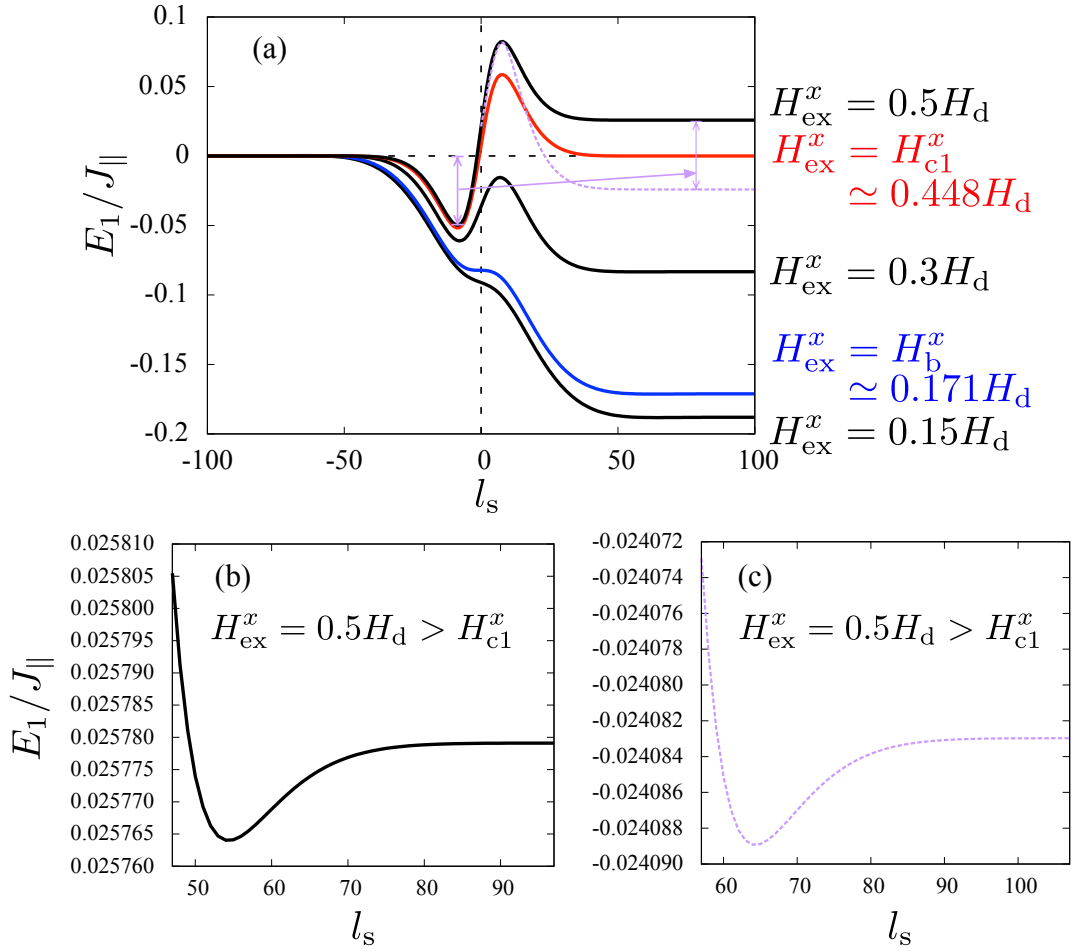

Figure 4.20: Energy profiles of a soliton when the soliton interaction is attractive. (a) Energy profiles obtained for $H^z_{\rm ex} = 4.5H_{\rm d}$ and typical values of $H^x_{\rm ex}$. Here $H^x_{\rm c1} \simeq 0.448H_{\rm d}$ is not the thermodynamic critical field, but the field at which the single soliton energy vanishes. The bottom panels are magnified images of $H^x_{\rm ex} = 0.5H_{\rm d}$ with (b) periodic and (c) free boundary conditions. There is a small local minimum also inside the system, in addition to oscillating structure further inside the system.

that $M^x_{l_{\rm s}} < 0$ at negative $l_{\rm s}$. We can consider the single soliton solution in which the soliton center is at $l_{\rm s}$ and the moment at $l_{\rm s}$ is given by $(M^{x,*}_{l_{\rm s}}, 0, M^{z,*}_{l_{\rm s}})$,[11] and minimize the energy with respect to $l_{\rm s}$ and $M^x_{l_{\rm s}}$. Note that $l_{\rm s}$ takes only integer values in our case. For example, for the field $\vec{H}_{\rm ex} = (1.0, 0.0, 4.5)H_{\rm d}$, we obtain $l_{\rm s} = -9$ and $M^x_{l_{\rm s}} \simeq -0.97639$. Actually we see from

[11] $M^z_{l_{\rm s}} = \sqrt{1 - (M^x_{l_{\rm s}})^2}$.

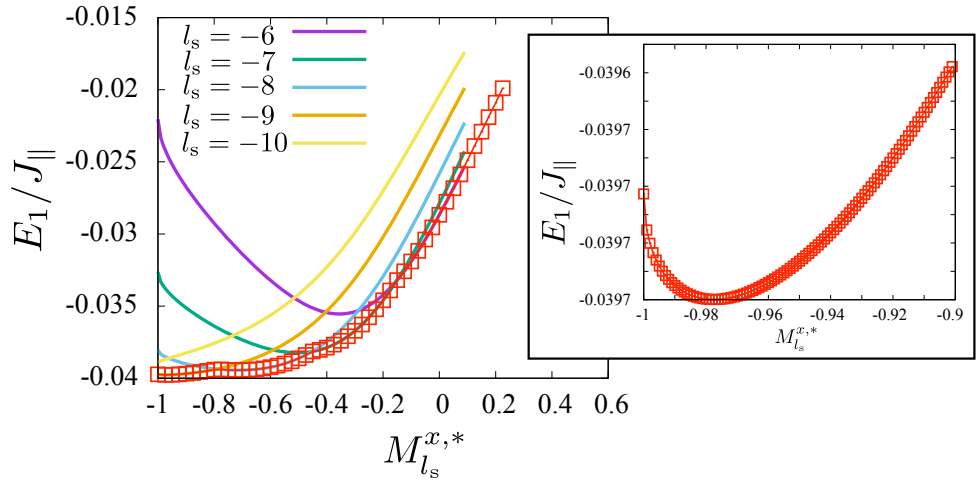

Figure 4.21: Energy profiles. Solid lines are the energy as a function of $M_{l_s}^x$ when the virtual soliton center is fixed at l_s, and squares are the energy minimized with respect to l_s for each $M_{l_s}^{x,*}$. The global minimum is at around $M_{l_s}^{x,*} = -0.978$ and $l_s = -9$. The right panel shows the magnified image around the global minimum.

Figs. 4.22(a) and (b) that the state where the virtual soliton with its center at $l_s = -9$ describes

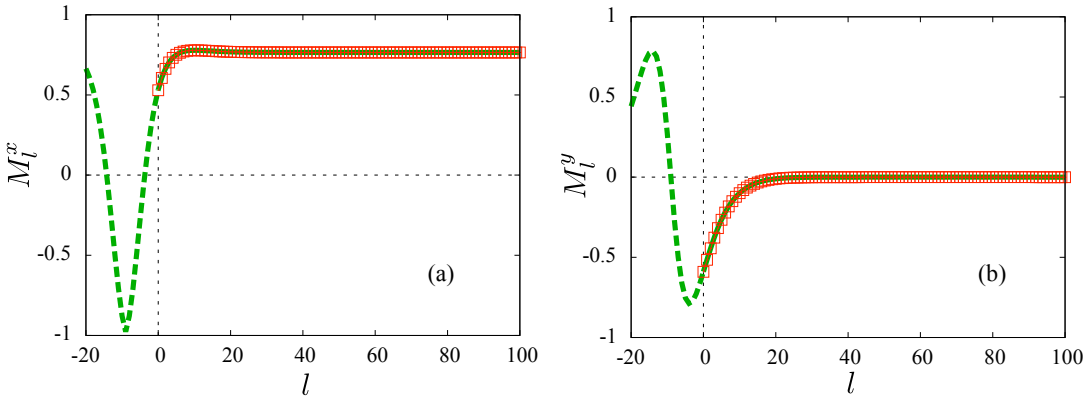

Figure 4.22: Spin profiles describing the surface twisted state for the field $\vec{H}_{\rm ex} = (1.0, 0.0, 4.5)H_{\rm d}$, which is higher than the H_0 line. The red squares with line describe the result obtained through Method II, while the line without symbol is the solution for the condition that $(M_{l_s}^x, M_{l_s}^y) \simeq (-0.97639, 0)$. The minimization condition gives that $l_s = -9$.

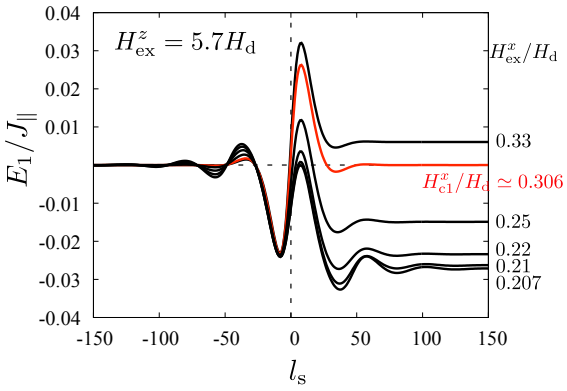

Figure 4.23: Energy profiles as a function of the soliton center position for $H_{\rm ex}^z/H_{\rm d} = 5.7$. The red line represents the profile for nucleation field $H_{\rm c1}^x$. The inflation instability occurs below $H_{\rm ex}^z/H_{\rm d} \approx 0.207$.

very well the surface twisted state appearing as a solution to Method II.

4.8.3 Inflation instability and barrier field

Here we discuss the inflation instability mentioned in Sect. 4.6.3. When the magnetic field changes from the region of complex κa to the pure imaginary region, $\mathrm{Re}(\kappa a)$ vanishes, and thus the soliton size diverges. Therefore this boundary defines the soliton instability but this is a crossover. However, we remark that this crossover line has been determined using the linear approximation. In the ordered phase distant from the phase boundary, this approximation is not justified and it is important to determine more precisely the instability field. This is necessary also for studying the barrier field in the whole phase diagram. Figure 4.23 shows the energy profile of the soliton for $H_{\rm ex}^z/H_{\rm d} = 5.7$, and $H_{\rm ex}^x/H_{\rm d}$ is decreased from 0.33. The oscillation becomes clearly visible with decreasing $H_{\rm ex}^x$ since the decay length related to the soliton size increases. In contrast to the cases considered in the previous subsections, the instability of the soliton-size divergence occurs at $H_{\rm ex}^x \approx 0.207$. Below this, an isolated soliton is unstable, but a periodic structure appears instead. Note that the periodic structure emerges even without the surface, while in the previous cases it is formed by the entry of many solitons through the surface. The instability field thus determined is shown in Fig. 4.24 with violet pentagons. This instability field shifts to slightly higher $H_{\rm ex}^x$ side from the crossover line given by the linear analysis, which is marked by the light-blue solid line. The barrier field line, as shown in Fig. 4.24 with green solid circles is well defined until it reaches the instability field line.

As a consequence, two processes form a periodic structure upon decreasing field: One is the entry of solitons from surface as a result of the vanishing surface barrier. The other is the deformation of unstable single soliton owing to the inflation instability.

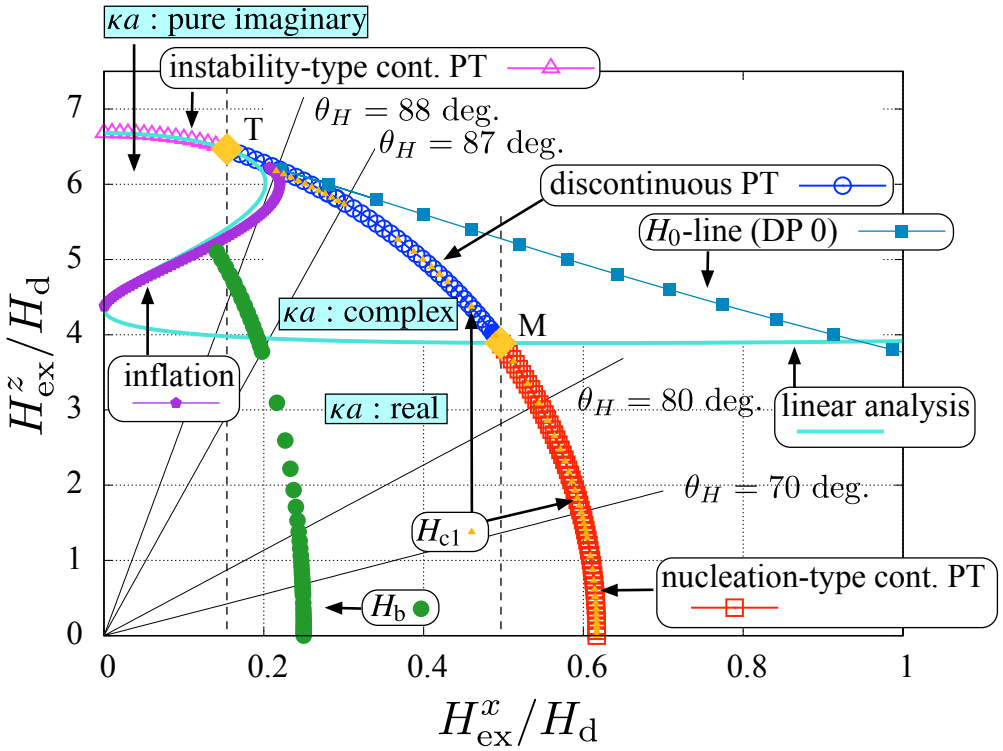

Figure 4.24: Barrier field $\vec{H}_{\rm b}$ in the phase diagram, by green circles. For reference, we also show the critical field $\vec{H}_{\rm c1}$ by small yellow triangles, at which the energy of a single soliton in the bulk is zero. The inflation instability field is shown with violet pentagons in addition to the phase boundary, the line based on the linear analysis, and H_0 line.

4.8.4 Comparison to experimentally observed hysteresis

Now we have constructed the surface barriers both in the repulsively and attractively interacting soliton regions. Figure 4.24 shows the barrier field line in the phase diagram. The barrier field appears in the whole phase diagram, and it is similar to the jump field at which a large jump in the hysteresis loop is observed in experiments for the micrometer-sized samples as shown in Fig. 4.25(b). The hysteresis observed in experiment for a given field angle, $\theta_H \equiv \tan^{-1}(H^z_{\rm ex}/H^x_{\rm ex})$, is shown in Figs. 4.2(b) and (c) as examples. However for the direct quantitative comparison, we need to take into account the effects of demagnetizing field, which reduces the total magnetization or even change the spin configuration. For the saturation field, we approximate it by using the demagnetization factor $\mathsf{N}_{\rm d}$, and the effective external field $\underline{\vec{H}}_{\rm ex}$ is given by $\underline{\vec{H}}_{\rm ex} = \vec{H}_{\rm ex} - \mathsf{N}_{\rm d}\vec{M}_{\rm u}$, where $\vec{M}_{\rm u}$ is a function of $\underline{\vec{H}}_{\rm ex}$ rather than the applied field $\vec{H}_{\rm ex}$. The effect is complicated because $\underline{\vec{H}}_{\rm ex}$ is neither parallel to $\vec{M}_{\rm u}$, nor to $\vec{H}_{\rm ex}$. Therefore the configuration excluding the demagnetizing field effect is desirable for more quantitative com-

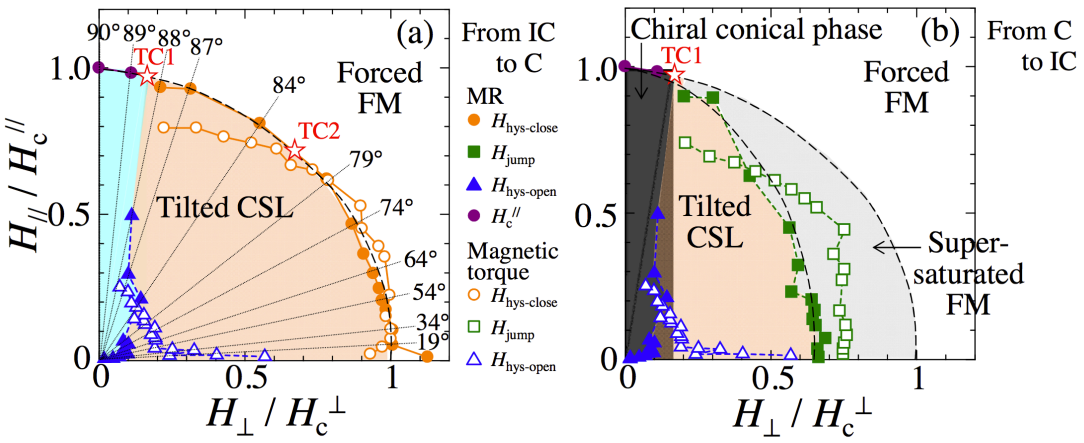

Figure 4.25: Phase diagram determined by magneto-resistance and magnetic torque measurements taken from Ref. [104]. Critical points suggested in the figure are obtained by referring to the critical points in Ref. [86]. The left panel (a) mainly shows the line at which the hysteresis closes, which is considered to be the thermodynamic phase boundary. The right panel (b) shows the jump field, at which a large jump of the magneto-resistance or magnetic-torque is observed in decreasing field.

label	width	thickness	length
sample 1	11.25μm	0.7μm	17.5μm
sample 2	8.5μm	0.5μm	21μm
sample 3	10μm	0.5μm	10μm

Table 4.2: Size of different samples. Length is along the helical axis, i.e. z-direction. Sample 3 is the one used in the magneto-resistance measurement shown in Fig. 4.25.

parison. The sample dimensions used in Fig. 4.25 are $10\mu\text{m} \times 0.5\mu\text{m} \times 10\mu\text{m}$(helical axis) for the magneto-resistance measurement and $13.4\mu\text{m} \times 12.0\mu\text{m} \times 17.6\mu\text{m}$(helical axis) for the magnetic torque measurement, which is not even a thin film. In the magneto-resistance measurement the field is tilted toward the helical axis from the normal direction to the plane, in which the demagnetization effect is maximized. An advantage of the normal direction is that the resistance curve in increasing field is smoother than that for the in-plane direction. (Compare 90 degs. and 0 degs. in Fig. 4.2(a).)

For the direct comparison under the tilted field, we use additional magneto-resistance measurement data using different samples, which is provided by R. Aoki and Y. Togawa[148]. Their sizes are shown in Table 4.2: Among them, the sample 1 was measured in two different sequences. In one sequence, the measurement was performed for $\theta_H = 0$ degs. three times. The other sequence measured five times for each field angle except for $\theta_H = 85$ degs. In the

following we compare the barrier field with the jump field $\vec{H}_{\rm jump}$ in decreasing field. The barrier field is defined by the field where the surface barrier disappears. We also compare the saturation field $\vec{H}_{\rm sat}$ at which the hysteresis closes in increasing field in the experiments[103, 104] with $H_{\rm c1}$ defined as the field where the single soliton energy becomes zero. This field is equivalent to the thermodynamic critical field of the nucleation-type continuous phase transition, while it is less than the field of the thermodynamic discontinuous phase transition. However, the difference from the latter is small, which means that the limit of metastability of the uniform state is close to the phase boundary, and we use this field for convenience. Comparison was made in Ref. [141] for the field perpendicular to the helical axis using the theoretical results $(H_{\rm b}/H_{\rm c} = 4/\pi^2)$ calculated for the sine-Gordon model.

Before comparing, we make a few remarks. It is likely that $\vec{H}_{\rm jump}$ in decreasing field is $\vec{H}_{\rm b}$. Below $H_{\rm b}$, a soliton can enter the system without energy barrier at the surface, and actually a surface barrier can be constructed again after more than one solitons enter the system depending on the field step. This implies that many solitons enter the system at the barrier field, and this leads to a large jump observed in experiments. On the other hand, it is ambiguous to identify the saturation field as either $H_{\rm c}$ or $H_{\rm c1}$, because the saturation process is not clear. Within the theory of the surface barrier, a soliton feels the energy barrier when it escapes as well, and the barrier remains up to the instability field. Note that the instability field at $H^z_{\rm ex} = 0$ is about 7 times larger than the critical field $H_{\rm c}$. We may identify $\vec{H}_{\rm sat}$ as either $\vec{H}_{\rm c}$ or $\vec{H}_{\rm c1}$ rather than $\vec{H}_0$ since the saturation field for $\theta_H = 0$ degs. in the film plane is almost the same as the $H_{\rm c}$ of the sufficiently large film, where the large hysteresis is no longer observed. The reason why the thermodynamic critical field appears only in increasing field is not clear, but it is likely that $H_{\rm c}$ or $H_{\rm c1}$ agrees with $H_{\rm sat}$ in increasing and $H_{\rm b}$ agrees with $H_{\rm jump}$ in decreasing.

On the basis of these arguments, let us compare experimental data and our calculations. Figure 4.26(a) shows the $H_{\rm b}$ and $H_{\rm jump}$ obtained by calculations and experiments for three samples, and Fig. 4.26(b) shows $H_{\rm c1}$ and $H_{\rm sat}$. Concerning the sample 1', the experiment was performed three times and the results are marked by three black solid squares at 0 degs., although in this scale they overlap with each other. For the sample 1, the field sweep was done five times for each angle except 85 degs., for which the field sweep was done once with a smaller field step. Hysteresis loops are shown in Fig. 4.27. It should be noted that the values of the jump field did not change within the five measurements for 30 and 80 degs. For 60 degs., there is a two-jump structure at the jump field in the second field-sweep, and the first small jump takes at the field higher by 50 Oe and the second large jump is at the field lower by 50 Oe than the $H_{\rm b}$ in the other field-sweeps. For simplicity, we do not show the jump field obtained for the second field-sweep in the panel (a). Robustness of the jump field with in the five measurements implies that the mechanism can be explained without including the randomness and stochastic process.

The calculated values $H_{\rm b}$'s and $H_{\rm c1}$'s are scaled so that $H_{\rm c1}(\theta_H = 0) = 1.8$ kOe. This value is the thermodynamic critical field obtained in an experiment where the magnetic field is applied in the plane of the sufficiently large film to eliminate the effects of the demagnetizing

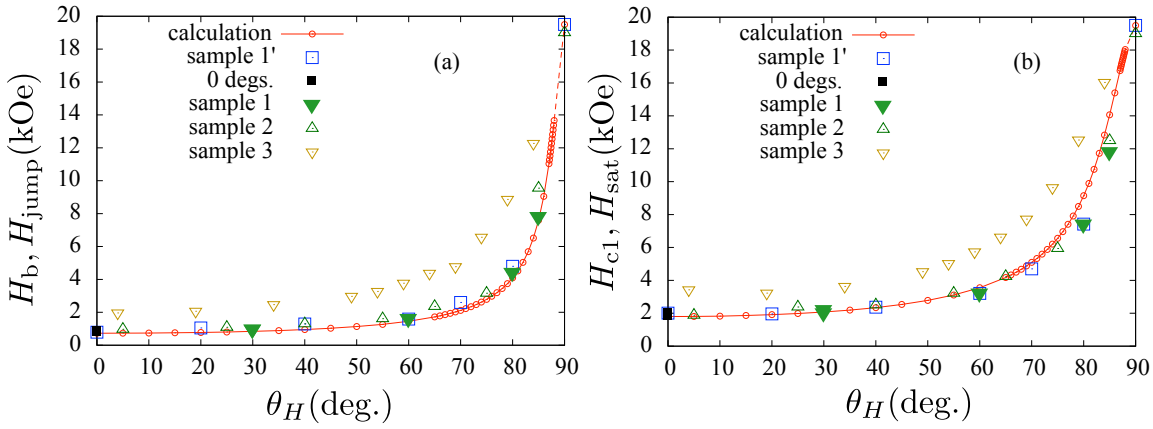

Figure 4.26: Comparisons between calculation results and experimental results. (a) $H_{\rm b}$ and $H_{\rm jump}$ and (b) $H_{\rm c1}$ and $H_{\rm sat}$. θ_H is the angle of the tilted field measured from the perpendicular field direction. The unit of the field is kOe, and we scale the fields obtained by calculation using the value of the critical field at $\theta_H = 0$ degs., which is 1.8 kOe. Note that the dashed lines of the calculations are just for eye-guides. The experimental data are offered by R. Aoki and Y. Togawa[149].

field[12]. In the experiment for a sufficiently large film, a large hysteresis is no longer observed. Note that the anisotropy is evaluated from the parallel critical field in a sufficiently large thin film. As a result, the scaled value obtained from the numerical calculation describes very well the parallel saturation field observed in the experiment for the micrometer-sized samples, though the agreement might be trivial in this case. This is because the saturation field for the micrometer-sized samples is the same as the thermodynamic critical field for the instability-type continuous phase transition. The importance is that the scaled value $H_{\rm c1}$ at $\theta_H = 0$ degs. is in a good agreement with the saturation field for the micrometer-sized samples. With this fact, we expect that the saturation field for the micrometer-sized samples is equivalent to the thermodynamic critical field.

In both panels (a) and (b) in Fig. 4.25, $H_{\rm b}$ and $H_{\rm c1}$ are in good agreement with $H_{\rm jump}$ and $H_{\rm sat}$, respectively, except for the sample 3. For the sample 3, the magnetic field is applied in the plane spanned by the helical axis and the direction normal to the film. For small θ_H, the field is almost perpendicular to the film, leading to a high demagnetizing field, which reduces the field inside the sample. Therefore, the demagnetizing field enhances the values of $H_{\rm c1}$ and $H_{\rm b}$. This causes a deviation of the calculation result from the experimental data.

Then we see more details of the data of the sample 1', 1 and 2, for which the in-plane demagnetizing field is extremely suppressed. First we focus on the barrier field shown in

[12]Precisely speaking the magnetic moment perpendicular to the film feels large demagnetizing field. Hence the purpose of the experiment for thin films is to minimize the demagnetization factors in the plane.

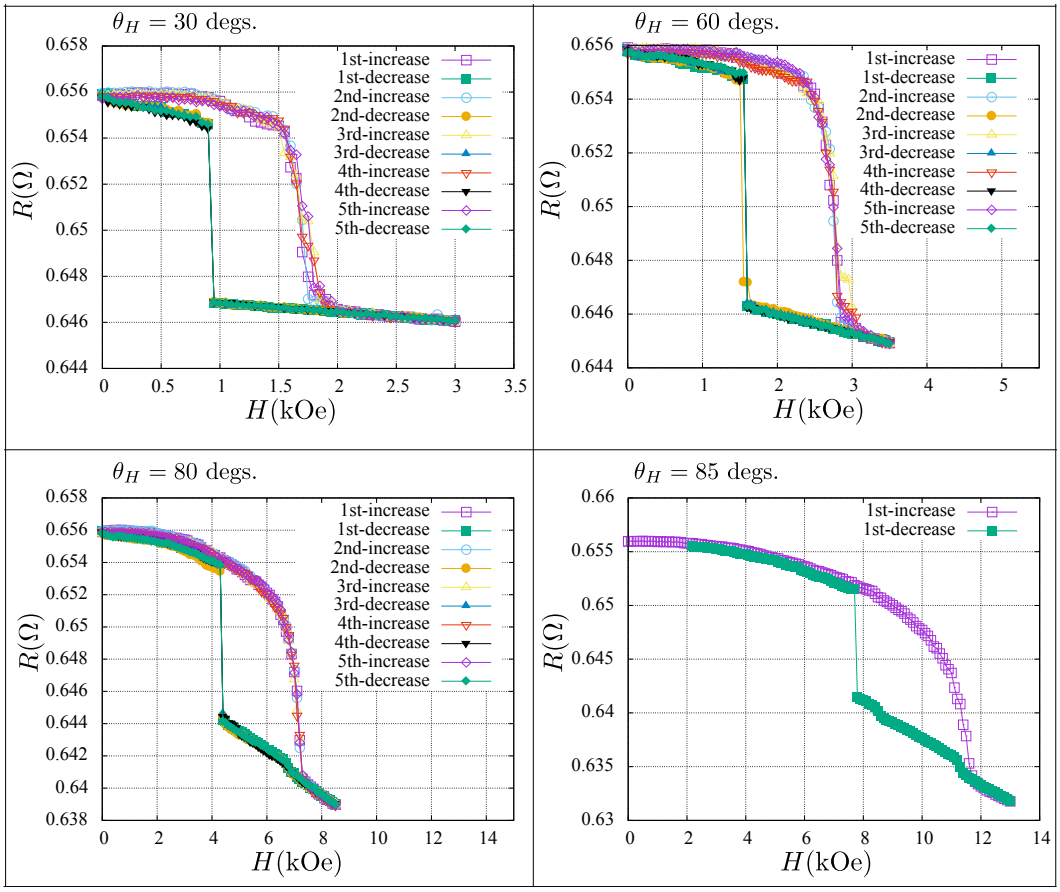

Figure 4.27: Raw data of magneto-resistance for sample1 provided by R. Aoki and Y. Togawa. Horizontal axes are the magnitude of the external magnetic field and vertical axes are the magneto-resistance. Five times field-sweeps are plotted in each panel except for $\theta = 85$ degs.

Fig. 4.26(a). The barrier field of the sample 1 is remarkably consistent with the calculation results. The data of the sample 1 is more reliable than the samples 1' and 2 upon excluding other extrinsic effects, because the multiple measurements were done, and the obtained value was confirmed to be reproducible. Though the data of the samples 1' and 2 are also in good agreement with the calculation results, extrinsic effects might cause these slightly higher jump fields. We speculate possible reasons below. In decreasing field, the uniform state is metastable below H_{c1}. It survives down to the spinodal point within the mean field picture. When thermal fluctuation or any perturbation is comparable to the energy barrier of the metastable state, solitons enter the sample. In addition, there are arguments on superconducting vortices that the barrier field does not work in increasing field. Note that increasing field in superconductors corresponds to decreasing field in the chiral soliton case. The reason why the barrier does not work is the following. The system is not completely uniform and there may be small areas where

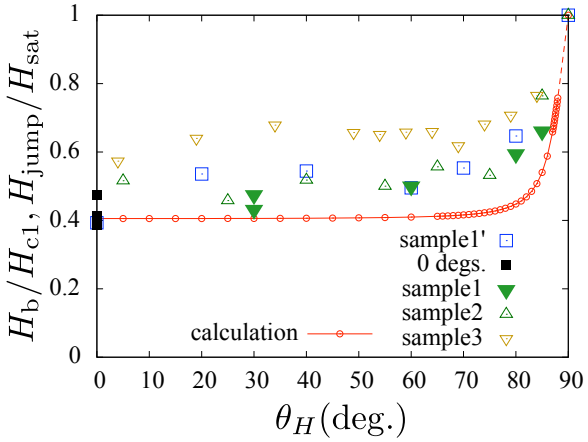

Figure 4.28: Ratios of H_b to H_{c1} and H_{jump} to H_{sat} as a function of the field angle θ_H. The dashed line is for eye guide.

the magnetic field is concentrated and stronger than the average strength because of defects or the sample shape such as corners. Because the vortices are the line defects, the locally strong field allows the vortices to enter the system. On the other hand, the chiral soliton is much larger object in the sense that the spins align inside the ab-plane. Thus the effects of inhomogeneous field around the surface is not dominant but cannot be excluded perfectly. These possible mechanisms increase the jump field and therefore the line obtained by the calculation can give the lower bound of the barrier field.

Second, we briefly comment on the saturation field. Though the saturation field is also in good agreement with calculation results, it tends to be lower than the calculated value in contrast to the jump field. Interestingly the lowered saturation fields at $\theta_H = 60$ and 80 degs. are reproducible. Although we do not basically justify identifying H_{sat} as H_{c1}, a possible reason may be as follows: Thin films reduce the in-plane demagnetization factor, and thus the out-of-plane component feels larger demagnetizing field. The y-component of the helical order[13] tends to be in the plane. This leads to the reduction of the critical field. In the next subsection we see the effects of an easy axis anisotropy for $\theta_H = 0$ degs. When it is weak, it reduces the critical field but does not affect the barrier field very much. We need further considerations to justify this scenario. We once again emphasize that the fields H_{jump} and H_{sat} for samples 1', 1, and 2 are in much better agreement with the calculation results than those for the sample 3, which is achieved by reducing the demagnetizing effect.

Finally we show the ratios H_b/H_{c1} and H_{jump}/H_{sat}, since the comparison between theory and experiment is easier. For example, though the jump field and the saturation field become about ten times larger at $\theta_H = 90$ degs. than those at $\theta_H = 0$ degs., the ratios are between 0.4 and 1. Figure 4.28 shows the ratio as a function of the angle of the tilted applied field. A theoretical expectation is that the ratio is constant for almost all the angle and grows steeply near the parallel field. The constant value is about 0.4. The experimental data have a similar

[13]Note that we define the z-axis by the helical axis and the magnetic field is applied in the xz-plane. In this geometry, the film surface is spanned by x- and z-axes.

behavior to the theoretical expectation, but the constant value for low θ_H is higher than 0.4. This comes from the tendency that the saturation field becomes lower than the calculated value for the sample 1. In addition, for the samples 1' and 2, this deviation can also be attributed to the high $H_{\rm b}$'s as we considered. Actually in this scale, the ratio shows scattered values at $\theta_H = 0$ degs. among the three measurements. However it is worthwhile to mention that the ratios for the samples 1 and 2 are closer to the calculated value than those for the sample 3. In the sample 3, the behavior of the curve is different: The curve is not flat for low θ_H's and show a slow increase between 70 and 85 degs. The demagnetization factor varies in the sample 3 as θ_H changes. This is reason that the behavior is different from that obtained by the calculation.

Before going to the skyrmion surface barrier, we make a general remark on hysteresis and an accompanying sharp jump. Hysteresis is due to metastable dynamics, and is observed when the transition to the equilibrium state is blocked. This transition requires nucleation processes, and sometimes a metastable state survives up to the limit of metastability when dynamics is adiabatic. The origin of the metastability in micrometer-sized $Cr_{1/3}NbS_2$ is related to the fact that soliton winding number changes only by solitons entering into the system, i.e., they are not nucleated in the bulk by low energy processes. The existence of the surface barrier is ubiquitous for the nucleation-type phase transitions, while the sharpness of the jump at the vanishing surface barrier depends on the individual details. For examples, superconducting vortices enter the system gradually and the magnetization curve in increasing field is almost the same as the thermodynamic one[105]. For skyrmions, the barrier never disappears and this will be discussed in the next subsection. The metastability of these emergent particles does not persist in bulk samples, because stochastic nucleation processes dominate. After all, micrometer-sized samples of $Cr_{1/3}NbS_2$ is a suitable playground to confirm the theory of the surface barrier.

4.8.5 Extension to skyrmion

Now, let us extend these results to another emergent particle in chiral magnets in higher dimensions, skyrmion[31, 32, 34]. The Bloch skyrmion in a two dimensional system can be constructed for the following Hamiltonian:

$$\mathcal{H} = \sum_{\boldsymbol{j}} \left\{ \sum_{\mu=x,y} \left[-J\vec{S}_{\boldsymbol{j}} \cdot \vec{S}_{\boldsymbol{j}+\hat{\mu}} - D\left(\vec{S}_{\boldsymbol{j}} \times \vec{S}_{\boldsymbol{j}+\hat{\mu}}\right) \cdot \vec{e}^{\mu} \right] - H_{\rm ex} S^z_{\boldsymbol{j}} - \frac{K}{2}\left(S^z_{\boldsymbol{j}}\right)^2 \right\}, \qquad (4.86)$$

where $\boldsymbol{j}$ runs over the sites of the square lattice. The system is two-dimensional in x- and y-directions. The first and second terms are the exchange interaction and the DMI of nearest neighbor pairs. The third and fourth terms are the Zeeman coupling with external magnetic field and a single ion anisotropy. $\vec{e}^{\mu}$ denotes the unit vector of the μ-direction in the spin space, while $\hat{\mu}$ in the real space. The magnetic field and anisotropy axis are in the z-direction and we consider the easy-axis case $K > 0$. In this subsection we also construct a soliton solution as well as a skyrmion solution, but note that this soliton is different from the one in previous

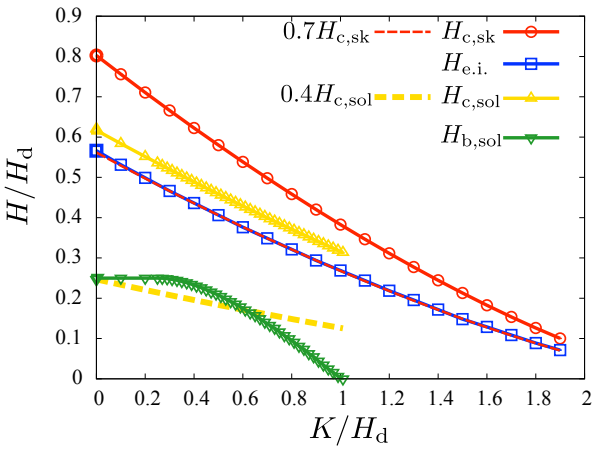

Figure 4.29: Easy axis anisotropy dependence of various magnetic field lines. The critical field and the elongation instability field of the skyrmion are denoted by $H_{\rm c,sk}$ and $H_{\rm e.i.}$, respectively. The red dashed line is given by $0.7H_{\rm c,sk}$. Also we add the easy axis anisotropy effects on the critical and barrier fields of the soliton given by yellow triangles and green inverted-triangles. The yellow dashed line stands for $0.4H_{\rm c,sol}$.

subsections. For consistency of the notation to the above, we write $\vec{S}_{\boldsymbol{j}}$ as $\vec{M}_{\boldsymbol{j}}$. The effective field is given by

$$\vec{H}_{\boldsymbol{j}}^{\rm eff} = \sum_{\mu=x,y} \left[J\left(\vec{M}_{\boldsymbol{j}+\hat{\mu}} + \vec{M}_{\boldsymbol{j}-\hat{\mu}}\right) + D\left(\vec{M}_{\boldsymbol{j}+\hat{\mu}} - \vec{M}_{\boldsymbol{j}-\hat{\mu}}\right) \times (\vec{e}^{z} \times \vec{e}^{\mu}) \right] + \left(H_{\rm ex} + KM_{\boldsymbol{j}}^{z}\right) \vec{e}^{z}. \tag{4.87}$$

The energy of the uniform state, $\vec{M}_{\rm u} = \vec{e}^{z} (|\vec{M}_{\rm u}| = 1)$, for the periodic boundary condition is given by

$$E_{\rm uni} = -N_{\rm 2d}\left(2J + H_{\rm ex} + \frac{K}{2}\right). \tag{4.88}$$

Here $N_{\rm 2d} = N_x N_y$ denotes the number of sites of the square lattice, and N_x and N_y are the number of sites along the x- and y-directions, respectively. An important remark is that the surface modulation is not "skyrmionic", but "solitonic". Here we have used the skyrmionic or solitonic surface spin structure in the sense that the surface modulation can be described by the virtual skyrmion or soliton. The solitonic surface spin structure extends in the surface area in three dimensions or surface edge in two dimensions and thus it lowers the total energy more than a skyrmion does. Actually we could consider an array of the skyrmionic surface spin structures along the edge, and in this case, the solitonic surface spin structure has a lower energy. We will see this later.

There is an instability mode in the low field, which is an elliptic elongation of a skyrmion. The excitation spectrum of an isolated skyrmion is calculated by Lin *et al.* for the lattice system[150], and by Schütte and Garst for a continuum system[151]. Here we adopt the lattice model and study the instability field as a function of the easy axis anisotropy, which is shown in Fig. 4.29. The elongation instability field is denoted by $H_{\rm e.i.}$ and the critical field

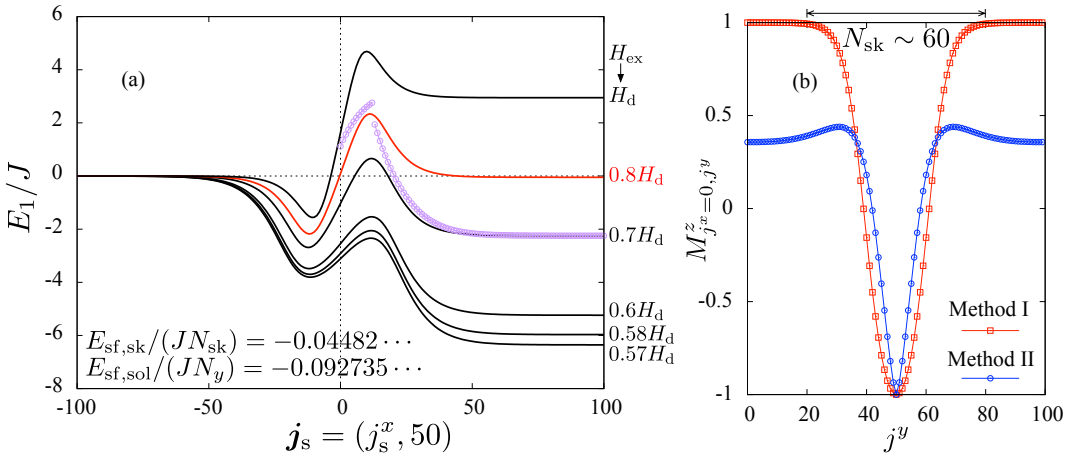

Figure 4.30: (a) Energy profile for zero easy-axis anisotropy. The purple line with circle is the energy of the skyrmion constructed by Method II for $H_{ex}/H_d = 0.7$, and the energy is shifted by the energy of the surface spin structure, $E_{sf,sol}/J$. We show the values of the energy density for surface spin structure for $H_{ex}/H_d = 0.7$, in the left panel. (b) Spin profiles of the skyrmion with $j_s^x = 0$ at the surface ($j^x = 0$). The red squares and the blue circles are the profiles for $H_{ex}/H_d = 0.7$ constructed by Method I and Method II, respectively. A characteristic size may be evaluated as $N_{sk} \sim 60$ and the energy density of the skyrmionic surface spin structure is given by the energy gain, which is the local minimum outside the system divided by N_{sk}.

is denoted by H_c. The phase transition between the skyrmion lattice and the uniform state in two dimensional system is nucleation-type continuous[137], and thus H_c is the same as H_{c1}, at which the single skyrmion energy becomes zero. We also plot $0.7H_c$ for an eye guide, which is quite similar to the elongation instability field. The surface barrier is maintained above the elongation instability field, below which an isolated skyrmion becomes unstable. This is a structure similar to that in the chiral soliton case; The instability occurs above the barrier field in decreasing field (see Sect. 4.8.3). We show the energy profiles as a function of the skyrmion position, which is mainly plotted using Method I (see Sect. 4.8). For comparison, we also construct an isolated skyrmion under the free boundary condition, which corresponds to Method II. We remark that the surface spin structure is solitonic and some of the obtained solutions are artificial, i.e., a condition imposed to fix the skyrmion position plays a role of a strong pinning and leads to a distortion of the skyrmion structure. Figure 4.30(a) shows the energy profiles for $K = 0$. We see from Fig. 4.30(a) that the energy profile for the field just above $H_{e.i.} \simeq 0.56H_d$ still has the energy barrier for the skyrmion entering and escaping from the system. When the skyrmion escaping from the system, the skyrmion constructed by Method II feels larger energy slopes. This is because the skyrmion feels the interaction with the surface modulation in addition to the energy increase of the single skyrmion near the boundary, which can be seen from the energy profile constructed by Method I. Let us discuss why the

surface is solitonic. We show the energy densities of the solitonic and skyrmionic surface spin structures in Fig. 4.30(a). Here the solitonic surface spin structure is uniform along the surface and the energy density is obtained by dividing the energy of the surface spin structure by the number of sites along the surface, N_y. On the other hand the skyrmionic surface spin structure is not uniform. The skyrmionic surface spin structure could be constructed by considering the virtual skyrmion array outside the system. The period of the virtual skyrmion array is determined by the competition between the one virtual skyrmion energy which is given by the local minimum outside the system in Fig. 4.30(a), and the positive interaction energy between virtual skyrmion. We neglect the interaction energy, and instead estimate the inter-skyrmion distance along the surface from Fig. 4.30(b), which shows the spin configuration at the surface ($\boldsymbol{j} \cdot \hat{x} = 0$) for the skyrmion of $\boldsymbol{j}_{\rm s} = (0, 50)$, and at the closest arrangement of skyrmions, the number of sites occupied by one skyrmion is about 60. This can be approximated as the number of sites contributing the energy gain of the surface spin structure by one skyrmion. Thus the energy density of the skyrmionic surface spin structure can be estimated by dividing the energy of the local minimum outside the system by $N_{\rm sk} \sim 60$. Note that the energy gain is overestimated in this way. Nevertheless, by comparing the energy densities of these two surface spin structures, we see that the solitonic surface spin structure has lower energy.

The interaction between the skyrmion and soliton is complicated and leads to the distortion of the skyrmion. Figure 4.31 shows the profiles of isolated skyrmions near the surface. The upper panels show the configurations using Method I, while the lower panels show those obtained using Method II. The left, middle, and right panels show the configurations obtained by imposing the condition that $\vec{M}_{\boldsymbol{j}_{\rm s}} = -\vec{e}^z$ at $\boldsymbol{j}_{\rm s} = (10, 50)$, $(20, 50)$, and $(50, 50)$, respectively. Actually in panels (d) and (e), the skyrmions are noticeably distorted. The solitonic surface spin structure surrounds the skyrmion fairly close to the surface. The distortion from both sides below and above $j^y \sim 50$ is more visible in Fig. 4.30(b). The blue circles represent $M^z_{\boldsymbol{j}=(0,j^y)}$ with the condition that $\boldsymbol{j}_{\rm s} = (0, 50)$. The surface modulation is formed around j^y ranging from 0 to 20 and from 80 to 100. The interaction distorts the skyrmion and it becomes narrower compared with that constructed by Method I. This changes the single skyrmion energy $E_{1,\rm sk}$ and we actually need to take account of this effect. The distortion in the soliton case should be slight, because it is one dimensional system and two solitons cannot be so close to each other. The skyrmions in the panels (d) and (e) are elongated because of the interaction with the surface modulation. We note the difference between them. The x-coordinate of the elongated skyrmion center $j^x_{\rm e,sk}$ in the panel (d) is shifted to the surface, i.e. $j^x_{\rm e,sk} < 10$. On the other hand in the panel (e), $j^x_{\rm e,sk} > 20$ and this means the center is shifted to the other direction. Qualitatively, the direction of the force on the skyrmion in the panel (d) is outward, while in the panel (e) it is inward, which leads the surface barrier. However we repeat that the quantitative description is more difficult because the deformation and the interaction with the surface modulation are important when a skyrmion enters and escapes from the system. The elongation direction suddenly changes depending on the position of the skyrmion imposed in the calculation, which is reflected in the purple line in Fig. 4.30(a).

For further interest, we study what enters the system instead of a skyrmion by decreasing

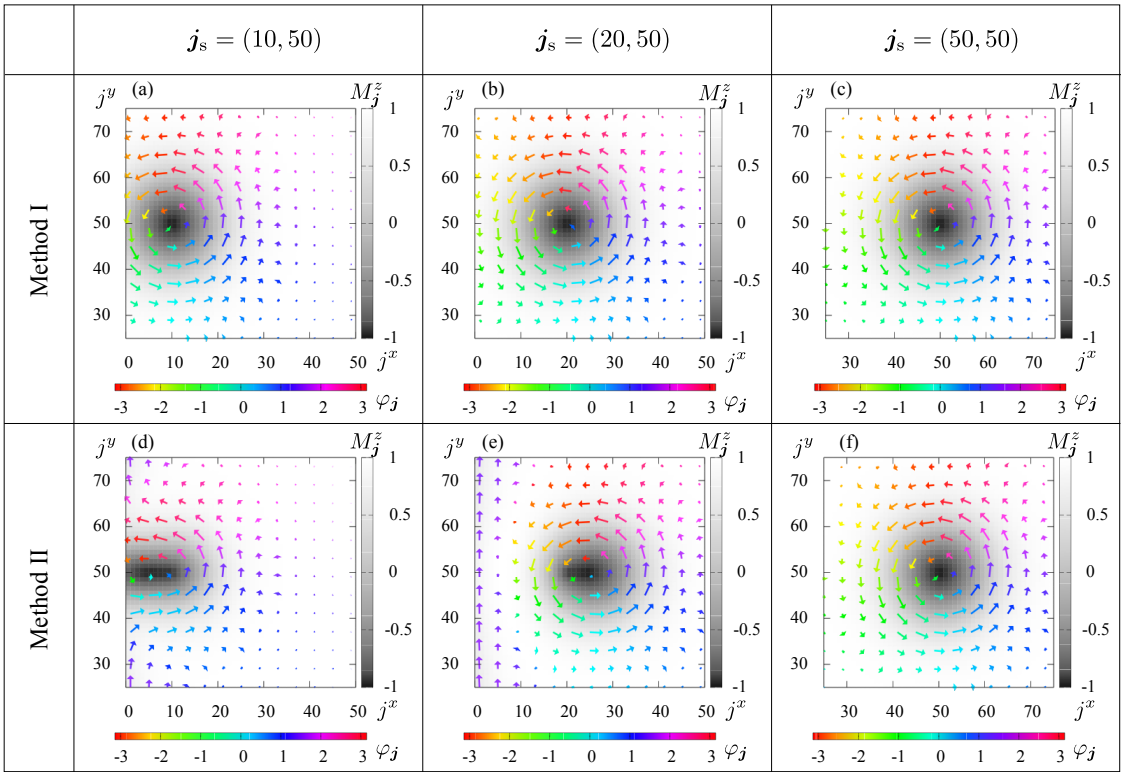

Figure 4.31: Skyrmion profiles near the surface. We set $H_\mathrm{ex}/H_\mathrm{d} = 0.7$. The configurations in the upper panels (a)–(c) are obtained by Method I, while those in the lower panels (d)–(f) are obtained by Method II. $\boldsymbol{j}_\mathrm{s}$ denotes the position of skyrmion which we specify as the condition to fix it when solving the equation. Colored arrows represent the in-plane components of spins, i.e., color describes the angle of the in-plane spin $\varphi_{\boldsymbol{j}} = \tan^{-1}(M_{\boldsymbol{j}}^y/M_{\boldsymbol{j}}^x)$, and arrows are the direction and magnitude of the in-plane spin. Gray-scale contour map represents $M_{\boldsymbol{j}}^z$.

the field. Below $H_\mathrm{e.i.}$, a skyrmion turns into a soliton, by its elongation. Thus it is important to study whether the surface barrier for the soliton exists or not. Actually when the anisotropy is zero the barrier field, $H_\mathrm{b,sol}$ is 0.4 times the critical field of the soliton, $H_\mathrm{c,sol}$ and the elongation instability field of the skyrmion $H_\mathrm{e.i.}$ is 0.7 times the critical field of the skyrmion, $H_\mathrm{c,sk}$. By considering that $H_\mathrm{c,sol} < H_\mathrm{c,sk}$, $H_\mathrm{b,sol}$ exists below $H_\mathrm{e.i.}$ For finite values of the anisotropy, we summarize these fields in Fig. 4.29: Yellow triangles represent the critical field of the soliton and green inverted triangles do the barrier field of the soliton. Yellow dashed line stands for the line of $0.4H_\mathrm{c,sol}$ for an eye-guide. In the presence of the anisotropy, which distorts the soliton, the barrier field no longer holds the relation $H_\mathrm{b} \simeq 0.4H_\mathrm{c}$. For stronger anisotropy the barrier field goes to zero rather quickly, and for $K > H_\mathrm{d}$ the barrier field is almost zero. Now we see the decreasing process, in which the uniform state remains even for the field below $H_\mathrm{c,sk}$. We continue to decrease the field down to the barrier field of the soliton for the relatively

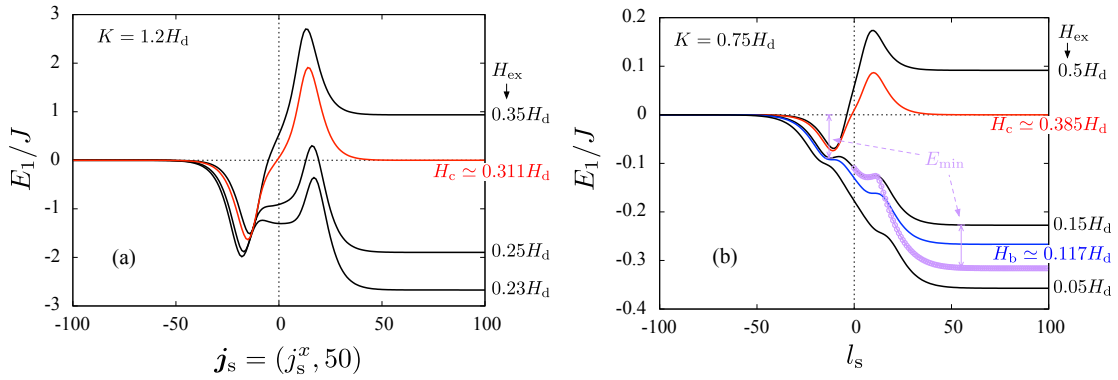

Figure 4.32: Energy profiles of (a) isolated skyrmion and (b) soliton for finite values of easy-axis anisotropy. The values are designated in the insets. The profiles are based on the solutions constructed by Method I, and the red and blue lines are the critical field of the nucleation-type phase transition and the barrier field, respectively. The values of the magnetic field are shown on the right side of each panel. The purple circles in the panel (b) are the energy profile based on Method II for $H_{\rm ex} = 0.15H_{\rm d}$.

small anisotropy, and the soliton enters the system instead of the skyrmion. For the relatively large anisotropy, the uniform state holds, and it is reasonable because the easy-axis anisotropy stabilizes the uniform state.

Interestingly, the energy profiles for the finite anisotropy are different from those we have seen before. The energy profiles for several values of the magnetic field for skyrmion and soliton cases are shown in Fig. 4.32 for the finite values of anisotropy. The values of the anisotropy and the magnetic field are shown in the figure. The left panel (a) is for the skyrmion and has no barrier field. The slope of the energy at the origin becomes zero for some value of field, but the surface barrier still exists. When we decrease the field further, the local minimum appears inside the system in addition to that outside the system. This double-local minima structure appears also in the soliton case more clearly as seen in the panel (b). The surface barrier of a soliton vanishes in contrast to that of a skyrmion. Thus we explain the energy profile of the soliton instead. At some field between $H_{\rm c}$ and $H_{\rm b}$ the slope at the origin becomes zero, and for the lower field, the additional local minimum structure appears inside the system, which is the same as in the skyrmion case. This structure can be obtained using Method II, as shown in Fig. 4.32 with purple circles. The deviation between the purple circles and the black curve originates from the interaction with the surface modulation and the energy gain of the surface modulation. In this case, the surface modulation is described by the virtual soliton at the point giving the local minimum outside the system rather than that inside the system. The virtual barrier, i.e. the presence of the local maximum outside the system, does not allow the entry of the solitons. Because of this, it is difficult to achieve the local minimum point inside the system, but we emphasize that it is in principle possible that the soliton is trapped by the

relatively deep potential well near the surface. Then we lower the field and finally achieve the barrier field at which the local minimum and maximum inside the system meet for the anisotropy ranging from 0.4 to 1. Below the barrier field, solitons can enter the system as well as the previous cases.

In conclusion of this subsection, we summarize the two dimensional system in decreasing field. The surface barrier always exists for a skyrmion when it is (meta)stable. Below the instability field, a skyrmion elongates to be a soliton. Note that the surface barrier of a soliton is still present, and the uniform state is maintained under the metastable dynamics. Thus we do not expect a sharp jump owing to the entry of many skyrmions in contrast to the soliton case. In addition, the instability of a skyrmion does not allow the drastic change of the metastable state either.

4.9 Summary of this chapter

In this chapter, we have investigated the uniaxial chiral magnet under tilted magnetic field. Laliena *et al.* obtained the ground state phase diagram, and found two multicritical points and discontinuous phase transition between two continuous phase transitions[86]. Following de Gennes's classification, continuous phase transitions are distinguished as the instability-type and nucleation-type[84, 101]. We have clarified the mechanism of the phase transitions and relation to solitons on the basis of the linear analysis. This analysis gives a clear picture of a single-q to the instability-type phase transition occurring at around $H_{\rm ex}^x \sim 0$. This transition can be described by the Landau theory of a distorted conical order. Since the Landau theory can describe the tricritical point, we expand the microscopic energy functional to obtain the Landau energy using the distorted conical order parameter and calculate the phase boundary and the location of the tricritical point. They are consistent with the numerical results, and in this sense our Landau expansion is valid.

When $H_{\rm ex}^z = 0$, the phase transition is nucleation-type and also continuous, but solitons play important roles there[83, 84]. This transition cannot be characterized by a small and local order parameter with a single q, but the winding number of solitons can be a generalized order parameter. This nucleation-type continuous phase transition line terminates at the multicritical point at which the soliton tail changes from a decay without oscillation to that with oscillation. This is equivalent to the change of the soliton interaction from repulsive to attractive.

We have also clarified the region where an isolated soliton can exist, and name its boundary in the uniform state the H_0 line. This line gives the upper bound of the magnetic field regarding the experimental condition for observing remnants of solitons. We have found that the main mechanism of the instability of an isolated soliton is due to the motion of spins towards the helical axis.

We have studied the surface barriers of repulsive and attractive solitons and calculated the barrier field $H_{\rm b}$ at which the surface barrier vanishes. The field $H_{\rm b}$ agrees with the field at which magneto-resistance in micrometer-sized samples is experimentally observed to jump.

We have concluded that the origin of hysteresis in micrometer-sized $Cr_{1/3}NbS_2$ is the surface barrier of solitons rather than the discontinuous phase transition in the bulk. In addition, we have constructed the surface configuration[107, 143, 144] on the basis of a virtual soliton outside the system. This picture holds even when solitons are unstable in the bulk. We have also study the surface barrier of skyrmions, which have similar structure in the energy profile. A skyrmion cannot enter the system from the surface and has an elongation instability field, which drives it into a soliton structure. Below this instability field, a soliton is still metastable and has a surface barrier and thus the uniform state is maintained in decreasing field. Hence we cannot expect no sharp jump related to skyrmions. In the presence of the anisotropy along the magnetic field and perpendicular to the DM vector, the energy profiles of solitons and skyrmions become more complicated and another local minimum appears inside the system.

We have understood the properties of the bulk-size system and micrometer-sized system under the tilted magnetic field without thermal fluctuation on the basis of the tilted chiral solitons.

Chapter 5

Summary and perspective

We have studied effects of magnetic field on a spin model of uniaxial chiral magnets such as $Cr_{1/3}NbS_2$ by use of analytical and numerical calculations. In this thesis we neglect temperature effects, but have found rich properties in this system depending on the field direction. We have clarified the physical properties inherent in the chiral magnets, particularly in non-reciprocal magnon dynamics in the conical state, ground states phase diagram in terms of soliton and single-q pictures, and metastable states, and elucidated richness induced by the field component parallel to the helical axis.

In Chap. 3, we have clarified the spectral structure of non-reciprocal spin waves when magnetic field is applied parallel to the helical axis. Transverse dynamical spin structure factor has two branches of peaks, and the intensity of one branch increases while the other's decreases with increasing field. The non-reciprocity grows in the spectral intensity although the two branches of magnon energy are always reciprocal for the field below the saturation strength. The spectral intensity is related to the eigenvectors of non-reciprocal magnons, in addition to the eigenenergies.

In Chap. 4, we have studied properties of chiral solitons[83, 84, 101, 138] under tilted magnetic field and their roles in the phase transitions of classical spins at zero temperature. Laliena *et al.*[86, 138] determined the phase diagram consisting of one ordered phase and one disordered phase in which the spins are polarized by magnetic field, which are separated by a single phase boundary. Moreover, they showed that two multicritical points separate the phase boundary into two continuous phase transition lines and one discontinuous phase transition line in between. This phase diagram has the same structure as that studied by Schaub and Mukamel[101] by regarding the parallel component $H^z_{\rm ex}$ as temperature T. We have performed a linear analysis of small deviation from the uniform spin structure in Sect. 4.3. This analysis categorizes the phase transitions into three types and reproduces the previous result of Laliena *et al.*[86, 138]: instability-type continuous phase transition, nucleation-type continuous phase transition, and discontinuous phase transition. Following Schaub and Mukamel[101], we call in this thesis the point separating the discontinuous and nucleation-type continuous phase transitions the *multicritical point*, and the other point separating the

discontinuous and instability-type continuous phase transitions the *tricritical point*. The linear analysis is equivalent to studying the asymptotic behavior of an isolated soliton when it exists. The multicritical point is located in this region and can be understood as the point on the phase boundary at which the soliton interaction changes its sign as done in T–$H_{\rm ex}^x$ phase diagram[101]. The sign change takes place not only on the phase boundary but also away from it. A single-q distorted conical order with small amplitude is described in the same analysis when the tail of soliton does not exist. The phase transition between the distorted conical and disordered phases is no longer described by the soliton picture. In Sect. 4.4, we have constructed the Landau energy of the distorted conical order including its higher harmonics in the instability analysis, which is consistent with the linear analysis, and determined the location of the tricritical point using the standard condition that the coefficients of the second and fourth order terms in the Landau expansion vanish.

An isolated soliton becomes unstable at the instability field $\vec{H}_0$, which is higher than the critical field $\vec{H}_{\rm c}$. We have determined its location called the H_0 line and clarified the mechanism of soliton instability for the realistic value of anisotropy for $Cr_{1/3}NbS_2$. It is caused by the spin motion towards the helical axis. We calculate the instability field by using the variational approach with respect to the spin at the soliton center. This idea is also useful in constructing in Sect. 4.8 the surface spin configuration for fields higher than H_0.

The surface barrier exists in a wide region of the phase diagram and leads to hysteresis experimentally observed in micrometer-sized samples. This is not associated with the discontinuous phase transition in the thermodynamic limit. The barrier disappears at field below the critical field $\vec{H}_{\rm c}$. We have calculated this barrier field $\vec{H}_{\rm b}$ and confirmed that the results agree quite well with the jump field at which sharp jumps are experimentally observed in magneto-resistance and magnetic torque in decreasing field. We have also demonstrated that the surface modulation[107, 143, 144] and the surface barrier come from the same physics below the instability field $\vec{H}_0$. Above $\vec{H}_0$, the surface modulation survives but the barrier has no meaning since solitons do not exist in the bulk. These arguments are also applicable to a skyrmion system. In addition, we have found that when solitons interact attractively, their interaction with the surface is also attractive.

We close this thesis with a few perspectives. One is about confirmation of attractive soliton interaction as an experimental evidence of the discontinuous phase transition. A direct identification of the discontinuous phase transition is still difficult because of extrinsic hysteresis caused by the surface barrier. One possibility to check attractive interaction is a Lorentz TEM experiment to observe oscillating spin profiles appearing in the soliton tail, or modulated structures near the surface or the interface of two domains with opposite chiralities[103]. The oscillation is an indication of attractive interaction between the solitons. In addition, we expect to observe a cluster formation of solitons and a soliton bound near the surface as a result of the attractive interaction. The material $Cr_{1/3}NbS_2$ under the tilted field has the following advantages for this purpose. First, attractive solitons are realized even at zero temperature, and thus we do not need to consider thermal fluctuation effects on attractive solitons. These effects are not obvious as explained in Ref. [100]. Second this region is rather wide for realistic values

of parameters. Therefore, controlling magnetic field at low temperatures is more promising than controlling perpendicular field around the critical temperature. We remark that a cluster structure of skyrmions was already observed in the conical phase, which was attributed to attractive interaction[152, 153].

Another perspective is about resonance of spin wave excitations and localized modulation, particularly virtual solitons near the surface or the interface of different chiral domains. One may measure the dynamical spin structure factor to study a chiral soliton lattice, which emerges under magnetic field perpendicular to the DM vector. Although this field direction does not induce non-reciprocity, the data of ferromagnetic resonance experiment has several modes, and some of them have not been identified yet[154]. To discuss them, it should be helpful to understand the whole structure of the excitation spectrum. In addition, a recent detailed experiment suggests the presence of another DM vector in the ab-plane[155], which causes non-reciprocity also in this configuration of magnetic field. We need further careful consideration on the presence of another DM vector in both theoretical and experimental studies, because the non-reciprocal propagation due to different mechanism such as the Damon–Eschbach mode[114–117] is also possible and the effects of the additional DMI on the spin structure are not clear. The resonance mode of virtual solitons is also an important issue. The modulated spin structures near the surface and the interface of two domains with different chiralities can be described by virtual solitons bound in a potential well. Its resonance frequency ω_0 is determined by their mass m and the curvature k at the potential minimum as $\omega_0 = \sqrt{k/m}$. However it is not simple how to formulate the mass m and this is a fundamental new issue. Since in experiments some unidentified resonance modes depend on the system size[155] and the localized modes have different size-dependence from that of the spin wave modes in the bulk, they may be related to these localized modes.

Appendix A

Ginzburg–Landau expansion

This appendix summarizes the systematic derivation of a coarse-grained field theory starting from microscopic Hamiltonians.

A.1 Ising model

We start with the Ising model as the simplest example. The partition function of this model is written as

$$\begin{aligned}\mathcal{Z} = \mathrm{Tr} e^{-\beta\mathcal{H}} &= \sum_{\{S_j\}=\pm 1} e^{-\beta\left[-J\sum_{\langle i,j\rangle} S_i S_j - H_{\mathrm{ex}}\sum_j S_j\right]} \\ &= \sum_{\{S_j\}=\pm 1} e^{\frac{1}{2}\sum_{i,j} J_{ij} S_i S_j + \sum_j H_j S_j} = \sum_{\{\boldsymbol{S}\}} e^{\frac{1}{2}\boldsymbol{S}^{\mathrm{T}}\hat{J}\boldsymbol{S} + \boldsymbol{H}^{\mathrm{T}}\cdot\boldsymbol{S}}. \end{aligned} \tag{A.1}$$

For the positive symmetric matrix A, we have the following formula about the gaussian integral with respect to the N component vector x

$$\int \mathcal{D}\boldsymbol{x} e^{-\frac{1}{2}\boldsymbol{x}^{\mathrm{T}}\hat{A}\boldsymbol{x} + \boldsymbol{x}^{\mathrm{T}}\boldsymbol{S}} \equiv \left(\prod_{i=1}^{N}\int_{-\infty}^{\infty}\frac{dx_i}{\sqrt{2\pi}}\right) e^{-\frac{1}{2}\boldsymbol{x}^{\mathrm{T}}\hat{A}\boldsymbol{x} + \boldsymbol{x}^{\mathrm{T}}\boldsymbol{S}} = \frac{1}{(\det\hat{A})^{1/2}} e^{\frac{1}{2}\boldsymbol{S}^{\mathrm{T}}\hat{A}^{-1}\boldsymbol{S}}. \tag{A.2}$$

Let us regard the interaction matrix $\hat{J}$ as the above inverse matrix $\hat{A}^{-1}$, and we have the interaction term that

$$e^{\frac{1}{2}\boldsymbol{S}^{\mathrm{T}}\hat{J}\boldsymbol{S}} = \frac{\displaystyle\int \mathcal{D}\boldsymbol{x} e^{-\frac{1}{2}\boldsymbol{x}^{\mathrm{T}}\hat{J}^{-1}\boldsymbol{x} + \boldsymbol{x}^{\mathrm{T}}\boldsymbol{S}}}{\displaystyle\int \mathcal{D}\boldsymbol{x} e^{-\frac{1}{2}\boldsymbol{x}^{\mathrm{T}}\hat{J}^{-1}\boldsymbol{x}}}. \tag{A.3}$$

The partition function also can be written down as

$$\mathcal{Z} = \sum_{\{\boldsymbol{S}\}} e^{\frac{1}{2}\boldsymbol{S}^{\mathrm{T}}\hat{J}\boldsymbol{S}+\boldsymbol{H}^{\mathrm{T}}\cdot\boldsymbol{S}} = \sum_{\{\boldsymbol{S}\}} \frac{\int \mathcal{D}\boldsymbol{x} e^{-\frac{1}{2}\boldsymbol{x}^{\mathrm{T}}\hat{J}^{-1}\boldsymbol{x}+(\boldsymbol{x}+\boldsymbol{H})^{\mathrm{T}}\cdot\boldsymbol{S}}}{\int \mathcal{D}\boldsymbol{x} e^{-\frac{1}{2}\boldsymbol{x}^{\mathrm{T}}\hat{J}^{-1}\boldsymbol{x}}} \tag{A.4}$$

$$= \frac{\int \mathcal{D}\boldsymbol{x} e^{-\frac{1}{2}\boldsymbol{x}^{\mathrm{T}}\hat{J}^{-1}\boldsymbol{x}} \sum_{\{\boldsymbol{S}\}} \exp[(\boldsymbol{x}+\boldsymbol{H})^{\mathrm{T}}\cdot\boldsymbol{S}]}{\int \mathcal{D}\boldsymbol{x} e^{-\frac{1}{2}\boldsymbol{x}^{\mathrm{T}}\hat{J}^{-1}\boldsymbol{x}}} \tag{A.5}$$

This kind of transformation is called Hubbard–Stratnovich transformation. Now it is easy to carry out the summation over spins. The partition function as a functional of Hubbard–Stratnovich field $\boldsymbol{x}$ is given by

$$\mathcal{Z} = \frac{\int \mathcal{D}\boldsymbol{x} e^{-\frac{1}{2}\boldsymbol{x}^{\mathrm{T}}\hat{J}^{-1}\boldsymbol{x}} \prod_j 2\cosh[(x_j+H_j)]}{\int \mathcal{D}\boldsymbol{x} e^{-\frac{1}{2}\boldsymbol{x}^{\mathrm{T}}\hat{J}^{-1}\boldsymbol{x}}}$$

$$= \frac{1}{[\det \hat{J}]^{1/2}} \int \mathcal{D}\boldsymbol{x} e^{-\frac{1}{2}\boldsymbol{x}^{\mathrm{T}}\hat{J}^{-1}\boldsymbol{x}+\sum_j \ln[2\cosh(x_j+H_j)]}. \tag{A.6}$$

This Hubbard–Stratonovich field $\boldsymbol{x}$ is not convenient to describe the magnetization properties. Instead, it is better to introduce $\boldsymbol{\varphi}$ such that $\boldsymbol{x} = \hat{J}\boldsymbol{\varphi}$ since the mean value of $\boldsymbol{x}$ is different from the magnetization. Let us rewrite the formula Eq. (A.2) for $\hat{A} = \hat{J}^{-1}$ with respect to $\boldsymbol{\varphi}$.

$$\det \hat{J} \int \mathcal{D}\boldsymbol{\varphi} e^{-\frac{1}{2}\boldsymbol{\varphi}^{\mathrm{T}}\hat{J}\boldsymbol{\varphi}+\boldsymbol{\varphi}^{\mathrm{T}}\hat{J}\boldsymbol{S}} \equiv \det \hat{J} \left(\prod_{i=1}^{N} \int_{-\infty}^{\infty} \frac{d\varphi_i}{\sqrt{2\pi}} \right) e^{-\frac{1}{2}\boldsymbol{\varphi}^{\mathrm{T}}\hat{J}\boldsymbol{\varphi}+\boldsymbol{\varphi}^{\mathrm{T}}\hat{J}\boldsymbol{S}}$$
$$= [\det \hat{J}]^{1/2} e^{\frac{1}{2}\boldsymbol{S}^{\mathrm{T}}\hat{J}\boldsymbol{S}}, \tag{A.7}$$

and the partition function is given by

$$\mathcal{Z} = \frac{\int \mathcal{D}\boldsymbol{\varphi} e^{-\frac{1}{2}\boldsymbol{\varphi}^{\mathrm{T}}\hat{J}\boldsymbol{\varphi}} \sum_{\{\boldsymbol{S}\}} \exp[(\hat{J}\boldsymbol{\varphi}+\boldsymbol{H})^{\mathrm{T}}\cdot\boldsymbol{S}]}{\int \mathcal{D}\boldsymbol{\varphi} e^{-\frac{1}{2}\boldsymbol{\varphi}^{\mathrm{T}}\hat{J}\boldsymbol{\varphi}}}$$

$$= \sqrt{\det \hat{J}} \int \mathcal{D}\boldsymbol{\varphi} e^{-\frac{1}{2}\boldsymbol{\varphi}^{\mathrm{T}}\hat{J}\boldsymbol{\varphi}} \sum_{\{\boldsymbol{S}\}} \exp[(\hat{J}\boldsymbol{\varphi}+\boldsymbol{H})^{\mathrm{T}}\cdot\boldsymbol{S}]. \tag{A.8}$$

The expectation value of φ can be calculated as

$$\langle \boldsymbol{\varphi} \rangle = \frac{1}{\mathcal{Z}} \sqrt{\det \hat{J}} \int \mathcal{D}\boldsymbol{\varphi} \boldsymbol{\varphi} e^{-\frac{1}{2}\boldsymbol{\varphi}^{\mathrm{T}} \hat{J} \boldsymbol{\varphi}} \sum_{\{\boldsymbol{S}\}} \exp[(\hat{J}\boldsymbol{\varphi} + \boldsymbol{H})^{\mathrm{T}} \cdot \boldsymbol{S}] \tag{A.9}$$

$$= \frac{1}{\mathcal{Z}} \lim_{\boldsymbol{y} \to 0} \frac{\partial}{\partial \boldsymbol{y}} \sqrt{\det \hat{J}} \int \mathcal{D}\boldsymbol{\varphi} e^{-\frac{1}{2}\boldsymbol{\varphi}^{\mathrm{T}} \hat{J} \boldsymbol{\varphi}} \sum_{\{\boldsymbol{S}\}} \exp[(\hat{J}\boldsymbol{\varphi} + \boldsymbol{H})^{\mathrm{T}} \cdot \boldsymbol{S} + \boldsymbol{\varphi}^{\mathrm{T}} \cdot \boldsymbol{y}] \tag{A.10}$$

$$= \frac{1}{\mathcal{Z}} \lim_{\boldsymbol{y} \to 0} \frac{\partial}{\partial \boldsymbol{y}} \sum_{\{\boldsymbol{S}\}} \exp\left[\frac{1}{2}(\boldsymbol{S} + \hat{J}^{-1}\boldsymbol{y})^{\mathrm{T}} \hat{J} (\boldsymbol{S} + \hat{J}^{-1}\boldsymbol{y}) + \boldsymbol{H}^{\mathrm{T}} \cdot \boldsymbol{S}\right] \tag{A.11}$$

$$= \frac{1}{\mathcal{Z}} \lim_{\boldsymbol{y} \to 0} \sum_{\{\boldsymbol{S}\}} (\boldsymbol{S} + \hat{J}^{-1}\boldsymbol{y}) \exp\left[\frac{1}{2}(\boldsymbol{S} + \hat{J}^{-1}\boldsymbol{y})^{\mathrm{T}} \hat{J} (\boldsymbol{S} + \hat{J}^{-1}\boldsymbol{y}) + \boldsymbol{H}^{\mathrm{T}} \cdot \boldsymbol{S}\right] \tag{A.12}$$

$$= \frac{1}{\mathcal{Z}} \sum_{\{\boldsymbol{S}\}} \boldsymbol{S} \exp\left(\frac{1}{2}\boldsymbol{S}^{\mathrm{T}} \hat{J} \boldsymbol{S} + \boldsymbol{H}^{\mathrm{T}} \cdot \boldsymbol{S}\right) = \langle \boldsymbol{S} \rangle \,. \tag{A.13}$$

This Hubbard–Stratonovich field may be convenient to be dealt. Finally we take the summation over $\boldsymbol{S}$ and obtain

$$\mathcal{Z} = \sqrt{\det \hat{J}} \int \mathcal{D}\boldsymbol{\varphi} e^{-\frac{1}{2}\boldsymbol{\varphi}^{\mathrm{T}} \hat{J} \boldsymbol{\varphi}} \prod_j 2\cosh\left(\sum_l J_{jl}\varphi_l + H_j\right) \equiv \sqrt{\det \hat{J}} \int \mathcal{D}\boldsymbol{\varphi} e^{-S[\boldsymbol{\varphi}]}, \tag{A.14}$$

$$S[\boldsymbol{\varphi}] = \frac{1}{2}\boldsymbol{\varphi}^{\mathrm{T}} \hat{J} \boldsymbol{\varphi} - \sum_j \ln\left[2\cosh\left(\sum_l J_{jl}\varphi_l + H_j\right)\right]. \tag{A.15}$$

Upon taking the continuum limit, the lattice variables are replaced by contniuous functio $\varphi_l \to \varphi(\boldsymbol{r})$, and the action becomes its functional. Note that the higher order correlations of φ_j have nontrivial connection to those of S_j. However the long range correlation can be simplify, for example as follows:

$$\langle \varphi_i \varphi_j \rangle = \langle S_i S_j \rangle - [J^{-1}]_{ij} \sim \langle S_i S_j \rangle \,. \tag{A.16}$$

A.2 Chiral magnet

In this case, each site spin takes an arbitrary point on the 2-sphere S_2 $\vec{S}_j = (S_j^x, S_j^y, S_j^z)$ with $(S_j^x)^2 + (S_j^y)^2 + (S_j^z)^2 = 1$, and the Hamiltonian includes the Dzyaloshinskii–Moriya term in one bond direction, in which we take the z-axis and call it the chiral axis. We introduce $J_\parallel$ and $J_\perp$ describing the symmetric exchange interaction along bond directions with the DMI and

without the DMI, respectively.

$$\mathcal{Z} = \mathrm{Tr}_{\{\boldsymbol{S}\}} e^{-\beta\mathcal{H}} = \int \left(\prod_j d\Omega_j\right) e^{-\beta\left[-\sum_{\langle i,j\rangle} J_\zeta \vec{S}_i\cdot\vec{S}_j - \sum_{\langle i,j\rangle_z} D(\vec{S}_i\times\vec{S}_j)_z - \vec{H}_{\mathrm{ex}}\cdot\sum_j \vec{S}_j\right]} \tag{A.17}$$

$$= \mathrm{Tr}_{\{\boldsymbol{S}\}} e^{\frac{1}{2}\sum_{\langle i,j\rangle,\mu,\nu} S_i^\mu J_{ij}^{\mu\nu} S_j^\nu + \sum_{j,\mu} H^\mu S_j^\mu} = \mathrm{Tr}_{\{\boldsymbol{S}\}} e^{\frac{1}{2}\sum_{\langle i,j\rangle} \vec{S}_i \check{J}_{ij} \vec{S}_j^\nu + \sum_j \vec{H}\vec{S}_j}$$

$$= \mathrm{Tr}_{\{\boldsymbol{S}\}} e^{\frac{1}{2}\boldsymbol{S}^{\mathrm{T}}\hat{J}\boldsymbol{S} + \boldsymbol{H}^{\mathrm{T}}\cdot\boldsymbol{S}}, \tag{A.18}$$

where $d\Omega_j = d\cos\theta_j d\phi_j/(4\pi)$ for $\vec{S}_j = (\sin\theta_j\cos\phi_j, \sin\theta_j\sin\phi_j, \cos\theta_j)$ The matrix $\check{J}_{ij}$ is a 3×3 matrix in spin space for the site pair i and j, and it is not necessarily symmetric. Vectors $\boldsymbol{S}$ and $\boldsymbol{H}$ have $3N$ components, and $\hat{J}$ is a $3N\times 3N$ symmetric matrix. For later convenience, we introduce symmetric matrix $\check{J}_\parallel$ and antisymmetric matrix $\check{J}_D$ such that $\check{J}_{jj\pm\hat{z}} = \check{J}_\parallel \pm \check{J}_D$ as well as $\check{J}_{jj+\hat{\delta}} = \check{J}_\perp$ for $\hat{\delta} = \pm\hat{x}, \pm\hat{y}$. The Hubbard–Stratonivich transformation is performed in the same way, and we obtain with the molecular field $\vec{H}_j^{\mathrm{eff}}[\boldsymbol{\varphi}] = \sum_l \check{J}_{jl}\vec{\varphi}_l + \vec{H}_j$ that

$$\mathcal{Z} = \sqrt{\det\hat{J}} \int \mathcal{D}\boldsymbol{\varphi} e^{-\frac{1}{2}\boldsymbol{\varphi}^{\mathrm{T}}\hat{J}\boldsymbol{\varphi}} \mathrm{Tr}_{\{\boldsymbol{S}\}} \left\{\exp[(\hat{J}\boldsymbol{\varphi} + \boldsymbol{H})^{\mathrm{T}}\cdot\boldsymbol{S}]\right\} \tag{A.19}$$

$$= \sqrt{\det\hat{J}} \int \mathcal{D}\boldsymbol{\varphi} e^{-\frac{1}{2}\boldsymbol{\varphi}^{\mathrm{T}}\hat{J}\boldsymbol{\varphi}} \prod_j \frac{\sinh\left|\vec{H}_j^{\mathrm{eff}}[\boldsymbol{\varphi}]\right|}{\left|\vec{H}_j^{\mathrm{eff}}[\boldsymbol{\varphi}]\right|} \equiv \sqrt{\det\hat{J}} \int \mathcal{D}\boldsymbol{\varphi} e^{-S[\boldsymbol{\varphi}]}, \tag{A.20}$$

$$S[\boldsymbol{\varphi}] = \frac{1}{2}\boldsymbol{\varphi}^{\mathrm{T}}\hat{J}\boldsymbol{\varphi} - \sum_j \ln\left(\frac{\sinh\left|\vec{H}_j^{\mathrm{eff}}[\boldsymbol{\varphi}]\right|}{\left|\vec{H}_j^{\mathrm{eff}}[\boldsymbol{\varphi}]\right|}\right). \tag{A.21}$$

We have the following:

$$\langle\vec{\varphi}_j\rangle = \langle\vec{S}_j\rangle\,,\ \langle\varphi_j^\mu\varphi_l^\nu\rangle \sim \langle S_j^\mu S_l^\nu\rangle \text{ for } \mu,\nu\in\{x,y,z\}. \tag{A.22}$$

Let us check that the stationary condition of the action with respect to $\vec{\varphi}_j$ leads to the mean field equation, Take the variation of the action:

$$\frac{\delta S[\boldsymbol{\varphi}]}{\delta\vec{\varphi}_j} = \sum_l \check{J}_{jl}\vec{\varphi}_l - \sum_l \left(\coth|\vec{H}_l^{\mathrm{eff}}[\boldsymbol{\varphi}]| - \frac{1}{|\vec{H}_l^{\mathrm{eff}}[\boldsymbol{\varphi}]|}\right)\frac{\partial|\vec{H}_l^{\mathrm{eff}}[\boldsymbol{\varphi}]|}{\partial\vec{\varphi}_j} \tag{A.23}$$

$$= \sum_l \check{J}_{jl}\vec{\varphi}_l - \sum_l \left(\coth|\vec{H}_l^{\mathrm{eff}}[\boldsymbol{\varphi}]| - \frac{1}{|\vec{H}_l^{\mathrm{eff}}[\boldsymbol{\varphi}]|}\right)\sum_\nu \frac{\partial|\vec{H}_l^{\mathrm{eff}}[\boldsymbol{\varphi}]|}{\partial\{\vec{H}_l^{\mathrm{eff}}[\boldsymbol{\varphi}]\}^\nu}\frac{\partial\{\vec{H}_l^{\mathrm{eff}}[\boldsymbol{\varphi}]\}^\nu}{\partial\vec{\varphi}_j} \tag{A.24}$$

$$= \sum_l \check{J}_{jl}\left\{\vec{\varphi}_l - \left(\coth|\vec{H}_l^{\mathrm{eff}}[\boldsymbol{\varphi}]| - \frac{1}{|\vec{H}_l^{\mathrm{eff}}[\boldsymbol{\varphi}]|}\right)\frac{\vec{H}_l^{\mathrm{eff}}[\boldsymbol{\varphi}]}{|\vec{H}_l^{\mathrm{eff}}[\boldsymbol{\varphi}]|}\right\} = 0 \tag{A.25}$$

$$\to\vec{\varphi}_l = \left(\coth|\vec{H}_l^{\mathrm{eff}}[\boldsymbol{\varphi}]| - \frac{1}{|\vec{H}_l^{\mathrm{eff}}[\boldsymbol{\varphi}]|}\right)\frac{\vec{H}_l^{\mathrm{eff}}[\boldsymbol{\varphi}]}{|\vec{H}_l^{\mathrm{eff}}[\boldsymbol{\varphi}]|} = f(|\vec{H}_l^{\mathrm{eff}}[\boldsymbol{\varphi}]|)\frac{\vec{H}_l^{\mathrm{eff}}[\boldsymbol{\varphi}]}{|\vec{H}_l^{\mathrm{eff}}[\boldsymbol{\varphi}]|}. \tag{A.26}$$

This is nothing but the self consistent equation.

Next we try to derive the GL equation. We consider the expansion of the logarithmic term in the action.

$$\ln \frac{\sinh x}{x} \simeq \ln \left(1 + \frac{x^2}{6} + \frac{x^4}{120} + \cdots \right) \sim \frac{1}{6}\left(x^2 - \frac{1}{5}x^4\right) + O(x^6). \tag{A.27}$$

We neglect the irrelevant terms on the order of $\mathcal{O}(\varphi^6, H_{\rm ex}^2, \varphi^3 H_{\rm ex})$. Note that

$$|\vec{H}_j^{\rm eff}|^2 = |\sum_l \check{J}_{jl}\vec{\varphi}_l|^2 + 2\sum_l \vec{H}_j \cdot \check{J}_{jl}\vec{\varphi}_l + |\vec{H}_j|^2. \tag{A.28}$$

Therefore we obtain the action expanded with respect to small φ and H as

$$S[\boldsymbol{\varphi}] = \frac{1}{2}\boldsymbol{\varphi}^{\rm T}\hat{J}\boldsymbol{\varphi} - \frac{1}{6}\sum_j \left\{ |\sum_l \check{J}_{jl}\vec{\varphi}_l|^2 + 2\sum_l \vec{H}_j \cdot \check{J}_{jl}\vec{\varphi}_l - \frac{1}{5}|\sum_l \check{J}_{jl}\vec{\varphi}_l|^4 \right\}. \tag{A.29}$$

We take the Fourier transform of $\vec{\varphi}_j$ as $\vec{\varphi}_j = \sum_{\boldsymbol{k}} \vec{\varphi}_{\boldsymbol{k}} e^{{\rm i}\boldsymbol{k}\cdot\boldsymbol{r}_j}$, though we use the different definition with respect to the normalization for the Fourier transform of the interaction matrix:

$$N^{-1}\sum_{i,j} \check{J}_{ij} e^{{\rm i}\boldsymbol{k}\cdot\boldsymbol{r}_i - {\rm i}\boldsymbol{k}'\cdot\boldsymbol{r}_j} = N^{-1}\sum_{i,j} \check{J}_{ij} e^{{\rm i}\frac{\boldsymbol{k}+\boldsymbol{k}'}{2}\cdot\boldsymbol{r}_{ij} + {\rm i}(\boldsymbol{k}-\boldsymbol{k}')\cdot\boldsymbol{R}_{ij}} = \sum_{\boldsymbol{r}_{ij}} \check{J}_{ij} e^{{\rm i}\boldsymbol{k}\cdot\boldsymbol{r}_{ij}} \delta_{\boldsymbol{k},\boldsymbol{k}'} = \check{J}_{-\boldsymbol{k}}\delta_{\boldsymbol{k},\boldsymbol{k}'}, \tag{A.30}$$

$$\boldsymbol{R}_{ij} = \frac{\boldsymbol{r}_i + \boldsymbol{r}_j}{2},\ \boldsymbol{r}_{ij} = \boldsymbol{r}_i - \boldsymbol{r}_j. \tag{A.31}$$

We have the relation that $\check{J}_{\boldsymbol{k}}^* = \check{J}_{-\boldsymbol{k}} = \check{J}_{\boldsymbol{k}}^{\rm T}$.[1] The explicit form in this case is given by

$$\check{J}_{\boldsymbol{k}} = \sum_{\delta=x,y} \check{J}_\perp 2\cos k_\delta a + \check{J}_\parallel 2\cos k_z a - \check{J}_D 2{\rm i}\sin k_z a \tag{A.32}$$

We obtain the action using to $\vec{\varphi}_{\boldsymbol{k}}$ as follows:

$$\begin{aligned} S[\boldsymbol{\varphi}] = \frac{N}{2}\sum_{\boldsymbol{k}} \vec{\varphi}_{-\boldsymbol{k}}^{\rm T}\check{J}_{\boldsymbol{k}}\vec{\varphi}_{\boldsymbol{k}} - \frac{N}{6}\Bigg[&\sum_{\boldsymbol{k}} |\check{J}_{\boldsymbol{k}}\vec{\varphi}_{\boldsymbol{k}}|^2 + 2\sum_{\boldsymbol{k}} \frac{\vec{H}_{-\boldsymbol{k}}}{N}\check{J}_{\boldsymbol{k}}\vec{\varphi}_{\boldsymbol{k}} \\ &- \frac{1}{5}\sum_{\boldsymbol{k}_1,\boldsymbol{k}_2,\boldsymbol{k}_3,\boldsymbol{k}_4} \delta_{\boldsymbol{k}_1+\boldsymbol{k}_2+\boldsymbol{k}_3+\boldsymbol{k}_4,\boldsymbol{0}} (\check{J}_{\boldsymbol{k}_1}\vec{\varphi}_{\boldsymbol{k}_1})^{\rm T}(\check{J}_{\boldsymbol{k}_2}\vec{\varphi}_{\boldsymbol{k}_2})(\check{J}_{\boldsymbol{k}_3}\vec{\varphi}_{\boldsymbol{k}_3})^{\rm T}(\check{J}_{\boldsymbol{k}_4}\vec{\varphi}_{\boldsymbol{k}_4}) \Bigg] \end{aligned} \tag{A.33}$$

$$\begin{aligned} = \frac{N}{2}\sum_{\boldsymbol{k}} \vec{\varphi}_{-\boldsymbol{k}}^{\rm T}\check{J}_{\boldsymbol{k}} \left(1 - \frac{\check{J}_{\boldsymbol{k}}}{3}\right)\vec{\varphi}_{\boldsymbol{k}} - \frac{N}{3}\vec{H}\check{J}_{\boldsymbol{k}=0}\vec{\varphi}_{\boldsymbol{k}=0} \\ + \frac{N}{30}\sum_{\boldsymbol{k}_1,\boldsymbol{k}_2,\boldsymbol{k}_3,\boldsymbol{k}_4} \delta_{\boldsymbol{k}_1+\boldsymbol{k}_2+\boldsymbol{k}_3+\boldsymbol{k}_4,\boldsymbol{0}} (\check{J}_{\boldsymbol{k}_1}\vec{\varphi}_{\boldsymbol{k}_1})^{\rm T}(\check{J}_{\boldsymbol{k}_2}\vec{\varphi}_{\boldsymbol{k}_2})(\check{J}_{\boldsymbol{k}_3}\vec{\varphi}_{\boldsymbol{k}_3})^{\rm T}(\check{J}_{\boldsymbol{k}_4}\vec{\varphi}_{\boldsymbol{k}_4}). \end{aligned} \tag{A.34}$$

[1] Note that $\check{J}_{ij}^T = \check{J}_{ji}$

Note that $\vec{H}_{-\boldsymbol{k}} = \vec{H} N \delta_{\boldsymbol{k},0}$. The norm means that

$$(\check{J}_{\boldsymbol{k}}\vec{\varphi}_{\boldsymbol{k}})^{\dagger}(\check{J}_{\boldsymbol{k}}\vec{\varphi}_{\boldsymbol{k}}) = (\check{J}_{-\boldsymbol{k}}\vec{\varphi}_{-\boldsymbol{k}})^{\mathrm{T}}(\check{J}_{\boldsymbol{k}}\vec{\varphi}_{\boldsymbol{k}}). \tag{A.35}$$

We consider long wave-length modulations and fluctuations, i.e., expand quantities in $\boldsymbol{k}$. The first term is reduced as

$$\begin{aligned}\left(\check{J}_{\boldsymbol{k}} - \frac{\check{J}_{\boldsymbol{k}}^2}{3}\right) = \check{J}_{\boldsymbol{k}} - \frac{1}{3}\Big\{4\Big[\check{J}_{\perp}^2(\cos k_x a + \cos k_y a)^2 \\ +2\check{J}_{\perp}\check{J}_{\parallel}(\cos k_x a + \cos k_y a)\cos k_z a + \check{J}_{\parallel}^2 \cos^2 k_z a\Big] \\ -2\mathrm{i}\left[\check{J}_{\perp}(\cos k_x a + \cos k_y a) + \check{J}_{\parallel}\cos k_z a\right]\check{J}_D \sin k_z a - \check{J}_D^2 \sin^2 k_z a\Big\} \qquad \text{(A.36)} \\ = \frac{3T_{\mathrm{c}}^*}{T}(1 - \frac{T_{\mathrm{c}}^*}{T})\check{1} + 2\mathrm{i}(k_z a)\left(2\frac{T_{\mathrm{c}}^*}{T} - 1\right)\check{J}_D + (k_{\perp}a)^2\left(2\frac{T_{\mathrm{c}}^*}{T} - 1\right)\check{J}_{\perp} \\ + \left[\left(2\frac{T_{\mathrm{c}}^*}{T} - 1\right)\check{J}_{\parallel} + (k_z a)^2\left(\frac{D}{T}\right)^2\check{1}_D\right], \qquad \text{(A.37)}\end{aligned}$$

where $T_{\mathrm{c}}^* = (4J_{\perp} + 2J_{\parallel})/3$ and $\check{1}_D = \mathrm{diag}(1,1,0)$. We retain the temperature dependence only for the first term of Eq. (A.37), and for the other terms set T to T_{c}^*. Then we reduce the action to the form

$$\begin{aligned}S[\boldsymbol{\varphi}]/N = -\vec{H}^{\mathrm{T}}\vec{\varphi}_{\boldsymbol{k}=0} + \frac{1}{2}\sum_{\boldsymbol{k}}\Bigg\{\left[3\frac{T - T_{\mathrm{c}}^*}{T_{\mathrm{c}}^*} + \frac{J_{\perp}}{T_{\mathrm{c}}^*}(k_{\perp}a)^2 + \frac{J_{\parallel}}{T_{\mathrm{c}}^*}(k_z a)^2\right]\vec{\varphi}_{-\boldsymbol{k}}^{\mathrm{T}}\vec{\varphi}_{\boldsymbol{k}} \\ +\frac{2\mathrm{i}D}{T_{\mathrm{c}}^*}(k_z a)\left(\varphi_{-\boldsymbol{k}}^x\varphi_{\boldsymbol{k}}^y - \varphi_{-\boldsymbol{k}}^y\varphi_{\boldsymbol{k}}^x\right) + \left(\frac{D}{T_{\mathrm{c}}^*}\right)^2(k_z a)^2\left(\varphi_{-\boldsymbol{k}}^x\varphi_{\boldsymbol{k}}^x + \varphi_{-\boldsymbol{k}}^y\varphi_{\boldsymbol{k}}^y\right)\Bigg\} \\ + \frac{27}{10}\sum_{\boldsymbol{k}_1,\boldsymbol{k}_2,\boldsymbol{k}_3,\boldsymbol{k}_4}\delta_{\boldsymbol{k}_1+\boldsymbol{k}_2+\boldsymbol{k}_3+\boldsymbol{k}_4,\boldsymbol{0}}\vec{\varphi}_{\boldsymbol{k}_1}^{\mathrm{T}}\vec{\varphi}_{\boldsymbol{k}_2}\vec{\varphi}_{\boldsymbol{k}_3}^{\mathrm{T}}\vec{\varphi}_{\boldsymbol{k}_4}. \qquad \text{(A.38)}\end{aligned}$$

Let us take the continuum limit. The procedure is as follows: $\sum_{\boldsymbol{k}} \to V\int d\boldsymbol{k}/(2\pi)^3$, and for $\vec{\varphi}_j = \vec{\varphi}(\boldsymbol{r}_j)$, $\vec{\varphi}_{\boldsymbol{k}} = N^{-1}\sum_j \vec{\varphi}_j e^{-\mathrm{i}\boldsymbol{k}\cdot\boldsymbol{r}_j} = V^{-1}\int d\boldsymbol{r}\vec{\varphi}(\boldsymbol{r})e^{-\mathrm{i}\boldsymbol{k}\cdot\boldsymbol{r}}$. With $N/V = 1/a^3$, we obtain

$$\begin{aligned}S[\boldsymbol{\varphi}] = \int\frac{d\boldsymbol{r}}{a^3}\Bigg\{-\vec{H}^{\mathrm{T}}\vec{\varphi}(\boldsymbol{r}) + \frac{3}{2}\frac{T - T_{\mathrm{c}}^*}{T_{\mathrm{c}}^*}|\vec{\varphi}(\boldsymbol{r})|^2 + \frac{27}{10}|\vec{\varphi}(\boldsymbol{r})|^4 \\ +\frac{J_{\perp}a^2}{2T_{\mathrm{c}}^*}\left(\left|\frac{\partial\vec{\varphi}(\boldsymbol{r})}{\partial x}\right|^2 + \left|\frac{\partial\vec{\varphi}(\boldsymbol{r})}{\partial y}\right|^2\right) + \frac{J_{\parallel}a^2}{2T_{\mathrm{c}}^*}\left|\frac{\partial\vec{\varphi}(\boldsymbol{r})}{\partial z}\right|^2 \\ + \frac{Da}{T_{\mathrm{c}}^*}\left(\varphi^x(\boldsymbol{r})\frac{\partial\varphi^y(\boldsymbol{r})}{\partial z} - \varphi^y(\boldsymbol{r})\frac{\partial\varphi^x(\boldsymbol{r})}{\partial z}\right) + \left(\frac{Da}{T_{\mathrm{c}}^*}\right)^2\left(\left|\frac{\partial\varphi^x(\boldsymbol{r})}{\partial z}\right|^2 + \left|\frac{\partial\varphi^y(\boldsymbol{r})}{\partial z}\right|^2\right)\Bigg\}. \qquad \text{(A.39)}\end{aligned}$$

We can neglect the last term since the DMI is usually weak compared to symmetric exchange interactions. When we recover the inverse temperature in the action, and then we have

$$S[\boldsymbol{\varphi}] = \frac{1}{T}\int \frac{d\boldsymbol{r}}{a^3}\left\{-\vec{H}_{\rm ex}^{\rm T}\vec{\varphi}(\boldsymbol{r}) + \frac{3}{2}(T-T_{\rm c}^*)|\vec{\varphi}(\boldsymbol{r})|^2 + \frac{27}{10}T_{\rm c}^*|\vec{\varphi}(\boldsymbol{r})|^4 \right. \\ + \frac{J_\perp a^2}{2}\left(\left|\frac{\partial\vec{\varphi}(\boldsymbol{r})}{\partial x}\right|^2 + \left|\frac{\partial\vec{\varphi}(\boldsymbol{r})}{\partial y}\right|^2\right) + \frac{J_\parallel a^2}{2}\left|\frac{\partial\vec{\varphi}(\boldsymbol{r})}{\partial z}\right|^2 \\ \left. + Da\left(\varphi^x(\boldsymbol{r})\frac{\partial\varphi^y(\boldsymbol{r})}{\partial z} - \varphi^y(\boldsymbol{r})\frac{\partial\varphi^x(\boldsymbol{r})}{\partial z}\right)\right\}. \tag{A.40}$$

Here we neglected the $\mathcal{O}(D^2)$ term. Let us consider the mean field theory again, and study the critical temperature in the absence of the magnetic field. The fee energy within the stationary approximation is given by $F_{\rm MF} = TS[\boldsymbol{\varphi}_{\rm MF}]$. We assume that $\vec{\varphi}_{\rm MF}(\boldsymbol{r}) = \varphi(\cos qz, \sin qz, 0)$, which reduces the free energy to

$$\frac{F_{\rm MF}}{N} = \frac{3}{2}(T-T_{\rm c}^*)\varphi^2 + \frac{27}{10}T_{\rm c}^*\varphi^4 + \frac{J_\parallel q^2a^2}{2}\varphi^2 + Dqa\varphi^2. \tag{A.41}$$

We minimize this with respect to φ and q. The equations are given by

$$J_\parallel a^2 q + Da = 0 \leftrightarrow q = -\frac{D}{J_\parallel a}, \tag{A.42}$$

$$3(T-T_{\rm c}^*)\varphi + \frac{54}{5}\varphi^3 + J_\parallel q^2a^2\varphi + 2Dqa\varphi = 0 \leftrightarrow \varphi^2 = \frac{5}{54}\left(3T_{\rm c}^* + \frac{D^2}{J_\parallel} - 3T\right). \tag{A.43}$$

Therefore we can evaluate that $T_{\rm c} = T_{\rm c}^* + D^2/3J_\parallel = (4J_\perp + 2J_\parallel + D^2/J_\parallel)/3$. The critical temperature in the lattice model is given by $T_{\rm c}^{\rm lattice} = (4J_\perp + 2\sqrt{J_\parallel^2 + D^2})/3$, and this agrees with $T_{\rm c}$ within the lowest order in $D/J_\parallel$. Next we consider the relations of parameters between the Schaub–Mukamel paper[101] and the lattice model. Let us consider for a while the case of $J_\perp = J_\parallel \equiv J$. Their model is described by the dimensionless quantities. Here we use J and λ as units of energy and spatial length, respectively. Here we introduce λ to expect that it corresponds to the length scale in Ref. [101] though the length scale is not explicitly specified there. We describe the dimensionless version of a quantity o as $\bar{o}$. The free energy density,

which is defined by $F_{\mathrm{MF}}[\boldsymbol{\varphi}] = \int d\boldsymbol{r} f$ is given by

$$\begin{aligned}\bar{f} = \bar{a}^{-3} \Bigg[& -\vec{\bar{H}}_{\mathrm{ex}}^{\mathrm{T}} \vec{\varphi}(\boldsymbol{r}) + \frac{3}{2}(\bar{T} - \bar{T}_{\mathrm{c}}^{*})|\vec{\varphi}(\boldsymbol{r})|^2 + \frac{27}{10}\bar{T}_{\mathrm{c}}^{*}|\vec{\varphi}(\boldsymbol{r})|^4 + \frac{\bar{a}^2}{2}\left|\frac{\partial\vec{\varphi}(\bar{\boldsymbol{r}})}{\partial\bar{\boldsymbol{r}}}\right|^2 \\ & + \bar{D}\bar{a}\left(\varphi^x(\boldsymbol{r})\frac{\partial\varphi^y(\boldsymbol{r})}{\partial\bar{z}} - \varphi^y(\boldsymbol{r})\frac{\partial\varphi^x(\boldsymbol{r})}{\partial\bar{z}}\right)\Bigg] \\ = \bar{a}^{-1} \Bigg[& -\frac{\vec{\bar{H}}_{\mathrm{ex}}^{\mathrm{T}}}{\bar{a}^2}\vec{\varphi}(\boldsymbol{r}) + \frac{3}{2}\frac{\bar{T} - \bar{T}_{\mathrm{c}}^{*}}{\bar{a}^2}|\vec{\varphi}(\boldsymbol{r})|^2 + \frac{27}{10}\frac{\bar{T}_{\mathrm{c}}^{*}}{\bar{a}^2}|\vec{\varphi}(\boldsymbol{r})|^4 + \frac{1}{2}\left|\frac{\partial\vec{\varphi}(\bar{\boldsymbol{r}})}{\partial\bar{\boldsymbol{r}}}\right|^2 \\ & + \frac{\bar{D}}{\bar{a}}\left(\varphi^x(\boldsymbol{r})\frac{\partial\varphi^y(\boldsymbol{r})}{\partial\bar{z}} - \varphi^y(\boldsymbol{r})\frac{\partial\varphi^x(\boldsymbol{r})}{\partial\bar{z}}\right)\Bigg]. \end{aligned} \tag{A.44}$$

We have four parameters now to be fixed independently, which are associated with $\bar{T}$,$\bar{H}_{\mathrm{ex}}$, $\bar{a}$, $\bar{D}$:

$$r = \frac{3}{2}\frac{\bar{T} - \bar{T}_{\mathrm{c}}^{*}}{\bar{a}^2}, \vec{v} = \frac{\vec{\bar{H}}_{\mathrm{ex}}}{\bar{a}^2}, b = \frac{27}{10}\frac{\bar{T}_{\mathrm{c}}^{*}}{\bar{a}^2}, Q = \frac{\bar{D}}{\bar{a}}. \tag{A.45}$$

The values equivalent to those of the Schaub–Mukamel paper are given by

$$1 = b = \frac{27}{10}\frac{\bar{T}_{\mathrm{c}}^{*}}{\bar{a}^2} = \frac{9}{5}\frac{1}{\bar{a}^2} \leftrightarrow \bar{a} = \frac{3}{\sqrt{5}},\ \frac{1}{2} = Q = \frac{\bar{D}}{\bar{a}} \leftrightarrow \bar{D} = \frac{\bar{a}}{2} = \frac{3}{2\sqrt{5}}. \tag{A.46}$$

In this case, the parameters r, v are given by $r = \frac{5}{18}\left(\bar{T} - \frac{2}{3}\right),\ \vec{v} = \frac{5}{9}\vec{\bar{H}}_{\mathrm{ex}}$.

References

[1] N. D. Mermin, Rev. Mod. Phys. **51**, 591 (1979).

[2] J. M. Kosterlitz and D. J. Thouless, J. Phys. C Solid State Phys. **5**, L124 (1972).

[3] J. M. Kosterlitz and D. J. Thouless, J. Phys. C Solid State Phys. **6**, 1181 (1973).

[4] J. M. Kosterlitz, J. Phys. C Solid State Phys. **7**, 1046 (1974).

[5] K. V. Klitzing, G. Dorda, and M. Pepper, Phys. Rev. Lett. **45**, 494 (1980).

[6] R. B. Laughlin, Phys. Rev. B **23**, 5632 (1981).

[7] D. J. Thouless, M. Kohmoto, M. P. Nightingale, and M. den Nijs, Phys. Rev. Lett. **49**, 405 (1982).

[8] M. Kohmoto, Ann. Phys. (N. Y). **160**, 343 (1985).

[9] F. D. M. Haldane, Phys. Rev. Lett. **61**, 2015 (1988).

[10] N. Nagaosa, J. Phys. Soc. Jpn. **75**, 042001 (2006).

[11] N. A. Sinitsyn, J. Phys. Condens. Matter **20**, 023201 (2008).

[12] N. Nagaosa, J. Sinova, S. Onoda, A. H. MacDonald, and N. P. Ong, Rev. Mod. Phys. **82**, 1539 (2010).

[13] C. L. Kane and E. J. Mele, Phys. Rev. Lett. **95**, 226801 (2005).

[14] C. L. Kane and E. J. Mele, Phys. Rev. Lett. **95**, 146802 (2005).

[15] S. Murakami, N. Nagaosa, and S.-C. Zhang, Science **301**, 1348 (2003).

[16] S. Murakami, N. Nagaosa, and S.-C. Zhang, Phys. Rev. Lett. **93**, 156804 (2004).

[17] M. Z. Hasan and C. L. Kane, Rev. Mod. Phys. **82**, 3045 (2010).

[18] X.-L. Qi and S.-C. Zhang, Rev. Mod. Phys. **83**, 1057 (2011).

[19] A. Altland and M. R. Zirnbauer, Phys. Rev. B **55**, 1142 (1997).

[20] A. P. Schnyder, S. Ryu, A. Furusaki, and A. W. W. Ludwig, Phys. Rev. B **78**, 195125 (2008).

[21] A. P. Schnyder, S. Ryu, A. Furusaki, and A. W. W. Ludwig, AIP Conf. Proc. **1134**, 10 (2009).

[22] S. Ryu, A. P. Schnyder, A. Furusaki, and A. W. W. Ludwig, New J. Phys. **12**, 65010 (2010).

[23] Y. Hatsugai, Phys. Rev. Lett. **71**, 3697 (1993).

[24] A. Fert, V. Cros, and J. Sampaio, Nat. Nanotechnol. **8**, 152 (2013).

[25] X. Z. Yu, Y. Onose, N. Kanazawa, J. H. Park, J. H. Han, Y. Matsui, N. Nagaosa, and Y. Tokura, Nature **465**, 901 (2010).

[26] S. S. P. Parkin, M. Hayashi, and L. Thomas, Science **320**, 190 (2008).

[27] A. M. Kosevich, B. A. Ivanov, and A. S. Kovalev, Phys. Rep. **194**, 117 (1990).

[28] A. A. Thiele, Bell Syst. Tech. J. **48**, 3287 (1969).

[29] A. A. Thiele, J. Appl. Phys. **41**, 1139 (1970).

[30] Y. Tu, J. Appl. Phys. **42**, 5704 (1971).

[31] A. N. Bogdanov and Yablonskii, Sov. Phys. JETP **68**, 101 (1989).

[32] A. N. Bogdanov and A Hubert, J. Magn. Magn. Mater. **138**, 255 (1994).

[33] B. A. Ivanov, V. A. Stephanovich, and A. A. Zhmudskii, J. Magn. Magn. Mater. **88**, 116 (1990).

[34] N. Nagaosa and Y. Tokura, Nat. Nanotechnol. **8**, 899 (2013).

[35] N. S. Kiselev, A. N. Bogdanov, R. Schäfer, and U. K. Rößler, J. Phys. D. Appl. Phys. **44**, 392001 (2011).

[36] R. Tomasello, E. Martinez, R. Zivieri, L. Torres, M. Carpentieri, and G. Finocchio, Sci. Rep. **4**, 6784 (2015).

[37] S. Parkin and S.-H. Yang, Nat. Nanotechnol. **10**, 195 (2015).

[38] W. Koshibae, Y. Kaneko, J. Iwasaki, M. Kawasaki, Y. Tokura, and N. Nagaosa, Jpn. J. Appl. Phys. **54**, 053001 (2015).

[39] F. Jonietz, S. Mühlbauer, C. Pfleiderer, A. Neubauer, W. Munzer, A. Bauer, T. Adams, R. Georgii, P. Boni, R. A. Duine, K. Everschor, M. Garst, and A. Rosch, Science **330**, 1648 (2010).

[40] X. Yu, N. Kanazawa, W. Zhang, T. Nagai, T. Hara, K. Kimoto, Y. Matsui, Y. Onose, and Y. Tokura, Nat. Commun. **3**, 988 (2012).

[41] J. Iwasaki, M. Mochizuki, and N. Nagaosa, Nat. Commun. **4**, 1463 (2013).

[42] W. Koshibae and N. Nagaosa, Nat. Commun. **7**, 10542 (2016).

[43] Y. Togawa, Y. Kousaka, K. Inoue, and J.-I. Kishine, J. Phys. Soc. Jpn. **85**, 112001 (2016).

[44] T. Okubo, S. Chung, and H. Kawamura, Phys. Rev. Lett. **108**, 017206 (2012).

[45] A. O. Leonov and M. Mostovoy, Nat. Commun. **6**, 8275 (2015).

[46] S. Hayami, S.-Z. Lin, and C. D. Batista, Phys. Rev. B **93**, 184413 (2016).

[47] T. Nagamiya, "Helical Spin Ordering—1 Theory of Helical Spin Configurations", in *Solid state physics*, Vol. 20 (Elsevier, 1968), pp. 305–411.

[48] I Dzyaloshinsky, J. Phys. Chem. Solids **4**, 241 (1958).

[49] T. Moriya, Phys. Rev. **120**, 91 (1960).

[50] S. Mühlbauer, B. Binz, F. Jonietz, C Pfleiderer, A Rosch, A Neubauer, R. Georgii, and P. Boni, Science **323**, 915 (2009).

[51] C Pappas, E Lelièvre-Berna, P Falus, P. M. Bentley, E Moskvin, S Grigoriev, P Fouquet, and B Farago, Phys. Rev. Lett. **102**, 197202 (2009).

[52] N Kanazawa, J.-H. Kim, D. S. Inosov, J. S. White, N Egetenmeyer, J. L. Gavilano, S Ishiwata, Y Onose, T Arima, B Keimer, and Y Tokura, Phys. Rev. B **86**, 134425 (2012).

[53] M Janoschek, M Garst, A Bauer, P Krautscheid, R Georgii, P Böni, and C Pfleiderer, Phys. Rev. B **87**, 134407 (2013).

[54] X. Z. Yu, N Kanazawa, Y Onose, K Kimoto, W. Z. Zhang, S Ishiwata, Y Matsui, and Y Tokura, Nat. Mater. **10**, 106 (2011).

[55] S Seki, X. Z. Yu, S Ishiwata, and Y Tokura, Science **336**, 198 (2012).

[56] Y. Togawa, T Koyama, K Takayanagi, S Mori, Y Kousaka, J Akimitsu, S Nishihara, K Inoue, A. S. Ovchinnikov, and J.-I. Kishine, Phys. Rev. Lett. **108**, 107202 (2012).

[57] S. Heinze, K. von Bergmann, M. Menzel, J. Brede, A. Kubetzka, R. Wiesendanger, G. Bihlmayer, and S. Blugel, Nat Phys **7**, 713 (2011).

[58] A. Fert and P. M. Levy, Phys. Rev. Lett. **44**, 1538 (1980).

[59] A Crépieux and C Lacroix, J. Magn. Magn. Mater. **182**, 341 (1998).

[60] H. Yang, A. Thiaville, S. Rohart, A. Fert, and M. Chshiev, Phys. Rev. Lett. **115**, 267210 (2015).

[61] T. Moriya and T. Miyadai, Solid State Commun. **42**, 209 (1982).

[62] T. Miyadai, K. Kikuchi, H. Kondo, S. Sakka, M. Arai, and Y. Ishikawa, J. Phys. Soc. Jpn. **52**, 1394 (1983).

[63] Y. Ishikawa and M. Arai, J. Phys. Soc. Jpn. **53**, 2726 (1984).

[64] S. X. Huang and C. L. Chien, Phys. Rev. Lett. **108**, 267201 (2012).

[65] R. L. Melcher, Phys. Rev. Lett. **30**, 125 (1973).

[66] M. Kataoka, J. Phys. Soc. Jpn. **56**, 3635 (1987).

[67] J.-H. Moon, S.-M. Seo, K.-J. Lee, K.-W. Kim, J. Ryu, H.-W. Lee, R. D. McMichael, and M. D. Stiles, Phys. Rev. B **88**, 184404 (2013).

[68] F. Garcia-Sanchez, P. Borys, A. Vansteenkiste, J.-V. Kim, and R. L. Stamps, Phys. Rev. B **89**, 224408 (2014).

[69] K. Zakeri, Y Zhang, J Prokop, T.-H. Chuang, N Sakr, W. X. Tang, and J Kirschner, Phys. Rev. Lett. **104**, 137203 (2010).

[70] M Mena, R. S. Perry, T. G. Perring, M. D. Le, S Guerrero, M Storni, D. T. Adroja, C. Rüegg, and D. F. McMorrow, Phys. Rev. Lett. **113**, 47202 (2014).

[71] K. Di, V. L. Zhang, H. S. Lim, S. C. Ng, M. H. Kuok, J. Yu, J. Yoon, X. Qiu, and H. Yang, Phys. Rev. Lett. **114**, 047201 (2015).

[72] Y. Iguchi, S. Uemura, K. Ueno, and Y. Onose, Phys. Rev. B **92**, 184419 (2015).

[73] S. Seki, Y. Okamura, K. Kondou, K. Shibata, M. Kubota, R. Takagi, F. Kagawa, M. Kawasaki, G. Tatara, Y. Otani, and Y. Tokura, Phys. Rev. B **93**, 235131 (2016).

[74] Y. Onose, T. Ideue, H. Katsura, Y. Shiomi, N. Nagaosa, and Y. Tokura, Science **329**, 297 (2010).

[75] M. Mochizuki, X. Z. Yu, S. Seki, N. Kanazawa, W. Koshibae, J. Zang, M. Mostovoy, Y. Tokura, and N. Nagaosa, Nat. Mater. **13**, 241 (2014).

[76] J. Iwasaki, A. J. Beekman, and N. Nagaosa, Phys. Rev. B **89**, 064412 (2014).

[77] C. Schütte and M. Garst, Phys. Rev. B **90**, 094423 (2014).

[78] E. I. Rashba, Sov. Phys. Solid State **2**, 1109 (1960).

[79] W. L. McMillan, Phys. Rev. B **14**, 1496 (1976).

[80] J.-I. Kishine, K. Inoue, and Y. Yoshida, Prog. Theor. Phys. Suppl. **159**, 82 (2005).

[81] I. E. Dzyaloshinskii, Sov. Phys. JETP **19**, 960 (1964).

[82] I. E. Dzyaloshinskii, Sov. Phys. JETP **20**, 223 (1965).

[83] I. E. Dzyaloshinskii, Sov. Phys. JETP **20**, 665 (1965).

[84] P. G. de Gennes, "Phase Transition and Turbulence: An Introduction", in *Fluctuations, instability, and phase transitions* (Springer US, Boston, MA, 1975), pp. 1–18.

[85] A. A. Abrikosov, *Fundamentals of the Theory of Metals* (North Holland, 1988).

[86] V. Laliena, J. Campo, J.-I. Kishine, A. S. Ovchinnikov, Y. Togawa, Y. Kousaka, and K. Inoue, Phys. Rev. B **93**, 134424 (2016).

[87] C. Pappas, L. J. Bannenberg, E. Lelièvre-Berna, F. Qian, C. D. Dewhurst, R. M. Dalgliesh, D. L. Schlagel, T. A. Lograsso, and P. Falus, Phys. Rev. Lett. **119**, 047203 (2017).

[88] S. A. Brazovskii, Sov. Phys. JETP **41**, 85 (1975).

[89] A. Tonomura, X. Yu, K. Yanagisawa, T. Matsuda, Y. Onose, N. Kanazawa, H. S. Park, and Y. Tokura, Nano Lett. **12**, 1673 (2012).

[90] A. O. Leonov, "Twisted, localized, and modulated states described in the phenomenological theory of chiral and nanoscale ferromagnets", Ph.D thesis (Technische UniversitaÌĹt Dresden, 2011).

[91] A. O. Leonov, arXiv:1409.2177 (2014).

[92] A. E. Jacobs and M. B. Walker, Phys. Rev. B **21**, 4132 (1980).

[93] E. Müller-Hartmann, Phys. Lett. **23**, 521 (1966).

[94] L Kramer, Phys. Lett. **23**, 619 (1966).

[95] A. E. Jacobs, Phys. Rev. B **4**, 3029 (1971).

[96] M. C. Leung, J. Low Temp. Phys. **12**, 215 (1973).

[97] B. I. Halperin and D. R. Nelson, Phys. Rev. Lett. **41**, 121 (1978).

[98] D. R. Nelson and B. I. Halperin, Phys. Rev. B **19**, 2457 (1979).

[99] S. C. Kapfer and W. Krauth, Phys. Rev. Lett. **114**, 035702 (2015).

[100] Y. Nishikawa and K. Hukushima, Phys. Rev. B **94**, 064428 (2016).

[101] B. Schaub and D. Mukamel, Phys. Rev. B **32**, 6385 (1985).

[102] M. Shinozaki, S. Hoshino, Y. Masaki, A. N. Bogdanov, A. O. Leonov, J.-I. Kishine, and Y. Kato, arXiv:1705.07778 (2017).

[103] Y. Togawa, T. Koyama, Y. Nishimori, Y. Matsumoto, S. McVitie, D. McGrouther, R. L. Stamps, Y. Kousaka, J. Akimitsu, S. Nishihara, K. Inoue, I. G. Bostrem, V. E. Sinitsyn, A. S. Ovchinnikov, and J. Kishine, Phys. Rev. B **92**, 220412 (2015).

[104] J.-I. Yonemura, Y. Shimamoto, T. Kida, D. Yoshizawa, Y. Kousaka, S. Nishihara, F. J. T. Goncalves, J. Akimitsu, K. Inoue, M. Hagiwara, and Y. Togawa, Phys. Rev. B **96**, 184423 (2017).

[105] C. P. Bean and J. D. Livingston, Phys. Rev. Lett. **12**, 14 (1964).

[106] P. G. de Gennes, *Superconductivity of Metals and Alloys* (W.A. Benjamin, NewYork, 1966), p. 274.

[107] J. Iwasaki, M. Mochizuki, and N. Nagaosa, Nat. Nanotechnol. **8**, 742 (2013).

[108] L. L. Foldy and S. A. Wouthuysen, Phys. Rev. **78**, 29 (1950).

[109] J.-I. Kishine and A. Ovchinnikov, "Theory of Monoaxial Chiral Helimagnet", in *Solid state physics*, Vol. 66 (Elsevier, 2015), pp. 1–130.

[110] P. De Gennes, Solid State Commun. **6**, 163 (1968).

[111] M. Luban, D. Mukamel, and S. Shtrikman, Phys. Rev. A **10**, 360 (1974).

[112] R. D. Parks, *Superconductivity: Part 2*, Superconductivity (Taylor & Francis, 1969).

[113] P. M. Chaikin and T. C. Lubensky, *Principles of Condensed Matter Physics* (Cambridge University Press, 2000).

[114] R. W. Damon and J. R. Eshbach, J. Phys. Chem. Solids **19**, 308 (1961).

[115] R. Q. Scott and D. L. Mills, Phys. Rev. B **15**, 3545 (1977).

[116] R. E. Camley, Phys. Rev. Lett. **45**, 283 (1980).

[117] N. S. Almeida and D. L. Mills, Phys. Rev. B **37**, 3400 (1988).

[118] F. Garcia-Sanchez, P. Borys, R. Soucaille, J.-P. Adam, R. L. Stamps, and J.-V. Kim, Phys. Rev. Lett. **114**, 247206 (2015).

[119] T. Weber, J. Waizner, G. Tucker, R. Georgii, M. Kugler, A. Bauer, C. Pfleiderer, M. Garst, and P. Böni, arXiv:1708.02098 (2017).

[120] N. E. Bonesteel, Phys. Rev. B **47**, 11302 (1993).

[121] A. Zheludev, G. Shirane, Y. Sasago, N. Kiode, and K. Uchinokura, Phys. Rev. B **54**, 15163 (1996).

[122] A. Zheludev, S. Maslov, G. Shirane, Y. Sasago, N. Koide, and K. Uchinokura, Phys. Rev. Lett. **78**, 4857 (1997).

[123] A Zheludev, S Maslov, G Shirane, Y. Sasago, N. Koide, and K. Uchinokura, Phys. Rev. B **57**, 2968 (1998).

[124] A. Zheludev, S. Maslov, G. Shirane, I. Tsukada, T. Masuda, K. Uchinokura, I. Zaliznyak, R. Erwin, and L. P. Regnault, Phys. Rev. B **59**, 11432 (1999).

[125] S. Mühlbauer, S. N. Gvasaliya, E. Pomjakushina, and A. Zheludev, Phys. Rev. B **84**, 180406 (2011).

[126] S. Mühlbauer, S. Gvasaliya, E. Ressouche, E. Pomjakushina, and A. Zheludev, Phys. Rev. B **86**, 024417 (2012).

[127] J. Chovan, M. Marder, and N. Papanicolaou, Phys. Rev. B **88**, 064421 (2013).

[128] S. Mühlbauer, G. Brandl, M. Månsson, and M. Garst, Phys. Rev. B **96**, 134409 (2017).

[129] A. N. Bogdanov, U. K. Rößler, M. Wolf, and K.-H. Müller, Phys. Rev. B **66**, 214410 (2002).

[130] I Sosnowska, T. P. Neumaier, and E Steichele, J. Phys. C Solid State Phys. **15**, 4835 (1982).

[131] I. Sosnowska and A. Zvezdin, J. Magn. Magn. Mater. **140-144**, 167 (1995).

[132] A. V. Zalessky, A. A. Frolov, T. A. Khimich, A. A. Bush, V. S. Pokatilov, and A. K. Zvezdin, Europhys. Lett. **50**, 547 (2000).

[133] J.-G. Park, M. D. Le, J. Jeong, and S. Lee, J. Phys. Condens. Matter **26**, 433202 (2014).

[134] G. Gitgeatpong, Y. Zhao, P. Piyawongwatthana, Y. Qiu, L. W. Harriger, N. P. Butch, T. J. Sato, and K. Matan, Phys. Rev. Lett. **119**, 1 (2017).

[135] G. Gitgeatpong, M. Suewattana, S. Zhang, A. Miyake, M. Tokunaga, P. Chanlert, N. Kurita, H. Tanaka, T. J. Sato, Y. Zhao, and K. Matan, Phys. Rev. B **95**, 245119 (2017).

[136] K. Chen and D. P. Landau, Phys. Rev. B **49**, 3266 (1994).

[137] A. A. Leonov, A. N. Bogdanov, and U. K. Roessler, arXiv:1001.1292 (2010).

[138] V. Laliena, J. Campo, and Y. Kousaka, Phys. Rev. B **94**, 094439 (2016).

[139] M. Shinozaki, S. Hoshino, Y. Masaki, J.-I. Kishine, and Y. Kato, J. Phys. Soc. Jpn. **85**, 074710 (2016).

[140] J. D. Livingston, Phys. Rev. **129**, 1943 (1963).

[141] M. Shinozaki, Y. Masaki, R. Aoki, Y. Togawa, and Y. Kato, in preparation (2017).

[142] M. Shinozaki and Y. Masaki, unpublished (2017).

[143] M. N. Wilson, E. A. Karhu, D. P. Lake, A. S. Quigley, A. N. Bogdanov, U. K. Rößler, and T. L. Monchesky, Phys. Rev. B **88**, 214420 (2013).

[144] S. A. Meynell, M. N. Wilson, H. Fritzsche, A. N. Bogdanov, and T. L. Monchesky, Phys. Rev. B **90**, 014406 (2014).

[145] H. Du, W. Ning, M. Tian, and Y. Zhang, Europhys. Lett. **101**, 37001 (2013).

[146] S. Rohart and A. Thiaville, Phys. Rev. B **88**, 184422 (2013).

[147] J. Sampaio, V. Cros, S. Rohart, A. Thiaville, and A. Fert, Nat. Nanotechnol. **8**, 839 (2013).

[148] R. Aoki and Y. Togawa, Priv. Commun.

[149] Y. Masaki, R. Aoki, Y. Togawa, and Y. Kato, in preparation (2017).

[150] S.-Z. Lin, C. D. Batista, and A. Saxena, Phys. Rev. B **89**, 24415 (2014).

[151] C. Schütte and M. Garst, Phys. Rev. B **90**, 94423 (2014).

[152] A. O. Leonov, T. L. Monchesky, J. C. Loudon, and A. N. Bogdanov, J. Phys. Condens. Matter **28**, 35LT01 (2016).

[153] J. C. Loudon, A. O. Leonov, A. N. Bogdanov, M. C. Hatnean, and G. Balakrishnan, arXiv:1704.06876 (2017).

[154] F. J. T. Goncalves, T. Sogo, Y. Shimamoto, Y. Kousaka, J. Akimitsu, S. Nishihara, K. Inoue, D. Yoshizawa, M. Hagiwara, M. Mito, R. L. Stamps, I. G. Bostrem, V. E. Sinitsyn, A. S. Ovchinnikov, J. Kishine, and Y. Togawa, Phys. Rev. B **95**, 104415 (2017).

[155] F. J. T. Goncalves and Y. Togawa, Priv. Commun.